

Cutting Force Modelling for Drilling of Fiber-Reinforced Composites

THÈSE N° 5289 (2012)

PRÉSENTÉE LE 17 FÉVRIER 2012

À LA FACULTÉ DES SCIENCES ET TECHNIQUES DE L'INGÉNIEUR
LABORATOIRE DES OUTILS INFORMATIQUES POUR LA CONCEPTION ET LA PRODUCTION
PROGRAMME DOCTORAL EN SYSTÈMES DE PRODUCTION ET ROBOTIQUE

ÉCOLE POLYTECHNIQUE FÉDÉRALE DE LAUSANNE

POUR L'OBTENTION DU GRADE DE DOCTEUR ÈS SCIENCES

PAR

Mihai-Bogdan LAZAR

acceptée sur proposition du jury:

Prof. H. Bleuler, président du jury
Prof. P. Xirouchakis, directeur de thèse
Prof. I. Botsis, rapporteur
Prof. A. Georgiadis, rapporteur
Dr O. Pierard, rapporteur



ÉCOLE POLYTECHNIQUE
FÉDÉRALE DE LAUSANNE

Suisse
2012

Abstract

Although used in a very large variety of applications, drilling is one of the most complex and least understood manufacturing processes. Most of the research on drilling was done in the field of metal cutting for mechanical parts since, in this case, high precision and quality are needed. The use of composite materials in engineering applications has increased in recent years, and in many of these applications drilling is one of the most critical stages in the manufacturing process. This is because it is among the last operations in the manufacturing plan of composite parts. Delamination and extensive tool wear are among the problems which drilling of composite materials are currently facing.

A major difference between metallic and composite plates is their structure: isotropic for metals and anisotropic for composite materials; meaning that while for metallic materials all the structure will respond in a similar manner under the machining loads, the composite structure will have localized responses from the same loads, leading to defects in the internal structure of the remaining work-piece material (i.e. delamination). Delamination can lead to failure in use and parts with such defects are usually discarded. Delamination is not usually visually detectable and special testing is necessary, affecting the costs of the final parts. Delamination during drilling was found to occur at tool entry (peel-up) or tool exit (push-out) and depends on the loads at inter-laminar level.

The work presented in the current thesis focuses in providing reliable information about the thrust and torque distribution along the drill radius (and work-piece thickness) during drilling for varying cutting parameters, drill geometry and work-piece material. Such data should assist in the development of delamination models capable of capturing the influence of the drill geometry and cutting parameters on delamination onset and propagation during both exit and entry of the drill in the work-piece.

A cutting force model is proposed to obtain the elementary cutting force distribution along the drill radius which is able to account for changes in axial feed rate and drill geometry. Based on oblique cutting, forces are considered on both rake and relief faces. A generic relationship in the form of a transformation matrix is developed to relate oblique cutting to drilling, valid for any drill geometry. The mathematical description of the drill geometry in the scope of cutting force modeling has been revised. The kinematics of the drilling process is now taken into account for (i) all geometrical parameters of the drill and for (ii) the elementary cutting forces decomposition. Additionally, a new drill type and its geometric features have been described mathematically and the definition of the geometrical parameters has been generalized so that other drills types or variations could be easily implemented into the model. It proved therefore possible to adopt simpler expressions for the empirical force coefficients of the cutting force model. Up to four empirical coefficients are used, which are calculated from experiments for each work-piece material and drill type.

Most experimental investigations on drilling fiber reinforced composites analyze only the total thrust and torque generated during drilling or separately the forces caused by the chisel edge and cutting lips by drilling with or without a pilot hole. The later type of analysis suggested that is possible to obtain more detailed information about the distribution of the loads in drilling from the analysis of the forces variation during tool entry into the work-piece. Pursuing this direction, an experimental analysis method is proposed to obtain the axial and tangential elementary cutting force distribution along the tool radius or work-piece thickness. The cutting force distribution obtained experimentally was used to calibrate the cutting force model, rather than the total thrust and torque. The experimentally obtained cutting force distribution can also be used alone for analyzing the drilling process (i.e. the loads distribution among the plies of the composite laminate and how this load is influenced by changes in the drill geometry and the cutting conditions).

Keywords: drilling, fiber reinforced composites, cutting forces

Résumé

Bien qu'il soit utilisé dans une très grande variété d'applications, le perçage est l'un des processus les plus complexes et les moins compris de la fabrication. La plupart des recherches sur le perçage a été faite dans le domaine de la découpe de métal pour les pièces mécaniques, car, dans ce cas, une haute précision et la qualité sont nécessaires. L'utilisation de matériaux composites dans les applications d'ingénierie a augmenté ces dernières années, et dans beaucoup de ces applications le perçage est l'une des étapes les plus critiques dans le processus de fabrication. Ceci est dû au fait qu'il est parmi les dernières opérations dans le plan de la fabrication de pièces composites. Le délaminage et l'usure intensive des outils sont parmi les problèmes que le perçage des matériaux composites est actuellement confronté.

Une différence majeure entre les plaques métalliques et composites est leur structure: isotrope pour les métaux et anisotrope pour les matériaux composites, ce qui signifie que, pour les matériaux métalliques toute la structure réagira de la même manière sous les charges d'usinage, la structure composite aura des réponses localisées aux mêmes charges, conduisant à des défauts dans la structure interne du reste de matériaux de la pièce à travailler (à savoir le délaminage). Le délaminage peut conduire à des pannes lors de l'utilisation et les pièces avec de tels défauts sont habituellement mises au rebut. Le délaminage n'est pas détectable visuellement et des tests spéciaux sont nécessaires, affectant les coûts des pièces finales. Délaminage lors du perçage se produit à l'entrée de l'outil (Peel-up) ou à la sortie de l'outil (push-out) et dépend de la charge au niveau inter-laminaire.

Le travail présenté dans cette thèse porte actuellement à fournir des informations fiables sur la répartition du couple et de la poussée le long du rayon de perçage (et l'épaisseur de la pièce à travailler) pendant le perçage pour différents paramètres de coupe, géométries de perçage et matériaux de la pièce à travailler. Ces données devraient aider à l'élaboration de modèles de délaminage capables de capter l'influence de la géométrie de perçage et paramètres de coupe sur l'apparition de l'initiation du délaminage et sa propagation au cours de l'entrée et la sortie de la perceuse dans la pièce à travailler.

Un modèle de effort de coupe est proposé afin d'obtenir la distribution de effort de coupe élémentaire le long du rayon de perçage qui est capable de tenir compte des changements dans la vitesse d'avance axiale et la géométrie de perçage. Basées sur la coupe oblique, les efforts sont considérées à la fois sur la face de coupe et la face de dépouille. Une relation générique sous forme d'une matrice de transformation est développée pour lier la coupe oblique au perçage, valable pour toute géométrie de perçage. La description mathématique de la géométrie de perçage dans le cadre de la modélisation des efforts de coupe a été révisée. La cinématique du processus de perçage est maintenant prise en compte pour (i) tous les paramètres géométriques du perçage et pour (ii) la décomposition des efforts de coupe élémentaires. En plus, un nouveau type de perçage et ses caractéristiques géométriques ont été décrits mathématiquement et la définition des paramètres géométriques a été généralisée de telle façon que d'autres types de perçage ou variations puissent être facilement implémentées dans le modèle. Il s'est avéré donc possible d'adopter des expressions plus simples pour les coefficients d'effort empiriques du modèle d'effort de coupe. Jusqu'à quatre coefficients empiriques sont utilisés, qui sont calculées à partir des expériences pour chaque matériau de pièce à usiner et chaque type de perçage.

La plupart des investigations expérimentales sur le perçage composites en fibres renforcés analysent uniquement la poussée et le couple totaux générés lors du perçage ou séparément les efforts causés par l'arête centrale et les lèvres de coupe par perçage avec ou sans un trou pilote. Le dernier type d'analyse suggère qu'il est possible d'obtenir des informations plus détaillées sur la répartition des charges dans le perçage à partir de l'analyse de la variation des efforts lors de l'entrée de l'outil dans la pièce à travailler. Poursuivant sur cette voie, une méthode d'analyse expérimentale est proposée pour obtenir les distributions des efforts de coupe axiale et tangentielle le long du rayon outil ou l'épaisseur de la pièce à travailler. La distribution de l'effort de coupe obtenue expérimentalement a été utilisée pour calibrer le modèle de l'effort de coupe, plutôt que la poussée et le couple totaux. La distribution de l'effort de coupe obtenue expérimentalement peut aussi être utilisée seule pour analyser le processus de perçage (i.e. la distribution des charges entre les plis du composite stratifié et comment cette charge est influencée par des changements dans la géométrie de perçage et les conditions de coupe).

Mots clé: perçage, composites renforcés de fibre, effort de coupe

Acknowledgments

The research presented in the current thesis has been carried out in the Laboratory of Computer Aided Design and Production (LICP) and the experiments at Electro-Mechanic Workshop (AEM) within the Swiss Federal Institute of Technology Lausanne (EPFL), which exclusively assured the funding.

I would firstly like to thank professor Paul Xirouchakis, the supervisor of my PhD thesis for providing guidance throughout all the stages of the work towards the completion of the thesis. In particular, looking back, I value most his critical comments which I have learned to understand only at later times.

I also deeply appreciate the assistance of Oliver Avram (post-doctoral assistant in LICP at that time) and Karim Collomb (mechanic, AEM) for their assistance in planning and conducting the experimental session.

Many thanks are also addressed to former and current laboratory members and friends passing through or related to EPFL for their support and advices during the last five years.

Lastly, I would like to thank my family, especially my beloved wife and daughter for their constant encouragement and source of inspiration.

Lausanne
24th January 2012

Table of contents

	Page
Abstract (en)	3
Resume (fr)	5
Acknowledgements	7
Table of Contents	9
List of Tables	11
List of Figures	12
List of Symbols	14
1. Introduction	17
1.1 Motivation	18
1.2 Research organization	19
2. Background and theory	23
2.1 Drilling as a machining process	24
2.2 Drilling tools. Classification and terminology	26
2.3 Drilling process analysis	33
2.4 Particularities in drilling fiber reinforced composites	36
3. Cutting force model for drilling	39
3.1 Introduction	40
3.2 Oblique to drilling coordinate system transformation	42
3.3 Elementary cutting forces. Thrust and torque.	46
3.4 Extended derivations	52
3.4.1 Chisel edge angle (ψ) and the web angles (β)	52
3.4.2 Point angle (p) and manufacturer's point angle (p')	53
3.4.3 Cutting angle (μ) and the kinematics of the drilling process	55
3.4.4 Inclination angle (i)	56
3.4.5 2 nd Euler rotation angle (τ)	57
3.4.6 Normal rake angle (α_n) along the cutting lips	58
3.4.7 Relief angle (γ) along the cutting lips	65
3.4.8 Normal rake (α_n) and relief (γ) angles along the chisel edge	69
3.4.9 Element's dimensions (dr , dl , dx) and depth of cut (t_c)	73
3.4.10 Elemental forces in oblique coordinate system (F_{n1} , F_{f1} , F_{n2} , F_{f2})	75
3.5 Mathematical representation of 2 drill geometries	79
3.5.1 Point angle (p)	80
3.5.2 Web angle (β)	81
3.5.3 Inclination angle (i)	81
3.5.4 2 nd Euler rotation angle (τ)	82
3.5.5 Normal rake angle (α_n)	82
3.5.6 Relief angle (γ)	83
3.5.7 Chip flow angle (η_c)	84
3.5.8 Number of flutes (N)	85
4. Experimental analysis of the drilling process	87
4.1 Introduction	88
4.2 Experimental setup	90
4.3 Experimental planning	97
4.4 Experimental analysis of cutting force distribution	101
4.5 Results and discussion	105

	Page
5. Model calibration and validation	111
5.1 Introduction	112
5.2 Empirical coefficients (K_c , K_f and K_p)	114
5.3 Model results and discussion	120
6. Conclusions	129
6.1 On experimental analysis of the drilling process	130
6.2 On modeling the cutting forces in drilling	132
6.3 Outlook	134
7. Bibliography	137

List of Tables

	Page
Table 3.1 – State-of-art in definition of normal rake angle	59
Table 4.1 – Characteristics and mechanical properties of work-pieces	91
Table 4.2 – Summary of experimental setup	96
Table 4.3 – Parameters influencing the cutting force measurements in drilling	98
Table 4.4 – Cutting parameters	100
Table 4.5 – Maximum thrust and torque	105
Table 5.1 – Expressions for specific cutting pressure K_c	114
Table 5.2 - State of art in the definition of elementary cutting forces	116
Table 5.3 – Obtained empirical coefficients	120

List of Figures

	Page
Fig. 2.1 – Orthogonal and oblique cutting models	24
Fig. 2.2 – Nomenclature of a twist drill	27
Fig. 2.3 – Sample cutting force measurement during drilling (CFRP, 10mm thickness, tapered drill reamer (T1), $n=500\text{rpm}$, $f=0.2\text{mm/rev}$) – a) thrust; b) torque	34
Fig. 2.4 – Delamination during drilling of composite laminates	36
Fig. 2.5 – Schematics of fiber cutting during orthogonal cutting model [28]	37
Fig. 3.1 – Oblique and drilling coordinate system for a point A on the cutting lip of a twist drill	42
Fig. 3.2 – Determining the transformation matrix by two consecutive Euler rotations	43
Fig. 3.3 – Elementary cutting forces defined in oblique cutting	46
Fig. 3.4 – Illustration of the extrusion of the work-piece material under the tool for orthogonal cutting [30]	49
Fig. 3.5 – Top view of a generic twist drill introducing the web thickness ($2w$), the chisel edge angle (ψ) and the web angle (β)	52
Fig. 3.6 – The difference between the point angle (p) and the manufacturer's point angle (p')	53
Fig. 3.7 – Sketch to assist in the derivation of the manufacturer's point angle (p')	54
Fig. 3.8 – Local velocities and the cutting angle (μ)	55
Fig. 3.9 – The inclination angle (i) in drilling	56
Fig. 3.10 – Introducing the 2 nd Euler angle of rotation (τ)	57
Fig. 3.11 – Rake angles in oblique cutting	59
Fig. 3.12 – Definition of the helix angle (θ)	60
Fig. 3.13 – Derivation sketches for the normal rake angle (α_n)	61
Fig. 3.14 – Definition of the reference relief angle (γ_0)	65
Fig. 3.15 – Derivation sketch for the static relief angle (γ_s)	67
Fig. 3.16 – Rake (α) and relief (γ) angles along the cutting edge	70
Fig. 3.17 – Static rake angle ($\alpha_{s, \text{ch-T2}}$) for the chisel edge area of a 2-facet twist drill	71
Fig. 3.18 – Definition of the uncut chip area (A_c) in drilling	74
Fig. 3.19 – Components of F_{n1} in X'Y'Z' coordinate system	75
Fig. 3.20 – Components of F_{f1} in X'Y'Z' coordinate system	76
Fig. 3.21 – Components of F_{n2} and F_{f2} in X'Y'Z' coordinate system	78
Fig. 3.22 – Drills modeled mathematically in the current PhD thesis (T1 and T2)	79
Fig. 3.23 – Point angle (p) variation with the radius for the considered drills	80
Fig. 3.24 – Inclination angle (i) variation with the radius for the considered drills	81
Fig. 3.25 – 2 nd Euler angle of rotation (τ) variation with the radius for the considered drills	82
Fig. 3.26 – Normal rake angle (α_n) variation with the radius for the considered drills	83
Fig. 3.27 – Relief angle (γ) variation with the radius for the considered drills	84
Fig. 4.1 – 9255B Kistler dynamometer outlining the useful area for force measurements	91
Fig. 4.2 – Work-piece and hole numbering system	92
Fig. 4.3 – Hole configuration on work-piece and hole numbering system	92
Fig. 4.4 – Experimental setup details of work-piece assembly	93
Fig. 4.5 – Experimental setup overview	93
Fig. 4.6 – Photographs and measured profiles of the drills used in experiments	95
Fig. 4.7 – Map of cutting parameters employed in drilling fiber reinforced composites by references	99
Fig. 4.8 – Sample cutting force measurement during drilling (CFRP, 10mm thickness, tapered drill reamer (T1), $n=500\text{rpm}$, $f=0.2\text{mm/rev}$) – a) thrust; b) torque	101
Fig. 4.9 – Elementary (forces per unit length) axial (a,c,e,g) and tangential (b,d,f,h) force distribution along the drill radius for selected cutting parameters, CFRP/GFRP work-pieces and tapered drill reamer T1	106
Fig. 4.10 – Elementary (forces per unit length) axial (a,c,e,g) and tangential (b,d,f,h) force distribution along the drill radius for selected cutting parameters, CFRP/GFRP work-pieces and 2-facet twist drill T2	107

	Page
Fig. 4.11 – Elementary (forces per unit length) axial (a,c,e,g) and tangential (b,d,f,h) force distribution along the drill radius for selected cutting parameters, CFRP/GFRP work-pieces and 8-facet twist drill T3	108
Fig. 4.12 – Axial (a,c) and tangential (b,d) load distribution on each ply for selected cutting parameters (CFRP, ply thickness 0.25mm)	109
Fig. 4.13 – Axial (a,c) and tangential (b,d) load distribution on each ply for selected cutting parameters (GFRP, ply thickness 0.15mm)	110
Fig. 5.1 – Sample cutting force measurement during drilling (CFRP, 2-facet twist drill (T2), $n=2750\text{rpm}$, $f=0.14\text{mm/rev}$) – a) thrust; b) torque	117
Fig. 5.2 – Influence of spindle speed and axial feed on maximum thrust (a,b) and torque (c,d) respectively for raw data and filtered curves (CFRP, 2-facet twist drill (T2))	118
Fig. 5.3 – Comparison between predicted (M1 model, fitted on the distribution curves) and experimental elementary cutting force components distribution along the radius for $f=0.14\text{mm/rev}$, 2-facet twist drill and both work-piece materials	122
Fig. 5.4 – Comparison between experimental and predicted results for axial elementary cutting force component distribution along the radius for $f=0.14$ and 0.20mm/rev (T2/CFRP)	123
Fig. 5.5 – Comparison between predicted and experimental (filtered) results for maximum thrust and torque for varying axial feed, T2 and both work-piece materials, M1 fitted on the experimental distributions	124
Fig. 5.6 – Comparison between predicted and experimental (filtered) results for maximum thrust and torque for varying axial feed, T2 and both work-piece materials, M1 fitted on the total forces values	125
Fig. 5.7 – Comparison between experimental and predicted results of the current model and [3]	126
Fig. 5.8 – Comparison between predicted (M1 model, fitted on the distribution curves) and experimental elementary cutting force components distribution along the radius for $f=0.14\text{mm/rev}$, tapered-drill reamer and both work-piece materials	127
Fig. 5.9 – Comparison between predicted and experimental (filtered) results for maximum thrust and torque for varying feed rate, T1 and both work-piece materials, M1 fitted on the total forces values	128

List of symbols

Symbol	Description	Equation	Units
r	Radial coordinate		[mm]
R	Outer radius of drill		[mm]
D	Drill diameter		[mm]
R_c	Radius defining the chisel edge area		[mm]
$T1$	Tapered drill reamer – drill no. 1		-
$T2$	2-facet twist drill – drill no. 2		-
$T3$	8-facet twist drill – drill no. 3		-
ρ	Point angle		[°]
ρ'	Manufacturer's point angle	3.49	[°]
ρ_{T1}	Point angle function for drill T1	3.153	[°]
ρ_{T2}	Point angle function for drill T2	3.154	[°]
ρ_l	Point angle along the cutting lips		[°]
i	Inclination angle	3.54, 3.55	[°]
w	Web thickness	3.42	[mm]
ψ	Chisel edge angle	3.42	[°]
θ	Helix angle (reference)		[°]
θ_l	Local helix angle	3.60	[°]
H	Helix pitch	3.60	[mm]
N	Number of flutes		-
N_{T1}	Number of flutes function for drill T1	3.165	-
N_{T2}	Number of flutes function for drill T2	3.166	-
f	Axial feed		[mm/rev]
n	Spindle speed		[rpm]
V_D	Cutting speed at the periphery of the drill	2.1	[mm/min]
f_r	Axial feed rate	2.2	[mm/min]
f_t	Axial feed per tooth	2.3	[mm/rev]
V	Local velocity at radial coordinate r	3.52	[mm/sec]
V_n	Axial velocity	3.50	[mm/sec]
V_t	Tangential velocity at radial coordinate r	3.51	[mm/sec]
μ	Cutting angle	3.53	[°]
β	Web angle	3.43	[°]
β_{T1}	Web angle function for drill T1	3.155	[°]
β_{T2}	Web angle function for drill T2	3.156	[°]
XYZ	Drilling coordinate system		
X'Y'Z'	Local coordinate system of cutting element		
$X_3Y_3Z_3$	Intermediary coordinate system		
$T_{X'Y'Z',XYZ}$	Transformation matrix from X'Y'Z' to XYZ coordinate systems	3.11	
$T_{XYZ,X'Y'Z'}$	Transformation matrix from XYZ to X'Y'Z' coordinate systems	3.9	
$T_{XYZ,X_3Y_3Z_3}$	Transformation matrix from XYZ to $X_3Y_3Z_3$ coordinate systems	3.6	
$T_{X_3Y_3Z_3,X'Y'Z'}$	Transformation matrix from $X_3Y_3Z_3$ to X'Y'Z' coordinate systems	3.8	
τ	2 nd Euler angle of rotation	3.3	[°]
α	Rake angle		[°]
α_n	Normal rake angle	3.91	[°]
α_s	Static rake angle		[°]
$\alpha_{n, ch-T2}$	Normal rake angle for the chisel edge region of drill T2	3.127	[°]
$\alpha_{n, ch-T1}$	Normal rake angle for the chisel edge region of drill T1	3.158	[°]
α_{n-T1}	Normal rake angle function for drill T1	3.159	[°]
α_{n-T2}	Normal rake angle function for drill T2	3.160	[°]
γ	Relief angle	3.110	[°]
γ_s	Static relief angle		[°]
γ_0	Reference relief angle		[°]
γ_n	Normal relief angle	3.111	[°]
γ_{ch-T1}	Relief angle for the chisel edge region of drill T1	3.161	[°]

Symbol	Description	Equation	Units
γ_{T1}	Relief angle function for drill T1	3.162	[°]
γ_{T2}	Relief angle function for drill T2	3.163	[°]
η_c	Chip flow angle	3.164	[°]
dx	Cutting element's width	3.128	[mm]
dr	Cutting element's size along the radial direction		[mm]
dl	Cutting edge length of the element	3.129	[mm]
t_c	Depth of cut	3.131	[mm]
A_u	Uncut chip area	3.16, 3.19	[mm ²]
c_l	Contact length on relief face	3.21	[mm]
R_e	Cutting edge radius		[mm]
α_c	Critical rake angle		[°]
A_c	Contact area on relief face	3.20	[mm ²]
K_c	Specific cutting pressure coefficient (or function)		[N/mm ²]
K_{c1}	Empirical coefficient in the specific cutting pressure function		[N/mm ²]
K_{c2}	Empirical coefficient in the specific cutting pressure function		[N/mm ²]
K_f	Friction coefficient		[-]
K_p	Specific pressure on the relief face		[N/mm ²]
F_{n1}	Elemental force normal on the rake face	3.23	[N]
F_{n1x}	Component of F_{n1}	3.134	[N]
F_{n1y}	Component of F_{n1}	3.135	[N]
F_{n1z}	Component of F_{n1}	3.133	[N]
F_{n1xy}	Projection of F_{n1} on X'Y' plane	3.132	[N]
F_{f1}	Elemental force tangent to the rake face along chip flow direction	3.24	[N]
F_{f1x}	Component of F_{f1}	3.148	[N]
F_{f1y}	Component of F_{f1}	3.149	[N]
F_{f1z}	Component of F_{f1}	3.139	[N]
F_{f1n}	Projection of F_{f1} on plane normal to the cutting edge	3.137	[N]
F_{f1p}	Projection of F_{f1} on the cutting edge	3.138	[N]
F_{f1ny}	Projection of F_{f1} on the tangential direction (Y axis)	3.140	[N]
F_{f1xy}	Projection of F_{f1} on plane X'Y'		[N]
F_{n2}	Elemental force normal to relief face	3.25	[N]
F_{n2y}	Component of F_{n2}		[N]
F_{n2z}	Component of F_{n2}		[N]
F_{f2}	Elemental force tangent to relief face		[N]
F_{f2y}	Component of F_{f2}		[N]
F_{f2z}	Component of F_{f2}		[N]
g_{1x}	Geometric factor	3.33	[-]
g_{1y}	Geometric factor	3.34	[-]
g_{1z}	Geometric factor	3.35	[-]
g_{2x}	Geometric factor	3.36	[-]
g_{2y}	Geometric factor	3.37	[-]
g_{2z}	Geometric factor	3.38	[-]
F_x	Elemental force component along radial direction (lateral)	3.30	[N]
F_y	Elemental force component along tangential direction (torque)	3.31	[N]
F_z	Elemental force component along drill axis direction (thrust)	3.32	[N]
F_Z	Thrust	3.39	[N]
M_Z	Torque	3.40	[N*mm]
F_X	Lateral force	3.41	[N]
F_{z1}	Component of the axial force measured by the dynamometer		[N]
F_{z2}	Component of the axial force measured by the dynamometer		[N]
F_{z3}	Component of the axial force measured by the dynamometer		[N]
F_{z4}	Component of the axial force measured by the dynamometer		[N]
F_{x1+2}	Component of the force along X direction measured by the dynamometer		[N]

Symbol	Description	Equation	Units
F_{x3+4}	Component of the force along X direction measured by the dynamometer		[N]
F_{y1+4}	Component of the force along X direction measured by the dynamometer		[N]
F_{x2+3}	Component of the force along X direction measured by the dynamometer		[N]
a	Distance between the center of the dynamometer plate and the sensor lines along the X axis		[m]
b	Distance between the center of the dynamometer plate and the sensor lines along the Y axis		[m]
x	X coordinate of the drilled hole from the dynamometer's center		[m]
y	Y coordinate of the drilled hole from the dynamometer's center		[m]
h_e	Engagement height	4.3	[mm]
(r_i, h_i)	Coordinate of a point on drill profiles		([mm],[mm])
F_{z_i}	Thrust force for engagement up to point (r_i, h_i)	4.4	[N]
M_{z_i}	Torque for engagement up to point (r_i, h_i)	4.5	[N*m]

Chapter 1

Introduction

1.1 Motivation

The use of long-fiber reinforced composites is extending beyond the initial applications in aerospace and military fields, driven by the advances in manufacturing technologies which made the production process more cost effective. Long fiber reinforced composite materials offer excellent and highly customizable mechanical properties, while being much more lightweight than metallic alloys. However, their processing technology is still in the incipient stage with many restrictions in shape and structure forming, all these restrictions making the part design and manufacture more difficult and expensive. Extensive research and development is currently undergoing to overcome such restrictions and difficulties in various stages of their production. Our work is aiming to bring contributions in the machining processes of these types of materials.

As parts made out of fiber reinforced composites are usually integrated in a mechanical assembly, drilling is the most often encountered machining process in the production plan of such parts. Drilling occurs mainly during the last stages of the manufacturing process in order to create fixing features like holes. Drilling of long-fiber reinforced composites is governed by different physical laws than drilling of metals (brittle chip formation in opposition to plastic deformation) – this being the reason that current industrial practice are not fully understood and optimized.

Two major problems are highlighted: delamination defect and excessive tool wear. Delamination (and overall hole quality) is a critical aspect of the drilling process, as it can lead to failure in use and parts with such defects are usually discarded. Furthermore, delamination is usually not detectable for the eye and special inspection process is necessary. The excessive tool wear make the drilling process of long fiber reinforced composites very expensive as only a limited number of holes can be drilled with one particular drill.

From the process planning point of view, delamination defect was found to be related to the thrust force generated during drilling, force which for a given work-piece and material combination depends on the drill geometry and the cutting conditions. Tool wear is believed to be related to both cutting forces and thermal loads with more complex material properties dependence.

A major difference between metallic and composite components is their structure: isotropic for metals and anisotropic for composite materials; meaning that while for metallic materials all the structure will respond in a similar manner under the machining loads, the composite structure will have localized responses from the same loads, leading to defects in the internal structure of the remaining work-piece material (i.e. delamination). Therefore, we find important for studying the onset of such defects the existence of a cutting force model which can provide the distribution of the loads on the composite structure in addition to only the total loads needed to characterize the drilling process in metallic materials. To obtain such model, a better description of the drill geometry and its relationship to the elemental oblique (or orthogonal) cutting elements is needed than currently developed (which include many assumptions and simplifications). Additionally, the experimental analysis of the drilling process has to be extended to capture the distribution of the cutting forces needed to validate such method. We will then be able to provide better tools for understanding and eliminating delamination defects and to a certain extent reduce tool wear.

1.2 Research organization

Early literature surveys found that limited information on the mathematical modeling of the drills geometries is available. The most detailed mathematical model for drill geometry exists for the conical twist drill, the most commonly employed drill geometry in metal cutting, while other drill types are not addressed almost at all. The exact drill geometry definition remains in most cases proprietary to the manufacturers which are not willing to disclose such information. Literature reports also that the conical twist drill (considered among the best performer in the metal drilling process) is not particularly suitable for drilling fiber-reinforced composites, and new geometries have been proposed (like the tapered drill reamer). The geometrical definition of a drill has to be related to the orthogonal and oblique cutting models. Therefore, in the current PhD thesis we are proposing a generic methodology for defining mathematically the geometry of drill in the light of cutting force modeling (i.e. oblique cutting model).

When looking into the models for predicting cutting forces, a strong theoretical and analytical background was found for metal cutting, while composite cutting theory is only in an incipient stage. Prediction of the cutting forces takes place based orthogonal or oblique cutting models, providing a unified physical analysis for all traditional machining processes based on chip-forming (see figure 2.1). However, even for metals, all models suitable for drilling have a strong empirical component (i.e. no pure analytical model has been proposed and validated). These models are labeled as mechanistic models (with mixed components of analytical and empirical parts). The shear angle theory was initially proposed by Merchant in [1] for metal cutting, and creates the basics of many other later models which extend and complete its application range. However, due to the fact that chip forming mechanism is based on plastic deformation it is only applicable in theory for metal cutting. It was postulated that the cutting of composite materials should be based on fracture mechanics theory, as chip separation occurs rather by fracture than plastic deformation. However, currently no analytical model was proposed for composite machining and all the few proposed models for these materials are either empirical or using the same shear plane theory as for metals.

Using orthogonal or oblique cutting framework to model the cutting forces in drilling allows the determination of the elementary cutting forces on each point on the cutting edges of a drill. To compare the elementary cutting forces with actual experimental data proved rather difficult and of little practical interest in metal drilling. Although many cutting force models for drilling are proposed based on orthogonal and oblique cutting (such as [2], [3], [4], [5] etc.), no attempt was noted to validate the cutting forces distribution along the drill radius, which we believe to be a critical aspect if one is interested how the drilling load is distributed in the structure of the composite work-piece.

Modeling of the cutting forces in drilling as well as mathematical description of the drill geometry for the purpose of cutting force modeling represents the modeling part of the thesis and is presented in chapter 3. In the modeling of the cutting forces the particularities of drilling composite materials have been taken into account, although the approach is mechanistic (i.e. forces are modeled as normal/tangential to cutting surfaces in oblique cutting framework) and could be applicable to metals as well.

The implementation of even an empirical model for predicting the cutting forces according to the oblique cutting model (which by definition needs to be always calibrated by experiments) valid for a wide variety of geometrical cases (for a given case of work-piece and tool material combination) as needed in drilling will allow the estimation of the drilling loads on the composite structure. The distribution of the loads over the hole radius or drilling distance from the tool tip will give an image of the load distribution on each ply in the composite structure and how this distribution varies with the cutting parameters of the drilling process as well as the geometrical parameters of the drill. Comparing these distributions for different tool geometries and cutting conditions the most suitable cutting parameters can be identified and improvements can be proposed for drill design.

The most important aspect in analyzing the load distributions on the composite structure is to analyze the delamination defect. It will be possible to relate the cutting parameters and drill geometry with the

delamination onset and propose means of avoiding it. Based on fracture mechanics, a delamination onset model for drilling was proposed by Hocheng and others ([6], [7], [8] etc.) – a “critical thrust force value” over which limit delamination occurs at drill exit. Due to lack of prediction models of the thrust force for composite materials, the delamination onset model can only be applied after conducting experiments or on-line within a controller. Furthermore, the model assumes a simplified distribution of the thrust force along the drill radius (in its simplest case, constant load acting in the center of the drill). Such assumption does not allow capturing the effect of changing cutting parameters or drill geometrical parameters on the distribution. Our cutting force model will allow accurate off-line prediction of the total thrust force (and additionally torque), but also its distribution on each ply of the laminate. We will show the strong influence of the drill geometry and feed rate on the actual load distribution. Additionally, providing information about the tangential component of the elementary cutting forces (contributing to torque in drilling), such models can be extended to take into consideration mixed-mode fractures (with two or more loading directions – more information on fracture mechanics theory can be found in [9]). In addition to improving the accuracy of predicting exit-delamination, mixed-mode fracture modeling of delamination during drilling might be able to predict entry-delamination, currently not fully understood. Numerical simulations are also used to model delamination onset and propagation ([10], [11], [12], [13], [14] etc.) but they suffer from the same lack of information about the distribution of the drilling forces within the composite structure.

The geometrical modeling of the drill geometry was confirmed and completed by optical measurements for 3 drill types, while the cutting force model was calibrated and validated experimentally for each tool type and 2 different long-fiber composite materials (carbon fiber/epoxy and glass fiber/epoxy) and for a wide range of cutting conditions within practical domain.

The experimental session is fully described in the chapter 4 of the current thesis and the results were published in [15]. When comparing with other experimental measurements of the cutting forces in drilling ([16], [17], [18], [2] etc.), the experiments reported in the thesis have focused on obtaining as well the distribution of the elementary cutting forces in axial and tangential directions along the drill axis and work-piece thickness. The classical method of recording the cutting forces (thrust and torque) throughout the drilling process from drill entry to full engagement and drill exit was used, without employing pilot holes. The distribution was obtained in the post-processing stage of the experimental thrust and torque curves. By considering the drill geometry (cutting profiles) and the cutting parameters, the thrust and torque variation with the drilling time has been split into stages, allowing the determination of the contribution of each stage to the cutting forces, therefore obtaining a distribution of the elementary cutting forces along both the drill radius and work-piece thickness. Experimentally determined distribution curves of axial and tangential force components are for the first time presented and discussed for varying cutting conditions and different drills and work-pieces (composite materials).

The distribution of the elementary cutting forces as well as the total values of thrust and torque have been used to calibrate the cutting force model and to validate its results as detailed in chapter 5. The mechanistic model (presented in chapter 3) uses three empirical coefficients which need to be determined experimentally: specific cutting pressure on the rake face (K_c), friction coefficient (K_f) and specific pressure on the relief face (K_p). These coefficients can also be defined as functions of various parameters (such as normal rake angle – α_n , cutting velocity – V etc.). Several expressions for these coefficients have been tested and the best results were found with a total of only 4 empirical coefficients (i.e. the specific cutting pressure on the rake face – K_c as a function of the normal rake angle α_n , while the other coefficients remain constant). Results show the capabilities of the model to predict the distribution of the elementary cutting force components in axial and tangential directions as well as the total thrust and torque values. Furthermore, the model captures the changes in distribution with the changes in cutting parameters (notably the axial feed rate) and drill type as shown in the experimental results, proving its usefulness for further studies on delamination.

Summarizing, the current PhD thesis proposes a change of focus for the drilling process analysis especially aimed at drilling composite materials towards the distribution of the elementary cutting forces along the cutting edges. Therefore, we propose (i) an improved mechanistic model capable to predicting the distribution of elementary cutting forces along drill radius and validated as such and (ii) a new experimental method to analyze the distribution of the cutting forces along the drill radius and work-piece

thickness. The mechanistic cutting force model for drilling is notable for (i) using up to 4 empirical coefficients (whereas similarly positioned models use 12 empirical coefficients); (ii) considering the forces acting on the relief face; (iii) introducing a transformation matrix to relate the elementary cutting forces defined in oblique cutting framework to drilling (providing an easy and drill-type-independent way of applying to drilling existing or new force models developed in oblique cutting framework); (iv) considering the drilling process kinematics (represented by the cutting angle – μ) for all derivation of the angles defining the geometry of the cutting elements and forces decompositions (whereas previously was ignored at least for the cutting lip region of a drill); (v) mathematically describing a new type of drill (tapered-drill reamer) for the purpose of cutting force modeling.

Chapter 2

Background and theory

2.1 Drilling as a machining process

The current work lies in the scientific and engineering domain of *machining*, which is a more generic term for *metal cutting*, used to refer to machining processes applicable to metallic materials. Machining processes refer to the industrial process in which parts are shaped by removal of unwanted material. The traditional chip-forming processes are turning, boring, drilling and milling, while grinding and honing are abrasive processes. Non-traditional machining processes refer to other means of part shaping, such as electro-discharge, ultrasonic, electrochemical and laser machining.

Drilling is hence a traditional machining process based on chip-forming. In metal cutting, material is removed as a plastically deformed chip of appreciable dimensions, while in the case of some other non-metallic materials (like fiber-reinforced composites hereby treated) the material is removed by fracture [13], and the chips are powder-like [19].

For all traditional machining process based on chip-forming on metallic and non-metallic materials alike, a fairly unified physical analysis can be carried out using basic orthogonal and oblique cutting models (fig. 2.1). In the frame of oblique and orthogonal cutting models one can compare and relate other traditional machining process based on chip-formation and unified theories of the cutting forces development can be applied.

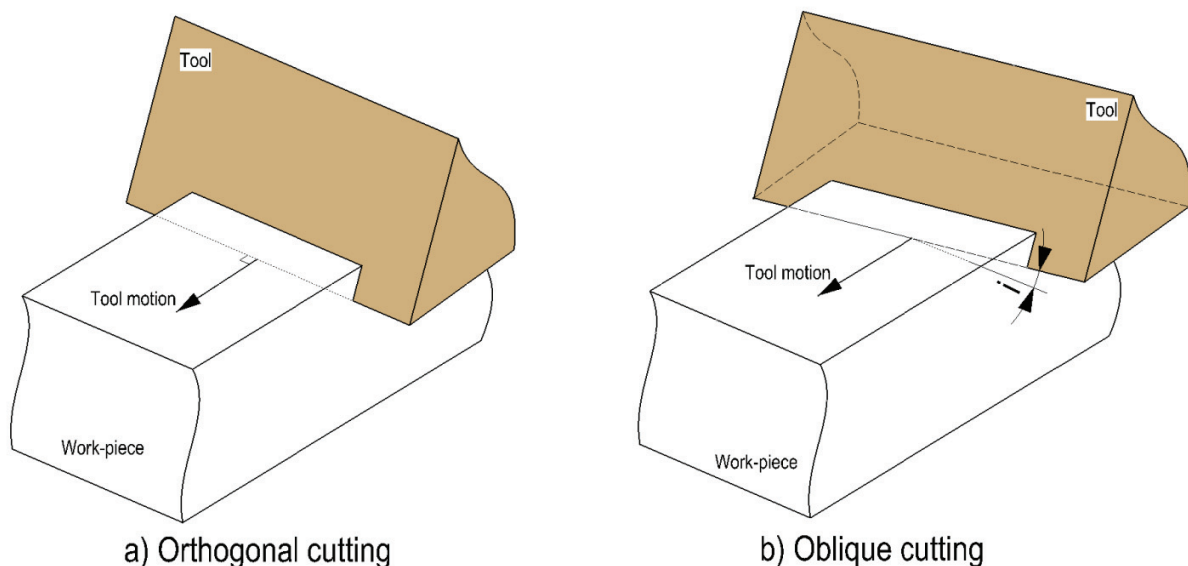


Fig. 2.1 – Orthogonal and oblique cutting models

The difference between oblique and orthogonal cutting models is the inclination angle (i) which is zero in the case of orthogonal cutting. The presence of an inclination angle (i) between the cutting edge and the normal to the tool motion direction (in the plane defined by the cutting edge and tool motion direction) generates a third force component (referred to as lateral force component) when compared with the planar situation of the cutting forces in orthogonal cutting. This effect makes illustrating certain theories and the mathematical derivations associated more complicated. Therefore, in many cases orthogonal cutting is assumed for simplifications reasons ($i=0^\circ$). Most of the traditional machining processes have a geometrical configuration as in the oblique cutting model. However, to validate certain force models specifically designed experiments are conducted according to the orthogonal cutting model.

Drilling, the standard process for producing holes, is among the most common material removal process. Drilling is performed by a tool (named “drill”) which is rotated by the spindle of a machine. The work-piece and the revolving drill (although in some cases the work-piece can be revolving and attached to the

spindle) are positioned by movements of the machine table and/or the spindle assembly. When drilling starts, a linear movement (along the drill rotating axis) occurs between the rotating drill and work-piece. Most of the time drilling operations are performed on specialized drilling machines of different configurations (upright, radial or specialized), but drilling can also be performed on lathes, boring mills and milling machines.

Geometrically, drilling is one of the most complex machining processes, mainly due to the complex geometry of the drills. The difficulty of producing drills with consistent geometries has traditionally limited accuracy, although drill consistency and repeatability has greatly increased recently with the advent of CNC drill grinders. The same complexity of the tool geometry has inhibited the introduction of new tool materials, so that the productivity gains in drilling have lagged those made in turning and milling over the past 30 years. Drilling is applied to a large variety of materials in different industries, but has been mostly studied for metals cutting. In recent years, non-metallic materials (plastics, ceramics and composite materials) are steadily replacing metallic parts in various industries. As the processes governing the cutting process in these novel materials are not yet fully understood and modeled, drilling is often employed as used for metallic structures, leading to a high degree of failures and low efficiencies.

Drilling performance depends on the materials involved, the drill geometry, the cutting parameters (spindle speed and the axial feed rate) and the process conditions (i.e. cooling, lubricant, fixturing etc.). An overview of the current industrial practices with respect to the materials involved and the drill geometries is presented in the next subchapter dedicated to the drilling tools (2.2), while the methods employed in the analysis of the drilling process are presented in subchapter 2.3. Chapter 2.4 introduces the particularities of drilling long fiber reinforced composite materials.

2.2 Drilling tools. Classification and terminology

A drill is an end-cutting tool which has one or more straight or helical flutes, and which may have a hollow body for the passage of cutting fluid and chips during the generation of a hole in a solid or cored material. Drills vary widely in form, dimension, and tolerance. Drills are classified according to the material from which they are made, their lengths, shapes, number of flutes, point characteristics, shank style and size series. The best type of drill for a given application depends on the material to be drilled, its structural characteristics, the hole dimensions, whether the material to be drilled is cored or solid, whether a through or blind hole is required and the characteristics of the machine tool and fixture and the cutting conditions. Selecting the proper type of drill for a given application requires consideration of all these factors. Drill manufacturers offer the same type drill with slight variations in both configuration and metallurgy. These slight variations strongly affect drill life and hole quality especially for small diameter drills.

A wide variety of types of drills are employed. No clear classification currently exists, although we will try to provide a few categories further on based on a review of drilling tools from [20]. Firstly, we note the drills to be either made from one body (usually referred to as regrindable drills) or employing inserts (spade drills, indexable, etc.). Our work focuses on the regrindable drills and hence the indexable drills category will not be further discussed. Regrindable drills are usually limited in the maximum diameter, while the drills with inserts are limited in the minimum diameter. The later are often employed in other industries other the metal cutting (i.e. mining industry) due to the possibility to make them as large as needed, although smaller diameter ones are suitable for metal cutting applications.

Another particular type of drill are the so-called “core drills” (or “trepanning drills”) which only cut an annular groove at the hole periphery and leave a solid core at the hole center. These drills cut more efficiently than conventional drills because they cut less material overall and no material at low velocities near the center of the hole. Core drills are most often used for holes larger than 40mm even though they are available in drills sizes down to 12mm (or even lower). These types of drills are interesting for drilling fiber reinforced composites as well, as the overall thrust (causing delamination) force is much lower than other solutions. However, as the practical applications in fiber reinforced composites often require hole of smaller diameters they cannot normally be employed.

Regrindable drills come in a wide variety of shapes: twist drills (often referred to as regular drills as they are the most common type of drills), gundrills, counterdrills (i.e. stepped or subland drills), pilot drills, drill-reamers etc.

Twist drills are the most common type of drills, but differ widely from their geometry point of view. They are called “twist drill” due to the presence of one or more helical channels for chip evacuation along their body, feature called “flute”. However, the case when the helical angle is zero and the flutes are straight (called “zero helix” or “straight flute”) is also considered as a twist drill type. The experimental work in the current PhD thesis is done with 2 twist drills (2-facet and 8-facet twist drills) and a tapered-drill reamer (which can be regarded as a twist drill with zero helix angle); hence an in-depth view of these types of drills will be presented in the current chapter.

Figure 2.2 introduces the nomenclature of the twist drills features.

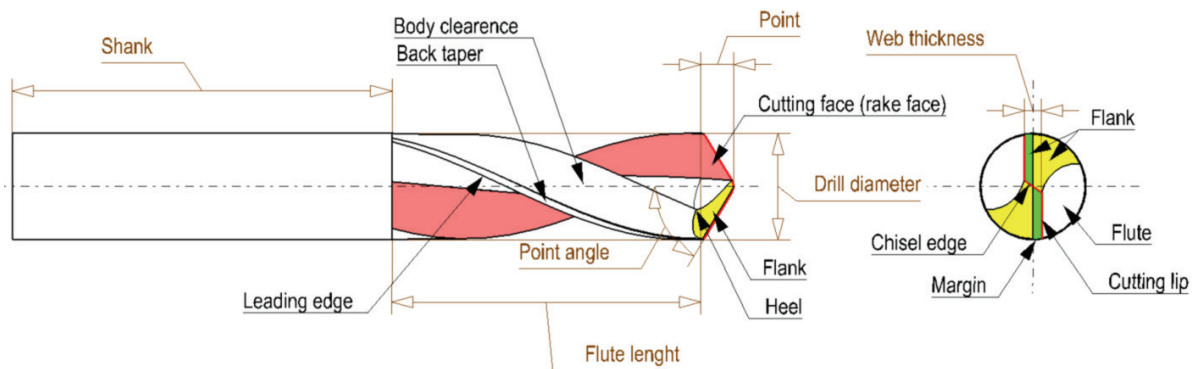


Fig. 2.2 – Nomenclature of a twist drill

The main features of the twist drills that play an important role in the analysis of the drilling process are further discussed below.

a) Cutting edges

In drilling, cutting takes place along the following cutting edges: chisel edge, cutting lips and the leading edges. The chisel edge and the cutting lips are the main cutting areas and are responsible for most of the work in material removal, while the cutting on the leading edge is referred to as “reaming”, with the purpose of finishing the hole surface. Theoretically, no cutting should take place along the leading edge, but due to work-piece deformation under the thrust force, some material is removed. The final hole surface will always have a conical shape (rather than a perfect cylinder) after the removing of the process loads and assuming the deformations of the work-piece are in the domain of elasticity.

Throughout the current thesis the “*cutting edge*” term is used to denote both the chisel and the cutting lip edges, while “*chisel edge*” and “*cutting lip*” terms are used to refer to the particular cutting edges they represent.

In the cutting lips area the cutting is the most efficient and it is desired to have as small as possible size of the chisel edge. The drill strength is dependent directly on the web size, and the chisel edge is the cutting edge associated with the web. Due to highly negative rake angle and low local cutting speeds, the chisel edge area is one of the least effective cutting regions, with the highest elemental cutting forces. Even as the chisel edge area is usually less than 20% of the drill diameter, it seldom accounts for about 50% of the thrust force.

The chisel edge positions the drill before the main cutting lips begin to cut, and stabilizes the drill throughout the cutting process. It also affects the drill’s centering characteristics (skidding and wandering at entry). In some cases additional grinding operations is performed on the tool point to lower the size of the chisel edge, referred to as “*web thinning*”.

The main cutting edges are the cutting lips, which affect the torque, thrust, radial forces, power consumption, drilling temperature, and entry and exit burr formation.

The size and orientation of each cutting edge can be defined from the following parameters:

- Web thickness (w);
- Chisel edge angle (ψ);
- Point angle(-s) (ρ);
- Helix angle (θ);
- Drill diameter (D);

Normally all of these parameters are provided in the drill's specifications or can be fairly easily measured by optical means. Some are introduced in fig.2.2, and more extensively discussed in chapter 3.

b) Helix angle (θ)

The helix angle (θ) is defined as the angle between the leading edge and a parallel to the drill axis. It is the main parameter in the control of the cutting face geometry (rake face) along the cutting lips area of the drill. Helix angle affects the efficiency of the cutting (increasing with the angle) but also the strength of the drill (decreasing with the angle).

Standard helix drills have a helix angle of approximately 30° and are used for drilling malleable and cast irons, carbon steels, stainless steels, hard aluminum alloys, brass, bronze, plexiglass and hard rubber. Low (slow) helix drills have helix angles of approximately 12° . They have increased strength and are used for drilling high-temperature alloys and other hard to machine materials. They are also used for brass, magnesium, aluminum alloys and similar materials, since they provide quick ejection of chips at high penetration rates, especially for shallow holes. High (quick) helix drills have helix angles of approximately 40° , as well as wide, polished flutes and narrow lands. They are used for drilling low strength non-ferrous materials such as aluminum, magnesium, copper, zinc, plastics and for low-carbon steels. Zero helix (straight flute) drills have a 0° helix angle. They are used for materials which produce short chips such as brass, other nonferrous materials and cast iron. They are especially common in horizontal drilling applications. Low or zero helix drills can be used for holes with length to diameter ratios exceeding 4 provided coolants (pressure-fed through the tool) are used to evacuate chips.

The helix angle affects not only the chip ejection capability of a drill, but also its cross-sectional strength, area moments of inertia and rigidity. Some evidence indicates that a spiral flute counters the tendency of a straight flute drill to buckle. According to [20], the torsional stiffness of a drill varies parabolically with the helix angle and reaches a maximum at a helix angle of approximately 28° . The radial stiffness of a drill decreases with increasing helix angle, and reaches a minimum at a helix angle of about 35° . The axial stiffness also varies parabolically with the helix angle, with a minimum occurring at 20° . The allowable thrust and critical cutting speed are also affected by the helix angle, especially for small diameter drills. On the performance side, an increase in helix angle results in increased rake angles (more efficient cutting) and lower torque and thrust.

c) Number of flutes

The number of flutes may vary from one to four, with two being the most common choice. The optimum number of flutes on a drill depends on the drill diameter, the work material, required hole quality and hole exit conditions. Generally, one-flute drills are used for deep hole drilling, two-flute drills are used for most general purpose applications, and three- and four-flute drills are used for close tolerance work and for drilling interrupted holes or through holes in work-pieces with inclined exit surfaces. For a given set of cutting parameters the number of flutes strongly influences the chip load on each flute, hence the loads are shared on more edges. Additional flutes provide better hole quality because they have more margins for guiding the tool. An interesting 4-flutes design has two flutes that cut to center and two flutes separated from the chisel edge by an undercut, as the case of the tapered-drill reamer (or "one-shot" drill) considered in our experiments and detailed in chapter 3.5.

d) Web and flute geometry

The strength of the drill is largely determined by its web and flute sizes. The two main conflicting parameters in drill body design are adequate flute area for efficient chip disposal and high drill rigidity to reduce deflections and increase dynamic stability. The ratio of the web thickness to the drill diameter directly affects the drill's torsional and bending strength. For conventional two-flute drills, this ratio is usually about 0.21:1. The flute-to-land ratio also significantly affects the drill's strength (conventional drills

have a flute-to-land ratio of about 1.1:1, which provides a flute space area of 45 to 55% of the total cross-sectional area, suitable for general purpose applications with most work materials). These ratios can be optimized for specific work materials and hole depths.

Parabolic (rolled-heel) flute forms increase the chip space and enhance chip ejection and therefore widely used for dry and deep hole applications. The use of parabolic flutes with high helix angles (greater than 30°) further improves chip ejection. Parabolic drills have a heavier core, approximately 40% the diameter compared with 20% of standard twist drills; the heavier core adds rigidity and increases stability when drilling deep holes and harder materials. Drills of this type are used not only for soft materials, such as plastics, aluminum, copper and low-carbon steel, but also for stainless steel, cast iron and nodular iron.

e) Material

Twist drills are most commonly made of HSS (high-speed steels), HSS-Co, solid WC (carbide steels), or with WC tips or heads brazed on a steel body. Special applications employ twist drills made of solid ceramics, with PCD (Polycrystalline Diamond) edges or tips brazed on a steel body, PCD heads brazed on a WC (Tungsten Carbide, commonly referred to simply as “carbide”) body, PCBN (Polycrystalline Cubic Boron Nitride) and ceramic tips, and PCD veined on a WC body.

The greatest improvements in productivity have resulted from the acceptance of solid carbide (Tungsten Carbide - WC) drills. Compared with HSS drills, carbide drills permit an increase in productivity by a factor of 2 to 10, and increase the hole quality. Solid carbide drills are especially well suited for high-throughput precision hole manufacturing. Solid ceramic and cermet and PCBN- and PCD-tipped drills are used at higher speeds than carbide drills. Ceramic drills can be used for fiber-reinforced composites, but their application in ferrous materials has been limited by a lack of machine tools with sufficient speed capability and acceleration/deceleration rates for the spindle slide reversal in blind holes. PCD-veined drills eliminate concerns about the integrity of the braze interface with carbide blank. PCD drills have been used extensively to drill aluminum alloys, other non-ferrous alloys, and fiber-reinforced composites at conventional and high speeds. Solid ceramics and even more PCD drills have the disadvantage of being expensive for general applications.

Generally, improved drill rigidity has a positive effect on most aspects of the drilling operation. A stiffer drill exhibits less of vibration and deflection, which allows the use of higher speeds and feed rates and produce better hole quality and longer tool life.

Early experiments in drilling fiber-reinforced composites [21] have shown that the HSS drills are the least suitable for this application with extreme levels of tool wear. Carbide drills perform better, but are outmatched by the extremely high-priced PCD drills.

f) Point geometry

One very important feature of a twist drill is its point geometry. It determines the characteristics of the drill's cutting edges introduced earlier. The principal geometric features of the point are the point angle(-s) (ρ), web thickness (w), chisel edge angle (ψ) and the relief angle (γ).

The point angle (ρ) is defined as the angle of the cone obtained by rotation about the drill axis of the cutting lips. Some twist drills can have multiple point angles (as for “double angle point” drills) or this angle is not constant (as for “radial/racon point” drills). More information and comments on the definition of the point angle (ρ) can be found in chapter 3.4.2.

The cutting lip length is inversely related to the point angle.

An optimum point angle which yields maximum drill life and hole quality exists for every work material. A standard 118° point is used for general purpose drilling of readily machined materials. Point angles

smaller than 118° are preferred for many cast irons, copper, fiber aluminum alloys, die castings and abrasive materials. Point angles greater than 118° are used for hard steels and other difficult materials. Generally, a lower point angle reduces thrust force while increasing torque; the thrust force varies parabolically with the point angle and reaches a minimum value at roughly 118° , the point angle used on standard drills.

The cutting edge is formed by the intersection of the cutting face (rake face) and the flank face; a straight shape of lip is desirable because it generally provides maximum tool life. Specialized drill designs with concave lips (e.g. racon point drills) are used for some steels, since a concave lip induces more strain in the chip and improves chip breaking.

The rake angle (α , defined generally as the angle between the rake face and the normal to the local velocity vector in the plane formed by the cutting edge and velocity vector) distribution across the main cutting edges depends on the flute helix angle. The flute helix angle reaches the maximum at the margin and decreases to zero at the center. Similarly, the rake angle decreases near the web; it is typically negative at the center of the drill and roughly equal to the helix angle at the outer corner. Lip correction can be used to reduce the rake angle and increase the edge strength along the main cutting edge; it generates a constant rake (helix) angle along the entire length of the cutting edge. Lip correction is used especially for inhomogenous materials such as cast iron, and when small, discontinuous chips are desired. A 0° to 5° positive rake angle produced by lip correction or the use of straight flute drills provides a strong edge for general purpose drilling of hard and brittle materials such as cast iron, metal-matrix aluminum composites, stainless steel, steel alloys, nickel-chrome steel, titanium alloys and high-temperature alloys. A small or neutral rake angle will not help chip evacuation and may cause material build-up on the cutting edges in softer materials.

The chisel edge is the blunt cutting edge at the center of the drill. It is formed by the flank surface ground on the drill web. The ratio of the web to core diameter to the drill diameter is usually large. The optimal web thickness depends primarily on the work material. The web thickness is usually about 15 to 20% of the drill diameter for large drills, but may reach 50% of the diameter for small drills, which require a proportionately heavier web to maintain stiffness. Because it cuts slowly and has a large negative rake angle, the chisel edge produces a chip by an extrusion or smearing action (in metal drilling), rather than by cutting. Because the chisel edge chips have a less direct path to the flutes, they are more likely that material build-up will occur. The chisel edge contributes substantially to the thrust force; the size of the contribution depends on the relative lengths of the chisel and main cutting edges. The chisel edge contributes roughly 50% of the thrust for a drill with a typical web thickness equal to 20% of the diameter. If the web thickness to diameter ratio is increased to 30%, the chisel edge thrust doubles; if the ratio is further increased to a 40%, it will increase by a factor of 2 (or a factor of 4 when compared to a 20% web drill). The three common approaches to reducing problems associated with the chisel edge are: (i) reducing the chisel edge length by web-thinning or splitting the drill point, (ii) changing the shape of the chisel edge to improve its cutting action, and (iii) eliminate the chisel edge altogether.

The nature of the cutting edge (referred to as the edge treatment) is another important factor influencing the cutting forces. A sharper cutting edge will cut better, but it is more prone to chipping or breaking. It is very difficult to assess the edge treatment for a particular tool, considering the fact that it might vary along the cutting edges.

A wide variety of drill point and body configurations have been developed to improve aspects of drill performance such as the drill's centering ability, thrust force and rigidity. Briefly, the common types of points include the following.

- **Conventional point or conical point** is the most common type of drill point ground on standard, 118° point drills. The chisel edge is either conventional (with conical relief) or two faceted (which results in a flat or blunt chisel), and has a high negative rake angle (-50° to -60°). Conventional drills tend to "walk" or drift during entry and thus often require a centering hole. They are most commonly used in applications which do not require high precision or production rates. The

conical point can be ground to provide a small crown (0.07 to 0.2mm depending on the drill diameter) along the chisel edge, which results in significant improvement in the chisel edge cutting action and centering characteristics.

- **Radial/racon point** is a type of drill that has an arch-shaped radiused point, resulting in a more positive rake angle at the center. The radial tip provides a self-centering effect; it can therefore drill more accurate holes than a conventional drill. The cutting edge is longer than on a conventional point, resulting in slightly higher torque and thrust, but also lower edge temperatures and stresses since the heat and forces generated during drilling are spread out over a larger area. Radial points thin the chip at the outer corner, protecting the corner and margin from wear, reducing burr formation, and improving drilled surface finish and tool life.
- **Web thinned point**, is a conventional point with the chisel edge thinned by grinding a notch at the chisel edge corner with a radiused wheel. There are several variations of the web thinning. This operation reduces the chisel edge length, reducing thrust and improving chip evacuation from the center of the drill. Reducing the chisel edge length also improves the drill centering properties. The web is typically thinned to a diameter between 8 and 12% of the drill diameter. Lip correction can be used to thin the chisel edge as well.
- **Split point** is often referred to as a crankshaft drill. It is produced by notch type web thinning. There are two or three similar variations of this point style. The most common split point type is a special case of the web-thinned point with a much smaller residual chisel edge length (typically 2 to 3% of the diameter). There are however a number of drill point designs, which use a modified split with a S-shaped secondary cutting edges. The S-form split reduces secondary edge wear and drill failures when drilling hard materials. The notches in split point drills are prone to build-up when drilling soft materials and prone to edge chipping when drilling tough alloys. The notches on the crankshaft or true split point often do not reduce the chisel edge length, but generate two small cutting edges, one on each side of the chisel edge passing ahead of center. This point is self-centering and also reduces the thrust force, especially when drilling work-hardening materials. The split point is especially common on long drills, such as crankshaft oil hole drills, and on small diameter (<12mm) drills. It is also a preferred point configuration for drilling titanium, stainless steel, and high-temperature alloys.
- **Helical/spiral point** has an "S" contour with a radiused crown chisel that reduces the thrust force and makes the drill self-centering. It eliminates the need for web thinning. In general, a spiral point drill has a thicker web than a conventional drill because a thin S-shaped chisel edge limits its effectiveness when drilling soft materials. The main advantage of this point is that it reduces burr formation at drill exit. Helical points are weaker than split points and require a special drill grinder.
- **Bickford point** is a combination of the helical and racon point geometries. The helical point is ground on the center of the drill, while the racon point is used for the outer portion of the drill. This point combines the benefits of both the helical and racon points.
- **Four-facet chisel point**, also called bevel ground point has a chisel edge formed by the intersection of primary and secondary relief planes ground on the flank, producing a less negative rake angle as compared to the conventional point. The more favorable chisel edge geometry reduces the thrust force, improves centering accuracy, and increases drill life. This is the most common point on microdrills and can be used successfully with most work-piece materials.
- **Double angle points** are ground with a corner break (chamfer) to reduce the included point angle at the drill periphery, resulting in four-facet lips. The reduced peripheral point angle reduces corner wear and burr formation at breakthrough and improves size accuracy; the abrupt change in point angle also serves to split or break the chip. This point is particularly effective when drilling brittle ferrous or hard materials with severe break-through conditions.
- **Multi-facet points** are most easily classified by the number of facets, or the number of primary and secondary relief surfaces ground on the flank. As the number of facets is increased, the point becomes increasingly difficult to grind consistently.
- **Brad point** has a web thinned center point ground on an acute point angle (less than 120° and usually 90°) and slightly concave main lips. The outer corner functions as a trepanning tool. The center point length is usually equal to 20 to 30% of the diameter. The brad point is designed for drilling accurate, round holes in sheet metal with minimal burr formation. A disk or slug of material is produced at exit.

- **Non-chisel edge drills (inverted point drills)** have an inverted point angle near the drill's center (greater than 180°). Grinding the inverted center section, splits the cutting lips into two segments and serves to split the chip.

As can be noted, a wide variety of drill types exist. A lot of research and development of the drilling geometries has actually taken place in industry rather than in research centers. Although many published studies are approaching the design and performance aspects of drilling tools, they cannot provide a comprehensive overview of the current state-of-art and industrial practices.

In selecting test cases for modeling, we have looked at drills often employed in reported studies on drilling fiber reinforced composites. An additional constrain was to use tools for which enough information exists to describe them mathematically or to be of simple geometry. We have therefore employed a 2-facet twist drill commonly used in metal cutting; a tapered drill reamer – developed especially for drilling composite materials and reported to provide high performance [16], [22]; and a 8-facet twist drill suitable for drilling both metals and composite materials. The geometry of the first two drills has been modeled mathematically in the current thesis, while the third one was only employed in experiments but not described mathematically due to difficulties to assess the geometric details of the web-thinning feature. The above mentioned drills are introduced and discussed in chapter 3.5.

2.3 Drilling process analysis

Drill performance cannot be analyzed without consideration of the process parameters. Cutting parameters (spindle speed and axial feed), cutting conditions (dry, with coolant or lubricant), work-piece characteristics (material, geometry, structure etc.), fixturing configuration and the machine tool are to be considered as well in the drilling process analysis.

In addition to the tool geometry, the major operating parameters to be specified in drilling process analysis are the spindle speed (n [rpm]) and axial feed (f [mm/rev]). They are referred to as the cutting parameters.

The rotating speed of the spindle (n) is the main factor to influence the cutting velocity (V [mm/min]). In drilling the cutting speed varies along the radial direction, and as a reference is usually expressed at the periphery of the drill. Ignoring the feed, the cutting speed at the periphery can be expressed as:

$$V = \pi \cdot D \cdot n \quad [\text{mm/min}] \quad (2.1)$$

where D is the drill diameter.

The axial feed (f , often simply referred to as “*feed*”) is the tool advancement per revolution along its cutting path in mm/rev. The feed rate (or axial speed) f_r (or V_n) is the speed at which the tool advances into the part in [mm/min], and is related to f through the spindle speed n by:

$$f_r = f \cdot n \quad (2.2)$$

The feed per tooth (f_t [mm/rev]) depends on axial feed (f) and the number of flutes N ([-]), and is used to calculate the depth of cut (t_c – introduced in chapter 3.4.9):

$$f_t = \frac{f}{N} \quad (2.3)$$

The feed rate (or axial speed) is the input parameter provided to the machine tool. The (axial) feed is usually employed in drilling process analysis as more representative in describing the process. However, in many cases confusion is made between the two, although the units can provide an easy way of identifying the reference. Throughout the thesis document we refer almost always to the axial feed (f).

The usage of coolant or lubricant has a strong influence on the cutting forces by aiding the chip evacuation and lowering the friction forces and the temperature of the drill, although it is difficult to mathematically account for their influence into a drilling model. Furthermore, unless the coolant and lubricant is provided through holes in the drill or the work-piece thickness is small, the amount of lubrication or coolant reaching the cutting area varies during the drilling process.

Clamping configuration of the work-piece as well as the machine tool also affect the drilling process. Usually its effect on the drilling process is analyzed separately by finite element studies.

Drilling process analysis usually involves the calculation of the drilling forces, which are used to estimate the drill loads, power consumption, thermal loads and hole quality aspects.

The cutting forces measured during drilling experiments are referred to as thrust (axial force – F_z [N]) and torque (rotational momentum – M_z [Nm]). During typical drilling experiments these forces are measured on the time scale from drill entry into the work-piece to full engagement and drill exit from the material. The following figure (fig. 2.3) introduces an example of such measurements extracted from our own experimental investigation on drilling fiber reinforced composites (carbon fiber with epoxy matrix – CFRP

– of 10mm in thickness) using a tapered drill reamer at a spindle speed $n=500\text{rpm}$ and axial feed of $f=0.2\text{mm/rev}$. The different stages of drilling with this particular tool have been outlined. The chisel edge engages almost instantly, while the rest of the cutting edges are becoming engaged in drilling gradually until full engagement is obtained. Once the drill pierces through the bottom surface of the work-piece, the full engagement stage finishes and drill is gradually exiting the work-piece until all the cutting edges are out. Axial downwards movement of the drill might continue a little more, until the drill is extracted from the work-piece (usually at very high speeds). Starting with full engagement stage the leading edges of the drill come in contact with the work-piece, action referred to as “reaming”. They remain in contact until the drill is pulled out of the work-piece, although the contact length varies.

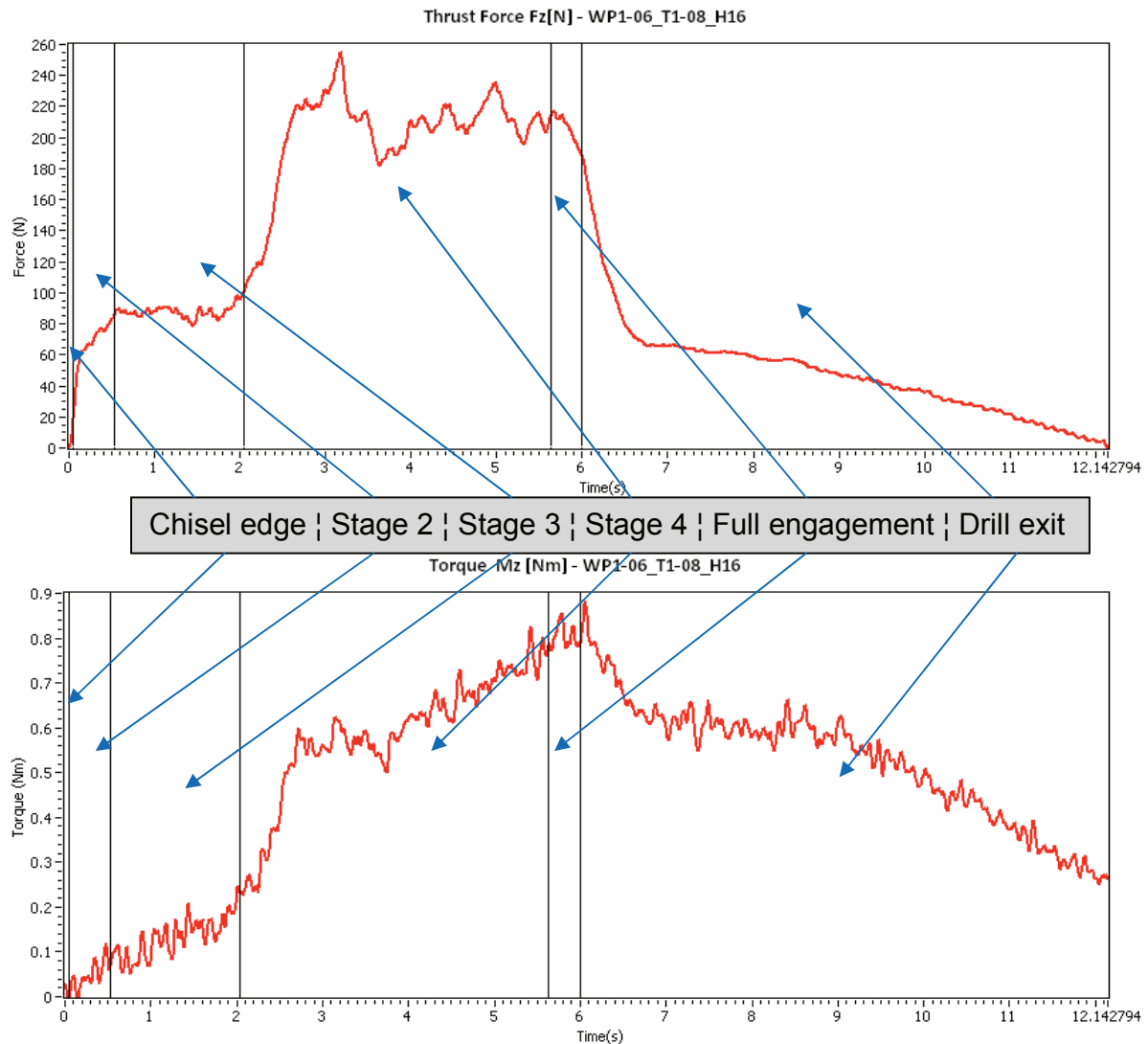


Fig. 2.3 – Sample cutting force measurement during drilling (CFRP, 10mm thickness, tapered drill reamer (T1), $n=500\text{rpm}$, $f=0.2\text{mm/rev}$) – a) thrust; b) torque

Knowing the axial speed (f_r – eq. 2.2), one can relate the time coordinate to the distance to be drilled, allowing the identification of full engagement stage, when theoretically one should obtain the maximum values for thrust and torque. The maximum values of thrust and torque are the first stage of characterization of the cutting forces during drilling operations. These values vary for each tool/work-piece combination, drilling geometry, cutting parameters and conditions.

As these forces are important in the process optimization, research has focused on means to predict them. The approach used in simulating other machining processes, in which the forces are calculated by multiplying the uncut chip area by previously measured cutting pressures (in orthogonal or oblique cutting tests), can be applied to drilling, but is not well suited to the process. This is due in part to the influence of the drill point geometry on the process performance: for a given spindle speed and feed rate, drills with different point configurations yield the same total uncut chip area but often produce significantly different forces.

Empirical models (as functions of spindle speed and axial feed) have been developed ([23], [24], etc.) to estimate the maximum thrust and torque forces for a drilling case. These types of models are often sufficient to estimate the power consumption, aid the clamping design or even tool wear rate estimation. However, they provide little information to a user interested in optimizing the drill geometry or studies on the quality related aspects of the drilling process (i.e. exit burrs, delamination etc.).

In view of this fact, drilling forces can be more effectively simulated by dividing the drill's cutting edges into small segments which can be treated as oblique cutting edges, determining the forces on each element by oblique cutting measurements or calculations, and summing the results to calculate total loads.

The configuration of the oblique cutting element varies extensively along the radius of one drill, but also for each different tool. The current analytical models in the framework of oblique and orthogonal cutting developed for other machining operations (turning, milling, etc.) are not able to provide accurate predictions for such a wide range of rake and inclination angles as encountered in only one drill geometry case. Therefore to estimate these forces experimental methods are usually employed. The experiments can either be run for oblique cutting cases, or drilling, both methods being quite challenging. To be able to find the elemental forces in oblique cutting to use in calculating the drilling forces implies testing a large number of oblique cutting cases, while trying to maintain similar overall conditions as in drilling (same tool and work-piece material and other conditions). Some aspects as the curvature of the rake face for twist drills are close to impossible to replicate in oblique cutting experiments. This task has proved too difficult to be attempted, except for a few simplified studies.

The other solution is to continue the analysis of the cutting forces curves obtained directly from drilling experiments to obtain the distribution of the axial and tangential forces along the radius, a solution which is encouraged by the advancement of the force measurement equipment and data processing capabilities. [2] and [13] have attempted using this method, but mainly to fit their prediction model, rather than present the results of this analysis and discuss them. Due to the noisy nature of the raw measurement data and the significant differences between each drilling case, the method is not yet developed at its full potential. In chapter 4, it is attempted to perfect the experimental analysis to obtain complete distribution of the forces for generic drilling cases.

When developing cutting force models for drilling, the desire is to obtain a good separation between the geometrical and kinematic factors of the process from the material specific factors (like specific cutting pressure and friction coefficient), so that the model becomes portable across different combinations of drill/work-piece materials. However, due to the complexity of the drill point geometry and the kinematic process, the material and geometric factors are difficult to separate. Furthermore, usually 2 models are required to describe the drilling process, one suitable for the cutting lips and one for the chisel edge, as in the case of one of the recent cutting force model presented in [2]. In chapter 3 an improved cutting force prediction model is introduced. Although it will be shown that the geometrical and material related factors are not fully separated, the proposed model can predict resulting cutting forces with good accuracy using up to 4 empirical coefficients to account for material specific factors (when 12 empirical coefficients are employed by a similar model – for a full review of the topic see chapter 5.2). Additionally, the current model is generally applicable to all areas of a generic drill (both chisel edge and cutting lip), providing that the geometry of the drill can be described mathematically.

2.4 Particularities in drilling fiber reinforced composites

In recent years, the number of applications of fiber reinforced composites has increased driven by the developments in their manufacturing processes and their weight to mechanical properties ratio. Industries like aerospace were among the first to adopt these types of materials, but in recent years they found their way into automotive and other industries. With increase usage, new demands are made in terms of the economy of the manufacturing processes; therefore the manufacturing processes of fiber reinforced composites have to become more reliable and efficient.

The term “*composite material*” generally refer to materials with at least two distinctive constituents, combined to give a unique combination of properties. The term “*fiber reinforced composite material*” refer to a composite material with one of the constituents being in the form of fiber, usually in combination with a resin (generally referred to as a “*matrix*”). The reinforcing “*fiber*” or “*fabric*” provides strength and stiffness to the composite, whereas the matrix gives rigidity and environmental resistance. The fibers can be long or short. Short fiber composite materials usually have lower properties than continuous (or long) fibers, although their properties are rather isotropic (like in the case of metals). Long-fiber reinforced composites are usually made out of laminated plies, although other methods and types exist. The current study addresses particularities in the drilling of the long-fiber reinforced composite laminates; although the methods derived hereby can be applied to other types of composites as well as other materials.

Drilling as a manufacturing process is often encountered among the last operations of the manufacturing plan, where requirements of reliability and quality are higher due to increase cost of discarding the part at this late stage. Most of the parts processed by drilling operation are in the shape of plates, with thickness varying from under 1mm to 10-20mm. The thin plates to be drilled are common to the fabrication of electronic boards, while the thicker ones are employed as structural parts in aerospace industry. Composite parts with higher thickness than 15-20mm are very uncommon due to problems occurring during the curing process.

An important particularity of the fiber composite materials is their anisotropy. Besides the anisotropy of these materials caused by the finite number of fiber directions (playing an important role in the part design), another degree of anisotropy is introduced by the weaknesses of the inter-ply interface, as they are made out as a stack of layers. While in use, the fiber reinforced part is designed so that the main loads act along the direction of the fiber, rather than perpendicular on it. Only out of the ordinary situations may cause loads acting along their weak direction, and in most of the cases these loads are external and produce little if no internal defects. However, drilling is an operation which in most cases introduces loads along their weakest direction (perpendicular on the fiber directions and inter-ply interface) and furthermore, the loads act differently on each ply during the process causing internal damage. The figure below (2.4) introduces the defect of delamination – the inter-ply separation of a layered structure during drilling operations.

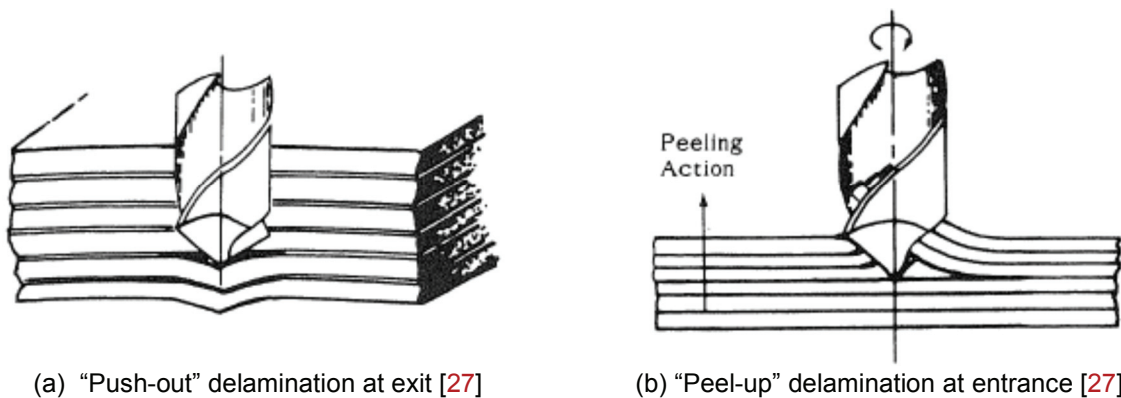


Fig. 2.4 – Delamination during drilling of composite laminates

Delamination is an internal defect and in most cases is not visible with the naked eye. Solutions like C-Scan, X-Ray computerized tomography [25] or shadow moiré laser based imaging technique [26] are available for detecting delamination, but they are expensive and time consuming. While material scientists are trying to define the conditions for the onset of delamination using fracture mechanics theory, researchers in the manufacturing field are attempting to assess more accurately the loading conditions appearing when drilling fiber reinforced composites. Models for delamination onset like those introduced by [12] or [27] are able to determine the critical thrust force over which delamination occurs at tool exit. Little modeling resources are available for entrance delamination. While exit delamination is believed to develop as a mode I fracture, entrance delamination can be modeled only by mode II fracture or mixed-mode [9]. However, although the tools to model the onset of delamination are becoming available, little work has been done to actually determine (prediction or measurement) the loading distribution on each ply occurring during drilling. Experimental measurement or empirical predictions of maximum thrust and torque values are, in the author's opinion insufficient to assess the loading conditions causing delamination.

A deeper experimental analysis of the drilling process is desired, which could allow us to estimate the loads on each ply in various drilling stages. As the experimental measurements of the cutting forces could be affected by the delamination, the experimental analysis has to be doubled by a prediction model to be widely applicable.

When attempting cutting force predictions using the orthogonal or oblique cutting model, another particularity is noted in comparison with metal cutting. During the machining process on metallic materials, the chips are formed by plastic deformation, while during machining of fiber reinforced materials the chips are formed by brittle fractures, as exemplified by the following figures. While continuous (or in general large chips) are obtained in metal cutting, powder-like chips are reported in long-fiber composites machining.

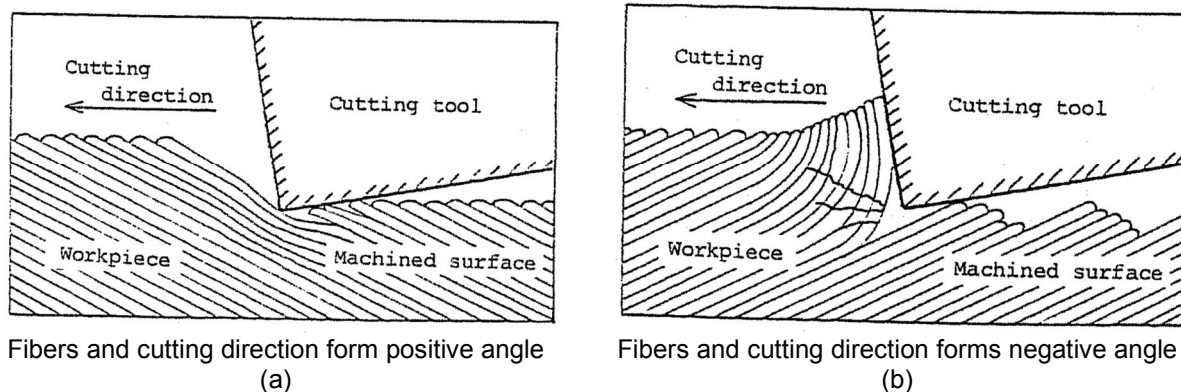


Fig. 2.5 – Schematics of fiber cutting during orthogonal cutting model [28]

It is believed that the chip is formed by at least two fractures, one along the fiber direction and one perpendicular to it (the order depending on the configuration). The fracture planes are very difficult to assess, considering that the relative orientation between the cutting and fiber directions vary widely in drilling along the cutting edges, with different geometry, cutting parameters or pattern of the composite material. Although there are fracture mechanics models to predict the onset of a crack and its direction of propagation, they are not yet applied to machining process, due to the reasons outlined above and also the fact that such models would be difficult to calibrate experimentally. The shear plane theory for metal cutting ([1], [29], etc.) is obviously not applicable in the case of machining fiber reinforced materials.

As a consequence to the fracture-based chip formation mechanism, heat is mostly generated by friction during the machining process of fiber reinforced composites. However, these materials do not dissipate

the generated heat as easily as the metals, and it is believed that temperature buildup in the tool is one of the causes of extensive tool wear reported – another problem in machining fiber reinforced composites.

The new challenges encountered in drilling (and machining in general) of fiber reinforced composites need to be addressed in order to optimize these processes. Currently the same tool geometries as in metals are employed and there is a lack of information in selecting the cutting parameters suitable for a defect free drilling process. The work in the current thesis attempts to address a few of these challenges, by introducing a new cutting force model and a methodology of analyzing the drilling process with focus on the cutting force distribution along the tool radius and height. Our mechanistic cutting force model for drilling, able to capture the variation of the elementary forces along cutting edges is notable for:

- (i) Using fewer empirical coefficients (up to 4, whereas similarly positioned models use 12 empirical coefficients);
- (ii) Considering the forces acting on the relief face (which we will show to be important in the case of composite materials);
- (iii) Introducing a transformation matrix to relate the elementary cutting forces defined in oblique cutting framework to drilling (providing an easy and drill-type-independent way of applying to drilling existing or new force models developed in oblique cutting framework);
- (iv) Considering the drilling process kinematics (represented by the cutting angle – μ) for all derivation of the angles defining the geometry of the cutting elements and forces decompositions (whereas previously was ignored at least for the angles describing the cutting lip region of a drill);
- (v) Mathematically describing a new type of drill (tapered-drill reamer) for the purpose of cutting force modeling.

Experiments were carried out in the current thesis using two types of commercially available bi-directional long-fiber reinforced composite laminates: carbon-fiber reinforced epoxy (further referred to as CFRP) and glass-fiber reinforced epoxy (referred to as GFRP). The exact specifications of these materials are presented in chapter 4.2.

Chapter 3

Cutting force model for drilling

3.1 Introduction

As shown in chapter 2.3, cutting forces occurring during drilling process are important for the process analysis. Although cutting forces in drilling (thrust and torque) are often derived starting from an oblique/orthogonal cutting model, it is very difficult to relate it to other machining operations, mainly due to the large variation of element's geometry, not encountered in any other machining processes, as well as due to some particularities of the drilling process (i.e. cutting around the chisel edge). Therefore, most of the times, cutting force models are developed separately for drilling, although based on the same principle of oblique (or orthogonal) cutting.

One of the most accurate published cutting force prediction models for drilling is presented in detail in [2] and has been applied to fiber reinforced composites in [3]. In spite of the complexity of the model and the number of empirical coefficients the geometric and dynamic effects are not fully isolated from the material properties. As the shear angle theory (introduced by Merchant in [1] and [29]) has no theoretical reason to be applied to composite materials (because the cutting process is based on fracture rather than plastic deformation), the model uses a mechanistic approach in defining the cutting forces (as normal and friction forces on the rake face). Two different models (with respect to the empirical coefficients) are used for the cutting lips and chisel edge of the drill respectively and the forces on the clearance face are not modeled (although Rubenstein [30] and other propose a model to consider them). The model is also notable for introducing the idea of model calibration based on the cutting forces distribution along the radius obtained experimentally, rather than the total maximum forces. Calibration for the radial distribution of the cutting forces is much more complex, as it involves tedious post-processing of the experimental results (discussed in more detail in chapter 4.4 and published in [15]). However, it has the advantages that it minimizes the number of experiments needed for calibration and provides an accurate distribution curve along the tool radius, suitable for the study of drill geometry performance and various local defects especially relevant for composite materials (i.e. delamination).

It is found that most of the cutting force models (mentioned above or [31]) for drilling provide equations for thrust and torque, developed starting from forces defined in the oblique or orthogonal cutting model. If one wants to change the assumptions on the orientation of elementary forces in the oblique (or orthogonal) cutting model, one has to decompose the forces each time to reach equivalent thrust and torque equations. It was found of practical importance to adopt a generally accepted oblique to drilling transformation as proposed by Altintas in [32]. Therefore, in section 3.2, we introduce a transformation matrix to relate vectors defined in oblique cutting to drilling reference systems, assumption-free and valid for any type of drill geometry and even for the chisel edge region as long as the drill geometry can be modeled mathematically.

In chapter 3.3 a normal/friction force model is proposed in an oblique cutting framework similar to [2], but including the second pair of normal/friction forces on the clearance face (based on suggestions in [30]). Using three coefficients (specific pressure on rake face coefficient, friction coefficient and specific pressure on relief face – some of them defined as functions – for details see chapter 5.2), the model is later calibrated for experiments conducted using two different drills from a geometric point of view (tapered drill reamer and 2-facet twist drill) on two work-piece materials (bi-directional carbon- and glass-fiber reinforced epoxy).

The geometrical parameters of a generic drill needed for the modeling of the cutting forces are derived and discussed extensively in chapter 3.4, in the same order as they are introduced in chapters 3.2 and 3.3. As they are normally part of the cutting force model, in order to keep their definition clear, the decision was made to separate them. In chapter 3.5, two case studies of drill geometry also used in experiments are introduced, including the particular values of the geometrical parameters and their variation along the drill radius.

Later on, the methodology to obtain experimentally the elementary force distribution along the drill radius is detailed in chapter 4 and published in [15]. The model calibration methodology and discussions about the model's performance is presented in chapter 5.

Summarizing, in this chapter a cutting force model for drilling of fiber reinforced composites is proposed, which considers also the forces acting on the relief face (which we will later show play a much more significant role than in metal drilling), and it is notable for using fewer empirical coefficients defined intuitively (3 coefficients, some of them defined as functions, resulting in up to 4 empirical coefficients in comparison with 12 in [2], a similar mechanistic cutting force model for drilling – for details see chapter 5.2). Additionally, for the first time a transformation matrix is practically implemented in a cutting force model for drilling to relate oblique cutting to drilling, in a generic manner, while previous models decompose each elementary force component individually. Of notable interest are also the improvements in the definition of the geometrical parameters of the drill geometry needed for the cutting force modeling:

- Most geometrical parameters (like web angle – β , point angle – p , normal rake angle – α_n , etc.) are now defined in a more generic way as functions along drill radius, including the chisel edge area. Previously point angle (p) was considered a constant parameter, making it difficult to model multi-stage or variable point angle drills; web angle (β) and normal rake angle (α_n) were only defined along the cutting lips, etc..
- The influence of the process kinematics (through the cutting angle – μ) is now considered for all geometrical parameters of the drill and along all the cutting edges, including but not limited to: inclination angle (i – chapter 3.4.4), normal rake angle (α_n – chapter 3.4.6 and 3.4.8), relief angle (γ – chapter 3.4.7 and 3.4.8), depth of cut (t_c – chapter 3.4.9), etc. Previous models were ignoring the influence of the cutting angle (μ) along the cutting lips, on the grounds that it is too small and can be therefore ignored. We will show in chapter 5.3 that considering the influence of the cutting angle (μ) on the normal rake angle (α_n , and the rest of the angles) along the cutting lips is critical in capturing a local increase of the elemental cutting forces.
- An additional angle (named “2nd Euler rotation angle – τ , see chapter 3.4.5) has been introduced in the derivation of the transformation matrix and element's dimensions for simplification reasons.
- A suggestion for a correction of the point angle (p) to a more representative definition for cutting force modeling – “manufacturer's point angle” (p' , chapter 3.4.2), although not employed in the final model for reasons discussed in the same chapter.
- A discussion on the validity of the rake (α) and relief (γ) angles equations employed in previous models along the chisel edge in chapter 3.4.8 and a new equation to determine them for a particular case of a straight chisel edge inclined from the drill axis (a particular case of drill not treated yet by other cutting force models).
- A complete mathematical description for cutting force modeling for a new type of drill (tapered drill reamer).

3.2 Oblique to drilling coordinate system transformation

Most cutting force prediction models use the oblique or orthogonal cutting models to estimate the elementary forces acting on an element of the cutting edge. An element is defined a small section of the cutting edges of a drill, for which oblique (in our case, or orthogonal as well in a generic manner) cutting can be assumed (i.e. the cutting direction, inclination angle and the angles defining the inclination of rake and relief faces are assumed to be constant across the width of the element). Along the cutting edges of drill, the elements will have different sizes for reasons discussed in chapter 3.3 and 3.4.9.

The elementary forces defined in oblique (or orthogonal) cutting models have to be decomposed along the thrust/torque/lateral directions as defined in the drilling operation and summed for all elements of the cutting edge to obtain the total values of thrust and torque (and occasionally lateral force). The total thrust and torque values are representative for describing the cutting forces in drilling. The measured lateral component should be zero for a perfect drill of minimum 2 flutes (due to the symmetry along the drill axis, the lateral force on a flute is canceled by the others) and therefore is only important when one wants to study the effects of symmetry imperfections on mechanical loads. Unless the drill has a single flute, the lateral force cannot be measured effectively, and this poses a significant problem in the calibration of drilling force models based on oblique cutting as compared with milling, turning or other machining processes.

In the current section, a simple, effective and generic method is proposed to separate the definition of the elementary forces defined in the oblique (or orthogonal) cutting model from their decomposition in the drilling coordinate system, by introducing a coordinate transformation matrix.

Fig. 3.1 shows the two coordinate systems for a point A on the cutting lip of a twist drill. XYZ is the coordinate system associated with the drilling process, with the X axis along the radial direction; the Z axis aligned with the drill axis and the Y axis, corresponding to the tangential direction, is perpendicular to both. The forces along the Z direction will contribute to the thrust, while the forces along the Y direction will generate the torque and along the X direction the lateral forces will be developed (which will be canceled by the action of the second flute).

The X'Y'Z' coordinate system is associated with the oblique cutting element, with the Y' axis aligned according to the local velocity vector (which due to the axial feed makes an angle greater than zero with the tangential direction – Y axis); the X' axis perpendicular to the Y' axis in the plane defined by the Y' axis and the cutting edge and Z' axis perpendicular to the X'Y' plane (which also includes the cutting edge).

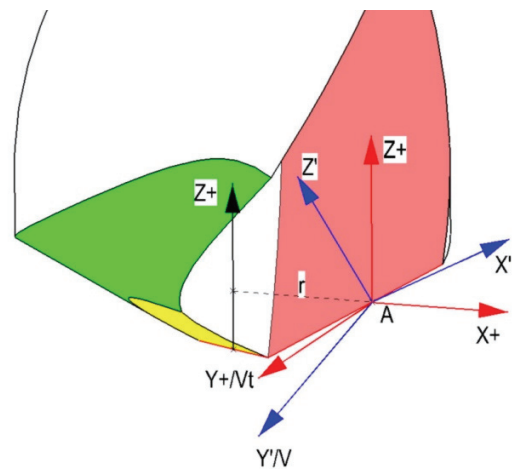


Fig. 3.1 – Oblique and drilling coordinate system for a point A on the cutting lip of a twist drill

The same coordinate system can be defined for a point on the chisel edge as well. In this particular case, for a chisel edge located in a plane perpendicular on the tool axis, X and X' axes will coincide.

A relationship can be found between the two coordinate systems for any point A on the cutting edge (either on the cutting lip region or the chisel edge) if the following angles are known:

- Point angle (p) defined as the angle between the cutting edge at point A and the tool axis (or its parallel through A – Z axis). The point angle is discussed in chapter 3.4.2.

- Web angle (β) defined as the angle at point A between the radial direction (X axis) and the projection of the cutting edge in a plane perpendicular to the drill axis (XY plane), as in fig. 3.4 and derived in chapter 3.4.1.
- Cutting angle (μ) defined as the angle at point A between the local velocity vector (V/Y' axis) and the tangential velocity (V_t – projection of the velocity vector on a plane perpendicular to the drill axis – XY plane). A discussion about this angle is presented in chapter 3.4.3, including the representative figure 3.8;
- Inclination angle (i) defined as the angle at point A between the X' axis (the normal to the velocity vector (V) in the plane containing both the velocity vector and the cutting edge) and the cutting edge. This angle was previously introduced in fig. 2.1-b for oblique cutting. An illustration for drilling is provided in fig. 3.9, while chapter 3.4.4 contains a discussion about its derivation.

All these angles are frequently used in describing drill geometries, their formulations are known and widely discussed and their particular values can be determined from basic parameters of the drill geometry found in suppliers' catalogues. In chapter 3.4, these angles and other parameters needed for describing the drill geometry are derived (when needed) as functions of the radial coordinate and discussed for general purposes, while in chapter 3.5 introduces their particular values for the drills employed in our study.

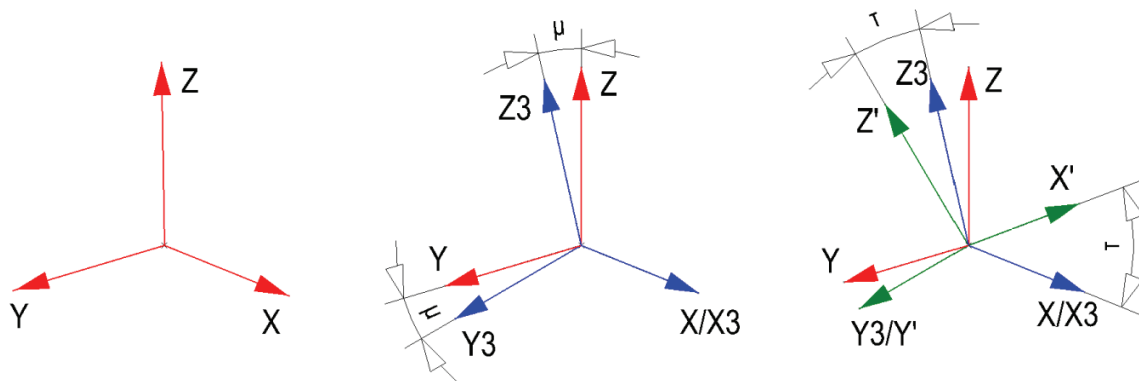
To transform a vector $\{v\}_{XYZ}$ defined in one coordinate system into another a transformation matrix (often called the direction cosine matrix regardless of how it is derived or represented) can be applied as follows:

$$\{v\}_{XYZ} = T_{X'Y'Z',XYZ} \cdot \{v\}_{X'Y'Z'} \quad (3.1)$$

$$\{v\}_{X'Y'Z'} = T_{X'Y'Z',XYZ}^{-1} \cdot \{v\}_{XYZ} = T_{X'Y'Z',XYZ}^T \cdot \{v\}_{XYZ} \quad (3.2)$$

It is noted that the transformation matrices have the property that their determinant is 1 and their inverse is equal to their transpose.

The transformation matrix from X'Y'Z' to XYZ can be obtained by either calculating the cosine of the angles between the respective axes, or by determining a sequence of Euler rotations from one system to the other. Between two arbitrary coordinate systems a maximum of three rotations are needed. For the particular case of transforming X'Y'Z' to XYZ only two rotations are required. It was found easier and more intuitive to use the Euler rotations to describe the transition from XYZ to X'Y'Z' as follows and after that to calculate its transpose for practical use. In fig. 3.2 the necessary Euler rotations are presented, where $X_3Y_3Z_3$ is the intermediate coordinate system and τ is the 2nd Euler angle of rotation, which can be found by eq.3.3 (its derivation is presented in chapter 3.4.5).



Starting system of coordinates 1st rotation about X*/X3 axis by μ angle 2nd rotation about Y3/Y' axis by τ angle

Fig. 3.2 – Determining the transformation matrix by two consecutive Euler rotations

$$\tau(r) = \arccos \left[\frac{\sin(p(r)) \cdot \cos(\beta(r))}{\cos(i(r))} \right] \quad (3.3)$$

The transformation matrix from XYZ to X'Y'Z can be computed by matrix multiplication of the two intermediary rotations:

$$T_{XYZ, X'Y'Z} = T_{XYZ, X_3Y_3Z_3} \times T_{X_3Y_3Z_3, X'Y'Z} \quad (3.4)$$

Where the intermediate matrices are determined through cosine direction method as follows:

$$T_{XYZ, X_3Y_3Z_3} = \begin{bmatrix} \cos(\theta_{X_3X}) & \cos(\theta_{X_3Y}) & \cos(\theta_{X_3Z}) \\ \cos(\theta_{Y_3X}) & \cos(\theta_{Y_3Y}) & \cos(\theta_{Y_3Z}) \\ \cos(\theta_{Z_3X}) & \cos(\theta_{Z_3Y}) & \cos(\theta_{Z_3Z}) \end{bmatrix} \quad (3.5)$$

The X axis coincides with X_3 hence $\theta_{X_3X} = 0^\circ$ and $\cos(\theta_{X_3X}) = 1$. The angle between X and Y_3 and respectively Z_3 will still be 90° , and the cosine of the respective angles 0. The rest of the angles can be expressed as functions of $\mu(r)$ as follows:

$$T_{XYZ, X_3Y_3Z_3} = \begin{bmatrix} 1 & 0 & 0 \\ 0 & \cos(\mu(r)) & \cos(90^\circ + \mu(r)) \\ 0 & \cos(90^\circ - \mu(r)) & \cos(\mu(r)) \end{bmatrix} = \begin{bmatrix} 1 & 0 & 0 \\ 0 & \cos(\mu) & -\sin(\mu) \\ 0 & \sin(\mu) & \cos(\mu) \end{bmatrix} \quad (3.6)$$

And

$$T_{X_3Y_3Z_3, X'Y'Z} = \begin{bmatrix} \cos(\theta_{X'X_3}) & \cos(\theta_{X'Y_3}) & \cos(\theta_{X'Z_3}) \\ \cos(\theta_{Y'X_3}) & \cos(\theta_{Y'Y_3}) & \cos(\theta_{Y'Z_3}) \\ \cos(\theta_{Z'X_3}) & \cos(\theta_{Z'Y_3}) & \cos(\theta_{Z'Z_3}) \end{bmatrix} \quad (3.7)$$

Y_3 coincides with Y' hence $\theta_{Y'Y_3} = 0^\circ$ and $\cos(\theta_{Y'Y_3}) = 1$. The angle between Y_3 (or Y') and X' and respectively Z' will still be 90° , and the cosine of the respective angles is 0. Expressing the rest of the angles in terms of the 2nd Euler rotation angle introduced previously we obtain:

$$T_{X_3Y_3Z_3, X'Y'Z} = \begin{bmatrix} \cos(\tau(r)) & 0 & \cos(90^\circ - \tau(r)) \\ 0 & 1 & 0 \\ \cos(90^\circ + \tau(r)) & 0 & \cos(\tau(r)) \end{bmatrix} = \begin{bmatrix} \cos(\tau) & 0 & \sin(\tau) \\ 0 & 1 & 0 \\ -\sin(\tau) & 0 & \cos(\tau) \end{bmatrix} \quad (3.8)$$

Replacing them in equation 3.4 we obtain:

$$T_{XYZ, X'Y'Z} = \begin{bmatrix} \cos(\tau(r)) & \sin(\tau(r)) \cdot \sin(\mu(r)) & \sin(\tau(r)) \cdot \cos(\mu(r)) \\ 0 & \cos(\mu(r)) & -\sin(\mu(r)) \\ -\sin(\tau(r)) & \cos(\tau(r)) \cdot \sin(\mu(r)) & \cos(\tau(r)) \cdot \cos(\mu(r)) \end{bmatrix} \quad (3.9)$$

While the properties of transformation matrixes state that:

$$T_{X'Y'Z',XYZ} = T_{XYZ,X'Y'Z'}^{-1} = T_{XYZ,X'Y'Z'}^T \quad (3.10)$$

It is found:

$$T_{X'Y'Z',XYZ} = \begin{bmatrix} \cos(\tau) & 0 & -\sin(\tau) \\ \sin(\tau) \cdot \sin(\mu) & \cos(\mu) & \cos(\tau) \cdot \sin(\mu) \\ \sin(\tau) \cdot \cos(\mu) & -\sin(\mu) & \cos(\tau) \cdot \cos(\mu) \end{bmatrix} \quad (3.11)$$

The transformation matrix can be used to transform any vector defined in X'Y'Z' to the XYZ coordinate system and its transpose is suitable for decompositions from XYZ to X'Y'Z'. It is valid for any drill geometry at any point on the cutting edge (including chisel edge) as long as the angles introduced previously can be determined. For most drills, the chisel edge is perpendicular to the drill axis, therefore orthogonal cutting can be assumed. In this case, the inclination angle (ι) becomes zero, the point angle (ρ) is 90° and the web angle (β) is also zero, therefore the 2nd Euler rotation angle (τ) becomes zero and the transformation matrix can be simplified. The cutting angle (μ) is only significant in the close vicinity of the drill axis, therefore one may choose to assume it to be zero for the cutting lip region, resulting in further simplification. We will however show in chapter 5.3 that the later simplification is not recommended at least for a part of the cutting lip close to the drill axis.

3.3 Elementary cutting forces in oblique cutting model

Experiments conducted in [13] on orthogonal cutting of uni-directional long-fiber composites revealed that the cutting mechanism is fracture-based, while in the case of metals it is based on plastic deformations. Furthermore, the powder-like chip is formed by a fracture in two stages; those directions vary with the fiber orientation with respect to the cutting direction. No theoretical model was found to describe the fracture-based cutting process of long fiber reinforced composites, while for metals the shear angle theory is widely used. Nevertheless, mechanistic cutting force models have been proposed for these types of material. These models consider the principal elemental forces as normal and tangential to the rake face. The forces on the relief face are usually ignored mainly based on the experience in metal cutting, where they play a rather small role in comparison with the forces on the rake face.

Orthogonal cutting experiments of uni-directional glass-fiber reinforced composites [33] revealed that, as in the case of metals, the depth of cut has a linear influence on both horizontal and vertical resultant force components, with the intercept above zero (attributed to forces acting on the relief face, which are believed to be independent of the change of depth of cut within practical boundaries). The same experiments report that the rake angle has a strong influence on the resultant cutting force (noted as higher than in the case of metals) while the relief angle has little if no influence. No similar oblique cutting experiments were found for composite materials.

For the current study, we will consider a mechanistic force model based on oblique cutting, considering both the forces acting on the rake and relief face as in fig. 3.3.

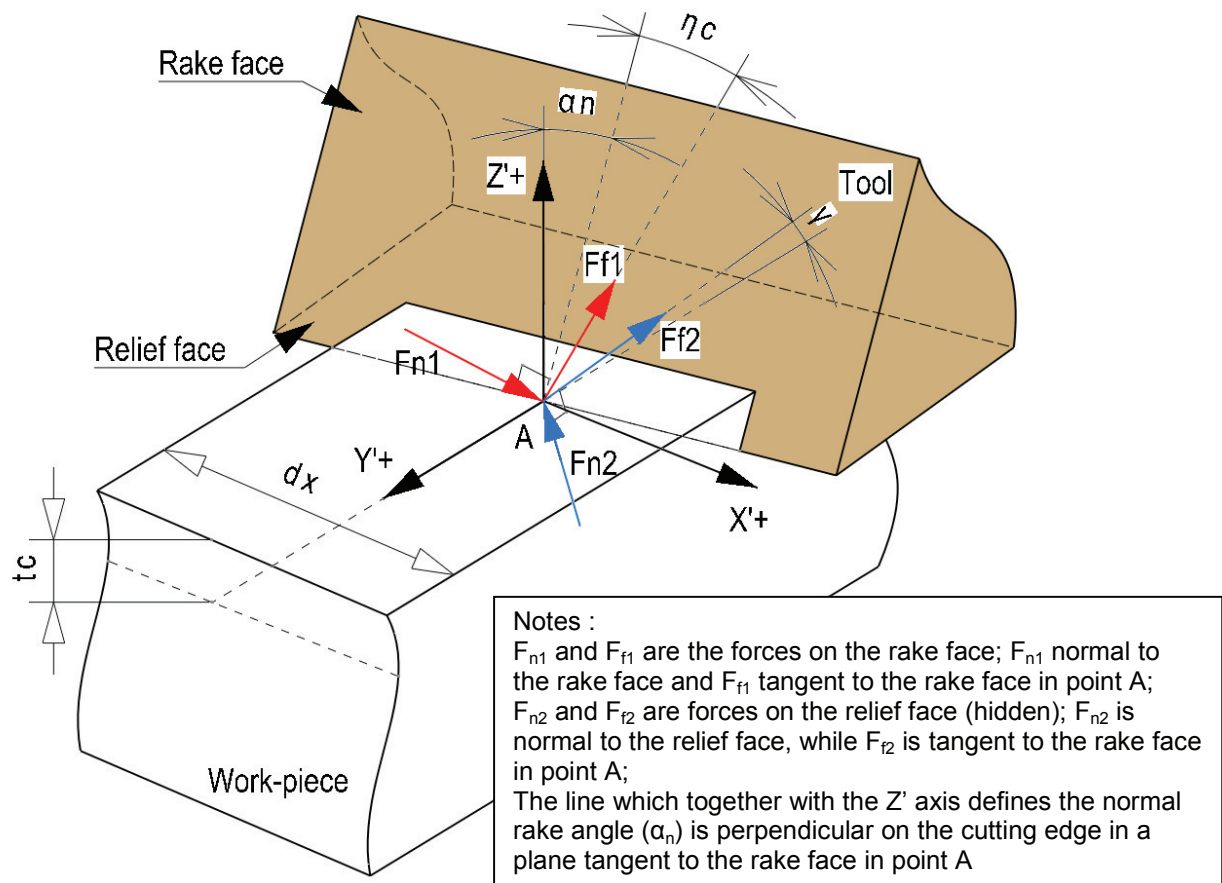


Fig. 3.3 – Elementary cutting forces defined in oblique cutting

On the rake face, normal (F_{n1}) and friction (F_{f1}) forces are represented in red, while forces on the relief face (F_{n2} and F_{f2} respectively) are colored blue. As usual, the force directions are normal and tangential to the respective surfaces (rake and relief). Furthermore, it is assumed that the friction force on the rake face (F_{f1}) acts along the chip flow direction, at an angle η_c (chip flow angle, discussed later) from the normal to the cutting edge lying on the rake face, while the friction force on the relief face (F_{f2}) acts along the projection of the velocity direction (Y' axis) on the relief face.

In addition to the angles presented in the previous section, determining the vector direction in the X'Y'Z' coordinate system requires the introduction of the angles defining the rake and relief faces in drilling as follows:

- Normal rake angle (α_n), defined as the angle between the rake face (or tangent to the rake face – if the rake face is not planar) at a point A on the cutting edge and the normal to both the cutting velocity vector and the cutting edge (Z' axis), measured in a plane perpendicular to the cutting edge at point A (see chapter 3.4.6 for a more extensive discussion and figure 3.10).
- Relief angle (γ) is the angle at point A between the relief face and the local velocity (along the Y' axis) measured in the Y'Z' plane (formed by the local velocity and the normal to both the velocity and the cutting edge). Discussions and derivations for this angle are presented in chapter 3.4.7.
- Chip flow angle (η_c) is a characteristic angle to oblique cutting and defines the direction of chip movement after separation from the work-piece. It is defined in the plane of the rake face (or tangent plane to the rake face at point A if the rake face is not planar) as the angle between the chip flow direction and the normal to the cutting lip. Oblique cutting experiments conducted on metals [34] concluded that it is proportional to the inclination angle by a factor between 0.9 and 1.0. This proportionality is known as the chip flow law of Stabler. The same is commonly assumed in drilling cutting force models, although Watson in [35] challenges this assumption by noting that the chip in drilling is usually complete across the cutting lip, and therefore there might be some restrictions in the variation of the chip flow angle in this region (cutting lip) and recommends using a constant value for the case of metal drilling. As unlike metals, the chip is powder-like in machining fiber reinforced materials, the current study does not identify such constrain on the variation of the chip flow angle and therefore the chip flow law of Stabler [34] is assumed valid. However, the current study identifies the need for experimental clarification in this direction.

The equations used to determine the values of these angles are derived and discussed in chapters 3.4.6, 3.4.7 and 3.4.8, while their values for the drills used in experiments are presented in chapter 3.5.

It is further assumed that the magnitude of the elementary forces acting on both rake and relief faces introduced above are as follows:

$$F_{n1} = K_c \cdot A_u \quad (3.12)$$

$$F_{f1} = K_f \cdot F_{n1} = K_f \cdot K_c \cdot A_u \quad (3.13)$$

$$F_{n2} = K_p \cdot A_c \quad (3.14)$$

$$F_{f2} = K_f \cdot F_{n2} = K_f \cdot K_p \cdot A_c \quad (3.15)$$

Where K_c [N/mm^2], K_f [-] and K_p [N/mm^2] are empirical coefficients representing the specific cutting coefficient, friction coefficient and specific contact pressure on relief face respectively. It is assumed that the friction coefficient is identical for both friction forces acting on rake and relief faces, as the materials are identical and the relative velocities comparable. These coefficients are extensively discussed in chapter 5.2.

It is noted that the proposed magnitude of the elemental cutting forces on the rake face are proportional to the uncut chip area (A_u – uncut chip section area in a plane perpendicular to velocity vector), while the relief forces are proportional to the contact area (A_c – on the relief face) as generally accepted by

researchers. By tests with restricted contact between tool and chip, [36] shows that for metals the contact area on the rake face plays also a role in the magnitude of the recorded forces, although it is not clear that the influence reported by the authors will be consistent for different work-piece materials and different cutting configurations. The difficulties in experimentally determining the contact area on the rake face and also the lack of the underlying model to calculate the contact area from the uncut chip area (A_u easily defined) have prohibited further studies in this direction.

From fig.3.3, it can be derived that the uncut chip area A_c [mm^2] is equal to:

$$A_u = t_c \cdot dx \quad (3.16)$$

Where t_c [mm] is the actual depth of cut which can be calculated for drilling starting from the feed f [mm/rev] (eq. 3.17 below, where $N[-]$ is the number of flutes – for more details see chapter 3.4.9) and dx [mm] is the element's width. In drilling the elements are defined of constant size along the radial direction – dr [mm]. Therefore, dx (and later dl) need to be calculated from dr using equation 3.18. A more detailed discussion about the definition of the oblique cutting elements in drilling is presented in chapter 3.4.9 and fig. 3.17, where the derivations of these equations are also presented.

$$t_c = \frac{f}{N} \cdot \cos(\mu) \cdot \cos(\tau) \quad (3.17)$$

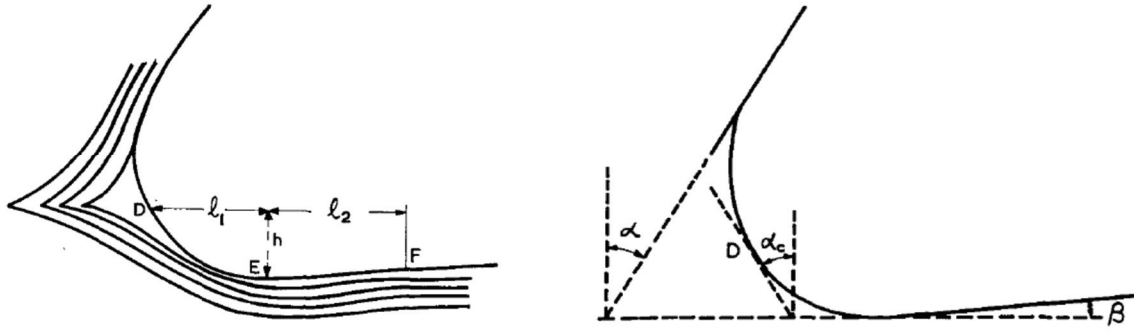
$$dx = \frac{dr}{\cos(\tau)} \quad (3.18)$$

After some simplifications, A_u reduces to the generally accepted equation:

$$A_u = \frac{f}{N} \cdot \cos(\mu) \cdot dr \quad (3.19)$$

It can be observed that, while the uncut chip area A_u is only influenced by the cutting angle (μ) (for the cutting lip region its influence is small and negligible and for the chisel edge area A_u decreases sharply towards the drill axis), the actual depth of cut (t_c) is also influenced by the 2nd Euler rotation angle (τ) or point angle (p), web angle (β) and inclination angle (i) (see eq. 3.3) and varies more widely even for the cutting lip region. The variation with the radius of the actual depth of cut (t_c) is usually ignored in cutting forces modeling, although it should have an influence on the chip velocity, chip flow angle (η_c) and, for the case of metals, on the shear angle.

A_c [mm^2] represents the contact area on the relief face. The forces acting on the relief face have been modeled in a similar manner to Rubenstein in [30] and [37], which estimates the contact area (A_c) in orthogonal cutting to be a function of the relief angle (γ), the cutting edge radius (R_e [mm]) and a critical rake angle (α_c) over which value ploughing is believed to occur instead of cutting [38]. This modeling approach is based on the fact that the cutting edge has a radius (R_e), and due to this radius a certain amount of work-piece material (which otherwise should be removed) is extruded under the tool as exemplified in figure 3.4. The extruded material is deformed both elastically and plastically. The thickness of the extruded layer (h) is defined by the point of stagnation D which is characterized by the critical rake angle (α_c). In general it was shown that the extruded layer is very small in comparison with the depth of cut, therefore its subtraction from the theoretical depth of cut (t_c – eq. 3.17) is not necessary. Point F on the relief face defines the end of the contact length (c_1 – DF in fig. 3.4a), and due to plastic deformations is usually at a lower level than point D . However, it is customary to assume only elastic deformations and a constant pressure along the complete contact area, assumption which is even more suitable for composite materials.



a) Illustration of the flow pattern of work-piece material approaching a tool of finite sharpness

b) Representation of the contour of the cutting edges of a tool illustrating the critical rake angle (α_c)

Fig. 3.4 – Illustration of the extrusion of the work-piece material under the tool for orthogonal cutting [30] (D – point of “stagnation”; α_c – critical rake angle; α – rake angle; β – relief angle (γ , as used in the current thesis); E, F – point on the relief face delimiting the contact segments l_1 and l_2 , h – the thickness of the extruded layer)

For oblique cutting the influence of the inclination angle (i) on the contact length on the relief face (c_l [mm]) has to be considered. Therefore, A_c is assumed:

$$A_c = c_l \cdot dl \quad (3.20)$$

Where

$$c_l = R_e \cdot \left\{ \cos(\alpha_c) + \frac{[1 - \sin(\alpha_c)]}{\tan(\gamma)} \right\} \cdot \cos(i) \quad (3.21)$$

Following simplification:

$$A_c = R_e \cdot \left\{ \cos(\alpha_c) + \frac{[1 - \sin(\alpha_c)]}{\tan(\gamma)} \right\} \cdot \frac{dr}{\cos(\tau)} \quad (3.22)$$

It is assumed that the cutting edge radius is constant along the cutting edges of the drill and as estimated by others [30, 38] around the value of 0.00762mm (0.0003 in), while the critical rake angle is 70° (-70° if measured in the same manner as for the normal rake angle, from the Z axis), according to [38].

Before proceeding, the elementary forces need to be expressed as vectors in the X'Y'Z' coordinate system. Their components have been derived in chapter 3.4.10. Considering their magnitude proposed by equations 3.12-15, we obtain the following relationships.

$$\{F_{n1}\}_{X'Y'Z'} = K_c \cdot A_u \cdot \begin{Bmatrix} -\cos(\alpha_n) \cdot \sin(i) \\ -\cos(\alpha_n) \cdot \cos(i) \\ -\sin(\alpha_n) \end{Bmatrix} \quad (3.23)$$

$$\{F_{f1}\}_{X'Y'Z'} = K_c \cdot A_u \cdot \begin{Bmatrix} K_f \cdot [\sin(\eta_c) \cdot \cos(i) - \cos(\eta_c) \cdot \sin(\alpha_n) \cdot \sin(i)] \\ -K_f \cdot [\cos(\eta_c) \cdot \sin(\alpha_n) \cdot \cos(i) + \sin(\eta_c) \cdot \sin(i)] \\ K_f \cdot \cos(\eta_c) \cdot \cos(\alpha_n) \end{Bmatrix} \quad (3.24)$$

$$\{F_{n2}\}_{X'Y'Z'} = K_p \cdot A_c \cdot \begin{Bmatrix} 0 \\ \sin(\gamma) \\ \cos(\gamma) \end{Bmatrix} \quad (3.25)$$

$$\{F_{f2}\}_{X'Y'Z'} = K_p \cdot A_c \cdot \begin{Bmatrix} 0 \\ -K_f \cdot \cos(\gamma) \\ K_f \cdot \sin(\gamma) \end{Bmatrix} \quad (3.26)$$

Using equation 3.1, the vectors can be transformed into the XYZ coordinate system. Of interest in drilling are the components in the Y and Z direction (F_y and F_z – see below), corresponding to tangential (torque) and axial (thrust) loads, while the lateral component (F_x) has only minor importance (for reasons previously discussed). The axial feed rate (f) only influences the forces acting on the rake face, therefore we have grouped them together before applying the coordinate system transformation:

$$\{\overline{F_{n1}} + \overline{F_{f1}}\}_{XYZ} = T_{X'Y'Z',XYZ} \cdot \{\overline{F_{n1}} + \overline{F_{f1}}\}_{X'Y'Z'} = K_c \cdot A_u \cdot \begin{Bmatrix} g_{1x} \\ g_{1y} \\ g_{1z} \end{Bmatrix} \quad (3.27)$$

$$\{\overline{F_{n2}} + \overline{F_{f2}}\}_{XYZ} = T_{X'Y'Z',XYZ} \cdot \{\overline{F_{n2}} + \overline{F_{f2}}\}_{X'Y'Z'} = K_p \cdot A_c \cdot \begin{Bmatrix} g_{2x} \\ g_{2y} \\ g_{2z} \end{Bmatrix} \quad (3.28)$$

The resultant force in the XYZ coordinate system will be calculated as follows:

$$\{\overline{F_R}\}_{XYZ} = \{\overline{F_{n1}} + \overline{F_{f1}}\}_{XYZ} + \{\overline{F_{n2}} + \overline{F_{f2}}\}_{XYZ} = \begin{Bmatrix} F_x \\ F_y \\ F_z \end{Bmatrix} \quad (3.29)$$

Where:

$$F_x = K_c \cdot A_u \cdot g_{1x} + K_p \cdot A_c \cdot g_{2x} \quad (3.30)$$

$$F_y = K_c \cdot A_u \cdot g_{1y} + K_p \cdot A_c \cdot g_{2y} \quad (3.31)$$

$$F_z = K_c \cdot A_u \cdot g_{1z} + K_p \cdot A_c \cdot g_{2z} \quad (3.32)$$

And g_{1x} , g_{2x} , g_{1y} , g_{2y} , g_{1z} and g_{2z} are geometric functions derived from the matrix multiplication operation in eq. 3.27 and 3.28:

$$g_{1x} = \cos(\tau) \cdot [-\cos(\alpha_n) \cdot \sin(i) + K_f \cdot [\sin(\eta_c) \cdot \cos(i) - \cos(\eta_c) \cdot \sin(\alpha_n) \cdot \sin(i)]] - \dots \\ \dots - \sin(\tau) \cdot [-\sin(\alpha_n) + K_f \cdot \cos(\eta_c) \cdot \cos(\alpha_n)] \quad (3.33)$$

$$g_{1y} = \sin(\tau) \cdot \sin(\mu) \cdot [-\cos(\alpha_n) \cdot \sin(i) + K_f \cdot [\sin(\eta_c) \cdot \cos(i) - \cos(\eta_c) \cdot \sin(\alpha_n) \cdot \sin(i)]] + \dots \\ \dots + \cos(\mu) \cdot [-\cos(\alpha_n) \cdot \cos(i) - K_f \cdot [\cos(\eta_c) \cdot \sin(\alpha_n) \cdot \cos(i) + \sin(\eta_c) \cdot \sin(i)]] + \dots \\ \dots + \cos(\tau) \cdot \sin(\mu) \cdot [-\sin(\alpha_n) + K_f \cdot \cos(\eta_c) \cdot \cos(\alpha_n)] \quad (3.34)$$

$$\begin{aligned}
g_{1z} &= \sin(\tau) \cdot \cos(\mu) \cdot [-\cos(\alpha_n) \cdot \sin(i) + K_f \cdot [\sin(\eta_c) \cdot \cos(i) - \cos(\eta_c) \cdot \sin(\alpha_n) \cdot \sin(i)]] - \dots \\
&\dots - \sin(\mu) \cdot [-\cos(\alpha_n) \cdot \cos(i) - K_f \cdot [\cos(\eta_c) \cdot \sin(\alpha_n) \cdot \cos(i) + \sin(\eta_c) \cdot \sin(i)]] + \dots \\
&\dots + \cos(\tau) \cdot \cos(\mu) \cdot [-\sin(\alpha_n) + K_f \cdot \cos(\eta_c) \cdot \cos(\alpha_n)] \quad (3.35)
\end{aligned}$$

$$g_{2x} = -\sin(\tau) \cdot [\cos(\gamma) + K_f \cdot \sin(\gamma)] \quad (3.36)$$

$$g_{2y} = \cos(\mu) \cdot [\sin(\gamma) - K_f \cdot \cos(\gamma)] + \cos(\tau) \cdot \sin(\mu) \cdot [\cos(\gamma) + K_f \cdot \sin(\gamma)] \quad (3.37)$$

$$g_{2z} = -\sin(\mu) \cdot [\sin(\gamma) - K_f \cdot \cos(\gamma)] + \cos(\tau) \cdot \cos(\mu) \cdot [\cos(\gamma) + K_f \cdot \sin(\gamma)] \quad (3.38)$$

As most of the angles vary with the radial coordinate of the point A from the drill axis, F_x , F_y and F_z are functions of the radius and axial feed rate (f). The F_y and F_z functions (for elemental size equal to unity, $dr=1$) will be compared with the data obtained experimentally for the cutting forces distribution along the drill radius (as obtained in chapter 4) for various cutting conditions in order to obtain the values of the 3 employed coefficients (K_c , K_f and K_p).

It is noted that the spindle speed (n [rpm]) is not a parameter for the cutting forces at this point, as the local velocity (function of the spindle speed as in eq. 3.52) does not affect the decomposition of the forces and geometrical parameters of the cutting element. Its influence can only be accounted for in a material property, such as the empirical coefficients (K_c , K_f and K_p), subject which is more extensively discussed in chapter 5.2.

As the positive direction of the Y axis is chosen to coincide with the tangential velocity (see fig. 3.1), F_y will always yield negative values under practical ranges of the considered angles. While the measurements of thrust and torque are always considered positive, for comparison with experimental data and calculating the total torque F_y will have its sign inverted.

To obtain the total thrust (F_z [N]) and torque (M_z [N*mm]) generated during drilling, functions 3.31 and 3.32, can be integrated in the following manner:

$$F_z = \int_{r=0}^{r=R} N \cdot F_z(r) \cdot dr \quad (3.39)$$

$$M_z = \int_{r=0}^{r=R} N \cdot F_y(r) \cdot r \cdot dr \quad (3.40)$$

Where r is the radial coordinate, R is the outer radius of the drill and N is the number of flutes. The torque will further be converted to [N*m] units for discussion, when the results of the cutting force model will be compared with the experimental data in chapter 5.

For a drill with two flutes ($N=2$) the total lateral force will be zero, as the action of each flute cancels the action of the other:

$$F_x = \int_{r=0}^{r=R} F_{y,flute=1}(r) \cdot dr - \int_{r=0}^{r=R} F_{y,flute=2}(r) \cdot dr \quad (3.41)$$

Although not the scope of the current PhD thesis, the analysis of the lateral force could help describe defects resulting from the asymmetry of the flutes as in [2]. Experimental testing with single flute drills could also be used to study the variation of the lateral force, although no published reports were found about such attempts.

3.4 Extended derivations

To provide clarity to the thesis, we have separated in this chapter the derivation and discussion about the geometrical parameters used in the definition of the cutting force model in chapters 3.2 and 3.3. The derivations presented hereby are mostly analytic and in general can be applied to any drill geometry, unless otherwise mentioned. In chapter 3.5, two different drills employed in the experiments are fully described mathematically, using the final equations obtained in the current chapter. The geometrical parameters are introduced in a logical order, similar to their introduction in the cutting force model.

Most of the equations introduced below are of practical importance to the cutting force model presented in this thesis, with the exception of the manufacturer's point angle (ρ') introduced in 3.4.2, which was not employed in the model.

3.4.1 Chisel edge angle (ψ) and the web angle (β)

The attached figure represents a top view of a generic twist drill, outlining the definitions of the web thickness ($2w$), the chisel edge angle (ψ) and the web angle (β) for a point A on the cutting lip.

The chisel edge is the segment of the cutting edge closest to the drill center with an orientation passing through the drill axis. In most cases the chisel edge is a straight line (or can be approximated as such) lying in a plane perpendicular to the drill axis. However, in some cases (like the 2-facet twist drill employed in our experiments) the chisel edge does not lie in a plane perpendicular to the drill axis, but an angle exists with the drill axis. Nevertheless, the chisel edge area can be defined by 3 geometrical parameters: web thickness ($2w$), chisel edge outer radius (R_c – see fig. 3.7) and the chisel edge angle (ψ , defined in a plane perpendicular to the drill axis). For all cases where the chisel edge can be approximated as a straight line, the following relationship can be easily deduced between the 3 parameters:

$$R_c = \frac{w}{\sin(\psi)} \quad (3.42)$$

The web angle (β) is defined as the angle measured in a plane perpendicular to the drill axis between the cutting edge and the radial direction at point A, as shown in the above figure. For any point on the chisel edge (if the chisel edge is a straight line), the web angle is zero, while for the cutting lips its equation can be easily deduced from figure 3.5:

$$\beta(r) = \begin{cases} 0, & 0 < r < R_c \\ \arcsin\left(\frac{w}{r}\right), & R_c \leq r \leq R \end{cases} \quad (3.43)$$

We also note that the web angle at radius R_c is equal to the chisel edge angle: $\beta(R_c) = \psi$.

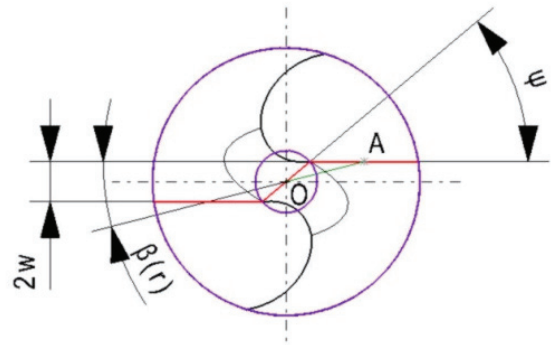


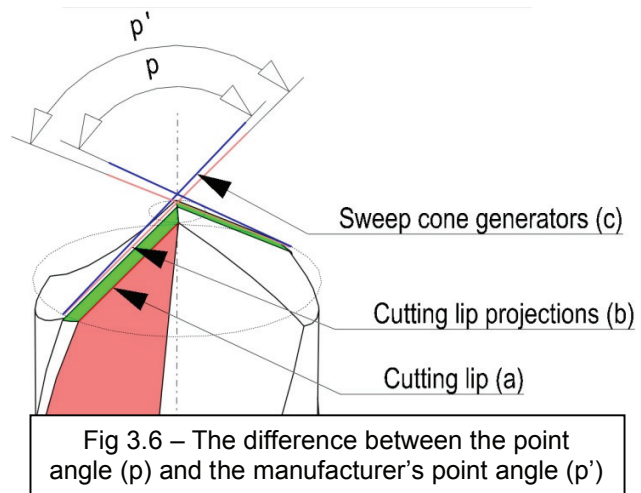
Fig 3.5 – Top view of a generic twist drill introducing the web thickness ($2w$), the chisel edge angle (ψ) and the web angle (β)

3.4.2 Point angle (p) and manufacturer's point angle (p')

The point angle is one of the most important characteristic of the drill. In general it is defined as the angle(-s) of the sweeping cone(-s) obtained by the rotation of the drill around its axis, and hereby referred to as “point angle” (p). As above defined, it has importance to describe the hole obtained for blind holes. In cutting force modeling, it is important as it defines the inclination of the cutting edges with respect of the drill axis, which is in fact half of the value of the point angle provided by drill manufacturers. For the chisel edge area, which usually lies in the plane perpendicular to the drill axis, the point angle is 180° (or 90° if we consider the angle with the drill axis) and as most of the drills have straight and un-segmented cutting lips, there is only one value provided as the point angle. However, there are drills where the cutting lips are segmented (tapered drill reamer, stepped drills etc.) or where they are curved (racon drills), where the point angle should be defined in stages or as functions (seldom provided by drill manufacturers). In the current thesis a generic approach is used to mathematically define the point angle – as a function of the radial direction, to accommodate the definition of this angle for any type of drill. For practical details, see chapter 3.5.1.

A difference exists between the point angle defined as the angle of the sweeping cone and the actual inclination between the cutting lips and the tool axis for all areas where the web angle (β) is different than zero, although this difference is most of the time ignored. The angle between the cutting lips and the drill axis is referred to as “manufacturer's point angle” (p') and can be calculated from the point angle and other geometrical parameters.

To exemplify this difference, fig. 3.6 is showing the tip of a generic twist drill, where the cutting lip (straight line - a), if extended, does not intersect the tool axis. By the tool rotation about its axis, the cutting lips generate a conical surface, which can be defined by its generators (lines c, lying in a plane parallel to both cutting lips and passing through the drill axis) which by definition, if extended, will intersect the tool axis. If we further project the cutting lip (a) on the same plane, the cutting lip projection (b) is obtained, which have a different inclination than the cone's generators (c).



A relationship can be found between the point angle (p) and the manufacturer's point angle (p'). Fig. 3.7 was constructed to assist with the derivation of this relationship starting from a projected view from the tip of a generic twist drill.

In the triangle $\Delta N_1T_1A_2$ (with the $\angle N_1T_1A_2=90^\circ$ in sketch along a-a), the segment N_1T_1 equals:

$$N_1T_1 = R - R_c \quad (3.44)$$

And A_2T_1 :

$$A_2T_1 = \frac{N_1T_1}{\tan p} = \frac{R - R_c}{\tan p} \quad (3.45)$$

Notes :

- O is the drill center;
- OA_1 is the chisel edge (of length R_c) and with half of the web thickness w ;
- A_1A_2 is the cutting lip segment, inclined with the manufacturing point angle (p') from the drill axis (represented in sketch along b-b). Its projection in XY plane perpendicular on the drill axis is A_1T_1 .
- ON_1 and N_1A_2 is the revolution contour obtained by the rotation of the drill along its axis, with segment ON_1 equal to the radius of the chisel edge and N_1A_2 inclined from the drill axis by the point angle (p). The projection of the contour on a plane perpendicular on the drill axis is OT_1 , segment equal in length with the radius of the drill.

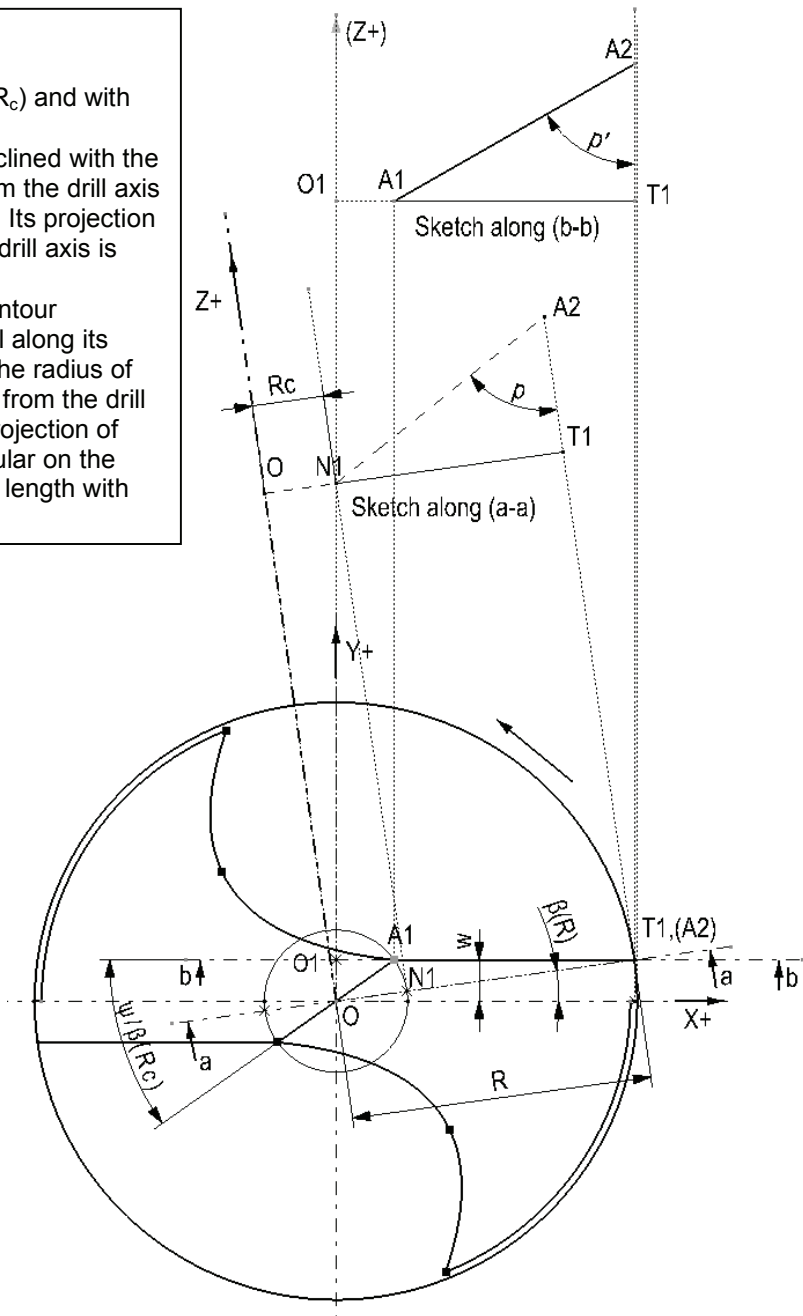


Fig.3.7 – Sketch to assist in the derivation of the manufacturer's point angle (p')

In the top view of the drill, from ΔOO_1T_1 (with the $\angle OO_1T_1=90^\circ$), O_1T_1 can be expressed as:

$$O_1T_1 = \frac{OO_1}{\tan(\beta(R))} = \frac{w}{\tan(\beta(R))} \quad (3.46)$$

Further on, from the top view of the drill, triangle ΔOO_1A_1 (with the $\angle OO_1A_1=90^\circ$), O_1A_1 can be expressed as:

$$O_1A_1 = \frac{OO_1}{\tan(\psi)} = \frac{OO_1}{\tan(\beta(R_c))} = \frac{w}{\tan(\beta(R_c))} \quad (3.47)$$

It is found more generic to work on the relationship with the angle $\beta(R_c)$ rather than the chisel edge angle (ψ) as we have shown their equality in chapter 3.4.1, in order to account for cases where the cutting lips have several segments (as the tapered drill reamer).

The length of the segment A_1T_1 can be calculated from the difference:

$$A_1T_1 = O_1T_1 - O_1A_1 = \frac{w}{\tan(\beta(R))} - \frac{w}{\tan(\beta(R_c))} = w \cdot \frac{\tan(\beta(R_c)) - \tan(\beta(R))}{\tan(\beta(R)) \cdot \tan(\beta(R_c))} \quad (3.48)$$

And from the triangle $\Delta A_1T_1A_2$ (with the $\angle A_1T_1A_2 = 90^\circ$ in sketch along b-b), the manufacturer's point angle (p') can be now derived:

$$\tan(p') = \frac{A_1T_1}{A_2T_1} = w \cdot \frac{\tan(\beta(R_c)) - \tan(\beta(R))}{\tan(\beta(R)) \cdot \tan(\beta(R_c))} \cdot \frac{\tan(p)}{R - R_c} \quad (3.49)$$

Using the above equation, the manufacturer's point angle (p') can be estimated from the point angle (p) and for the studied cases p' is usually 1-2° greater than p . However, the optical measurements of the drills used in the performed experiments during the current doctoral thesis, showed that the value supplied as the point angle in the catalogues by the manufacturers are usually rounded up to usual values like 118°, where in fact a difference of even a few degrees plus/minus was discovered from the advertised value. Therefore, it was decided that for the practical calculations presented in this thesis to use the measured values (as close as possible to the definition of the manufacturer's point angle – introduced in chapter 3.5), rather than the correction provided by eq. 3.49 from the value supplied in the drill's catalogues.

3.4.3 Cutting angle (μ) and kinematics of the drilling process

When drilling, an axial movement and a rotation are imposed to the drill. The axial feed (f) and the spindle speed (n) are used to describe separately these movements and are referred to as the drilling parameters. They have been introduced in chapter 2.3.

Due to the nature of the rotational movement about the drill axis, each point on the cutting edges will move at a different velocity (both in magnitude and direction). If we consider the velocity vector (V) decomposed along the axial and tangential directions, we observe that the axial velocity (V_n) is always constant while its tangential component (V_t) will vary with the radial coordinate, considering that the axial feed and speed rate are constant.

As each component of the local velocity is controlled separately by its respective cutting parameter, the magnitude of the axial and tangential components of the velocity can be easily deduced by:

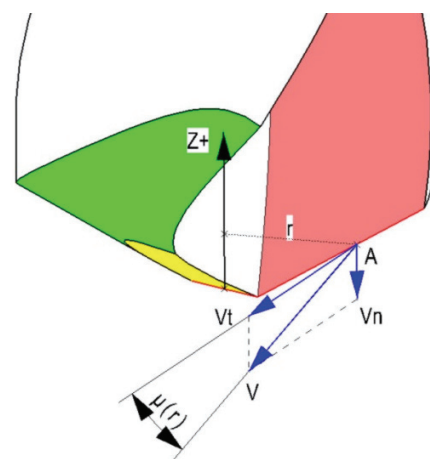


Fig. 3.8 – Local velocities and the cutting angle (μ)

$$V_n = \frac{f \cdot n}{60} \text{ [mm/s]} \quad (3.50)$$

$$V_t(r) = \frac{2\pi \cdot r \cdot n}{60} \text{ [mm/s]} \quad (3.51)$$

As exemplified in fig. 3.8, we can further calculate the magnitude of the resultant velocity:

$$V(r) = \sqrt{V_n^2 + V_t^2} = \sqrt{\left(\frac{f \cdot n}{60}\right)^2 + \left(\frac{2\pi \cdot r \cdot n}{60}\right)^2} = \frac{n}{60} \sqrt{f^2 + 4\pi^2 r^2} \text{ [mm/s]} \quad (3.52)$$

For cutting force modeling purposes, it is found very useful to introduce the cutting angle (μ), as the angle at a point on the cutting edge between the axial and tangential components of the velocity (measured in a plane perpendicular to the radial direction passing through the point). This angle, derived from fig. 3.8 using the equation below, will be used to describe the cutting direction at any point on the cutting edges (including the chisel edge).

$$\tan \mu(r) = \frac{f}{2\pi \cdot r} \Rightarrow \mu(r) = \arctan\left(\frac{f}{2\pi \cdot r}\right) \quad (3.53)$$

3.4.4 Inclination angle (i)

The inclination angle (i) is an angle characteristic to oblique cutting, defined as the angle between the cutting edge and the normal to the velocity vector in the plane containing both the velocity and the cutting edge. In drilling it is derived by the commonly accepted equation 3.54, although in many cases its simplified version is employed 3.55 (where the cutting angle is ignored).

$$i(r) = \arcsin[\sin(\beta) \cdot \cos(\mu) \cdot \sin(p) + \sin(\mu) \cdot \cos(p)] \quad (3.54)$$

$$i(r) = \arcsin[\sin(\beta) \cdot \sin(p)] \quad (3.55)$$

In [39] equation 3.55 was first introduced by the main authors, although in an appendix a reviewer presents the derivation of eq. 3.54, which considers the dynamic effects of the axial feed through the cutting angle (μ). Through our own derivation, we have reached the same form of the equation 3.54. As it is already published and accepted, we do not find of interest presenting the derivation proof in the current thesis. In figure 3.9, a generic twist drill is presented showing the inclination angle for an arbitrary point.

It is noted that the definition of the inclination angle as above is valid for the chisel edge area as well. However, the web angle (β) is always zero for the chisel edge, while the point angle (p) is in many cases equal to 90° , therefore the inclination angle becomes zero (and orthogonal cutting can be

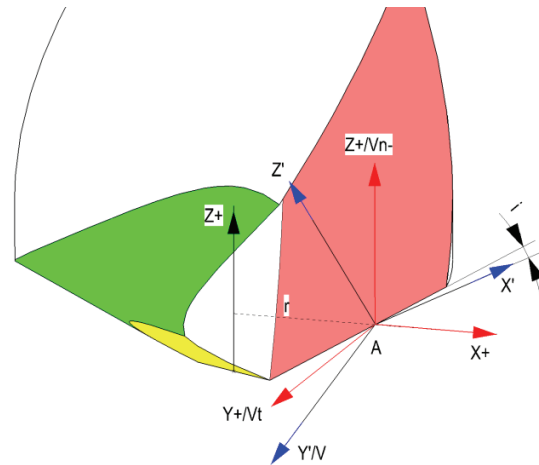


Fig. 3.9 – The inclination angle (i) in drilling

assumed). The 2-facet twist drill used in our experiments has the chisel edge inclined with an angle smaller than 90° from the drill axis, therefore an inclination angle greater than zero exists for the chisel edge area in this case. More details about this particular case are given in chapter 3.5.3.

3.4.5 2nd Euler rotation angle (τ)

The 2nd Euler angle of rotation (τ) is introduced as an auxiliary angle used to obtain the transformation matrix from drilling system of coordinates (XYZ) to oblique coordinate system (X'Y'Z'), those details are presented in chapter 3.2. More specifically, it describes the 2nd rotation about the Y' axis, as can be visualized in fig. 3.2 and 3.10 below.

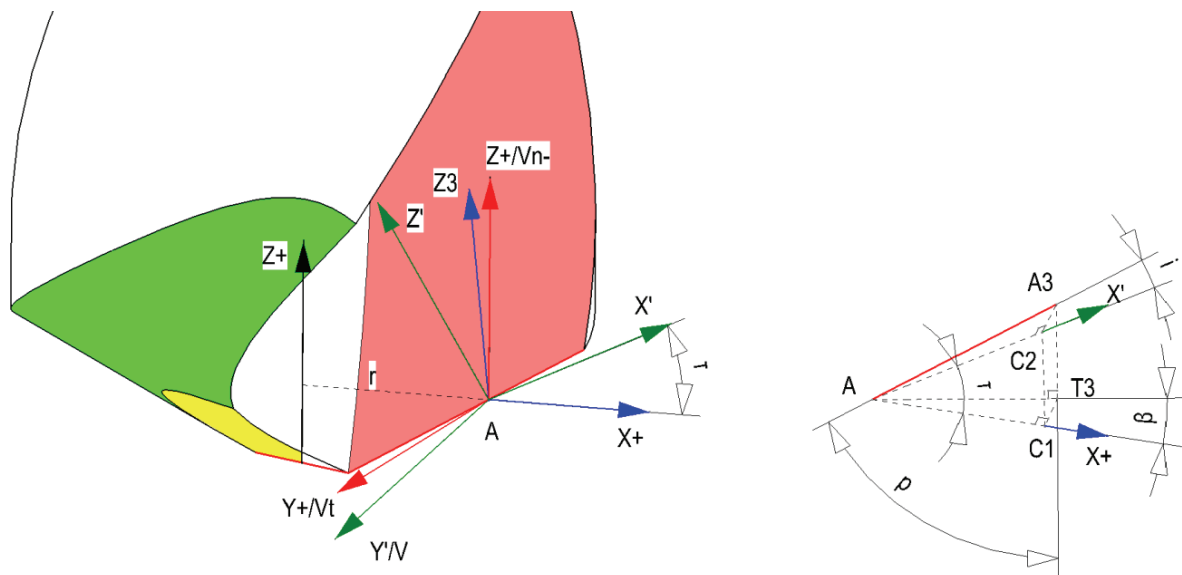


Fig. 3.10 – Introducing the 2nd Euler angle of rotation (τ)

As this angle is not used by any other cutting force models, we present below its derivation, starting from the angles introduced previously.

Let us assume a segment AA_3 of the cutting edge equal to unity. By projecting this segment on plane XY, we obtain the triangle ΔAT_3A_3 (with the $\angle AT_3A_3=90^\circ$). In this triangle the angle $\angle AA_3T_3$ is the point angle (p), as defined in 3.4.2. Therefore, we can deduce that:

$$AT_3 = \sin(p) \quad (3.56)$$

Furthermore, the angle between AT_3 and the X axis will be equal to the web angle (β) as defined in section 3.4.1. By considering the triangle ΔAC_1T_3 (with the angle $\angle AC_1T_3=90^\circ$), we obtain by projecting segment AT_3 on the X axis and we can determine that:

$$AC_1 = \sin(p) \cdot \cos(\beta) \quad (3.57)$$

Also, by the definition of the inclination angle (i) in section 3.4.4 of the current chapter, we find the angle $\angle C_2AA_3=i$, where AC_2 is the projection of AA_3 on $X'Z'$ plane. Therefore, from the triangle ΔAC_2A_3 (with the angle $\angle AC_2A_3=90^\circ$) we can calculate AC_2 as:

$$AC_2 = \cos(i) \quad (3.58)$$

Finally, from triangle ΔAC_1C_2 (with the angle $\angle AC_1C_2=90^\circ$), we can calculate the 2nd Euler angle of rotation (τ) as follows:

$$\cos(\tau) = \frac{AC_1}{AC_2} = \frac{\sin(p) \cdot \cos(\beta)}{\cos(i)} \quad (3.59)$$

As long as the point angle (p), web angle (β) and inclination angle (i) are defined as earlier in this chapter (sections 3.4.2; 3.4.1 and 3.4.4 respectively), the 2nd Euler angle of rotation can be used for any region of the drill (including the chisel edge), with the mention that it will vary with the radial coordinate. In section 3.5.4 the variation of this angle along the radial coordinate for the particular cases of drill geometries considered in the current thesis is presented.

3.4.6 Normal rake angle (α_n) along the cutting lips

The most important geometrical parameter in oblique or orthogonal cutting is the rake angle, which defines the orientation of the rake face with respect to the cutting direction (more specifically with the normal to the cutting direction in a plane containing both the cutting direction and the cutting edge, i.e. X'Y' plane in fig. 3.11). While for orthogonal cutting the situation is fairly simple and straightforward, in oblique cutting appears the problem of which plane to use to measure this angle. Therefore, 3 possible definitions were proposed:

- The **normal rake angle (α_n)** defined in oblique cutting as the angle between the rake face (or tangent to the rake face if the rake face is not planar) at a point A on the cutting edge and the normal (i.e. Z' in fig. 3.11) to both the cutting velocity (direction, i.e. Y') and the cutting edge, **measured in a plane perpendicular to the cutting edge in point A.**
- The **velocity rake angle (α_v)** defined in oblique cutting as the angle between the rake face (or tangent to the rake face if the rake face is not planar) at a point A on the cutting edge and the normal to both the cutting velocity (direction) and the cutting edge, **measured in the plane (i.e. Y'Z' plane in fig. 3.11) passing through point A and containing the axial and tangential components (V_n and V_t) of the cutting velocity.**
- The **effective rake angle (α_e)** defined in oblique cutting as the angle between the rake face (or tangent to the rake face if the rake face is not planar) at a point A on the cutting edge and the normal to both the cutting velocity (direction) and the cutting edge, **measured in the plane passing through point A and containing the cutting direction vector and the chip flow direction vector.**

Fig. 3.11 presents the various possibilities of defining the rake angle in oblique cutting. The subject as to which one is most representative has been discussed in the literature. The velocity rake angle (α_v) is the easiest to derive in drilling, while the effective rake angle (α_e) and normal rake angle (α_n) are more complex. To derive the effective rake angle (α_e) presumes assumptions have to be made with respect to the chip flow angle (η_c), a highly discussed angle both in oblique cutting and drilling (details in chapter 3.3). By experimental means [2] shows that the most relevant is the normal rake angle (α_n) and this conclusion is supported by several other published studies. Therefore, the current thesis assumes the normal rake angle (α_n) as the parameter to describe the rake face for oblique cutting.

In drilling, it is customary to consider distinctly the rake angle of the cutting lips and of the chisel edge as for each cutting edge the rake face is generated differently. Although we will eventually use a discontinuous function (similar to as the web angle was defined in chapter 3.4.1) to unify its definition, we will discuss them separately, starting with the rake angle for the cutting lip region.

[4], [39], [5] and [2] introduce various equations to calculate the normal rake angle in drilling for the cutting lip region of a twist drill as presented in table 3.1. All notations have been changed to adapt the notations used in the current thesis (see nomenclature).

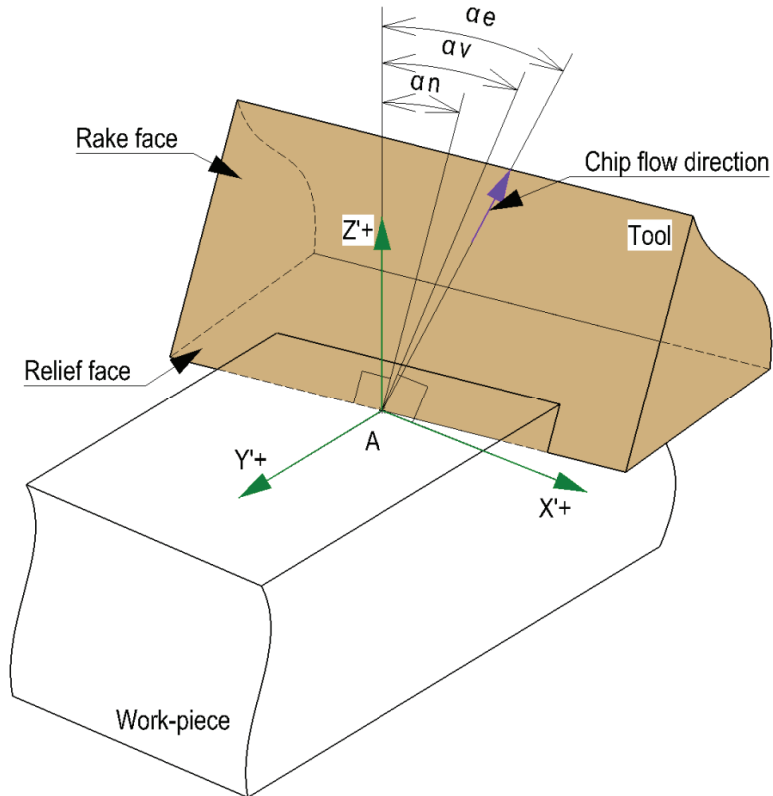


Fig. 3.11 – Rake angles in oblique cutting

Table 3.1 – State-of-art in definition of normal rake angle		Notes
Equations for normal rake angle (α_n)		
$\alpha_a = \arctan \left[\frac{\frac{r}{R} \cdot \tan(\theta)}{\sin(p)} \right] - \arctan \left[\frac{f}{2\pi \cdot r} \right]$	([4]-eq.14)	α_a – labeled “actual” rake angle by [4]’s authors
$\alpha_n = \arctan \left[\frac{\tan(\theta_l) \cdot \cos(\beta)}{\sin(p) - \frac{2\pi}{H} \cdot \cos(p)} \right] - \arctan[\tan(\beta) \cdot \cos(p)]$	([39]-eq.5)	-
$\alpha_n = \arctan \left[\frac{\tan(\theta_l) \cdot \cos(\beta)}{\sin(p) - \tan(\theta) \cdot \cos(p) \cdot \sin(\beta)} \right]$	([5]-eq.1)	-
$\alpha_n = \arctan \left[\frac{\frac{r}{R} \cdot \tan(\theta) \cdot \left(1 - \frac{w^2}{r^2}\right)^{0.5}}{\sin(p) - \cos(p) \cdot \left(\frac{r}{R} \tan(\theta)\right) \left(\frac{w}{r}\right)} \right] - \arctan \left[\frac{w \cdot \cos(p)}{(r^2 - w^2)^{0.5}} \right]$		Based on [39]

It can be observed that none of them considers the influence of the cutting angle (μ), which affects the cutting direction. As for the cutting lip region the cutting angle is usually small, the assumption that it is zero could seem reasonable. However, the influence of the normal rake angle over the elementary cutting forces is twofold: (i) it affects the decomposition of the cutting forces (as it appears a parameter in the geometrical factors defined by equations 3.33 to 3.35); (ii) it affects the specific cutting pressure (K_c) as later discussed in chapter 5.2. Therefore, we find that in particular cases small variations of the normal rake angle might have a strong influence on the elementary cutting forces and could allow capturing the variation of the elementary cutting forces with varying the feed.

Below we present the derivation of the normal rake angle (α_n) considering the cutting angle (μ).

We first have to introduce the helix angle (θ) which is usually supplied by the drill manufacturers and is the main parameter defining the surface of the rake face. As in fig. 3.12, the helix angle (θ) is defined as the angle between the tangent to the rake face and a parallel to the drill axis at the outermost point on the cutting edge ($r=R$), measured in a plane perpendicular on the radial direction.

In general, for a helical surface, the helix angle at a point on the helical surface found at distance r from the helix axis ($\theta_i(r)$) between the tangent to the surface and the axis can be found with the following relationship from the pitch (H) of the helix:

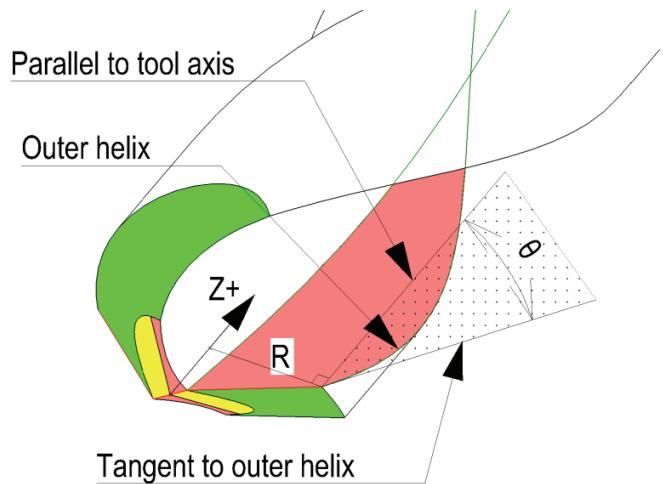


Fig. 3.12 – Definition of the helix angle (θ)

$$\theta_i(r) = \arctan\left(\frac{2 \cdot \pi \cdot r}{H}\right) \quad (3.60)$$

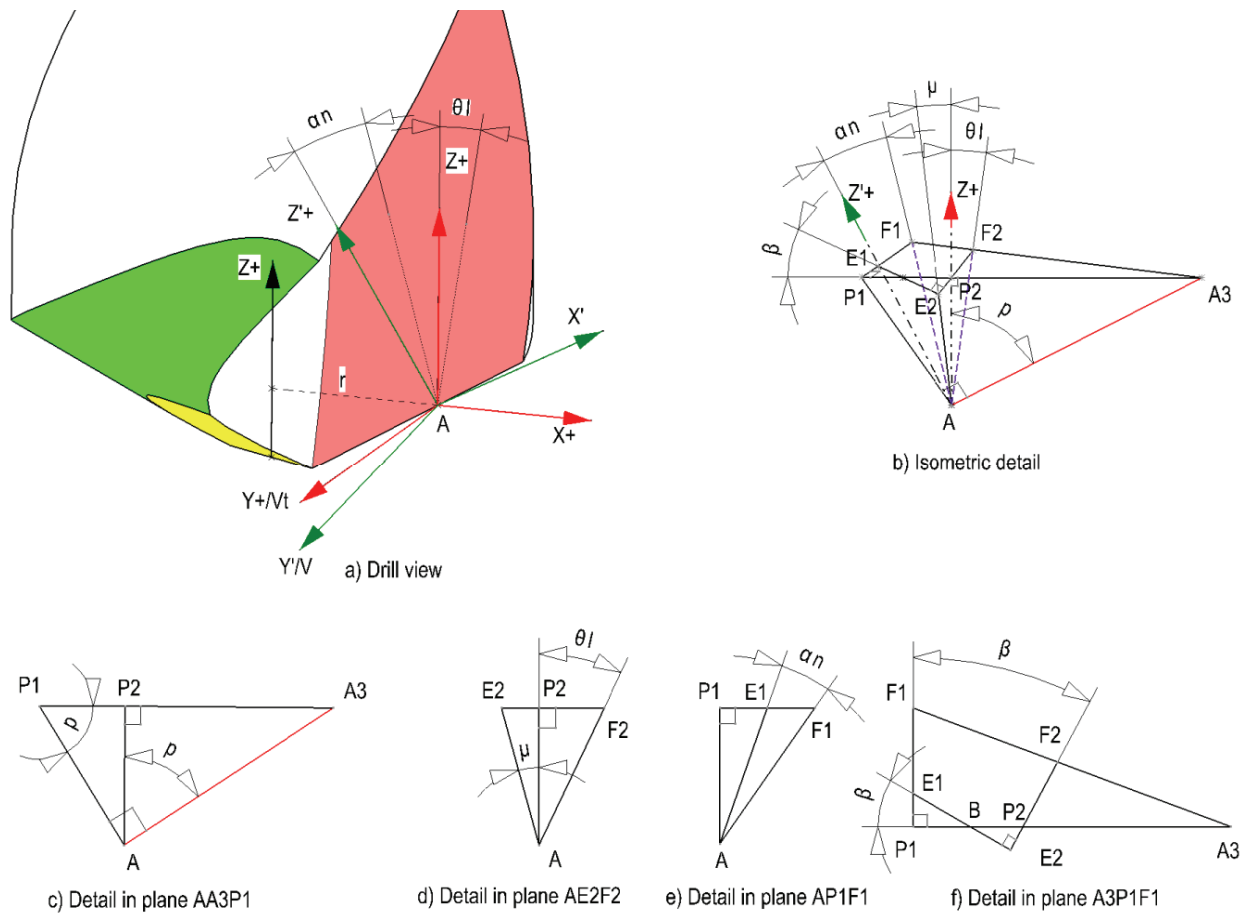
Therefore, knowing the helix angle (θ), defined at $r=R$, we can calculate the pitch of the helix (H , constant) and express the “local helix angle” (θ_i) as a function of the reference helix angle (θ):

$$\theta = \theta_i(R) = \arctan\left(\frac{2 \cdot \pi \cdot R}{H}\right) \Rightarrow H = \frac{2 \cdot \pi \cdot R}{\tan \theta} \quad (3.61)$$

Therefore:

$$\theta_i(r) = \arctan\left(\tan(\theta) \cdot \frac{r}{R}\right) \quad (3.62)$$

Fig. 3.13 has been constructed to assist in the derivation of the normal rake angle for an arbitrary point A on the cutting lip segment of a drill whose rake face can be defined by the local helix angle (θ_i) as introduced above. It is noted that for the reference helix angle (θ) equal to zero, the rake face will be planar, but the current derivation can still be applied.



Notes :

- Tangent plane to the rake face includes the following line segments: AA_3 (the cutting edge segment); AF_2 (in YZ plane); AF_1 (in plane normal to the cutting edge); A_3F_1 (parallel to XY plane);
- YZ plane includes the Y' axis (cutting direction, V) and the following line segments: AE_3 ; AP_2 (Z axis); AF_2 (on tangent plane to the rake face);
- Plane normal to the cutting lip at point A contains the following segments: AP_1 ; AE_1 (Z' axis); AF_1 (on tangent plane to the rake face);
- Plane parallel to XY plane through point A_3 contains the following line segments: A_3P_1 ; A_3F_1 (on tangent plane to the rake face); P_1F_1 (on plane normal to the cutting lip); E_2F_2 (on plane YZ); E_1E_2 ;
- Cutting direction corresponds to Y' axis;

Fig. 3.13 – Derivation sketches for the normal rake angle (α_n)

Let us assume a segment AA_3 along the cutting lip equal in length to unity. The tangent plane to the rake face at point A will pass through this segment (if the cutting lip is assumed to be a straight line) and its intersection with the YZ plane will define the segment AF_2 (with angle $\angle P_2AF_2$ being equal to the local helix angle – θ_l) and the intersection with the plane normal to the cutting lip AA_3 at point A will define the segment AF_1 (with angle $\angle E_1AF_1$ being the searched for normal rake angle – α_n). Points F_2, F_1, P_2, E_1, P_1 and E_2 were defined along the segments starting from A , by a plane parallel to XY (perpendicular to drill axis) through point A_3 . Segment AE_2 is defined along the normal to the cutting direction (Y' axis) in the YZ plane and point P_1 is defined as the intersection of A_3P_2 line with the plane normal to the cutting lip segment.

Considering ΔP_1AA_3 (with the angle $\angle P_1AA_3=90^\circ$, as the plane containing P_1, E_1 and F_1 lie in a plane perpendicular to AA_3) and AP_2 the altitude in point A , we can identify the point angle as the angle $\angle AP_1A_3$

and $\angle P_2AA_3$ (AP_2 is along the drill axis – Z which makes with the cutting lip segment the point angle as defined previously). Assuming the cutting lip segment AA_3 equal to unity, from fig. 3.13-c we can determine:

$$AP_1 = \frac{1}{\tan(p)} \quad (3.63)$$

$$A_3P_2 = \sin(p) \quad (3.64)$$

$$AP_2 = \cos(p) \quad (3.65)$$

$$P_2P_1 = \frac{\cos(p)}{\tan(p)} \quad (3.66)$$

$$A_3P_1 = \frac{1}{\sin(p)} \quad (3.67)$$

In plane F_2AE_2 (YZ) we find ΔF_2AE_2 and its altitude AP_2 , where $\angle F_2AP_2$ is equal to the local helix angle (θ_l) as previously defined and $\angle P_2AE_2$ equal to the cutting angle (μ) as AE_2 is perpendicular on the cutting direction (Y' axis) in the above mentioned plane. As we previously determined the length of AP_2 segment (by eq. 3.65) we can calculate:

$$F_2P_2 = \cos(p) \cdot \tan(\theta_l) \quad (3.68)$$

$$P_2E_2 = \cos(p) \cdot \tan(\mu) \quad (3.69)$$

The situation in plane $A_3P_1F_1$ (XY) is shown in fig. 3.13-f. As A_3P_1 is the projection of the cutting lip in a plane perpendicular on the drill axis (XY) and E_2E_1 is perpendicular on the cutting velocities plane (YZ), the angle between the two segments is the web angle (β) as defined in a previous section 3.4.1. It is also noted that the AE_3 segment is oriented along the intermediary axis of rotation Z_3 as introduced previously, while the AP_1 segment is oriented along another possible intermediary axis of rotation if a different sequence would have been considered.

In the ordinary triangle $\Delta F_2P_2A_3$, we will attempt to determine the angle $\angle F_2A_3P_2$, knowing that $\angle F_2P_2A_3 = (90^\circ - \beta)$ and the length of the segments F_2P_2 and A_3P_2 determined previously (3.68 and 3.64). We can write:

$$A_3F_2^2 = A_3P_2^2 + F_2P_2^2 - 2 \cdot A_3P_2 \cdot F_2P_2 \cdot \cos(90^\circ - \beta) \quad (3.70)$$

Substituting, we obtain:

$$A_3F_2 = \pm \cos(p) \cdot \sqrt{\tan^2(p) + \tan^2(\theta_l) - 2 \cdot \tan(p) \cdot \tan(\theta_l) \cdot \sin(\beta)} \quad (3.71)$$

We will only consider the positive solution as the negative solution is not practically occurring. The angle $\angle F_2A_3P_2$ can be determined from the same triangle from the generic theorem of Pythagoras:

$$F_2P_2^2 = A_3F_2^2 + A_3P_2^2 - 2 \cdot A_3F_2 \cdot A_3P_2 \cdot \cos(\angle F_2A_3P_2) \quad (3.72)$$

Where,

$$\cos(F_2A_3P_2) = \frac{A_3F_2^2 + A_3P_2^2 - F_2P_2^2}{2 \cdot A_3F_2 \cdot A_3P_2} \quad (3.73)$$

$$\cos(F_2A_3P_2) = \frac{\tan(p) - \tan(\theta_l) \cdot \sin(\beta)}{\sqrt{\tan^2(p) + \tan^2(\theta_l) - 2 \cdot \tan(p) \cdot \tan(\theta_l) \cdot \sin(\beta)}} \quad (3.74)$$

To be useful the value of $\angle F_2A_3P_2$ angle needs to be expressed as a tangent function rather than cosine:

$$\tan(F_2A_3P_2) = \pm \frac{\sqrt{1 - \cos^2(F_2A_3P_2)}}{\cos(F_2A_3P_2)} \quad (3.75)$$

$$\tan(F_2A_3P_2) = \pm \frac{\tan(\theta_l) \cdot \cos(\beta)}{\tan(p) - \tan(\theta_l) \cdot \sin(\beta)} \quad (3.76)$$

From the triangle $\Delta A_3P_1F_1$ ($\angle A_3P_1F_1 = 90^\circ$) in the same plane (fig. 3.13-f), knowing the angle $\angle F_1A_3P_1$ (equal to $\angle F_2A_3P_2$, determined above by eq. 3.76) and the length of A_3P_1 segment (3.67), we can determine the length of the P_1F_1 segment (as function of $\tan(\angle F_2A_3P_2)$):

$$\tan(F_1A_3P_1) = \frac{F_1P_1}{A_3P_1} \quad (3.77)$$

As the tangent function is expressed as the ration of 2 positive length segments; we will only consider the positive solution of eq. 3.76. We can determine the length of F_1P_1 segment as follows:

$$F_1P_1 = A_3P_1 \cdot \tan(F_1A_3P_1) \quad (3.78)$$

$$F_1P_1 = \frac{\tan(\theta_l) \cdot \cos(\beta)}{\sin(p) [\tan(p) - \tan(\theta_l) \cdot \sin(\beta)]} \quad (3.79)$$

From the same plane (fig. 3.13-f) we also need to determine the length of the E_1P_1 segment. As the angle between F_2E_2 and E_1P_1 is equal to the web angle (β), so does the angle between P_2P_1 and E_2E_1 . From ΔP_2E_2B ($\angle P_2E_2B = 90^\circ$) where P_2E_2 is expressed in eq. 3.69, we can determine P_2B as:

$$P_2B = \frac{P_2E_2}{\sin(\beta)} \quad (3.80)$$

$$P_2B = \frac{\cos(p) \cdot \tan(\mu)}{\sin(\beta)} \quad (3.81)$$

We also note that:

$$BP_1 = P_2P_1 - P_2B \quad (3.82)$$

And replacing P_2P_1 (eq. 3.66) and P_2B (eq. 3.81) results:

$$BP_1 = \cos(p) \left[\frac{1}{\tan(p)} - \frac{\tan(\mu)}{\sin(\beta)} \right] \quad (3.83)$$

From the triangle ΔE_1P_1B ($\angle E_1P_1B=90^\circ$) as in fig. 3.13-f, we can determine E_1P_1 :

$$E_1P_1 = BP_1 \cdot \tan(\beta) \quad (3.84)$$

$$E_1P_1 = \tan(\beta) \cdot \cos(p) \left[\frac{1}{\tan(p)} - \frac{\tan(\mu)}{\sin(\beta)} \right] \quad (3.85)$$

In the triangle ΔF_1P_1A ($\angle F_1P_1A=90^\circ$) as in fig. 3.13-e, we have already determined the length of the segments F_1P_1 (eq. 3.79), E_1P_1 (eq. 3.85) and AP_1 (eq. 3.63). According to its definition, the normal rake angle (α_n) can be identified as angle $\angle F_1AE_1$, which can be expressed as:

$$\alpha_n = \angle(F_1AP_1) - \angle(E_1AP_1) \quad (3.86)$$

Where angles $\angle F_1AP_1$ can be determined from ΔF_1P_1A ($\angle F_1P_1A=90^\circ$) and $\angle E_1AP_1$ from ΔE_1P_1A ($\angle E_1P_1A=90^\circ$):

$$\tan(\angle F_1AP_1) = \frac{F_1P_1}{AP_1} \quad (3.87)$$

$$\angle F_1AP_1 = \arctan \left[\frac{\tan(\theta_t) \cdot \cos(\beta)}{\sin(p) - \cos(p) \cdot \tan(\theta_t) \cdot \sin(\beta)} \right] \quad (3.88)$$

And

$$\tan(\angle E_1AP_1) = \frac{E_1P_1}{AP_1} \quad (3.89)$$

$$\angle E_1AP_1 = \arctan \left[\frac{\sin(\beta) \cdot \cos(p) - \sin(p) \cdot \tan(\mu)}{\cos(\beta)} \right] \quad (3.90)$$

Hence, by replacing these angles in eq. 3.86 it is obtained:

$$\alpha_n = \arctan \left[\frac{\tan(\theta_t) \cos(\beta)}{\sin(p) - \cos(p) \tan(\theta_t) \sin(\beta)} \right] - \arctan \left[\frac{\sin(\beta) \cos(p) - \sin(p) \tan(\mu)}{\cos(\beta)} \right] \quad (3.91)$$

Eq. 3.91 produces very similar results with the equivalent ones used in [39] and [2] (see table 3.1) if the cutting angle (μ) is assumed to be equal to zero. Considering the cutting angle, a difference up to several degrees in the value of α_n is observed for usual cases for the point on the cutting lip closest to the chisel edge, where the cutting angle is larger. However, this small difference (collaborated with the consideration of the cutting angle in the rest of the angles affecting the element's geometry and cutting forces decomposition) will allow us to capture the recorded increase of elementary cutting forces in the vicinity of the chisel edge with increasing the axial feed which otherwise should not be more pronounced than the rest of the cutting lip region. More discussions are included in chapter 5.2 and 5.3.

It is noted that eq. 3.91 can only be used to estimate the normal rake angle for cutting lips and it is not suitable for the chisel edge, mainly because there is no local helix angle (θ_t) for this region and the equivalent is differently derived. The rake angle along the chisel edge will be discussed in section 3.4.8 of the current chapter.

3.4.7 Relief angle (γ) along the cutting lips

The inclination of the relief face, characterized by the relief angle (γ , briefly introduced in fig. 3.3) plays only a minor role in the cutting forces. Its influence is often overlooked by the cutting force models proposed for drilling. As discussed in chapter 3.3, the relief angle (γ) is a parameter for the elementary forces acting on the relief face, which are usually independent with the depth of cut (axial feed). Often a constant empirical coefficient is employed to model these forces, or they are assumed to be zero.

However, in our study we note that the relative forces acting on the relief face are higher (in comparison with the rake forces) than in the case of metal drilling (see chapter 4). Therefore, we find important that the influence of the relief angle should be accounted for as accurately as possible.

The relief angle (γ , sometimes referred to as the clearance angle) is defined as the angle between the cutting direction and the tangent to the relief face measured in a plane normal to the radial direction (see fig. 3.3). A similar discussion about the plane in which this angle is defined exists just as in the case of the rake angle for oblique cutting model. However, it is generally accepted that the above definition is the most relevant considering that the relative movement between the cutting edge and work-piece is along the cutting direction. As in the case of rake angle, the cutting angle (γ) will influence the actual relief angle in practical drilling cases. Furthermore, as the cutting angle and relief angle are defined in the same plane, a distinction is usually made between the “static relief angle” (γ_s) which assumes the cutting angle to be equal to zero and “dynamic relief angle” (further on referred to simply as “relief angle”) calculated as:

$$\gamma = \gamma_s - \mu \quad (3.92)$$

The tool manufacturers usually provide the value of the reference relief angle (γ_0) which represents the static relief angle (measured between the tangent to the relief face and the tangential velocity vector measured in a plane perpendicular to the radial direction) defined at the outermost point on the cutting edge, as in fig. 3.14.

The mathematical definition of the relief face (sometimes referred to as the flank face as a whole) is usually much more complex than the rake face and strongly depends on the manufacturing process of the drill. The most common style of grinding the relief face is by a conical surface (as in figure 3.13), although also common are cases when several planar faces are used to ground the flank surface (as the 3 types of drills employed in our experiments).

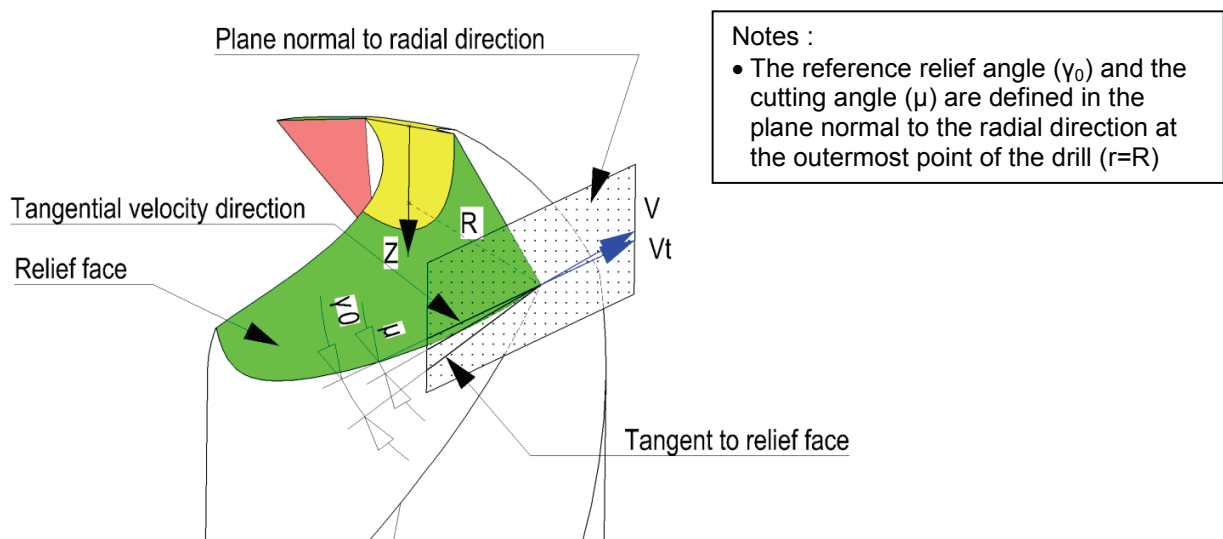


Fig. 3.14 – Definition of the reference relief angle (γ_0)

The conical grinding of the flank face has been widely discussed in the literature ([40], [41], etc.) as it is the most important operation to define the point of a drill (including point angle, chisel edge angle etc.) as well as the most commonly employed in practice. These studies show that in order to obtain certain drill point geometry several solutions exist for choosing the grinding parameters, and unless these parameters are known, the conical flank face cannot be described mathematically in a unique way. However, if the reference relief angle is known and if the cutting lip is assumed to be a straight line, the function of variation of the relief angle along the radius coordinate for the cutting lip region can be obtained starting from the fact that the cutting lip and the tangent to the relief face at the outermost point on the cutting edge have to be in the same plane.

[42] already derived a function for the static relief angle for the cutting lip region of a drill starting from the same assumption:

$$\tan(\gamma_s) = \frac{w}{r} \left(1 - \sqrt{\frac{r^2 - w^2}{R^2 - w^2}} \right) \text{ctg}(p) + \frac{R}{r} \sqrt{\frac{r^2 - w^2}{R^2 - w^2}} \tan(\gamma_0) \quad ([42] - \text{eq.24})$$

Where γ_0 is the static reference relief angle at $r=R$.

It is found that the shape of the above equation is not suitable for drills where the point angle varies, as the tapered drill reamer employed in our experiments. Therefore, we will attempt to obtain an equivalent function developed based on the web angle (β) rather than the web thickness (w).

For a generic drill, for which the reference relief angle (γ_0) is known at a point A_2 at a distance of R from the drill axis, we will attempt to derive the static relief angle at an arbitrary point A on the cutting lip as in fig. 3.15.

Let us assume a segment (A_2R_1) equal to unity along the tangent to the relief face at point A_2 on the cutting lip of a generic drill in the plane perpendicular to the radial direction (YZ). This segment with its projection (A_2P_3) on a plane perpendicular on drill axis (XY) at point A_2 will form the reference relief angle (γ_0).

From the resulting triangle ($\Delta R_1P_3A_2$, with angle $\angle R_1P_3A_2=90^\circ$) we can determine:

$$R_1P_3 = \sin(\gamma_0) \quad (3.93)$$

$$P_3A_2 = \cos(\gamma_0) \quad (3.94)$$

P_3A_2 is situated along the Y axis, while R_1P_3 along the Z axis. We will construct a parallel (P_3R_2) to the X axis (radial direction) through point P_3 , and a parallel (R_1R_2) to the cutting edge passing through R_1 . These two lines will intersect in point R_2 . The angle between R_1P_3 and R_1R_2 is equal to the point angle (p), as the angle between the cutting lip and the Z axis. From the triangle $\Delta R_1P_3R_2$ ($\angle R_1P_3R_2=90^\circ$) we obtain:

$$P_3R_2 = R_1P_3 \cdot \tan(p) = \tan(p) \cdot \sin(\gamma_0) \quad (3.95)$$

By projecting the point A_2 on P_3R_2 we obtain point P_4 and the angle $\angle P_4A_2P_3$ will equal the web angle (β , at R), since A_2P_3 is perpendicular on X axis and A_2P_4 is perpendicular to AA_2 (cutting lip); the later directions defining the web angle (β , as discussed in section 3.4.1).

Notes :

- AA_2 is a segment of the cutting lip, with A_2 the outermost point on the cutting lip ($r=R$);
- $AA_2R_1R_4$ is the plane tangent to the relief face;
- R_1R_4 is parallel to AA_2 (cutting lip);
- P_3R_2 is parallel to X axis;
- A_2P_4 is perpendicular to P_3R_2

a) Drill view

a) Isometric detail

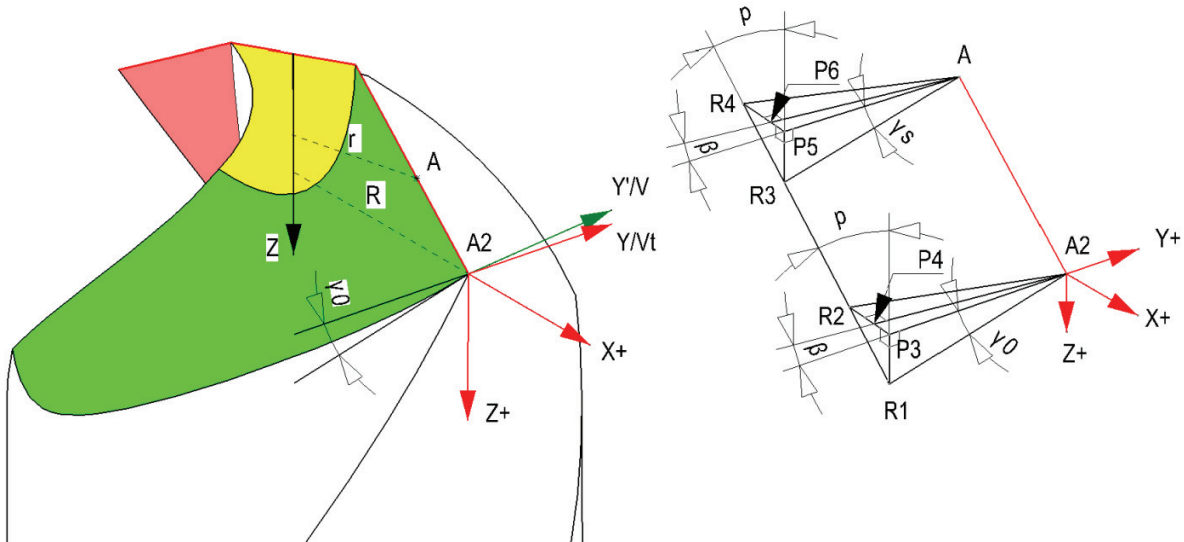


Fig. 3.15 – Derivation sketch for the static relief angle (γ_s)

From the resulting triangle ($\Delta P_3P_4A_2$, $\angle P_3P_4A_2=90^\circ$) we obtain:

$$P_3P_4 = P_3A_2 \cdot \sin(\beta(R)) = \cos(\gamma_0) \cdot \sin(\beta(R)) \quad (3.96)$$

$$A_2P_4 = P_3A_2 \cdot \cos(\beta(R)) = \cos(\gamma_0) \cdot \cos(\beta(R)) \quad (3.97)$$

We also note that:

$$P_4R_2 = P_3R_2 - P_3P_4 = \tan(p) \cdot \sin(\gamma_0) - \cos(\gamma_0) \cdot \sin(\beta(R)) \quad (3.98)$$

If we move our attention to the similar construction in an arbitrary point A on the cutting lip in fig. 3.15-b, we observe that the plane $R_1P_3P_5R_4$ is parallel to the cutting lip AA_2 and the plane XZ, hence the distance between the cutting lip and this plane will always be constant ($A_2P_4=AP_6$). Also, the two segments (A_2P_4 and AP_6) will be parallel. Furthermore, intersecting the plane tangent to the relief face (defined by points A, A_2 , R_1 and R_4) with two parallel planes (defined by $A_2P_3R_2$ and respectively AP_5R_4 , both planes perpendicular to drill axis), will result in parallel lines (i.e. A_2R_2 and AR_3), therefore we can state that the angles $\angle P_4A_2R_2$ and $\angle P_6AR_4$ are equal. With a constant side and angle, the right-angled triangles $\Delta A_2P_4R_2$ and ΔAP_6R_4 will be equal, and that $P_4R_2=P_6R_4$. Summarizing:

$$AP_6 = A_2P_4 = \cos(\gamma_0) \cdot \cos(\beta(R)) \quad (3.99)$$

$$P_6R_4 = P_4R_2 = \tan(p) \cdot \sin(\gamma_0) - \cos(\gamma_0) \cdot \sin(\beta(R)) \quad (3.100)$$

Similarly, the angle $\angle P_6AP_5$ is the web angle (β at r). From the triangle ΔAP_6P_5 ($\angle AP_6P_5=90^\circ$) we can obtain:

$$AP_5 = \frac{AP_6}{\cos(\beta)} = \frac{\cos(\gamma_0) \cdot \cos(\beta(R))}{\cos(\beta)} \quad (3.101)$$

And

$$P_5P_6 = AP_6 \cdot \tan(\beta) = \cos(\gamma_0) \cdot \cos(\beta(R)) \cdot \tan(\beta) \quad (3.102)$$

Also,

$$P_5R_4 = P_5P_6 + P_6R_4 \quad (3.103)$$

$$P_5P_4 = \cos(\gamma_0) \cdot \cos(\beta(R)) \cdot \tan(\beta) + \tan(p) \cdot \sin(\gamma_0) - \cos(\gamma_0) \cdot \sin(\beta(R)) \quad (3.104)$$

From the triangle $\Delta R_3P_5R_4$ ($\angle R_3P_5R_4=90^\circ$), knowing the angle $\angle P_5R_3R_4$ is the point angle (p – see justification above), we can obtain:

$$P_5R_3 = \frac{P_5R_4}{\tan(p)} \quad (3.105)$$

$$P_5R_3 = \frac{\cos(\gamma_0) \cdot \cos(\beta(R)) \cdot \tan(\beta) + \tan(p) \cdot \sin(\gamma_0) - \cos(\gamma_0) \cdot \sin(\beta(R))}{\tan(p)} \quad (3.106)$$

And from the triangle ΔR_3P_5A ($\angle R_3P_5A=90^\circ$), we can obtain the local static relief angle ($\gamma_s(r)=\angle R_3AP_5$). Angle $\angle R_3AP_5$ is the static relief angle at point A, since AR_3 is at the intersection between the tangent plane to the relief face and a plane R_3P_5A , perpendicular to the radial direction (X axis) in point A.

$$\tan(\gamma_s) = \frac{P_5R_3}{AP_5} \quad (3.107)$$

$$\tan(\gamma_s) = \cos(\beta) \cdot \left[\frac{\tan(\beta) - \tan(\beta(R))}{\tan(p)} + \frac{\tan(\gamma_0)}{\cos(\beta(R))} \right] \quad (3.108)$$

Or

$$\gamma_s(r) = \arctan \left\{ \cos(\beta) \cdot \left[\frac{\tan(\beta) - \tan(\beta(R))}{\tan(p)} + \frac{\tan(\gamma_0)}{\cos(\beta(R))} \right] \right\} \quad (3.109)$$

And replacing it in eq. 3.92 we obtain the dynamic relief angle:

$$\gamma(r) = \arctan \left\{ \cos(\beta) \cdot \left[\frac{\tan(\beta) - \tan(\beta(R))}{\tan(p)} + \frac{\tan(\gamma_0)}{\cos(\beta(R))} \right] \right\} - \mu(r) \quad (3.110)$$

Equation 3.110 is valid for the cutting lip region of a generic drill, providing the reference relief angle is known at a point R. For multi-stage point drills, the same equation can be used, with γ_0 defined at the outermost point of each stage, as discussed in chapter 3.5.

Although not employed in the current cutting force model, we have derived the equation of the normal relief angle (γ_n defined in a plane normal to the cutting edge) through a similar method as the normal rake

angle (α_n) has been derived. Equation 3.111 presents the resulting function of the normal relief angle (γ_n), although its derivation will not be included in this document.

$$\gamma_n = \arctan\left[\frac{\sin(\beta) \cdot \cos(p) - \sin(p) \cdot \tan(\mu)}{\cos(\beta)}\right] + \arctan\left[\frac{\cos(p) \cdot [\tan(p) \cdot \sin(\gamma_0) - \sin(\beta(R)) \cdot \cos(\gamma_0)]}{\cos(\beta(R)) \cdot \cos(\gamma_0)}\right] \quad (3.111)$$

It is noted that both functions are only valid for the cutting lip region of the drill.

3.4.8 Normal rake (α_n) and relief (γ) angles along the chisel edge

The chisel edge area is made out of 2 symmetric surfaces obtained through the point grinding operation together with the relief face (generally referred to as flank surface). The most common type of surface for the flank is conical, obtained by conical grinding methods. Often employed is also planar grinding (with two or more faces) especially for small diameter drills. Other solutions are presented and discussed in chapter 2.2. The chisel edge is in general characterized by a highly negative rake angle (resulting in inefficient cutting), while the relief angle is in general large as can be visualized in fig. 3.26 and 3.27.

In most studies focused on cutting forces in drilling it is assumed that the chisel edge is a straight line lying in a plane perpendicular to the drill axis. Such an ideal case only exists for planar grinding with a chisel edge in a plane perpendicular to the drill axis. For conical grinding the chisel edge is slightly a tri-dimensional S-shape, but according to many it can still be assumed as a straight line in a plane perpendicular to drill axis. For other grinding techniques, the resulting shape deviates more than the above mentioned cases.

Studies such as [40] and [41], focused on optimizing the grinding techniques, have proposed models to estimate the geometry of the chisel edge, both its shape and the rake and relief angles. They also show that the exact manufacturing parameters are needed to mathematically describe the chisel edge shape and angles, or the resulting function has several solutions.

Meanwhile, the studies focused on cutting force modeling assume a straight chisel edge in a plane perpendicular to the drill axis obtained by planar grinding. The resulting wedge is perfectly symmetric and the following relationship can be stated between the static rake (α_s) and relief angles (γ_s) along the chisel edge:

$$\gamma_s = 90^\circ - \alpha_s \quad (3.112)$$

The actual, rake and relief angle can be corrected considering the kinematics of the drilling process by the cutting angle (μ) as:

$$\alpha = \alpha_s - \mu \quad (3.113)$$

$$\gamma = \gamma_s + \mu \quad (3.114)$$

It is noted that the static rake and relief angles are constant, and orthogonal cutting is used to describe the cutting process for this region, therefore the angles are defined in a plane perpendicular to the cutting edge, which also contains the cutting direction. Fig. 3.16 exemplifies the situation.

At point A on the chisel edge we define the two coordinate system of oblique/orthogonal element (X'Y'Z') and drilling (XYZ). It can be observed that for the considered case (chisel edge lying in XY plane – i.e. perpendicular on the drill axis) the X and X' axes coincide and that orthogonal cutting occurs (chisel edge is also aligned with X axis). Fig. 3.16-b introduces a section view through point A along YZ plane (or Y'Z'). According to the drill direction of rotation, for point A anywhere between the drill center point until the end of the chisel edge in the direction of X+ (as currently defined) the wedge side on the Y+ axis side will act as the rake face, while the side towards Y- will act as a relief face. For point A placed on the other side of the chisel edge the X+ axis will change direction and so the role of the wedge sides. The static rake angle (α_s) is defined between the tangent to the wedge side acting as a rake face and the Z+ axis, while the static relief angle is defined as the angle between the tangent to the wedge side acting as a relief face and the Y axis. The dynamic rake and relief angles are defined from the same tangent to rake and relief faces respectively but considering the axes of the X'Y'Z' coordinate system as shown in fig. 3.16a and b.

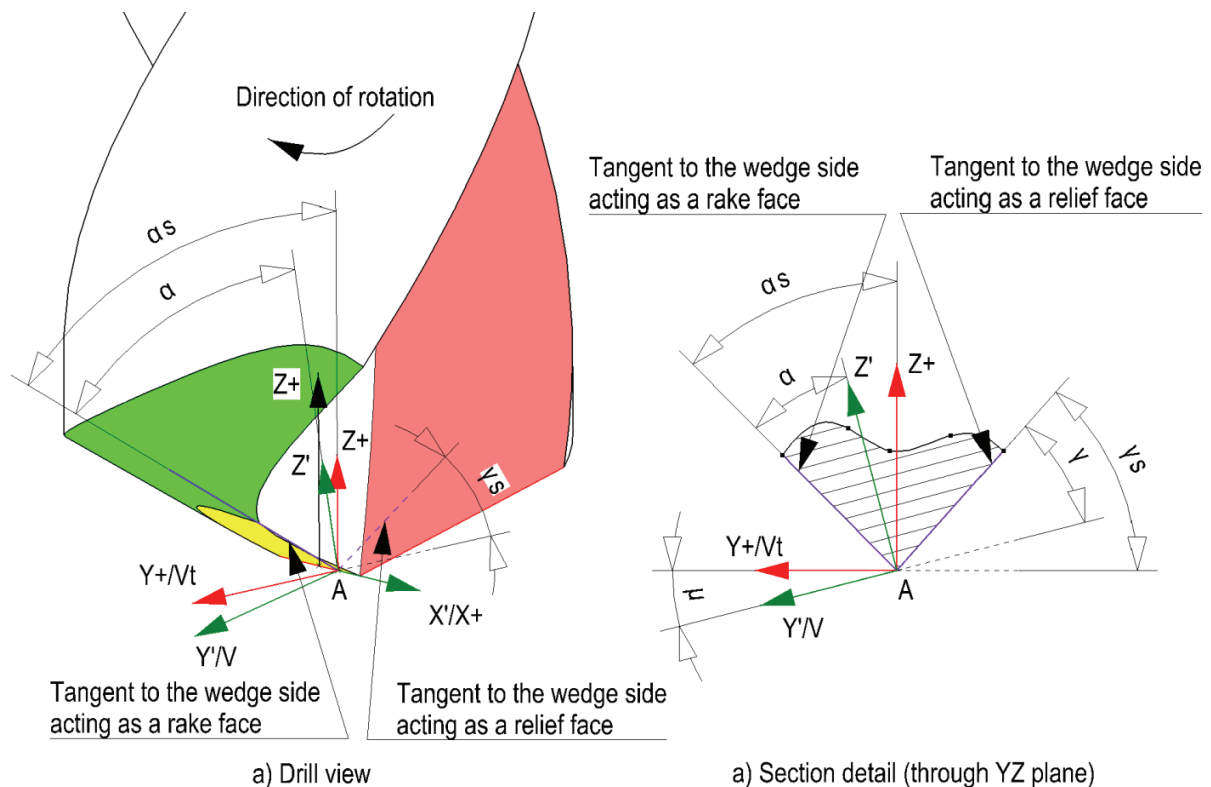


Fig. 3.16 – Rake (α) and relief (γ) angles along the cutting edge

The following equation (traced back to [43]) is used to calculate the rake and relief angles:

$$\alpha_s = -\arctan[\tan(p_t) \cdot \sin(\psi)] \quad ([43]\text{-eq.33})$$

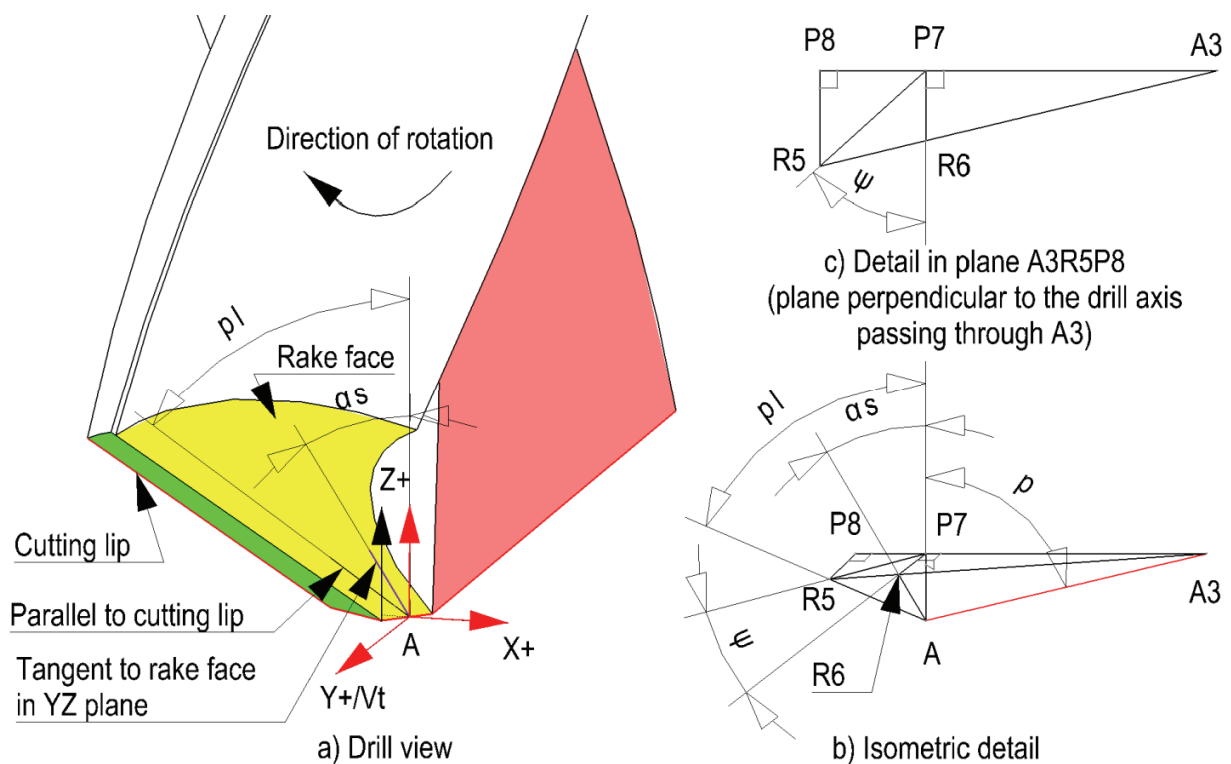
This equation is used in all cutting force models ([2], [3] etc.) to describe the chisel edge, in most cases for conical grounded drills without specifying the assumption based on which is developed. We were able to trace it back to [43] which is actually introducing it only for planar grinding of the chisel edge. We were able to confirm the validity of this equation for this case, with the mention that p_t refers to the point angle of the cutting lips (or more specifically the point angle of the cutting lip closest to drill axis for a stepped drill such as the tapered drill reamer, $p_t = p(R_c + dr)$).

By “guessing” the manufacturing parameters of the conical grinding process, we have also used the model described in [40] and [41] to estimate the static relief angle (γ_s) along the chisel edge for some particular cases, and we have found the results within 5° difference when compared with the simplified

planar grinding model described by [43]-eq.33. We find this difference acceptable considering the complexity of the model for estimating the angles of the chisel edge by the model introduced by [40] and [41] and the uncertainties introduced by not knowing the exact parameters of the conical grinding process.

Summarizing, equation [43]-eq.33 can be used to calculate the static rake angle, equation 3.113 the “dynamic” rake angle along the chisel edge, while equations 3.112 and 3.114 can be used to calculate the relief angle along the chisel edge for a drill with the chisel edge lying in a plane perpendicular to the drill axis ground by a planar flank like in the case of the tapered drill reamer employed (fig. 3.22) in our experiments.

However, it is still needed to derive an equation to estimate these angles for the case where the chisel edge makes an angle with the drill axis as the case of the 2-facet twist drill (fig. 3.22) used in our experiments. Therefore, considering this particular case, figure 3.17 has been constructed to assist the derivation of these angles.



- Notes :
- AA_3 is a chisel edge segment; AP_7 lies along $Z+$ axis; AR_5 is parallel to the cutting lip (of the other flute); P_7R_6 and P_8R_5 are parallel to $Y+$ axis;
 - AA_3R_5 lie on the rake face (planar, colored in yellow);
 - $A_3P_7P_8R_5$ is parallel to XY plane (perpendicular on the drill axis);
 - The chisel edge angle (ψ) is defined in a counter-clockwise direction from the projection on a plane parallel to XY plane of the chisel edge (A_3P_8) to the projection on the XY plane of the cutting lip P_7R_5 ;

Fig. 3.17 – Static rake angle ($\alpha_{s, ch-T2}$) for the chisel edge area of a 2-facet twist drill

The 2-facet twist drill is ground by 2 planar faces (green and yellow). The first planar face (green) is used to obtain the relief face along the cutting lips and chisel edge, while the 2nd planar face (yellow) grounds the rake face along the chisel edge. The first planar face is defined by the cutting lip and the chisel edge,

while the 2nd planar face is defined by the chisel edge and the intersection between the two faces. From our measurements the intersection of the two faces appears to make the same angle with the Z axis as the cutting lips (they are parallel), therefore a plane passing through point A (on the chisel edge) parallel to the cutting lip will intersect the rake face and the intersection will make an angle with the Z axis equal to the point angle of the cutting lips (further referred to as p_i , while the point angle of the chisel edge at point A will be referred to simply as point angle – p).

Based on this assumption and assuming a segment AA_3 equal to unity along the chisel edge we can derive the static rake angle (α_s) measured in a plane perpendicular to the radial direction (X axis). A plane ($A_3P_7P_8R_5$ as in fig. 3.17) perpendicular on the drill axis passing through point A_3 will cut the line (AR_5) defining the point angle of the cutting lips (referred to as p_i); the one defining the static rake angle (α_s) and a parallel to Z axis through point A in points R_5 , R_6 and P_7 respectively.

Starting from the triangle ΔAP_7A_3 ($\angle AP_7A_3=90^\circ$), where the chisel edge makes the point angle (p) with the Z axis (AP_7), we can express:

$$A_3P_7 = AA_3 \cdot \sin(p) = \sin(p) \quad (3.115)$$

$$AP_7 = AA_3 \cdot \cos(p) = \cos(p) \quad (3.116)$$

While from the triangle ΔAP_7R_5 ($\angle AP_7R_5=90^\circ$), where the point angle of the cutting lips is found (see fig. 3.17-b) we can calculate:

$$R_5P_7 = AP_7 \cdot \tan(p_i) = \tan(p_i) \cdot \cos(p) \quad (3.117)$$

$$AR_5 = \frac{AP_7}{\cos(p_i)} = \frac{\cos(p)}{\cos(p_i)} \quad (3.118)$$

From the construction in the plane ($A_3P_7P_8R_5$) perpendicular to the drill axis through A_3 we observe the chisel edge angle ($\angle R_5P_7R_6=\psi$, as defined in section 3.4.1), where P_8 is obtained by projecting point R_5 on the line A_3P_7 and the triangle $\Delta R_5P_8P_7$ ($\angle R_5P_8P_7=90^\circ$ and $\angle P_7R_5P_8=\psi$) and we can calculate:

$$R_5P_8 = R_5P_7 \cdot \sin(\psi) = \tan(p_i) \cdot \cos(p) \cdot \sin(\psi) \quad (3.119)$$

$$P_7P_8 = R_5P_7 \cdot \cos(\psi) = \tan(p_i) \cdot \cos(p) \cdot \cos(\psi) \quad (3.120)$$

We can also note that:

$$A_3P_8 = A_3P_7 + P_7P_8 = \sin(p) + \tan(p_i) \cdot \cos(p) \cdot \cos(\psi) \quad (3.121)$$

Furthermore, we can observe that triangles $\Delta A_3P_7R_6$ ($\angle A_3P_7R_6=90^\circ$) and $\Delta A_3P_8R_5$ ($\angle A_3P_8R_5=90^\circ$) are alike, meaning that:

$$\frac{R_5P_8}{R_6P_7} = \frac{A_3P_8}{A_3P_7} \Rightarrow R_6P_7 = \frac{R_5P_8 \cdot A_3P_7}{A_3P_8} = \frac{\tan(p_i) \cdot \cos(p) \cdot \sin(\psi) \cdot \sin(p)}{\sin(p) + \tan(p_i) \cdot \cos(p) \cdot \cos(\psi)} \quad (3.122)$$

And eventually, from ΔAP_7R_6 ($\angle AP_7R_6=90^\circ$) we can estimate the tangent of the static rake angle (α_s):

$$\tan(\alpha_s) = \frac{R_6P_7}{AP_7} = \frac{\tan(p_i) \cdot \cos(p) \cdot \sin(\psi) \cdot \sin(p)}{\sin(p) + \tan(p_i) \cdot \cos(p) \cdot \cos(\psi)} \cdot \frac{1}{\cos(p)} \quad (3.123)$$

$$\tan(\alpha_s) = \frac{\tan(p_l) \cdot \sin(\psi) \cdot \sin(p)}{\sin(p) + \tan(p_l) \cdot \cos(p) \cdot \cos(\psi)} \quad (3.124)$$

Or, considering that as defined the rake angle is negative (i.e. the rake face is on the side of the cutting direction with respect to the Z axis) around the chisel edge:

$$\alpha_s = -\arctan\left[\frac{\tan(p_l) \cdot \sin(\psi) \cdot \sin(p)}{\sin(p) + \tan(p_l) \cdot \cos(p) \cdot \cos(\psi)}\right] \quad (3.125)$$

We observe that this value is constant for a straight chisel edge. Furthermore, for this type of drill we have shown that, due to the inclination of the chisel edge with respect to the drill axis, an inclination angle (i) exists and oblique cutting occurs. Therefore, it is needed to estimate the normal rake angle (α_n). As the local helix angle (θ_l) is defined for the cutting lip region in the same way as the static rake angle (α_s) is defined along the chisel edge, equation 3.91 can be also used to relate the static rake angle (α_s) to the normal rake angle (α_n) for the chisel edge region of this particular 2-facet twist drill. Additionally, the web angle (β) is equal to zero along this region and 3.91 can be further simplified to:

$$\alpha_{n, ch-T2} = \arctan\left[\frac{\tan(\alpha_s)}{\sin(p)}\right] - \arctan[-\sin(p) \cdot \tan(\mu)] \quad (3.126)$$

$$\alpha_{n, ch-T2} = \arctan\left[\frac{\tan(\alpha_s)}{\sin(p)}\right] + \arctan[\sin(p) \cdot \tan(\mu)] \quad (3.127)$$

Where the normal rake angle along the chisel edge for the 2-facet twist drill (T2, as the notation adopted to represent this type of drill in the current PhD thesis – see chapter 3.5) is symbolized as $\alpha_{n, ch-T2}$.

Additionally, to express the relief angle along the chisel edge, equations 3.112 and 3.114 can be used, with the static rake angle expressed by equation 3.125. For practical values, see chapter 3.5.5 and 3.5.6.

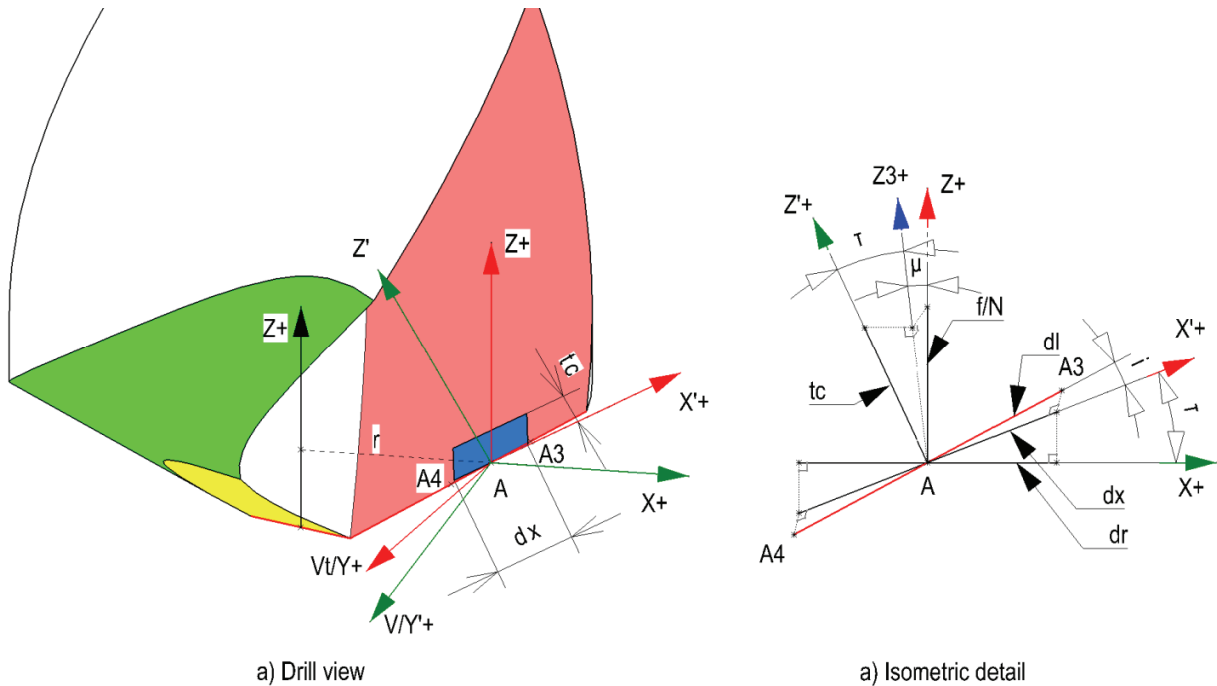
3.4.9 Element's dimensions (dr, dx, dl) and the depth of cut (t_c)

Although in the oblique or orthogonal cutting model, the uncut chip area (A_u) is easily defined as in fig. 3.3, the correlation to drilling is slightly more complicated. As defined in oblique (or orthogonal) cutting the uncut chip area (A_u) is defined in a plane perpendicular to the cutting direction and is calculated by the product of elemental width (dx) and depth of cut (t_c) – see eq. 3.16.

In drilling it is customary to define the elements to be constant along the radial direction (dr, along X axis). It is therefore needed to find the relationship between dr, as defined in drilling, and dx, as defined in oblique cutting. In drilling, the element's width (dx) will be defined along the X' axis. Of importance is also the cutting length of the element (dl), different than the element's width both in oblique cutting and drilling (see fig. 3.3 and 3.18).

As dr is oriented along the X axis and dx along X' axis, and noting that the angle between the two axes was previously defined as the 2nd Euler rotation angle (τ , calculated by eq. 3.3 derived in chapter 3.4.5) we can easily deduct the following relationship between the two from the fig. 3.18-b:

$$dx = \frac{dr}{\cos(\tau)} \quad (3.128)$$



- Notes :
- The construction starts by considering a segment of length dr along the X axis with its center in point A ;
 - A line passing through point A along X' axis will be delimited by planes perpendicular to X axis passing through the extremities of dr segment to obtain dx (the angle between dr and dx will be equal to the 2nd Euler angle of rotation, τ);
 - The cutting edge will be delimited by planes perpendicular to X axis passing through the extremities of dr segment to form dl (segment A_4A_3 passing through A , which makes the inclination angle, i , with dx);
 - Along Z axis, starting from point A , a segment will be defined of length f/N representing the axial feed per flute;
 - The f/N segment will be projected on the intermediary axis of rotation Z_3 , forming the cutting angle with the original segment. Through the upper extremity of this segment, a parallel line with dr will intersect Z' axis to form starting from A the depth of cut (t_c), at an angle equal to the 2nd Euler angle of rotation (τ) with the previous segment;

Fig. 3.18 – Definition of the uncut chip area (A_c) in drilling

Furthermore between dx and dl the following relationship can be deduced:

$$dl = \frac{dx}{\cos(i)} \quad (3.129)$$

Or, if equation 3.3 (2nd Euler angle of rotation) is used:

$$dl = \frac{dr}{\sin(p) \cdot \cos(\beta)} \quad (3.130)$$

The depth of cut of the element (t_c) can be calculated starting from the axial feed rate per flute (f/N), which is defined long the Z axis, while t_c is measured along the Z' axis:

$$t_c = \frac{f}{N} \cdot \cos(\mu) \cdot \cos(\tau) \quad (3.131)$$

It is noted that except the radial length of the element (dr) all other dimensions of the element vary with the radial coordinate. Additionally, to derive the above equation the assumption is made that the coordinate systems (XYZ and $X'Y'Z'$) are identical for any point on the cutting edge of the element (between A_3 and A_4). In reality, as the cutting edge does not lie on the plane XZ (except for the chisel edge region) the orientation of $X'Y'Z'$ coordinate system will change for each point on the cutting edge, therefore the above equations are only valid for very small values of dr .

3.4.10 Elementary cutting forces in $X'Y'Z'$ space (F_{n1} , F_{f1} , F_{n2} , F_{f2})

The components of the normal force on the rake face (F_{n1}) can be derived based on the normal rake angle (α_n) and the inclination angle (i). Fig. 3.3 has been used as the starting point to construct fig. 3.19 showing the components of this force (F_{n1x} , F_{n1y} , F_{n1z} along the $X'Y'Z'$ coordinate system axes) and F_{n1xy} its projection on $X'Y'$ plane.

The normal rake angle (α_n) is the angle measured in a plane normal to the cutting edge (which also contains the force normal to the rake face – F_{n1}) between the Z' axis and the normal to the cutting edge in the plane tangent to the rake face in point A (as per its definition presented in chapter 3.4.6); and can also be identified as the angle between the force normal to the rake face (F_{n1}) and its projection in $X'Y'$ plane (F_{n1xy}).

The angle between the projection of F_{n1} force on the $X'Y'$ plane and the Y' axis is the inclination angle (i) as both direction are perpendicular on the cutting edge (F_{n1xy} lies in a plane perpendicular on the cutting edge) and X' axis which define the inclination angle as detailed in chapter 3.4.4.

For the derivation we will assume F_{n1} equal to unity, although its magnitude has been defined in chapter 3.3.

F_{n1xy} and F_{n1z} can be easily expressed as:

$$F_{n1xy} = \cos(\alpha_n) \quad (3.132)$$

$$F_{n1z} = \sin(\alpha_n) \quad (3.133)$$

Furthermore F_{n1x} and F_{n1y} can be calculated from F_{n1xy} to obtain:

$$F_{n1x} = F_{n1xy} \cdot \sin(i) = \cos(\alpha_n) \cdot \sin(i) \quad (3.134)$$

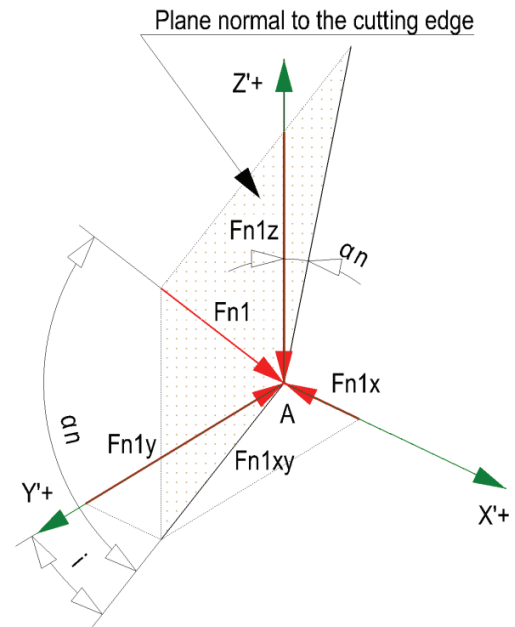


Fig. 3.19 – Components of F_{n1} in $X'Y'Z'$ coordinate system

$$F_{n1y} = F_{n1xy} \cdot \sin(i) = \cos(\alpha_n) \cdot \cos(i) \quad (3.135)$$

Therefore, considering the axes directions, we can write:

$$\{F_{n1}\}_{X'Y'Z'} = F_{n1} \cdot \begin{Bmatrix} -\cos(\alpha_n) \cdot \sin(i) \\ -\cos(\alpha_n) \cdot \cos(i) \\ -\sin(\alpha_n) \end{Bmatrix} \quad (3.136)$$

Determining the components (F_{f1x} , F_{f1y} , F_{f1z}) of the friction force (F_{f1}) on rake face is slightly more complicated, as the chip flow angle (η_c , discussed in chapter 3.3, which is defining the direction of the friction force) is defined in the plane tangent to rake face at point A from the normal to the cutting lip (see fig. 3.3 and 3.20).

To do this, we first project F_{f1} on the Z' axis obtaining the F_{f1z} component, while projecting the same vector on a plane parallel to $X'Y'$ passing through the tip of F_{f1} and F_{f1z} vectors we obtain F_{f1xy} . Further projecting F_{f1xy} on X' and Y' axes respectively we obtain F_{f1x} and F_{f1y} . Since we do not know the angle between F_{f1} and its projection (F_{f1z}) on Z' axis, we first project F_{f1} on the normal to the cutting edge on the plane tangent to the rake face to obtain F_{f1n} and F_{f1p} . By projecting F_{f1n} to Z' axis we obtain the same F_{f1z} (the projection of F_{f1} on the Z' axis) and F_{f1ny} , which makes the inclination angle with the Y' axis. We also identify the chip flow angle (η_c) as the angle between F_{f1} and F_{f1n} , according to its definition in chapter 3.3 (and fig. 3.3).

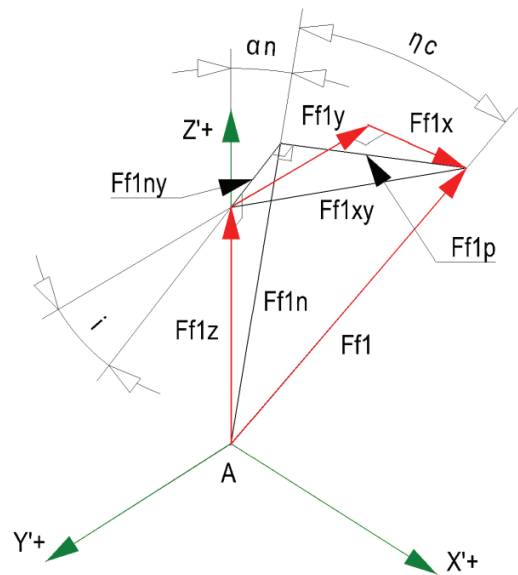


Fig. 3.20 – Components of F_{f1} in $X'Y'Z'$ coordinate system

Assuming for simplification that the F_{f1} vector is equal in magnitude with unity, its projection on the plane normal to the cutting edge (F_{f1n}) and F_{f1p} can be expressed as functions of the chip flow angle (η_c) as follows:

$$F_{f1n} = \cos(\eta_c) \quad (3.137)$$

$$F_{f1p} = \sin(\eta_c) \quad (3.138)$$

Furthermore, the Z' axis component of the friction force on the rake face (F_{f1z}) and F_{f1ny} can be calculated based on the rake angle (see definition in chapter 3.4.6):

$$F_{f1z} = F_{f1n} \cdot \cos(\alpha_n) = \cos(\eta_c) \cdot \cos(\alpha_n) \quad (3.139)$$

$$F_{f1ny} = F_{f1n} \cdot \sin(\alpha_n) = \cos(\eta_c) \cdot \sin(\alpha_n) \quad (3.140)$$

F_{f1xy} can also be determined from F_{f1z} , assuming that F_{f1} is equal to unity. Its derivation is however not needed as it will simplify in the end.

We observe that F_{f1x} and F_{f1y} can be computed if the angle between F_{f1x} and F_{f1xy} is known. The angle between F_{f1y} and F_{f1ny} is equal to the inclination angle (i , previously defined), therefore:

$$\langle (F_{f1y}, F_{f1xy}) \rangle = \langle (F_{f1ny}, F_{f1xy}) \rangle - i \quad (3.141)$$

Where,

$$\sin(\langle F_{f1ny}, F_{f1xy} \rangle) = \frac{F_{f1p}}{F_{f1xy}} = \frac{\sin(\eta_c)}{F_{f1xy}} \quad (3.142)$$

$$\cos(\langle F_{f1ny}, F_{f1xy} \rangle) = \frac{F_{f1ny}}{F_{f1xy}} = \frac{\cos(\eta_c) \cdot \sin(\alpha_n)}{F_{f1xy}} \quad (3.143)$$

Knowing that in general:

$$\sin(u \pm v) = \sin(u) \cdot \cos(v) \pm \cos(u) \cdot \sin(v) \quad (3.144)$$

$$\cos(u \pm v) = \cos(u) \cdot \cos(v) \mp \sin(u) \cdot \sin(v) \quad (3.145)$$

We can calculate:

$$\sin(\langle F_{f1y}, F_{f1xy} \rangle) = \frac{\sin(\eta_c) \cdot \cos(i) - \cos(\eta_c) \cdot \sin(\alpha_n) \cdot \sin(i)}{F_{f1xy}} \quad (3.146)$$

And,

$$\cos(\langle F_{f1y}, F_{f1xy} \rangle) = \frac{\cos(\eta_c) \cdot \sin(\alpha_n) \cdot \cos(i) + \sin(\eta_c) \cdot \sin(i)}{F_{f1xy}} \quad (3.147)$$

Following,

$$F_{f1x} = F_{f1xy} \cdot \sin(\langle F_{f1y}, F_{f1xy} \rangle) = \sin(\eta_c) \cdot \cos(i) - \cos(\eta_c) \cdot \sin(\alpha_n) \cdot \sin(i) \quad (3.148)$$

$$F_{f1y} = F_{f1xy} \cdot \cos(\langle F_{f1y}, F_{f1xy} \rangle) = \cos(\eta_c) \cdot \sin(\alpha_n) \cdot \cos(i) + \sin(\eta_c) \cdot \sin(i) \quad (3.149)$$

Summarizing, the components of the F_{f1} force in the X'Y'Z' coordinate system, considering the orientation of the axes, will be:

$$\{F_{f1}\}_{X'Y'Z'} = F_{f1} \cdot \begin{Bmatrix} \sin(\eta_c) \cdot \cos(i) - \cos(\eta_c) \cdot \sin(\alpha_n) \cdot \sin(i) \\ -\cos(\eta_c) \cdot \sin(\alpha_n) \cdot \cos(i) - \sin(\eta_c) \cdot \sin(i) \\ \cos(\eta_c) \cdot \cos(\alpha_n) \end{Bmatrix} \quad (3.150)$$

F_{f1y} has negative sign as it is oriented towards the negative direction of the Y axis.

As the forces on the relief face (F_{n2} and F_{f2}) are acting in $Y'Z'$ plane, it is very simple to derive them from the schematic (fig. 3.21) constructed starting from fig. 3.3 and knowing the relief angle between the Y' axis and the relief face measured in $Y'Z'$ plane.

$$\{F_{n2}\}_{X'Y'Z'} = F_{n2} \cdot \begin{Bmatrix} 0 \\ \sin(\gamma) \\ \cos(\gamma) \end{Bmatrix} \quad (3.151)$$

$$\{F_{f2}\}_{X'Y'Z'} = F_{f2} \cdot \begin{Bmatrix} 0 \\ -\cos(\gamma) \\ \sin(\gamma) \end{Bmatrix} \quad (3.152)$$

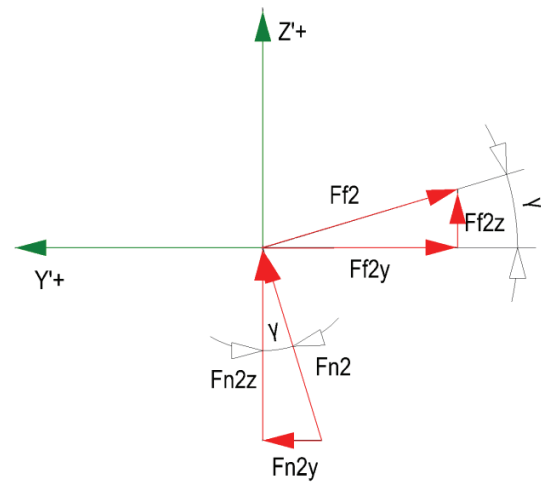


Fig. 3.21 – Components of F_{n2} and F_{f2} in $X'Y'Z'$ coordinate system

3.5 Mathematical representation of two drill geometries

In this chapter we will introduce the geometrical aspects of the two drill types modelled in the current PhD thesis:

- T1 – tapered drill-reamer (also known as a “one-shot” drill bit) is a tool specially designed for drilling fiber reinforced composites, but not suitable for metallic materials. The tool is made of solid carbide steels with small grain size (micro-grain). It has 4 straight flutes while only 2 are engaged in cutting initially. Due to the configuration chosen of 4 flutes, the chisel edge area is very small in comparison with other drills. The tool tip has a 2-stage point angle, featuring an unusually long tip. A diameter of 5.55mm was selected so that the tool tip was smaller than the work-piece thickness and full engagement was obtained, even if for a very short interval. The supplier is [Starlite Industries](#).
- T2 – 2-facet twist drill is a high-quality twist drill used extensively for drilling metallic materials. Unlike the conical twist drill, it has a straight chisel edge which makes an angle with the tool axis smaller than 180° . The flank faces are ground to planar surfaces, with no additional features. The material is also solid carbide steel. A 5.6mm diameter was selected from [Tusa Carbide](#).

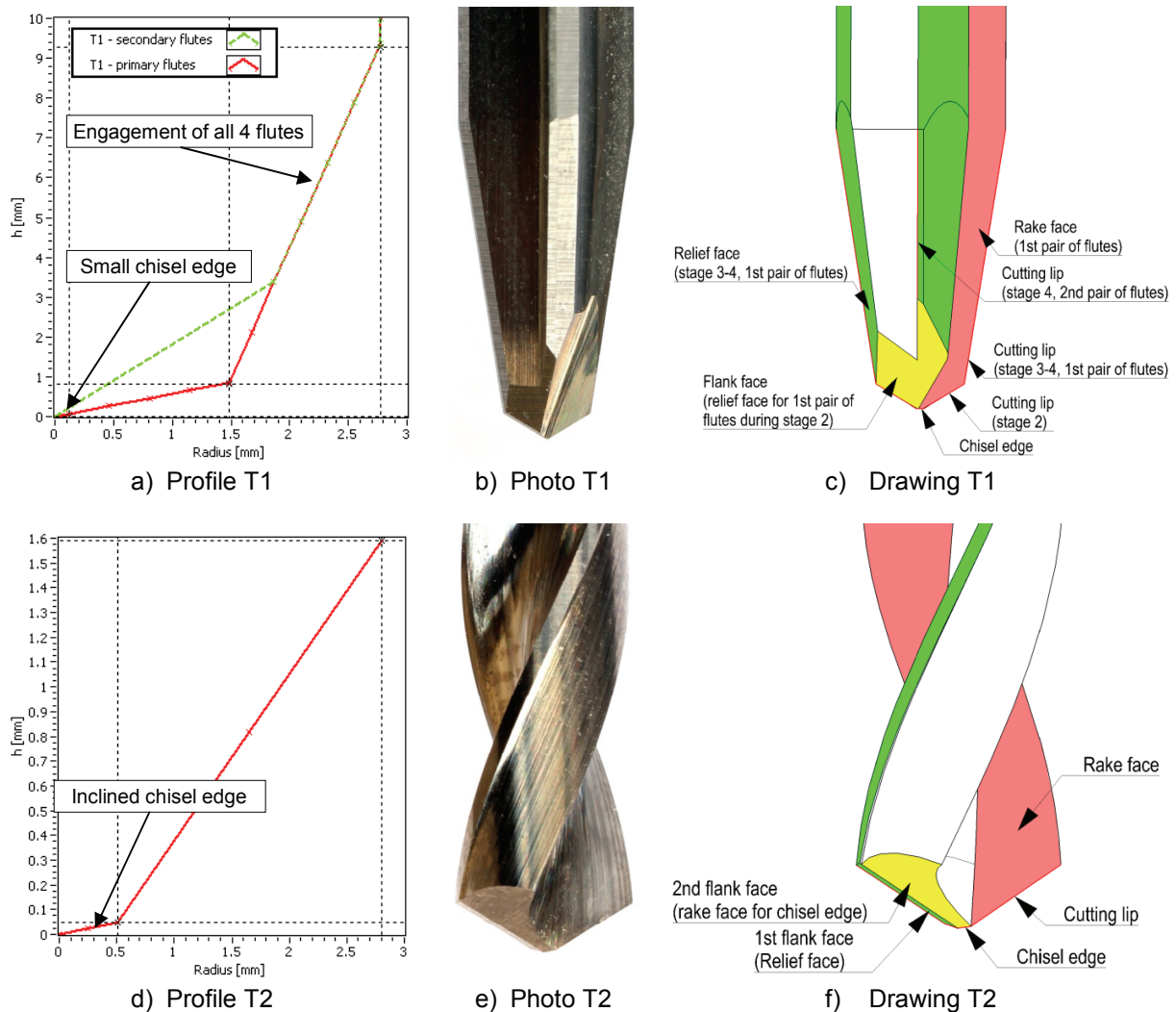


Fig. 3.22 – Drills modeled mathematically in the current PhD thesis (T1 and T2)

The above two drills are employed in our experiments, together with a third drill, which was not modeled mathematically. This later drill will be introduced in chapter 4, focusing on the experimental work. Figure 3.22 shows their photograph, the measured profiles (at the EPFL workshops using optical means) and a drawing based on an approximate 3D model to introduce their main features. The geometrical parameter of each drill will be introduced following the work-flow of the model development. Only parameters which change with the drill geometry will be outlined below.

All plots in the current chapter are calculated for an axial feed of 0.08mm/rev. The axial feed influences the cutting angle (μ), which will affect most of the angles presented hereby (for details see the specific derivations of each angle).

3.5.1 Point angle (ρ)

Point angle is one of the drill parameters usually supplied in drill catalogues. Its practical use is to define the angle of the revolution cone generated by the drill tip. Some theoretical remarks on the definition of the point angle (ρ) and the manufacturer's point angle can be read in chapter 3.4.2 (including fig. 3.6). Drills designed in stages have several point angles (as for T1). In the current thesis the following functions have been used to define the point angle (ρ) for each tool type considered (ρ_{T1} and ρ_{T2}), based on optical measurements:

$$p_{T1}(r) = \begin{cases} 90^\circ, & 0 < r < 0.125 \\ 59.5^\circ, & 0.125 < r < 1.485 \\ 8.6^\circ, & 1.485 < r < 2.773 \end{cases} \quad (3.153)$$

$$p_{T2}(r) = \begin{cases} 80.27^\circ, & 0 < r < 0.5075 \\ 56.75^\circ, & 0.5075 < r < 2.8 \end{cases} \quad (3.154)$$

Based on equations 3.153 and 3.154, fig. 3.23 plots the variation of the point angle along the drill radius for the two considered drills.

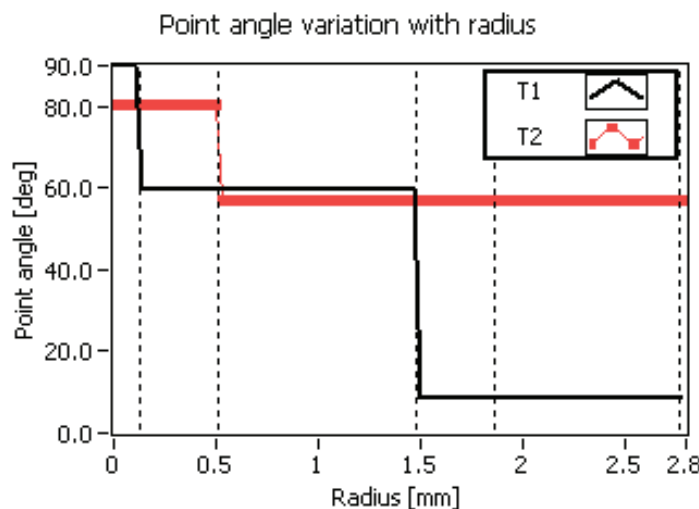


Fig. 3.23 – Point angle (ρ) variation with the radius for the considered drills

3.5.2 Web angle (β)

Web angle (β) is defined as the angle between the radial direction at a point on the cutting edges and the projection of the cutting edge on a plane perpendicular to the drill axis (as in fig. 3.5 and section 3.4.3). For the chisel edge area, the web angle will always be zero, while for the cutting lip region is variable with the radius as described by the generic equation 3.43. Considering the particularities of the two drills (i.e. web thickness), the following equations have been used to describe the web angle (β) of the two drills along their radius:

$$\beta_{T1}(r) = \begin{cases} 0^\circ, & 0 < r < 0.125 \\ \arcsin\left(\frac{0.115}{r}\right), & 0.125 < r < 2.773 \end{cases} \quad (3.155)$$

$$\beta_{T2}(r) = \begin{cases} 0^\circ, & 0 < r < 0.5075 \\ \arcsin\left(\frac{0.442}{r}\right), & 0.5075 < r < 2.8 \end{cases} \quad (3.156)$$

3.5.3 Inclination angle (i)

The inclination angle (i) is an angle characteristic to oblique cutting, defined as the angle between the cutting edge and the normal (X' axis as in fig. 3.9) to the velocity vector in the plane containing both the velocity and the cutting edge. In drilling it is derived by the commonly accepted equation 3.54, although in many cases its simplified version is employed (equation 3.55, with the cutting angle – μ – equal to zero).

Its variation along the radius for the two drills considered in the current thesis is outlined in figure 3.24. It is noted that usually for the chisel edge the inclination angle is zero (as in the case of T1, for which the point angle in this region is 90°). However, for T2 the chisel edge is inclined with respect to the tool axis with an angle (ρ) smaller than 90° , therefore a positive value of the inclination angle is recorded, increasing with the cutting angle (μ).

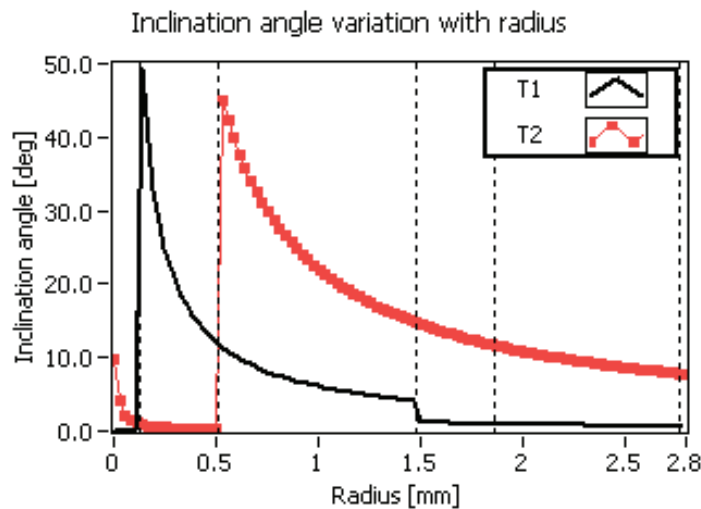


Fig. 3.24 – Inclination angle (i) variation with the radius for the considered drills

3.5.4 2nd Euler angle of rotation (τ)

This angle was introduced for simplification reasons as defined by equation 3.3, derived in chapter 3.4.5 (see also fig. 3.2 and 3.10). It is found interesting to present its variation along the radius for the drills employed in the current thesis in the following graph (fig. 3.25). This angle has a very important influence on the decomposition of the elementary cutting forces along the thrust and torque direction.

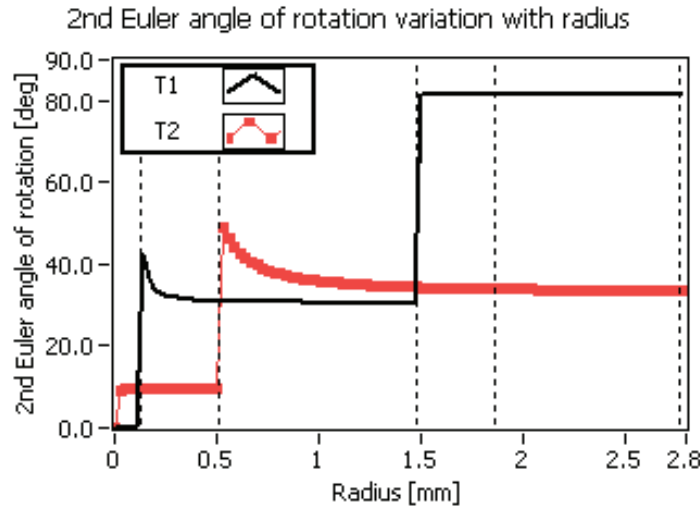


Fig. 3.25 – 2nd Euler angle of rotation (τ) variation with the radius for the considered drills

3.5.5 Normal rake angle (α_n)

The normal rake angle was found to be the representative angle to describe the orientation of the rake face in oblique cutting. It is defined as the angle between the rake face (i.e. the normal to the cutting edge lying in the plane tangent to the rake face – fig. 3.3) and the normal (i.e. Z' axis in fig. 3.3) to both the velocity vector and the cutting edge, measured in a plane perpendicular to the cutting edge. Extensive discussions can be found in sections 3.4.6 and 3.4.8.

Equation 3.91 is used to calculate the normal rake angle along the cutting lips starting from the reference helix angle (θ). According to the supplier' catalogue, T2 has a helix angle (θ) of 25°, while for drill T1 the helix angle is zero and therefore equation 3.91 could be simplified.

Equation 3.91 is valid only for the cutting lip region of both drills. For the chisel edge area, the needed equations were derived in chapter 3.4.8. Planar grinding is assumed for both drills, although T2 has an inclined chisel edge with respect to the drill axis. Therefore, [43]-eq.33 (presented in chapter 3.4.8) is used to derive the static rake angle (α_s) along the chisel edge for drill T1, and equation 3.113 to derive the normal (dynamic) rake angle. Together, they can be written as:

$$\alpha_{n,ch-T1}(r) = -\arctan[\tan(p_l) \cdot \sin(\psi)] + \mu(r) \quad (3.157)$$

With particular values (p_l in equation 3.157 equal to 59.5°; $R_c=0.125$ mm and $w=0.115$ mm to calculate the chisel edge angle ψ based on eq. 3.42) we obtain:

$$\alpha_{n, ch-T1}(r) = -\arctan\left[\tan(59.5^\circ) \cdot \frac{0.115}{0.125}\right] + \mu(r) \quad (3.158)$$

For drill T2, the chisel edge is inclined from the drill axis and oblique cutting is observed and discussed in chapter 3.5.3. Therefore, the same generic equation 3.91 (or its adapted and simplified version 3.127) was used to derive the normal rake angle, based on the static rake angle (α_s) which was shown to be equal to equation 3.125 (constant along the chisel edge).

Summarizing, the normal rake angles for the two drills were evaluated using the following functions (3.159 and 3.160, with α_n evaluated using 3.91, $\alpha_{n, ch-T1}$ by equation 3.158 and $\alpha_{n, ch-T2}$ by equation 3.127), while their plot is presented in fig. 3.26:

$$\alpha_{n-T1}(r) = \begin{cases} \alpha_{n, ch-T1}(r), & 0 < r < 0.125 \\ \alpha_n(r), & 0.125 < r < 2.773; \theta = 0^\circ \end{cases} \quad (3.159)$$

$$\alpha_{n-T2}(r) = \begin{cases} \alpha_{n, ch-T2}(r), & 0 < r < 0.5075 \\ \alpha_n(r), & 0.5075 < r < 2.8; \theta = 25^\circ \end{cases} \quad (3.160)$$

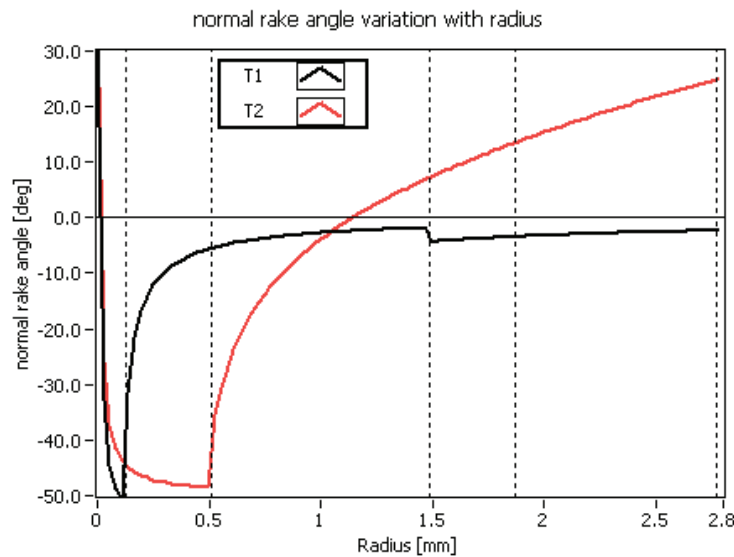


Fig. 3.26 – Normal rake angle (α_n) variation with the radius for the considered drills

3.5.6 Relief angle (γ)

Relief (or clearance) angle (γ) is the angle describing the relief face, defined as the angle between this surface (tangent to relief face) and the velocity vector at any point on the cutting edges of a drill, and measured in a plane normal to the radial direction. For discussions see chapter 3.4.7 and 3.4.8 and fig. 3.14.

For the cutting lip region, it is evaluated with equation 3.110, starting from a reference relief angle (γ_0), defined in a similar manner as the helix angle, at the outermost point of the cutting lip. For multi-stages drill points (as in T1) reference relief angles should be known at each stage, although they are not always provided by the drill manufacturers.

For the calculation, we have assumed $\gamma_0=14^\circ$ for all cutting lip segments of each drill considered hereby. For the chisel edge area, the wedge is symmetric and the static rake and the complement of the static relief angles are equal (see fig. 3.16). Equation 3.157 (used to estimate the rake angle along the chisel edge for T1) can be adapted to account for the inverse effect of the cutting angle:

$$\gamma_{ch-T1}(r) = \arctan\left[\tan(59.5^\circ) \cdot \frac{0.115}{0.125}\right] - \mu(r) \quad (3.161)$$

For the T2, drill, we have used the static rake angle (α_s) calculated according to equation 3.125, to estimate the static relief angle (γ_s , by equation 3.112) and further the “dynamic” relief angle (γ) by equation 3.114.

Summarizing, the following functions were used:

$$\gamma_{T1}(r) = \begin{cases} \gamma_{ch-T1}(r), & 0 < r < 0.125 \\ \gamma(r), & 0.125 < r < 1.485; \gamma_0 = 14^\circ; R = 1.485\text{mm} \\ \gamma(r), & 0.1485 < r < 2.773; \gamma_0 = 14^\circ; R = 2.773\text{mm} \end{cases} \quad (3.162)$$

$$\gamma_{T2}(r) = \begin{cases} 90^\circ + \alpha_s - \mu(r), & 0 < r < 0.5075 \\ \gamma(r), & 0.5075 < r < 2.8; \gamma_0 = 14^\circ; R = 2.8\text{mm} \end{cases} \quad (3.163)$$

When plotted against the radius, for equations 3.162 and 3.163 we obtain the following graph (fig. 3.27):

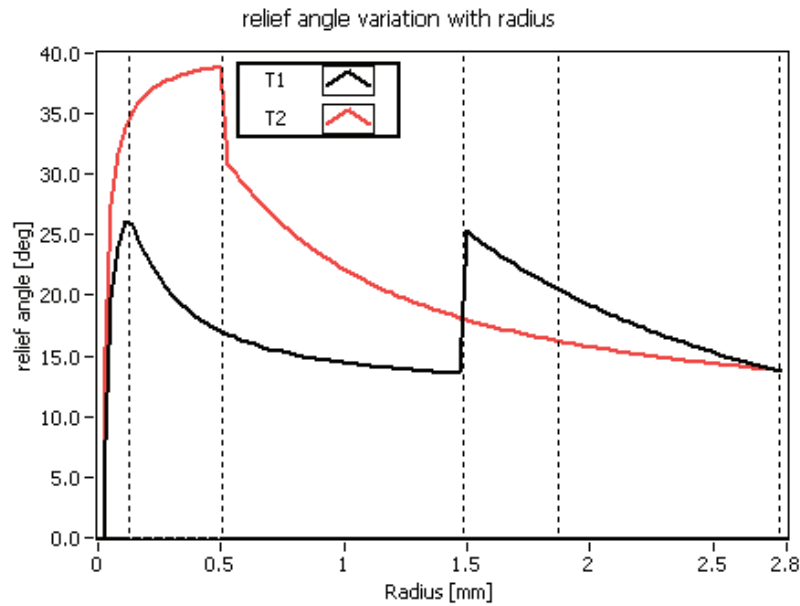


Fig. 3.27 – Relief angle (γ) variation with the radius for the considered drills

3.5.7 Chip flow angle (η)

As defined and discussed in chapter 3.3, the chip flow angle expression is based on the chip flow law of Stabler [34], which states that the chip flow angle is proportional to the inclination angle (i) by a factor

between 0.9 to 1. As the choice of the factor is rather empirical and the difference within the mentioned range is not significant, we have assumed the factor equal to unity for simplicity. Therefore:

$$\eta_c(r) = i(r) \quad (3.164)$$

3.5.8 Number of flutes (N)

In practice, most drills have two flutes, as the case of T2. However, T1 has 4 flutes although not all of them are always engaged in cutting. It was found that:

$$N_{T1}(r) = \begin{cases} 2, 0 < r < 1.868 \\ 4, 1.868 < r < 2.773 \end{cases} \quad (3.165)$$

$$N_{T2}(r) = 2, 0 < r < 2.8 \quad (3.166)$$

Chapter 4

Experimental analysis of the drilling process

4.1 Introduction

The use of long-fiber reinforced composites is extending beyond the initial applications in aerospace and military fields, driven by the advances in manufacturing technologies which made the production process more cost effective. Long fiber reinforced composite materials offer excellent and highly customizable mechanical properties, while being much more lightweight than metallic alloys. As parts made out of fiber reinforced composites are usually integrated in a mechanical assembly, drilling is the most often encountered machining process in the production plan of such parts. Drilling occurs mainly during the last stages of the manufacturing process in order to create fixing features like holes. Delamination is a critical aspect of the drilling process, as it can lead to failure in use and parts with such defects are usually discarded. Furthermore, delamination is usually not visually detectable and a special inspection process is necessary.

A major difference between metallic and composite plates is their structure: isotropic for metals and anisotropic for composite materials; meaning that while for metallic materials all the structure will respond in a similar manner under the machining loads, the composite structure will have localized responses from the same loads, leading to defects in the internal structure of the remaining work-piece material (i.e. delamination). Delamination was found to occur at tool entry (peel-up) or tool exit (push-out). The tool-exit delamination was found to be related to the thrust force generated during drilling [27, 12], force which for a given work-piece and material combination depends on the drill geometry and the cutting conditions.

Most experimental investigations on drilling fiber reinforced composites [16, 17, 18] analyze only the total thrust and torque generated during drilling or separately the forces caused by the chisel edge and cutting lips by drilling with or without pilot hole [2, 3]. The later studies suggested that is possible to obtain more detailed information about the distribution of the loads in drilling from the analysis of the forces variation during tool entry into the work-piece; this knowledge is useful for selecting appropriate drills and cutting conditions for drilling fiber reinforced composites, accurate modeling of delamination defects, improvements of cutting forces prediction models, drill geometry and process planning optimization.

The present experimental work is focused in determining the distribution of the drilling loads (thrust and torque) along the layered structure of long-fiber reinforced composite plates, and how this distribution varies with the cutting parameters and tool geometry. Carbon-fiber and glass-fiber reinforced materials are tested when drilling with 3 different tool geometries (introduced in chapter 4.2) for a wide range of cutting parameters. The choice of drills, work-pieces and cutting conditions (discussed in chapter 4.2) is based on practical considerations.

Unlike previous published experimental investigations, current experiments have attempted to determine the complete distribution without employing pilot holes. The pilot hole method was used [2, 3] to determine distinctively the contributions of the chisel edge and the cutting lips – a very coarse distribution. Increasing the resolution of the cutting force distribution would mean a complex experimental plan with pilot holes of various sizes, which would in general limit the range of cutting conditions and drill geometries to be tested. Difficulties might arise in obtaining accurate pilot holes without inducing defects like delamination. [2] also proposed the solution to obtain the cutting forces distribution by analyzing the cutting forces variation (their derivative) during the drill entry stage into the work-piece to obtain a distribution along the cutting lips. An illustrative example of the cutting forces (thrust and torque) variation during the drilling process was previously presented in fig. 2.3. In [2] a power law function was fitted on the thrust and torque entry curves for the cutting lip engagement only (with blind pilot hole), which was later analyzed in a similar manner to us to obtain the distribution along the cutting lips. However, using a given function limits the applicability of the method to single stage drills (like twist drills) where the chisel edge is restricted from cutting by means of pilot hole. Additionally, the question is raised if the power law is suitable to describe the entry thrust and torque curves for any drill. The fitting of the thrust and torque curves with a power law was done to obtain a smoother curve, which can be differentiated to obtain the elementary cutting forces.

Our initial tests have shown that even if the chisel edge lies in a plane perpendicular on the drill axis, the thrust and torque readings do not increase instantaneously when drill and work-piece make contact. Therefore, for such cases an inclination of the chisel edge with respect to the drill axis can be assumed when calculating the differential (the exact methodology is described in chapter 4.4) of the thrust and torque curves. Furthermore, instead of opting for a given function (i.e. power law) to decrease the noise of the thrust and torque time curves, using a smoothing filter will make the process applicable to all regions of the cutting edges and to multi-stage drills.

For the first time the distribution of the cutting forces both along the radius and work-piece thickness are presented and discussed, before being used in the calibration of the cutting force model (introduced in chapter 3). It will be shown that the maximum loads occur on the plies in contact with the tool tip. It is the moment when the drill tip exits the work-piece that is very likely to cause exit delamination. If the initial inter-laminar crack is as large as to extend beyond the boundaries of the future hole, or if additional propagation occurs as the drill continues its path towards exiting the work-piece is beyond the scope of the current thesis. We will however show that for particular cases the loads are significant for other areas of the drill tip than the chisel edge, concluding that it could be interesting to analyze both the onset and the propagation of the delamination defect (fracture).

We will also show, that although the two considered work-piece materials have different mechanical properties their machinability is comparable.

The experimental work on analyzing the drilling process of fiber reinforced composites presented in the current chapter has also been published in [15].

4.2 Experimental setup

In the current chapter we will introduce the equipment, drills and work-pieces used during the experiments and the reasoning in selecting them, together with the architecture of the final experimental setup.

The selection of the machine-tool and measurement equipment has been based rather on reasons of availability. A high-speed 5-axes CNC milling machine (C.B.Ferrari A152) readily available in AEM (Electro-Mechanic Work-shop) at EPFL was selected to conduct the drilling experiments. Additional aspiration and filtering equipment has been purchased in order to adapt the machine-tool to the demands of machining fiber-reinforced composites, producing powder-like chips hazardous to health and very abrasive.

A Kistler 9255B fixed-plate dynamometer was used to record the cutting forces, existing in the inventory of LICP laboratory at EPFL. Although the dynamometer was able to measure 3 force components (F_x , F_y , F_z) in 4 sensing points (suitable to calculate the torque about the Z axis, as detailed below), the cable collecting the data to the amplifier and later to a data-acquisition board, needed to be upgraded in order to gather individually the reading of the sensor in X and Y directions. Probably a better solution would have been to employ a rotating-dynamometer, to be mounted on the spindle of the machine tool, which would provide directly the F_z (thrust) and M_z (torque) data as needed in drilling. However, at the time of selection such a measuring device was able to operate up to 5000rpm and the desire was to test beyond this value.

The dynamometer data was passed through an amplifier and a data-acquisition board before being centralized on a laptop using the LabView software package. As mentioned in chapter 2.3, of interest in drilling are the determination of thrust and torque, which were calculated in the data-acquisition software based on the following equations:

$$\text{Thrust [N]:} \quad F_z = F_{z1} + F_{z2} + F_{z3} + F_{z4} \quad (4.1)$$

$$\text{Torque [Nm]:} \quad M_z = (y - b)(F_{x1+2}) + (b + y)(F_{x3+4}) + (a - x)(F_{y1+4}) + (a + x)(-F_{y2+3}) \quad (4.2)$$

Where F_{z1} .. F_{z4} ; F_{x1+2} ; F_{x3+4} ; F_{y1+4} ; F_{y2+3} are the 8 force components provided by the dynamometer at the 4 sensing points according to the layout introduced in fig. 4.1; a and b are the distances between the center of the dynamometer plate and the sensor lines along the X and Y axes (in our case $a=b=80\text{mm}$); x and y the coordinates of the drilled hole from the center of the dynamometer. Although in theory the torque could be calculated for any drilling point within the sensor perimeter, we found the results to be extremely noisy when drilling off-center, due to the latency of the sensors. As a matter of fact, the dynamometer' manufacturer only recommend torque measurement at the center of dynamometer and only provide a simplified version of the equation 4.2 with $x=y=0$.

Two types of work-pieces have been used: CFRP (bi-directional carbon-fiber/epoxy reinforced composite) and GFRP (bi-directional glass-fiber/epoxy reinforced composite), supplied by Carbon-Composite Technology GmbH. The two materials are frequently used for generic applications and they are considered representative of the long-fiber reinforced composite class of materials. We have opted for a bi-directional ply structure as they are more frequently employed in practice in comparison with uni-directional structures. Very common is also the laminate structure (easier to manufacture than the bulk structure), but is susceptible to inter-laminar defects such as delamination. Table 4.1 contains all the characteristics and mechanical properties of the work-pieces employed according to the supplier. No additional testing has been conducted by us to confirm these values, mainly because they are not critical to our modeling and experimental needs and are just informative. On request, the supplier provided us with approximated values of ply thickness, which were verified using measurements under microscope in our laboratories (introduced in table 4.1). The measurements have also indicated that the ply thickness

was quite variable; in our experimental results analysis we used a constant nominal value for the ply thickness.

Table 4.1 – Characteristics and mechanical properties of work-pieces

	CFRP	GFRP
Structure	Bi-directional (0°/90°) laminates of carbon fiber and epoxy matrix	Bi-directional (0°/90°) laminates of glass fiber and epoxy matrix
Fiber content	60%	60-70%
Temperature resistance	115°C	180°C
Flexural strength	0° = 1050 MPa; 90° = 900 MPa	approx. 350 MPa
Flexural E-Modulus	0° = 62 GPa; 90° = 60 GPa	approx. 22 GPa
Tensile strength	0° = 950 MPa; 90° = 900 MPa	approx. 240 MPa
Tensile E-Modulus	0° = 60 GPa; 90° = 60 GPa	-
Compression strength	-	approx. 500 MPa
Inter-Laminar-Shear-Strength	67 MPa	-
Fracture strain	approx. 1.6 - 1.7%	-
Density	1,56 g/cm ³	2 g/cm ³
Ply thickness	0.25mm	0.15mm

The selection of the work-pieces size was made based on the useful size of the dynamometer (the area between the 4 sensor as outlined in fig. 4.1), with additional space to provide fixturing. Thickness selection has been driven by the requirement to obtain full engagement of the cutting lips in drilling, therefore related to drill selection. As one of the drills intended to be employed in experiments (tapered drill reamer, T1) had an unusual long lip, it was opted for the maximum thickness available on the market, which was about 10mm. In general, the thickness of composite laminate parts is limited due to difficulty to obtain uniform temperatures during the curing stage of their manufacturing process. Therefore, all work-pieces have been ordered to the following dimensions 260x150x10mm.

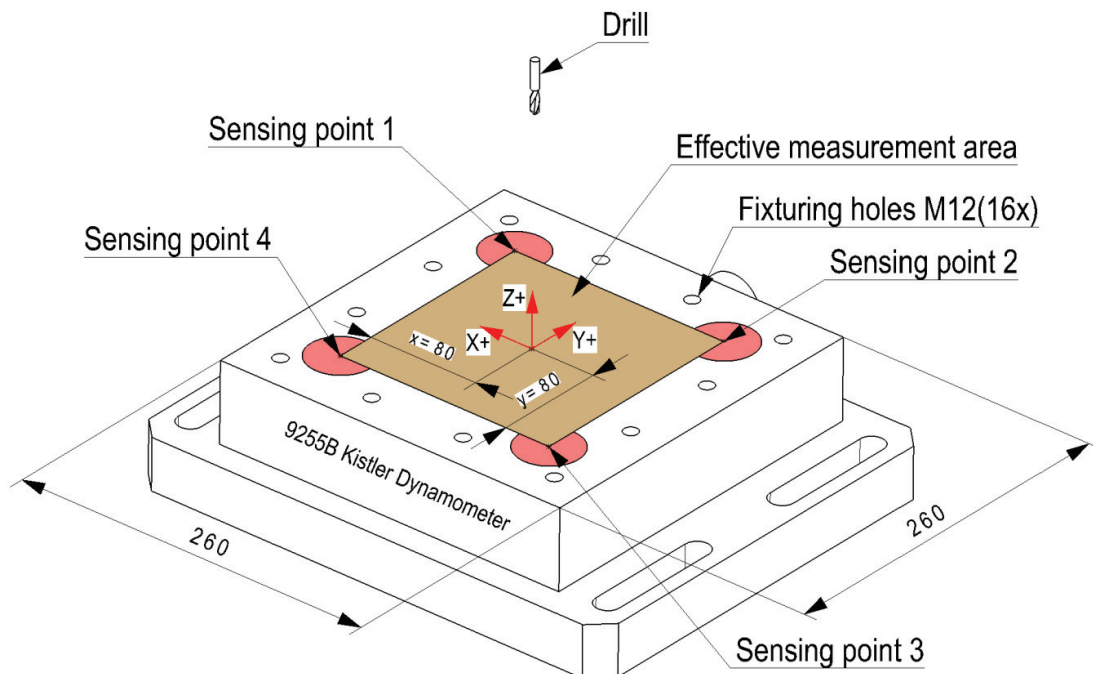


Fig. 4.1 - 9255B Kistler dynamometer outlining the useful area for force measurements

To obtain full engagement of the cutting lips in drilling with the least advantageous drill employed, the diameter of the holes was selected to slightly below 6mm (more specifically varying from 5.36 to 5.56mm

due to different suppliers, for details see the drill selection aspects below). As mechanical design handbooks [44] state that the influence of a hole in a plate extends to about $r\sqrt{3}$, a spacing of 30mm between holes assured that no interference occurred between two consecutive holes. Therefore, a configuration of 20 holes per plate was chosen as outlined in fig. 4.3. A work-piece and hole numbering system has also been employed as below.

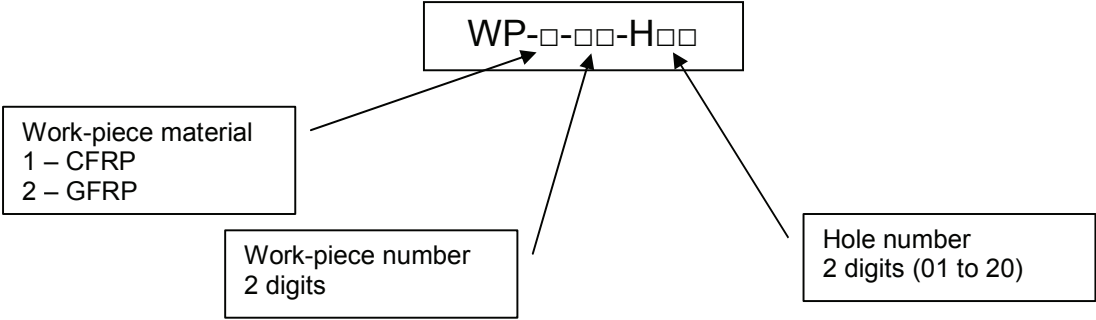


Fig. 4.2 – Work-piece and hole numbering system

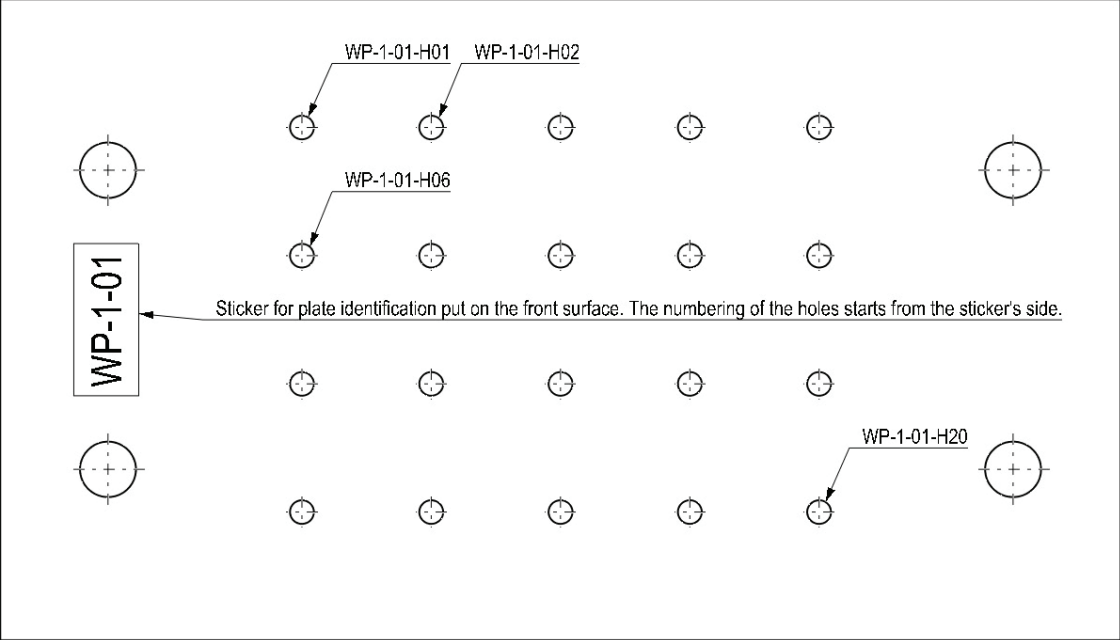


Fig. 4.3 – Hole configuration on work-piece and hole numbering system

An aluminum back-up plate, pre-drilled at a diameter slightly larger than the holes (6mm) made during the current experimental session was used to allow through drilling; minimize the chances of delamination and avoid un-wanted deformations which could affect the force readings.

The restriction to drill at the center of the dynamometer required the displacement of the work-piece and back-up plate with respect to the dynamometer for each hole. The displacement required different fixturing configuration for each hole. Our initial tests showed a strong influence of the fixture design on the data quality (i.e. noise levels). Therefore, we have employed an indexable table which was installed between the dynamometer and the work-piece/back-up plate assembly. This allowed a common fixturing design for all experiments and allowed accurate repositioning of the plates in such a way that we always drilled at the center of the dynamometer, decreasing also the amount of time needed to conduct experiments. The alignment was confirmed using work-shop tools at several stages during the

experiments. The use of the indexable table sped up the experiments significantly. The final experimental setup is presented in figures 4.4 and 4.5.

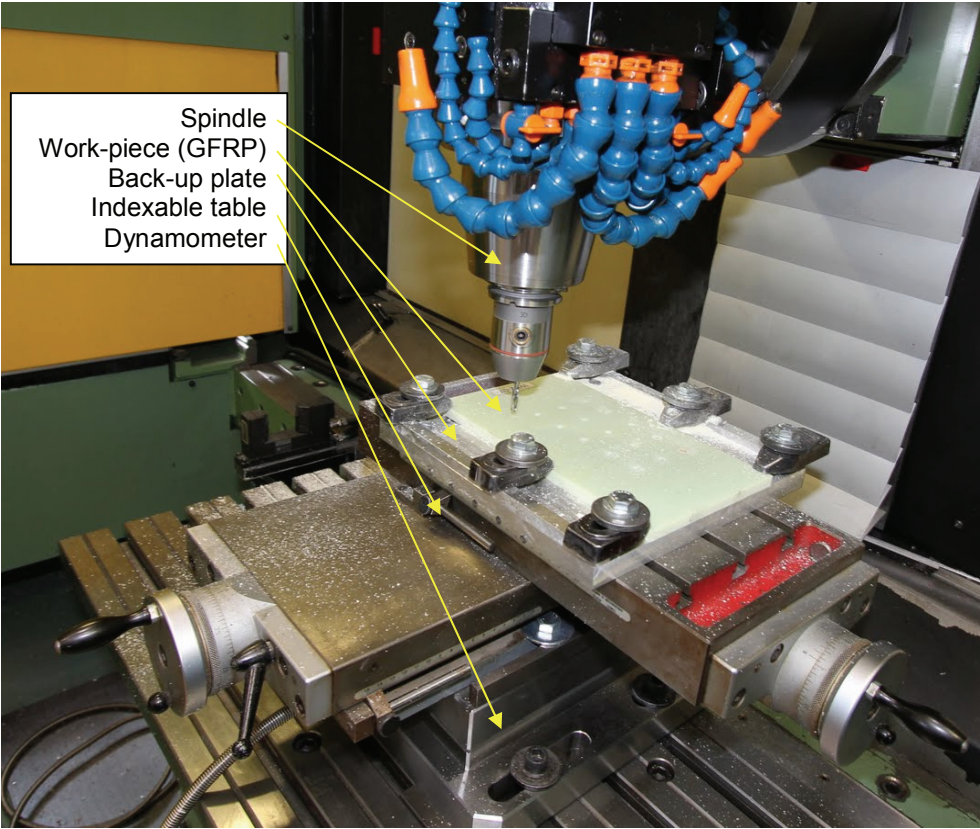


Fig. 4.4 – Experimental setup details of work-piece assembly

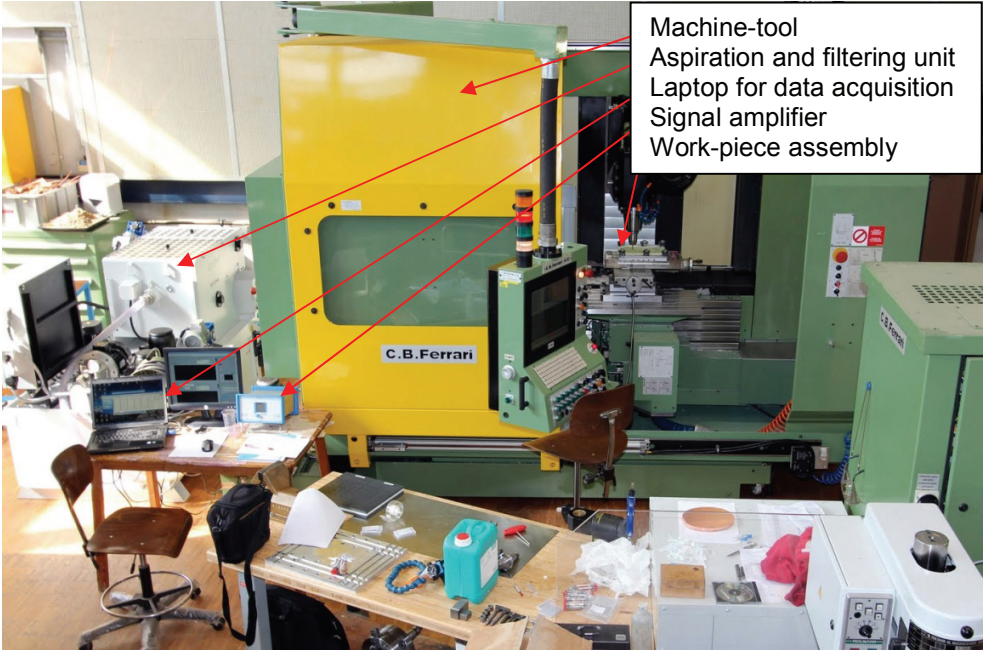


Fig. 4.5 – Experimental setup overview

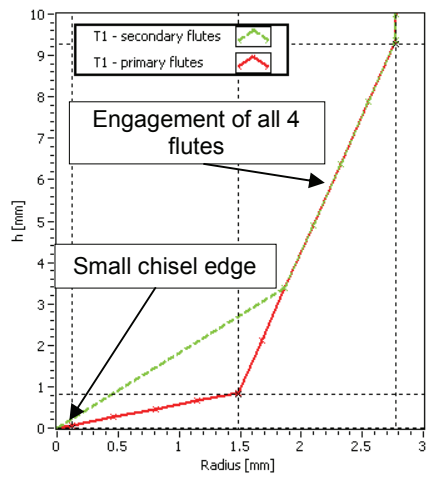
[16] and [22] are two studies introducing the performance of the drill developed specifically for long-fiber composite materials, named the tapered drill reamer (or “one-shot” drill bit), produced by Starlite Industries in United States of America. No records were found of other drills designed especially for these materials, and therefore this drill was the first one selected for our study. From the same company, we found another drill suitable for drilling both composite materials and metallic alloys (aluminum and titanium in particular), a so-called 8-facet drill (a twist drill with its point ground by 8 planar faces), which was also selected for our study. Furthermore, we have extended our search to drill manufacturers aiming at metallic materials, while looking for what we believe should perform on fiber reinforced composites as well. We also wanted to have a drill with similar material (solid carbide steel). We have therefore found a Swiss company (Tusa Carbide from Ticino) providing high-quality drills for metallic alloys mostly for the Asian market, but including in their catalogue recommendation on cutting conditions for plastic materials (i.e. short fiber reinforced plastics). We found a 2-facet twist drill which looked promising suitable for drilling long-fiber reinforced materials, while in the same time rather similar in geometry with the standard twist drills. Standard twist drills are often employed in experimental studies on drilling long-fiber reinforced materials published in the literature (i.e. [3], [17], [45], [46], [47], [48] etc.) and their mathematical modeling is well covered.

The tapered drill reamer (T1) and the 2-facet twist (T2) drills have been introduced in chapter 3.5 (and fig. 3.22) with the purpose of modeling their geometry mathematically. We reiterate hereby their description together with the 8-facet twist drill. It should be noted that the geometry of the 8-facet twist drill is rather complex and we were not able to describe it mathematically, mainly due to the existence of a web-thinning feature. The manufacturers were unwilling to disclose additional information of their geometry other than the basic parameters provided in their catalogue.

- T1 – tapered drill-reamer (also known as “**one-shot**” **drill bit**) is a tool specially designed for drilling fiber reinforced composites, but not suitable for metallic materials. The tool is made of solid carbide steels with small grain size (micro-grain). It has 4 straight flutes while only 2 are engaged in cutting initially. Due to the configuration chosen of 4 flutes, the chisel edge area is very small in comparison with other drills. The tool tip has a 2-stage point angle, featuring an unusual long tip. We have selected the diameter (5.55mm) so that the tool tip is smaller than the work-pieces thickness and full engagement is obtained, even if for a very short interval. The supplier is [Starlite Industries](#).
- T2 – 2-facet twist drill is a classical high-quality twist drill used extensively for drilling metallic materials. Unlike the conical twist drill, it has a straight chisel edge which makes an angle with the tool axis smaller than 180° . The flank faces are ground by planar surfaces, with no additional features. The material is also solid carbide steel. We have selected a 5.6mm diameter from [Tusa Carbide](#).
- T3 - 8-facet drill is a variant of the twist drill for increased efficiency in drilling fiber reinforced composites. The material is solid carbide steel (a common choice in tool material selection in metal cutting). Due to its geometric design with a helix angle this drill allows metallic chip removal in a same manner as a standard twist drill, therefore making it suitable for drilling both metals and composite materials. It features a web thinning grinding for minimizing the load concentration at the tool tip, as well as a secondary point angle. The diameter was selected as 5.36mm. The supplier is [Starlite Industries](#).

As the drilling depth was limited to 10mm, the tool lengths have been kept to a minimum found in the companies’ respective catalogue, although varied for each drill.

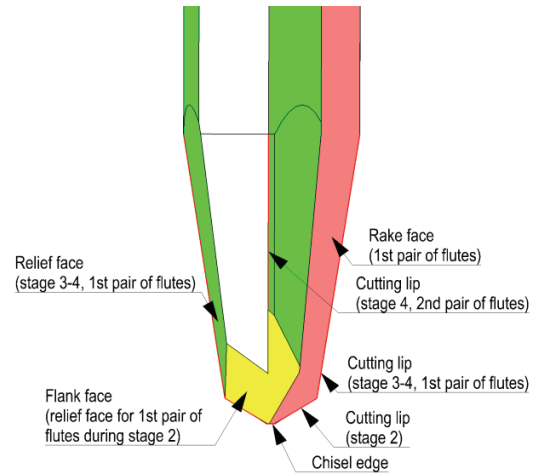
Drills have been numbered as TX-YY, where X is the type of drill (1 to 3) and YY is used to denote a certain drill item.



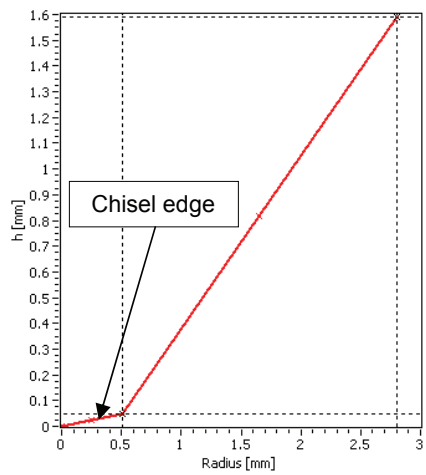
a) Profile T1



b) Photo T1



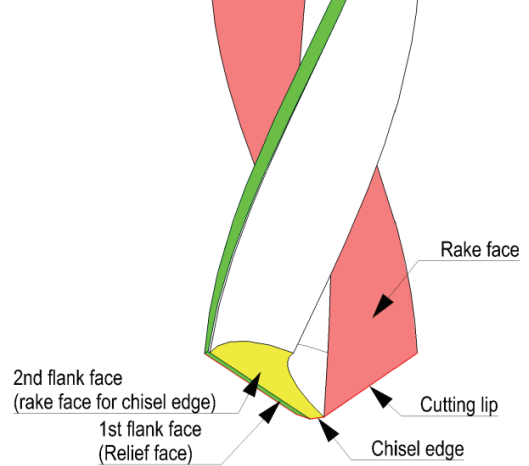
c) Drawing T1



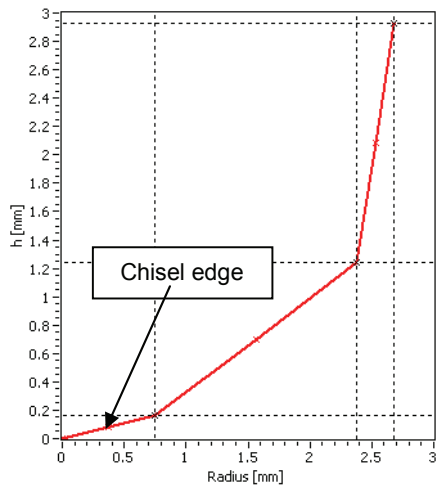
d) Profile T2



e) Photo T2



f) Drawing T2



g) Profile T3



h) Photo T3

Fig. 4.6 – Photographs and measured profiles of the drills used in experiments

For our analysis, we needed an accurate description of the tool tip profiles, which was impossible to construct based only on the geometrical parameters supplied by tool manufacturers. Therefore, an optical

measurement session was conducted in our laboratories to determine the tool tip profiles. The findings are reported in the sketches below (fig. 4.6), together with photographs of the drill tips.

The following table summarizes the experimental setup:

Table 4.2 – Summary of experimental setup

Machine-tool	High-speed 5-axes CNC milling machine (C.B.Ferrari A152) + aspiration and filtration unit (supplier C.B. Ferrari) + 2D indexable table (installed between dynamometer & work-piece)
Force measurement equipment	Fixed-plate dynamometer (Kistler 9255B) + 8-channel acquisition cable + Signal amplifier + Data acquisition cards (National Instruments)
Data acquisition software	Labview 10.0 (National Instruments)
Work-piece (WP1)	Bi-directional carbon-fiber reinforced epoxy CFRP – 260x150x10mm (Carbon-Composite Technology)
Work-piece (WP2)	Bi-directional glass-fiber reinforced epoxy (GFRP) – 260x150x10mm (Carbon-Composite Technology)
Drill (T1)	Tapered drill reamer Ø5.55mm (Starlight Industries)
Drill (T2)	2-facet twist drill Ø5.56mm (Tusa Carbide)
Drill (T3)	8-facet twist drill Ø5.36mm (Starlight Industries)

4.3 Experimental planning

The purpose of the current experimental investigation is the measurement of the cutting forces: thrust (axial force) and torque (rotational momentum). Along the drilling process, from tool entry to full engagement and tool exit from the material, the measured thrust and torque vary. We can relate this variation with the time variable and knowing the axial feed, we can easily translate these curves from the time coordinate to the drilling distance. The raw experimental data will provide time variations of both thrust and torque. If full engagement happens during the drilling process (no pilot hole), the values of thrust and torque should maintain almost constant values during this time interval. We can average and extract their values on the time frame of full engagement and we will obtain the maximum thrust and torque values for a set of experimental conditions. These values will provide the first level of comparison between the experimental and predicted data.

Further on, by correlating the time (or distance) curves of thrust and torque during tool entry (and exit) with the drill geometry, we can determine the variation of the forces with the radial engagement. The derivative of these curves will provide the distribution of the elementary forces along the tool radius. A challenge exists in determining the distribution along a chisel edge lying in a plane perpendicular to drill axis, because the chisel edge area becomes fully engaged at the moment the tool touches the work-piece, and hence we cannot obtain a distribution along the radial direction for the chisel edge. The initial tests showed however that the forces do not rise instantaneously when the drill and work-piece enter in contact even for chisel edges without any point angle. It is believed that it is due to the latency of the sensors to react to the loads. Therefore, we have found that we can safely assume a point angle of the chisel edge, with a value close, but lower than 90° for each tool from the initial tests, that will allow us to obtain a rough estimation of the distribution of the loads along the chisel edge without employing pilot holes. The disadvantages of using pilot-holes for obtaining the cutting forces distribution have been outlined in the previous chapter 4.1.

Summarizing, the experimental session has the objectives to measure or calculate based on original measurements the following:

- **Maximum thrust** [N] – single value
- **Maximum torque** [N*mm] – single value
- **Thrust/time curve:** Thrust(t[s]) – easily translated in thrust/distance curve: Thrust(d[mm]);
- **Torque/time curve:** Torque(t[s]) – easily translated in torque/distance curve: Torque(d[mm]);
- **Thrust distribution:** Thrust(r[mm]);
- **Torque distribution:** Torque(r[mm]);

The lateral force is not of interest in the current study, although the original measurements could allow its calculation if needed.

In the following table (4.3) the factors which are believed to influence the cutting forces in drilling are centralized. The current thesis is focused mainly in studying the influence of the drill geometry, cutting parameters and work-piece material properties. Therefore, in the experimental planning, the work-piece material, drill geometry and the cutting parameters (axial feed and spindle speed) are varied, while the others are kept constant.

The work-piece material and the drill geometry are discrete factors varying on 2 and 3 levels respectively as introduced in chapter 4.2. The axial feed (f) and the spindle speed (n) can be varied continuously. We have selected respectively 4 and 5 levels of variation for the cutting parameters, to cover 20 different cutting conditions (as many as the number of holes for each composite plate – see chapter 4.2).

In order to select the ranges of variation of the cutting parameters, a survey of the state of art was conducted. The ranges used by most important published studies on experimental drilling of fiber reinforced composites are summarized in figure 4.7.

Table 4.3 – Parameters influencing the cutting force measurements in drilling

Material properties	
Work-piece material machinability	The machinability is a combination of factors (based on the mechanical properties of the work-piece) which varies widely for each material. It is usually quantified as the specific cutting pressure coefficient (K_c) determined directly from machining experiments.
Tool/work-piece friction coefficient	Usually represented by the friction coefficient (K_f).
Geometrical parameters	
Drill geometry	The geometry of the drill is rather complex. It can be described by various sets of parameters, the most common ones presented here. The cutting edge radius (or sharpness) can quantify the tool wear status as well.
Drill diameter	
Number of flutes	
Point angle(-s)	
Web thickness	
Rake angle	
Relief angle	
Cutting edge radius	
Work-piece geometry	The thickness of the work-piece and its geometrical configuration (i.e. existence of pilot holes, cut-outs, inclined holes, variable thickness, etc.) will influence the variation of the cutting forces. The 2 parameters presented hereby usually can define the particular case of simple hole through constant thickness plates.
Thickness	
Pilot hole	
Fixturing configuration	The influence of the fixture on cutting forces is complex and open for discussion. Our initial tests showed that is greatly influencing the noise levels in the force measurements and the vibration levels.
Cutting conditions	
Axial feed	Will directly influence the depth of cut and the uncut chip area. It also defines the cutting angle (μ) which represents the kinematic aspect of the process.
Spindle speed	The influence of the speed extends upon the material properties mainly, although no definitive models are accepted. It also influences the noise in cutting forces measurements and vibration levels.
Coolant/lubricant usage	Liquids are used to cool the tool/work-piece and to provide lubrication in the case of metals. They affect the temperature field, but also lower the friction coefficient. Composite materials absorb moisture and this affects their mechanical properties, therefore coolants/lubricant are not usually employed in fiber-reinforced materials drilling.

The most practical range was found at axial feeds between 0.02 and 0.20 mm/rev and spindle speeds of 500 to 5'000rpm. We were initially planning to extend the domain of experimental testing at high-speeds (over 5'000rpm). However, due to the rather small diameters of the drill (under 6mm) the nominal torque values were seldom surpassed by the amplitude of its variation around the nominal value close to 5'000rpm and the noise exhibited the trend to increase with the spindle speed. Therefore, considering the equipment in our possession, we were not able to obtain suitable cutting forces measurements at higher spindle speeds, although the machine tool was able to reach up to 50'000rpm. Figure 5.1 shows a thrust and torque entry curve for a case exhibiting large amplitudes around the nominal (averaged) value. The raw curve is unsuitable to derivate in order to obtain the cutting forces distribution, while the smoothed curve (filtered) can be used, although it will exhibit greater variations between similar experimental cases and the confidence in the distribution obtained is smaller. Other studies ([2]), use a power law to fit the raw curves as discussed previously. The amplitude around the nominal value can be caused by the following reasons (i) misalignment of the hole axis with the center of dynamometer; (ii) imperfections in the symmetry of the drill; (iii) anisotropy of the material properties, believe to be more pronounced for composite materials; (iv) process induced vibrations; etc. From our experiments we have noted that the

amplitude increases with the spindle speed and is drastically affected by the fixturing design. The amplitude appears to be independent of the nominal value of the forces, therefore using higher diameter tools can be translated in better experimental results for analysis.

We also had the desire to test the influence of lubricant use. As coolant use is not recommended for composite materials as outlined previously, we wanted to capture in our model the possible reduction of the friction coefficient by using small amounts of sprayed lubricant (although for the same moisture issue can be raised for lubricant as in the case of coolant). However, we found that we were not able to assure a constant lubrication along the complete drilling process (it proved to be efficient at drill entry, but could not reach the tip of the drill as it emerged in the work-piece) and among different drills (some with long tip as the tapered drill reamer, while other with short tip).

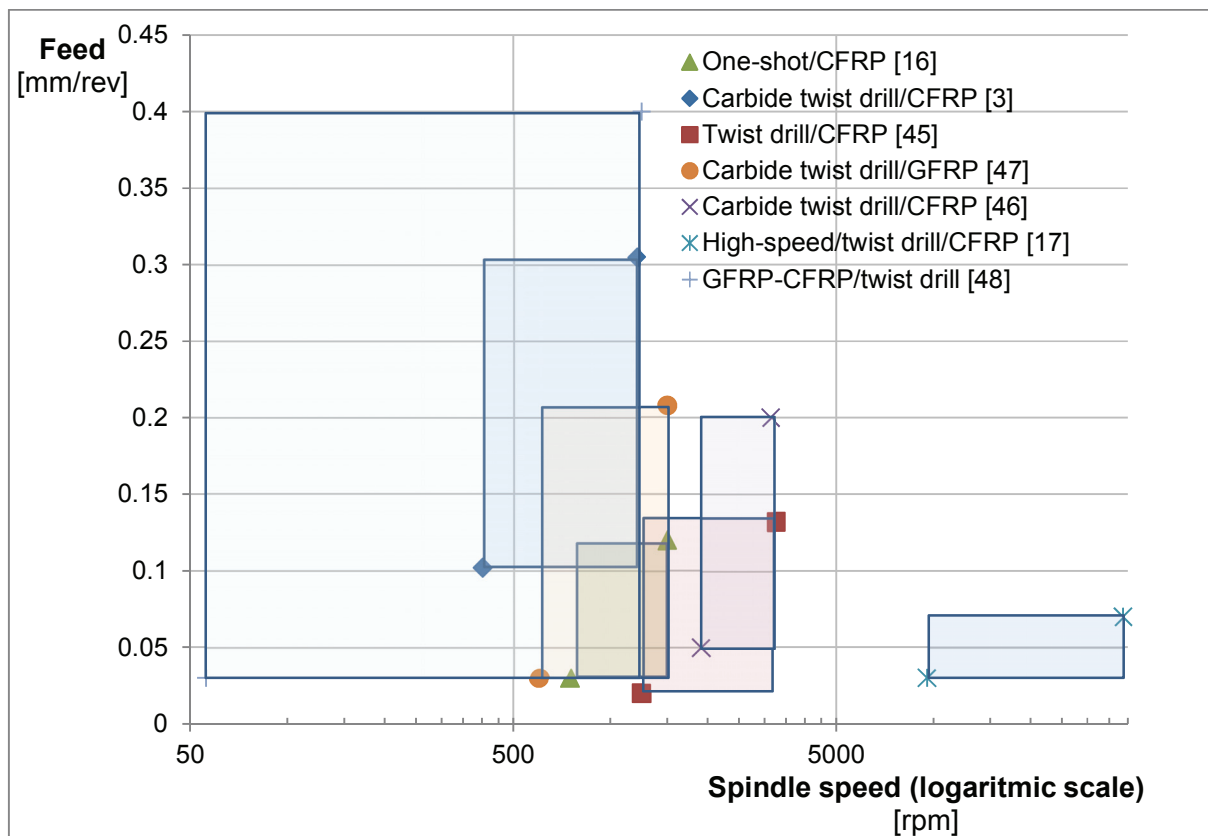


Fig. 4.7 – Map of cutting parameters employed in drilling fiber reinforced composites by references

Obtaining constant and strong fixturing configuration proved difficult at first, but introducing the indexable table (as discussed in chapter 4.3) showed constant amplitude levels for each hole position on a plate, while the magnitude of the amplitude was lowered to minimum among all the fixturing configurations tested.

Tool wear was another important issue to address. Many studies showed that extensive tool wear is to be expected when drilling fiber reinforced composites, especially with high-speed steels drills. For each work-piece material/drill combination, we have tested the variation of the cutting forces magnitude with the number of holes (using a constant set of cutting parameters believed to be the most prone to extensive tool wear, i.e. high spindle speed ($n=5'000\text{rpm}$) and low feed ($f=0.02\text{mm/rev}$)). The results showed that the maximum thrust and torque values increased by maximum 20% after 20 holes drilled with the same tool. Therefore, we have imposed the rule to use one drill item for no more than 5 holes (therefore, the influence of the tool wear should be below 5% of the maximum values of thrust and

torque). These tests were used also as repeatability tests, showing that in general there was no need to repeat one experimental case more than once.

Summarizing, 20 holes with varying cutting parameters were drilled for each work-piece/drill combination (one work-piece plate). Axial feed rate (f – [mm/rev]) and spindle speed (n – [rpm]) were varied on 4 and 5 levels respectively within ranges based on practical reasons and literature survey as in table 4.4. The drill was changed after each 5 holes. As 3 types of drills and 2 work-piece materials were tested, the experiment amounted to 120 holes across 6 work-pieces and using 24 drills.

Table 4.4 – Cutting parameters

		n [rpm]				
		500	1625	2750	3875	5000
f [mm/rev]	0.02	H01	H02	H03	H04	H05
	0.08	H06	H07	H08	H09	H10
	0.14	H11	H12	H13	H14	H15
	0.20	H16	H17	H18	H19	H20

The sampling rate of the data acquisition was varied with the spindle speed, as to obtain always about 10 points per drill each revolution.

4.4 Experimental analysis

The state of art in the analysis of the drilling process is reviewed in chapter 2.3. It is previously outlined that more information about the drilling process can be extracted from the classical measurements of cutting forces, more specifically the cutting forces distribution along the drill radius or within the work-piece thickness.

Fig. 4.8 shows a typical cutting force measurement (thrust F_z and torque M_z) for a drilling case using the tapered drill reamer (T1) on CFRP, $f=0.20$ [mm/rev]; $n=500$ [rpm]. The curves have been trimmed from tool entry (defined by a sharp increase in thrust) to just before the tool is pulled out from the work-piece (when thrust becomes again zero). Most published experimental investigations of the drilling process for both metals and other materials retain only the maximum values of the thrust and torque from analyzing the measured time-dependent curves.

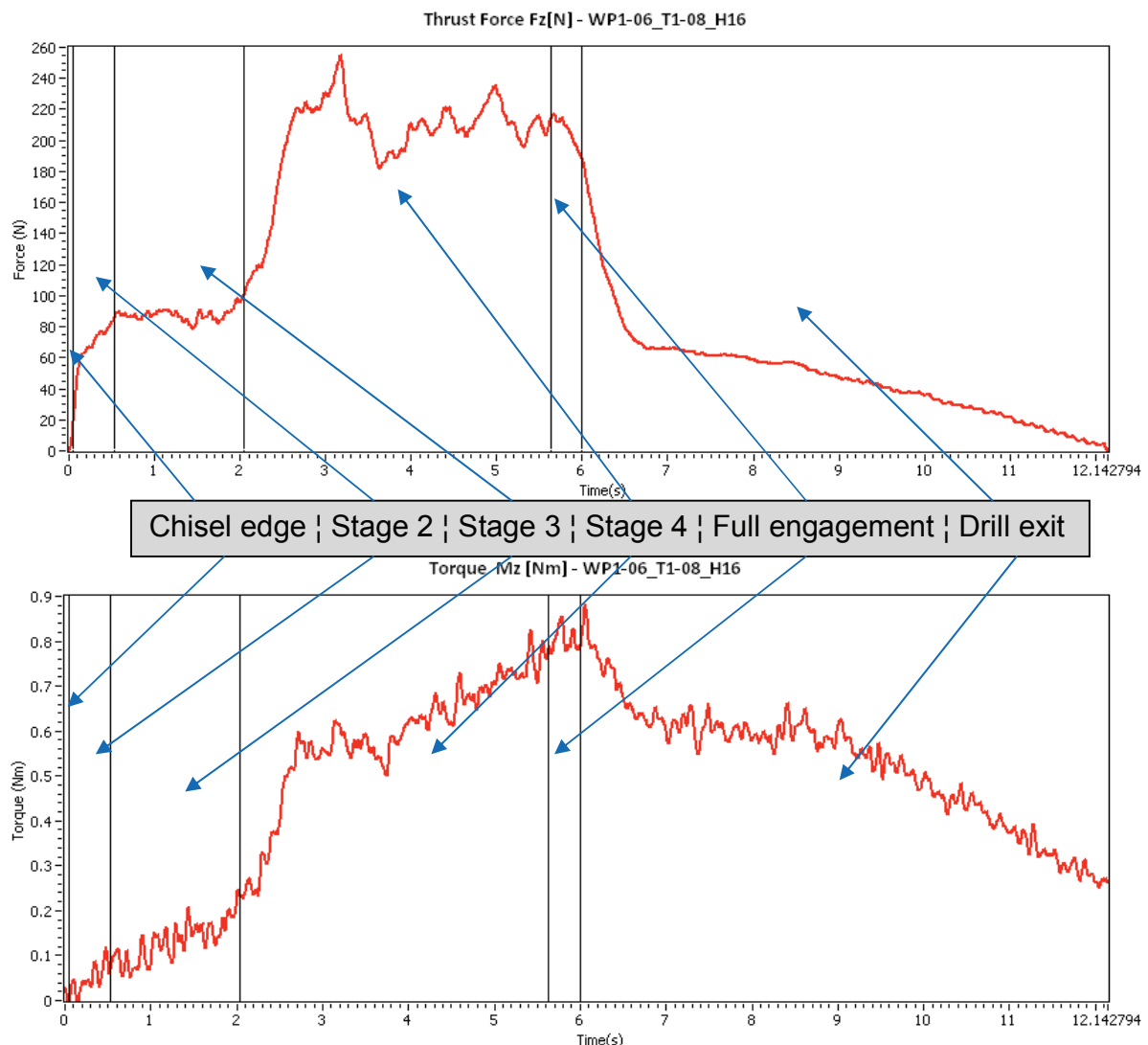


Fig. 4.8 – Sample cutting force measurement during drilling (CFRP, 10mm thickness, tapered drill reamer (T1), $n=500$ rpm, $f=0.2$ mm/rev) – a) thrust; b) torque

The time axis on thrust and torque curves can be easily related to the height (h_e) of the tool emerged in drilling, by knowing the axial speed (V_n):

$$h_e = V_n \cdot t \text{ [mm]} \quad (4.3)$$

Where the axial speed (V_n) is calculated from the cutting parameters (axial feed and spindle speed) with equation 3.50.

By using the tool profiles ($h(r)$ as in fig.4.6a, 4.6c and 4.6e), the radial engagement r_e at a point t in time (coinciding with a vertical engagement of h_e) can also be determined.

In fig. 4.8, we have indicated the drilling stages, based on drill T1's geometry. The first marked interval corresponds to the engagement of the small chisel edge. During the second one (Stage 2) the main cutting lips (with a point angle of 119° according to our measurements) become fully engaged. The thrust force increases sharply during these first two stages, while the torque is increasing much slower. During the stages 3 and 4, the long cutting lips (with a point angle of 17.2°) become engaged in cutting as well. In stage 4, the secondary flutes begin to cut as well, therefore while in stage 1 to 3 we have only 2 flutes engaged, during stage 4 there are 4 flutes engaged – resulting in the halving of the depth of cut per flute. Full engagement for this type of tool is obtained only for a short while (due to its very long tip), before the chisel edge pierces through the last plies of the work-pieces.

Theoretically, the maximum values for thrust and torque should be observed just before the tip of the drill exits the back of the plate. While this statement is true in the case of torque for almost all the experiments performed, the maximum thrust is usually obtained at the end of stage 4, at the beginning of the full engagement zone (in the case considered here, the maximum thrust is obtained during stage 4, probably due to the anisotropy of the work-piece material properties among other possible reasons). During the full engagement zone, the reaming forces (cutting with the side of the drill) add up to the measurements. The geometry and the cutting configuration in the reaming zone generate low elementary forces and particularly oriented in the tangential direction (and lateral, which are canceled by the cutting process of the opposite flute). The tangential elementary forces at this point have a noticeable effect on torque measurements as they are multiplied by the maximum possible arm. Furthermore, the thrust force is usually decreasing during this stage due to the deformation of the un-cut work-piece, which becoming thinner, is easier to deform.

We also observe that for tool diameters below 6mm, the torque is rather small. For the particular case presented above (fig. 4.8), the feed rate is at the maximum considered ($f=0.20\text{mm/rev}$), and the forces are also close to their maximum values recorded in our experiments. For smaller values of the feed rate (i.e. $f=0.02\text{mm/rev}$), the maximum torque is sometimes below 0.2 [Nm] , and therefore very noisy, especially at high spindle speeds. High-speed drilling tests are usually conducted at low feed rates, between 0.02 to 0.08mm/rev . We found difficult to analyze the torque measurements accurately at spindle speed over 5000rpm with the small diameter tool considered hereby.

Let us assume 2 time instances t_1 and t_2 from 0 to t_{\max} defined at the end of stage 4 (see fig. 4.8), $t_1 < t_2$. For a drilling case such as in the above example, we can extract the values F_{z1} , F_{z2} , M_{z1} and M_{z2} . F_{z1} and M_{z1} (F_{z2} and M_{z2} respectively) correspond to the total thrust and torque caused by the cutting process of the cutting edges for the drill engaged up to a height of h_1 (h_2) and radius r_1 (r_2) into the work-piece. h_1 , h_2 can be calculated using equation 4.3 based on the cutting parameters, while r_1 and r_2 can be obtained by tracing the tool profile graphs (fig.4.6a, 4.6c and 4.6e).

For the resulting element of the cutting lip segment defined by the points (r_1, h_1) and (r_2, h_2) , we can calculate the axial (F_z) and tangential (F_y) forces acting on it, using the following equations:

$$Fz[(r_1, h_1), (r_2, h_2)] = Fz_2 - Fz_1 \quad (4.4)$$

$$Fy[(r_1, h_1), (r_2, h_2)] = \frac{Mz_2}{r_2} - \frac{Mz_1}{r_1} \quad (4.5)$$

For more reliable numerical results, we can assume the average torque to act in the middle of the element, and re-write equation 4.5 as:

$$Fy[(r_1, h_1), (r_2, h_2)] = \frac{Mz_2 - Mz_1}{\frac{r_2 - r_1}{2}} \quad (4.6)$$

For our analysis we can calculate the normalized (per unit length) values of the axial and tangential forces on the selected cutting lip element along the r and h directions:

$$\frac{\partial Fz[(r_1, h_1), (r_2, h_2)]}{\partial r} = \frac{Fz[(r_1, h_1), (r_2, h_2)]}{r_2 - r_1} \quad (4.7)$$

$$\frac{\partial Fz[(r_1, h_1), (r_2, h_2)]}{\partial h} = \frac{Fz[(r_1, h_1), (r_2, h_2)]}{h_2 - h_1} \quad (4.8)$$

$$\frac{\partial Fy[(r_1, h_1), (r_2, h_2)]}{\partial r} = \frac{Fy[(r_1, h_1), (r_2, h_2)]}{r_2 - r_1} \quad (4.9)$$

$$\frac{\partial Fy[(r_1, h_1), (r_2, h_2)]}{\partial h} = \frac{Fy[(r_1, h_1), (r_2, h_2)]}{h_2 - h_1} \quad (4.10)$$

Equations 4.7 to 4.10 will give the average distribution along the radius and thickness respectively, from the tool tip of the elementary axial and tangential cutting forces per unit length acting on each element of the cutting lip.

Due to the noisy nature of the thrust and torque curves, considering very small elements will not provide conclusive results. Therefore we have opted for discretization adapted to the drill geometry, first with focus on the drilling stages of the drill geometries and later according to the ply thickness of the composite materials considered.

The first analysis (with uneven discretization according to the drill geometry) will show the loads acting along each segment of the cutting lips. For large segments, as outlined in the tool profile (fig.4.6a, 4.6c and 4.6e), we have considered 2 elements for each segment of the tool profiles, while for small segments (as the chisel edge of the tapered drill reamer T1) we have considered only one element. The results of equations 4.7 and 4.9 are divided by the number of flutes (N) engaged at each stage in cutting. There are 2 flutes for tools T2 and T3. T1 tool uses 2 flutes up to the last stage (stage 4, as described in fig.3), where the secondary flutes are becoming engaged in cutting and therefore N=4.

This type of analysis is useful for evaluating the drill geometry performance stage by stage and for calibrating our cutting force prediction model presented in chapter 3.

To be able to compare all different types of drills employed in our experiments a second analysis on the same principles is further carried on. In this case, the discretization is done in equal elements along the height direction (dh), with a size equal to the ply thickness (0.25mm for CFRP and 0.15mm for GFRP work-pieces – see table 4.1). This analysis will provide the load distribution within the composite structure (for each ply), the loads responsible for causing the delamination defect. As we are interested in the distribution of the loads among the plies, in this analysis we do not divide the forces acting on each

element by the number of flutes and we do not normalize the loads. It should be noted however, that the loads calculated as such will act on 2 (or 4) different areas, symmetrically displaced about drilling axis.

For many experimental cases, the raw measurements of thrust and torque are too noisy for the analysis to be carried out directly. Therefore, smoothing techniques have been tested (like B-spline fitting technique and averaging functions). For the first type of analysis (radial distribution of elementary cutting forces) we have employed a B-spline fitting technique, which proved fairly reliable for the complete set of experimental conditions (different geometries, work-piece materials and cutting parameters), while for the second one (ply distribution of the loads) we used a moving averaging function. However, during the work on the model calibration (presented in chapter 5), we have found difficulties in using the smoothed curves obtained by B-spline fitting, mainly due to the inconsistencies (not being constrained to pass through the start and end point) at tool entry and just before the full engagement stage. We have therefore employed a moving average function before the trimming of the raw curves within the limits of interest. This method preserved much better the boundary conditions at the start and end of the analyzed interval of cutting forces. The length of the moving average window has been adapted to the sampling rate and noise levels for each experimental case.

The post-processing of the measured raw data of thrust and torque according to the description above has been implemented in Labview 10.0 and takes into consideration the profiles of the drills as per figures 4.6a, 4.6c and 4.6e and the cutting parameters as described in the experimental planning. As the theory itself can be implemented in any other curve fitting software, the actual source files are not presented nor discussed in the thesis. They are however available electronically together with the raw data measurements.

4.5 Results and discussion

As mentioned in chapter 4.3 the effective number of experiments was 120 holes, although more were drilled as preparatory experiments. The current thesis will not present the raw and processed results of all the experiments, but rather a representative selection to justify the arguments introduced. All of them are however available electronically.

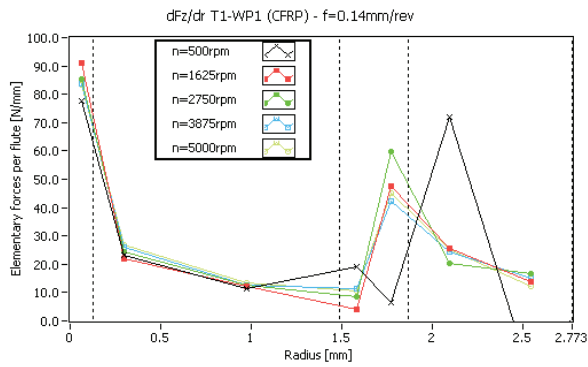
For comparison with other published results of experimental studies ([3], [16], [22], [18], etc.) we start by introducing the maximum values of the cutting forces (thrust and torque). Previous mentioned studies use different cutting conditions (especially different drill diameter, the most major factor affecting the magnitude of the thrust and torque values), therefore a direct comparison is impossible. As the complete list of 120 holes is too extensive, a selection of cases with extreme cutting parameters for each drill/work-piece combination is presented in table 4.5. It is noted that the current values are around the expected values, considering the values reported in experiments published in literature (see references above) and exhibit similar trends. A graphic comparison of experimental and predicted results with [3] is illustrated in fig. 5.7.

Table 4.5 – Maximum thrust and torque

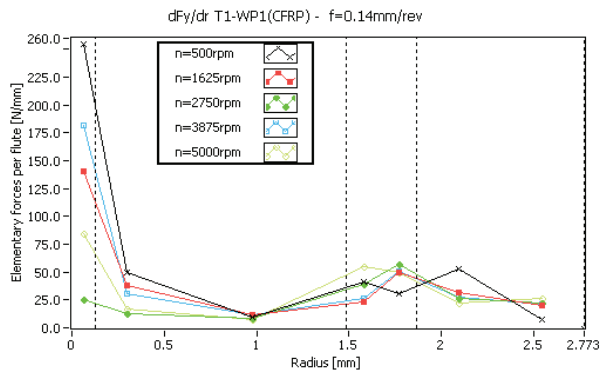
Tool	Work-piece	f [mm/rev]	n [rpm]	Thrust [N]	Torque [Nm]
T1	CFRP	0.02	500	103.6	0.35
		0.20	5000	222.5	0.89
	GFRP	0.02	500	34.9	0.32
		0.20	5000	284.6	1.02
T2	CFRP	0.02	500	58.1	0.27
		0.20	5000	96.6	0.63
	GFRP	0.02	500	26.8	0.23
		0.20	5000	94.0	0.57
T3	CFRP	0.02	500	83.0	0.39
		0.20	5000	189.2	0.63
	GFRP	0.02	500	46.7	0.14
		0.20	5000	162.7	0.69

In the current chapter we focus on the results of the experimental analysis as presented in chapter 4.4. More results will be introduced in chapter 5 when the cutting force model is calibrated and compared with the experimental results.

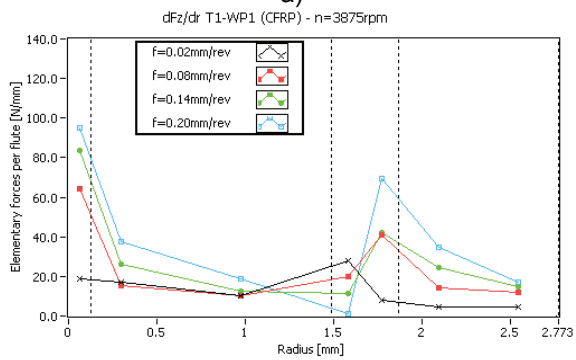
Figures 4.9a to 4.9h present the radial distribution of the elementary forces per flute for the tapered drill reamer T1 for selected cases of the experimental plan. It is noted that the radial distributions of the elementary cutting forces are expected to be discontinuous functions, as from one stage to another the geometry of the element (rake angle, inclination angle) and the angles of decomposition along axial and tangential directions (point angle, inclination angle) are changing sharply. The stages are outlined by the vertical cursors. As expected, we observe a load concentration (for both axial and tangential forces) on the chisel edge. Additionally, the cutting along the 3rd stage (see figures 4.6a and 4.8) seems to generate an unusual amount of axial force (thrust) due to the drastic change in point angle (see fig. 3.23, triggering changes in rake and inclination angles). Introducing the secondary flutes during the 4th stage seems to lower the loads experienced by each flute, by halving the actual depth of cut. The second point in stage 3 triggers an unexpected rise in axial force. An explanation of this effect is attempted in chapter 5.3. The spindle speed seems to have little if no effect on the axial forces (with the exception of the second point of stage 3, discussed above), while its effect is not clear for the tangential forces, and seems to be concentrated towards the tool center. Due to the sensitivity in calculating the elemental tangential force close to the tool center, this effect can be attributed to the accuracy of the measurements. Feed rate seems to have a clear and almost linear influence on both the axial and tangential elementary forces for most of the drilling stages.



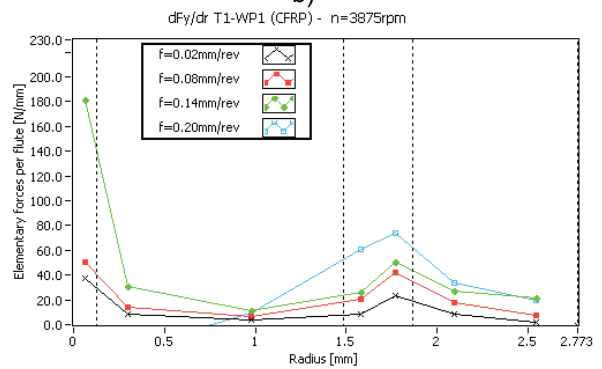
a)



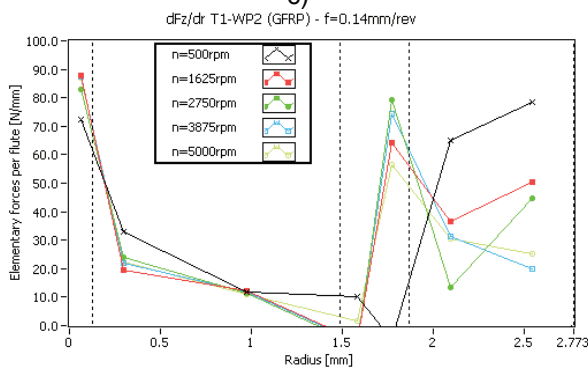
b)



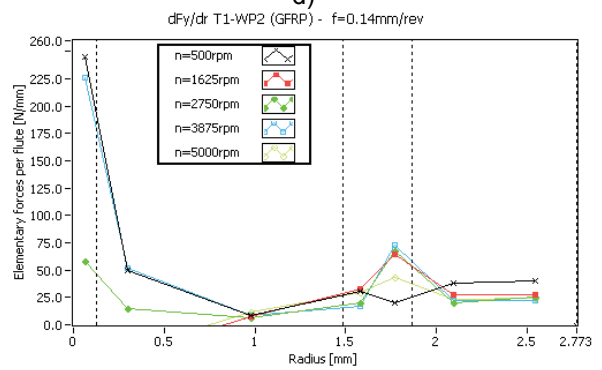
c)



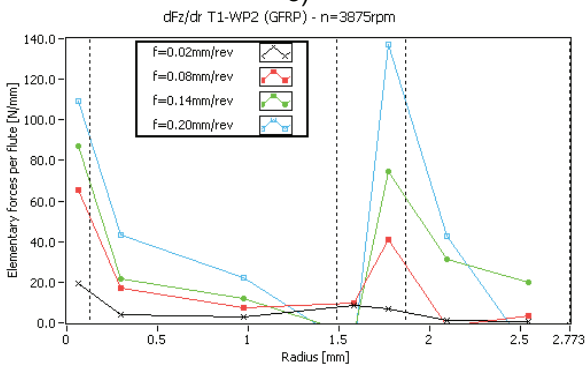
d)



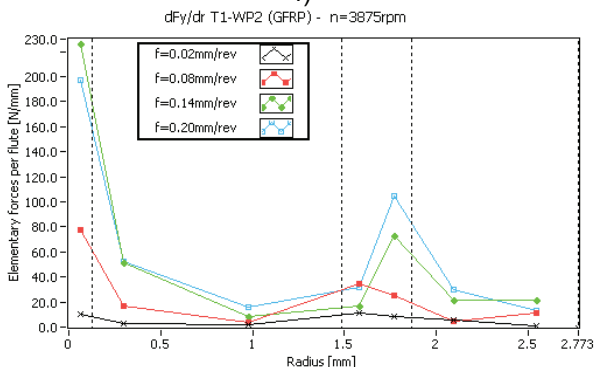
e)



f)



g)



h)

Fig. 4.9 – Elementary (forces per unit length) axial (a,c,e,g) and tangential (b,d,f,h) force distribution along the drill radius for selected cutting parameters, CFRP/GFRP work-pieces and tapered drill reamer T1

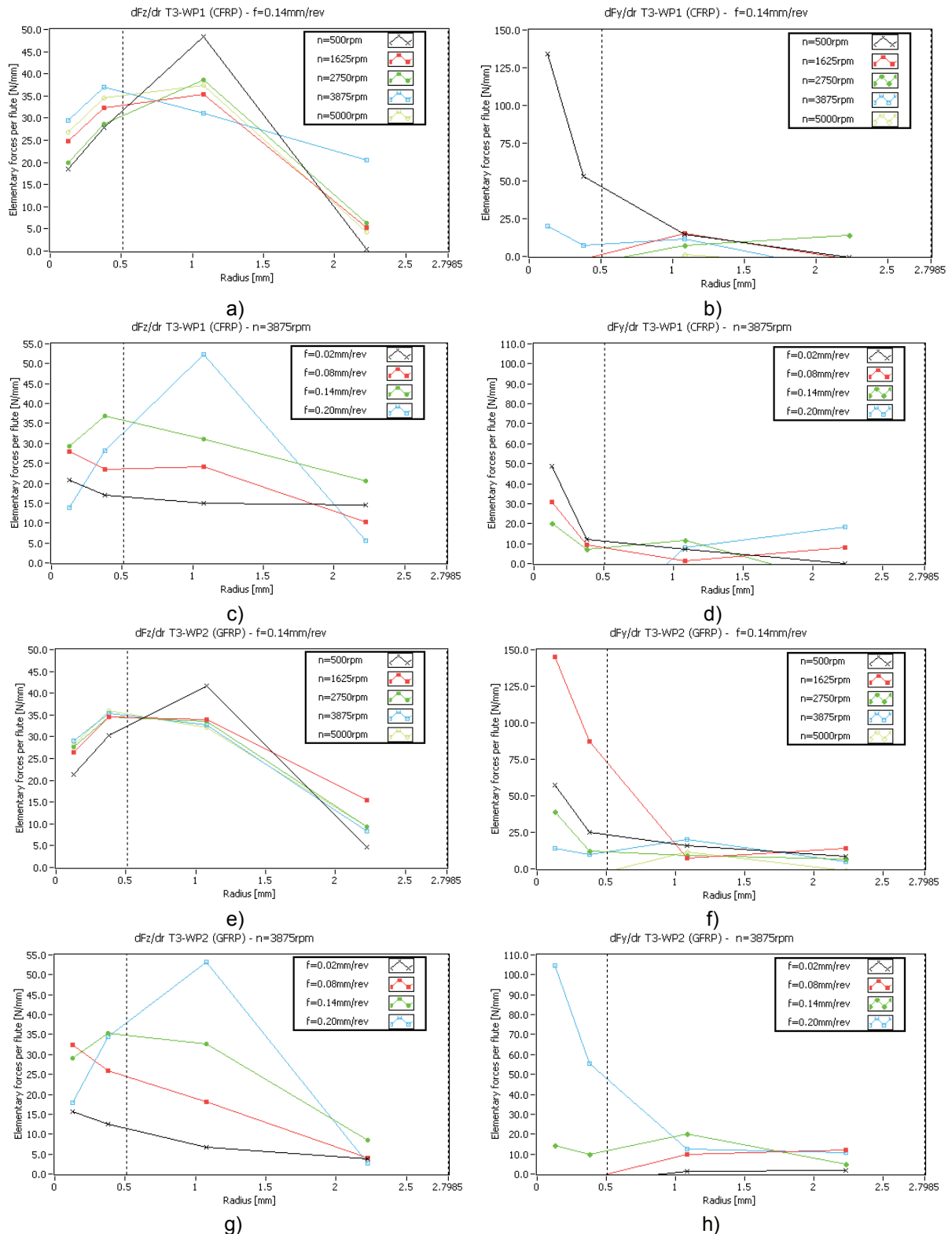
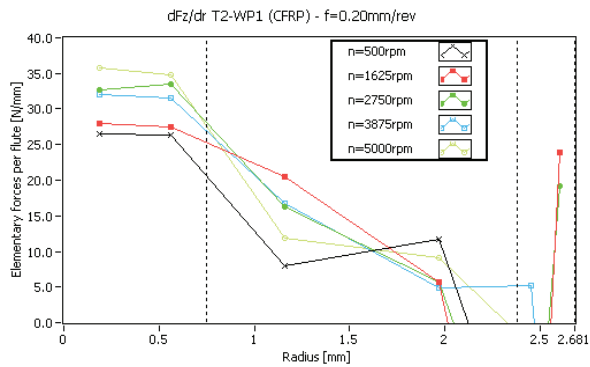
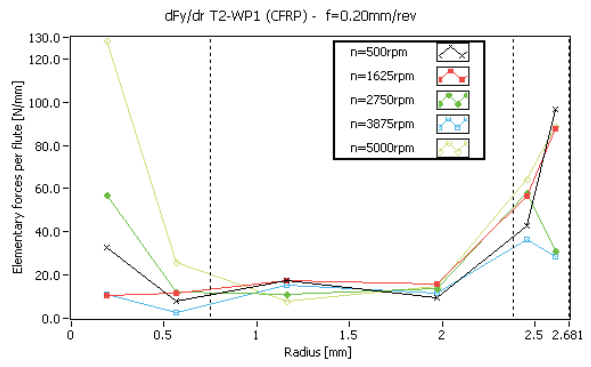


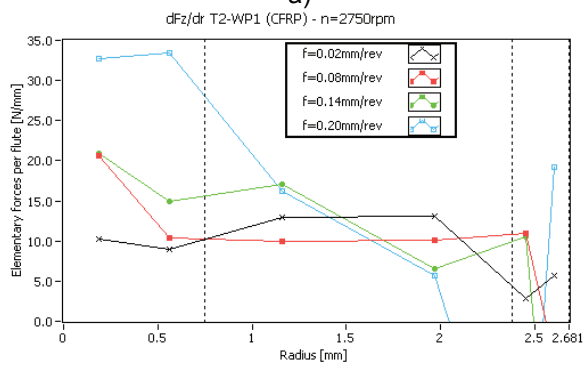
Fig. 4.10 – Elementary (forces per unit length) axial (a,c,e,g) and tangential (b,d,f,h) force distribution along the drill radius for selected cutting parameters, CFRP/GFRP work-pieces and 2-facet twist drill T2



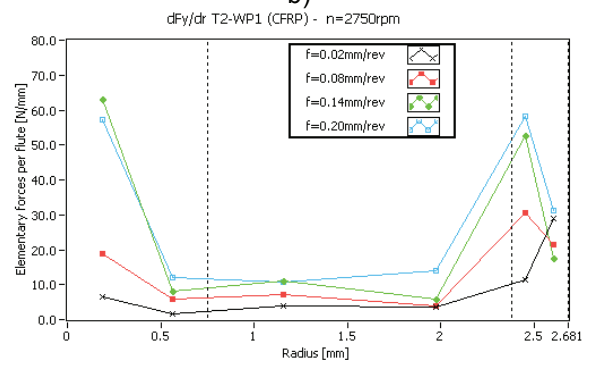
a)



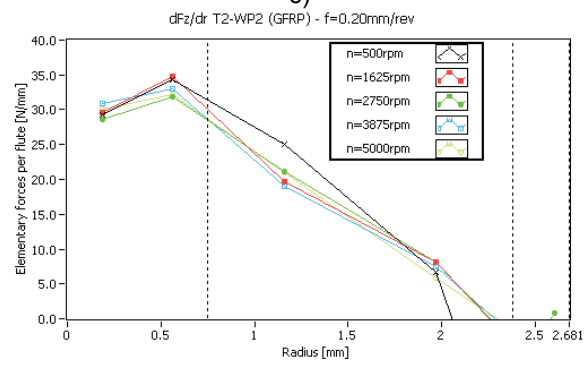
b)



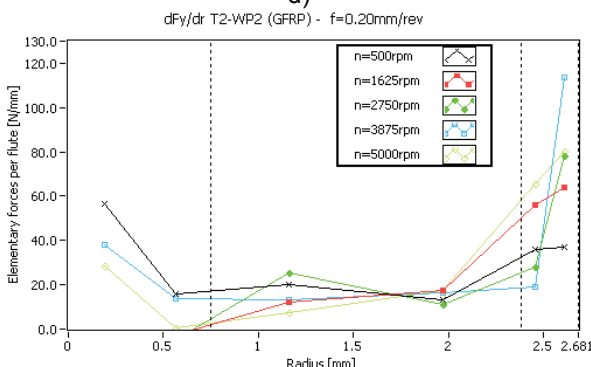
c)



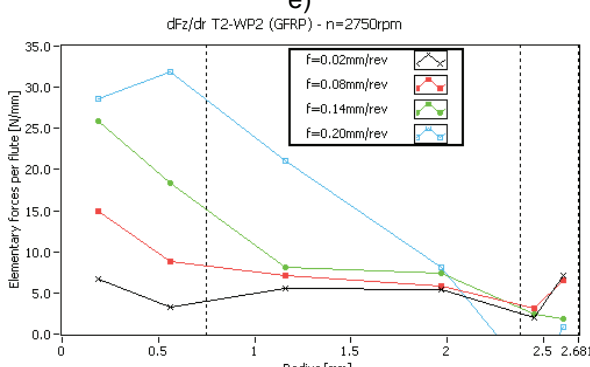
d)



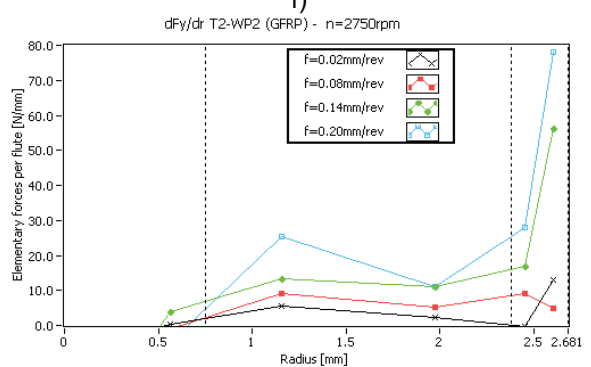
e)



f)



g)



h)

Fig. 4.11 – Elementary (forces per unit length) axial (a,c,e,g) and tangential (b,d,f,h) force distribution along the drill radius for selected cutting parameters, CFRP/GFRP work-pieces and 8-facet twist drill T3

Figures 4.10a to 4.10h introduce the results for the 2-facet twist drill (T2). As the cutting edges of this drill has only 2 segments (cutting lip and chisel edge) only 2 drilling stages are noted, marked by vertical cursors. At low feed rates, the load concentration seems to occur as expected on the chisel edge. However, as the feed rate increases, the loads on the first part of the cutting lip are increasing more rapidly, becoming the critical area. The cutting is less efficient in the vicinity of the transition point from stage 1 to 2 due mainly to the highly negative rake angle (see fig. 3.26). However, this only could not explain why the elementary axial forces are increasing more rapidly with the feed rate at the beginning of stage 2 than at the end of stage 1. However, from stage 1 to 2 the point and the inclination angles are also changing sharply, which should translate into a different decomposition of the forces along axial and tangential directions.

Graphs 4.11a to 4.11h present the results for the 8-facet twist drill (T3). We observe the distribution along the radius to be more evenly, with load concentrations at the chisel edge and the last stage (see fig. 4.6e). The influences of spindle speed and feed rate seem to be similar overall with T1, although for drilling CFRP we note a more clear increase in forces with the spindle speed, especially at high feed rates. However, this effect does not seem to appear when drilling GFRP. It is also noted that the increase of elementary axial force per unit length at the beginning of stage 2 with the feed rate is not as pronounced as for T2. We believe is due the web thinning feature, making the cutting more efficient.

Furthermore, in figures 4.12 and 4.13 the calculated loads acting on each ply are presented. Equations 4.8 and 4.10 were used to calculate the axial and tangential loads for a constant ply height interval (dh equal to 0.25mm for CFRP and 0.15mm for GFRP). It is noted that the loads have not been normalized (divided by the distance from the tool tip interval). Additionally, the results are not divided by the number of flutes, so that the total load on each ply is obtained, although the loads are in fact applied in 2 (or 4) points symmetrically displaced from the drill axis.

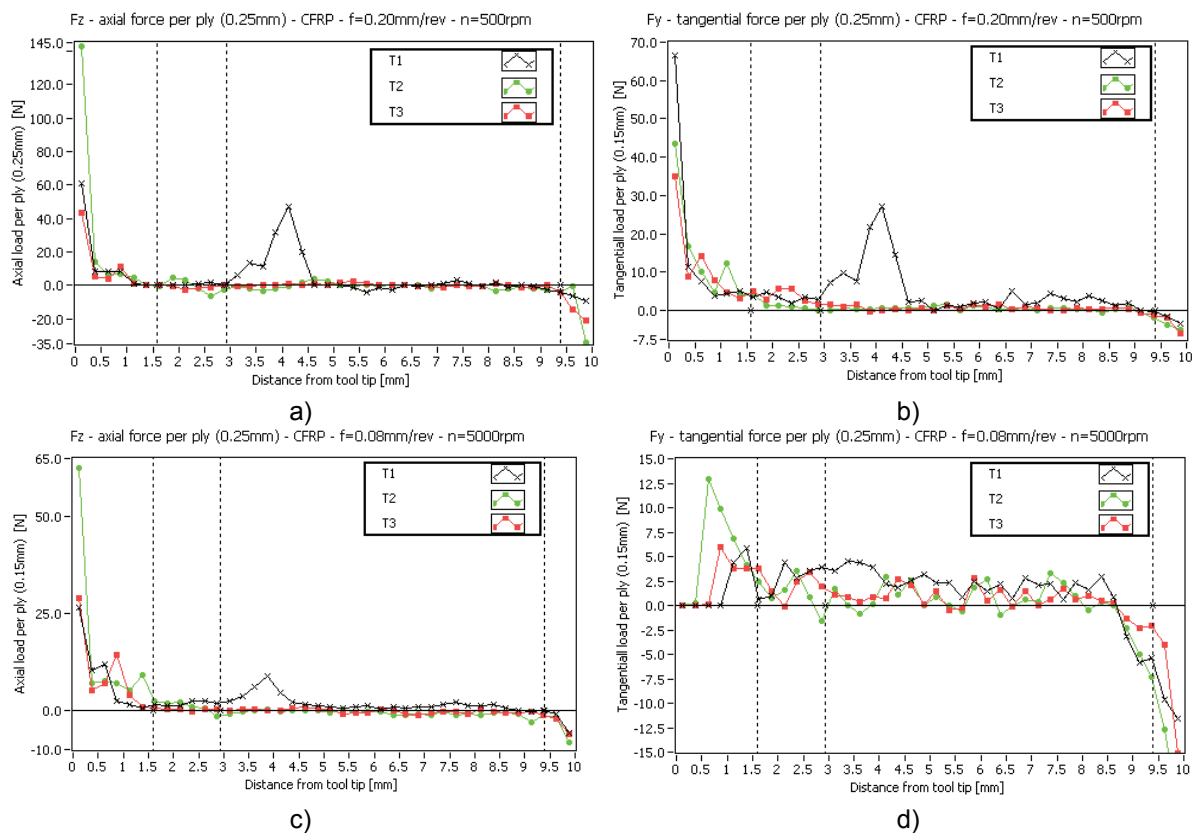


Fig. 4.12 – Axial (a,c) and tangential (b,d) load distribution on each ply for selected cutting parameters (CFRP, ply thickness 0.25mm)

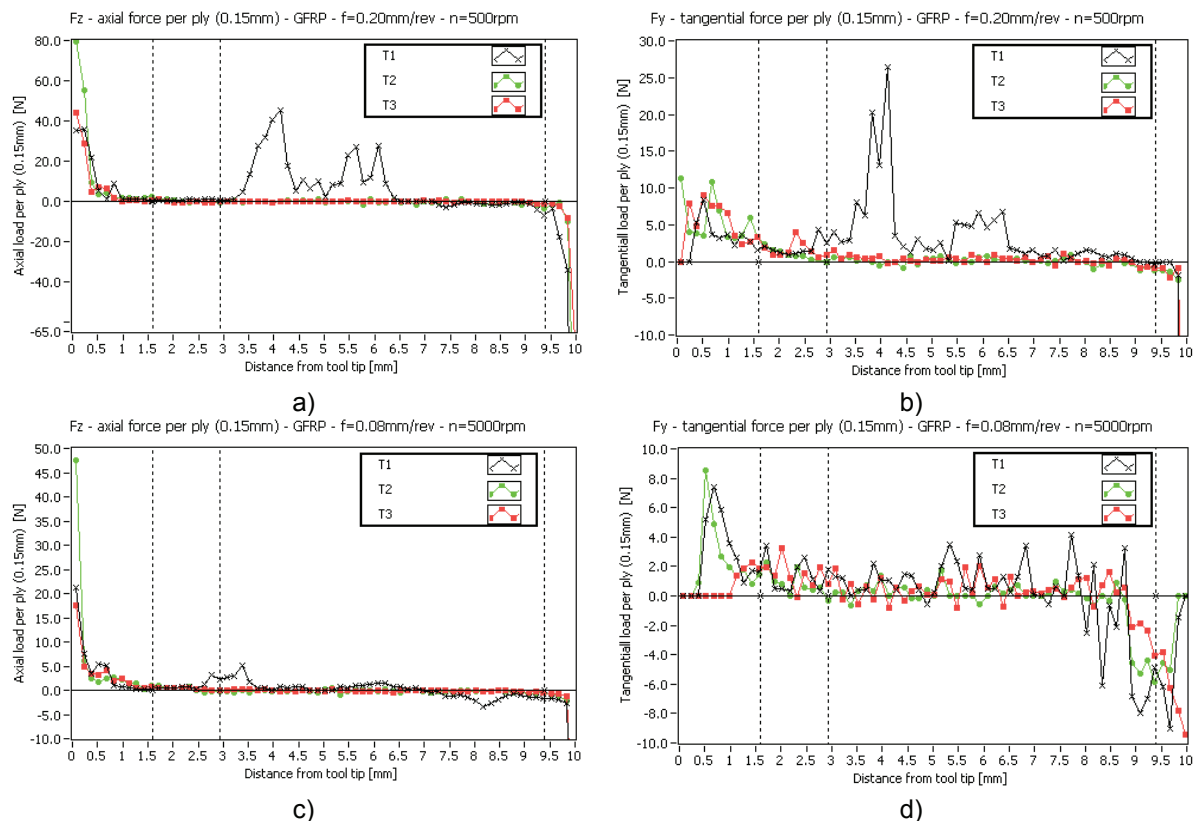


Fig. 4.13 – Axial (a,c) and tangential (b,d) load distribution on each ply for selected cutting parameters (GFRP, ply thickness 0.15mm)

This analysis allows the comparison of different drill geometries with respect to the chances of delamination. As expected we observe that on the first ply from the tool tip almost always act the highest loads. For the tapered drill reamer (T1), the loads are significant during the stage 3 as well. T2 (2-facet twist drill) generated the maximum amount of axial load per ply, while the maximum tangential load is usually greater for T1 (tapered drill reamer). T3 (8-facet twist drill) seems to be the best performer, probably due to the web-thinning feature, which will make the cutting process more efficient in the close vicinity of the chisel edge, in comparison with T2. We also observe a decrease in cutting forces just before the drills are exiting the work-piece (last 1-2 plies), which we believe to be due to the deformation of the last plies (with or without delamination actually occurring).

The graphs have been plotted for several selected experimental conditions. Overall we observe the same trends as in the previous analysis: feed rate has a strong influence on both axial and tangential loads per ply, while spindle speed has little or no influence.

Chapter 5

Model calibration and validation

5.1 Introduction

The three empirical coefficients (the specific cutting pressure on the rake face K_c and on the relief face K_p and the friction coefficient K_f) of the cutting forces in the drilling model presented in chapter 3 are to be determined experimentally, by fitting the model functions (equation 3.31 and 3.32) on the distribution of the tangential and axial elementary cutting forces obtained experimentally by a methodology presented in chapter 4.4 (sample distribution curves as in figures 4.9, 4.10 and 4.11).

It should be noted that the analytical model in chapter 3 was developed initially in Mathcad 13 software, with assistance in the geometrical derivation by 3-dimensional constructions in Catia V5. On the other side the experimental data was gathered using Labview 10 software together with the post-processing of the raw data to obtain the distribution curves. The shear amount of experimental data (time dependent curves of thrust and torque for 120 holes) and the rather complex structure of the input factors (cutting parameters, work-piece material and drill type) caused difficulties in conducting the fitting in Mathcad 13. It was found more efficient to conduct the fitting in the Labview 10 software, where there was easy access to all the raw data and post-processing parameters.

Fitting of the experimental data to calculate the empirical coefficients can be made on the cutting forces (axial and tangential) distribution or on the total values of thrust and torque. Except [2] and [3] all other cutting force models presented in literature are calibrated for the total thrust and torque. It was opted for the first method in order to give a practical significance to the cutting force distribution functions (equations 3.31 and 3.32), to allow the model to be used for drill geometry studies or delamination. This method has also the advantage to reduce the number of experimental drill cases needed to calibrate the model or to increase the number of the empirical coefficients in order to increase accuracy (see model introduced by [2]).

Therefore, the model described analytically in chapter 3, was implemented in Labview 10 as a “model function”, which allows in principle two operations: (i) starting from guess values, the model functions (equations 3.31 and 3.32) can be fitted on experimental data (distribution of the axial and tangential elementary forces) to obtain solutions for the empirical coefficients and (ii) using the solution of the empirical coefficients (or any other values) as parameters the model function can be called to provide results (axial and tangential elementary cutting force distribution for a given case of cutting parameters, work-piece material and drill type).

The model has been constructed for two drill geometries as introduced in chapter 3.5. The definition of the elementary cutting forces and their transformation from oblique to drilling coordinate system to obtain the thrust and torque are generic (independent of the drill geometry and type, summarized by equation 3.30 to 3.32), although they employ functions to define the geometrical parameters of the drill. These functions are stand-alone (for the two considered drills they are presented in chapter 3.5, while they are discussed for generic cases in chapter 3.4) and can be easily changed to account for new drill geometries. Therefore, the model can be very easily adapted for different drills of the same type with different geometrical parameters (i.e. different point angle, helix angle, diameter, web thickness etc.) by only changing various constants in the equations presented in chapter 3.5. For different drill types it is very likely that the functions defining the variation of the geometrical parameters with radius have to be re-worked or adapted accordingly, but never-the-less once these functions are determined they can be easily plugged-in the model.

The experimental data fitting procedure (obtaining solutions for the empirical coefficients) was done using the build-in Levenberg-Marquardt algorithm in Labview 10. The overall program was constructed such as to allow any number and selection of experimental test cases to be used for calculating the empirical coefficients. The fitting was done (i) on the experimentally determined distribution curves of axial and tangential forces (obtained through a methodology presented in chapter 4) or (ii) on the total thrust and torque values. For the first fitting case, in theory only one experimental case is needed to determine a set

of coefficients (introduced in detail in chapter 5.2), although if the final number of empirical coefficients employed is greater than two times the number of points on the distribution curves (as both axial and tangential elementary forces are used) the number of experimental cases used for calibration needs to be increased. However, to properly capture the variation of the forces with the axial feed rate at least two test cases with different feed rate should be considered, displaced as far as possible to cover the desired range. From our tests we have found that with 4 experimental cases covering the experimental range the solution found is almost identical with using all the experimental cases (20) for a combination of drill type and work-piece material. When fitting with the total values of thrust and torque at least two test cases are needed with different feed rates. If a more complex structure of the empirical coefficients is employed (than considered in the current PhD thesis) more than two test cases are needed (the number of test cases is half the number of empirical coefficients employed for fitting on the total values of thrust and torque). The prediction results were proved very good for the minimum number of experiments needed to obtain a solution of the empirical coefficients.

After determining the empirical coefficients, the model results are compared with the experimental obtained distribution of axial and tangential elementary cutting forces and with the total thrust and torque (which within the model are calculated by equations 3.39 and 3.40).

Summarizing, this chapter includes a detailed discussion about the empirical coefficients used in our model (chapter 5.2) while in the second part the results of the model are compared with the experimental data (in chapter 5.3) – both the elementary cutting forces distribution (axial and tangential) and the total values of thrust and torque are compared for various configurations of the empirical coefficients and different fitting strategies (distribution and total values of thrust and torque). It will be shown that using up to 4 coefficients, the model introduced in the current thesis provides reasonable predictions of both distribution and total cutting forces in drilling fiber reinforced composites. Increasing the complexity and the number of empirical coefficients slightly increases the performance of the model. Fitting on the total thrust and torque provides better results for these values, but in general the distributions of the elementary forces are not captured accordingly.

5.2 Empirical coefficients (K_c , K_f and K_p)

The cutting force model introduced in the current thesis in chapter 3, uses three empirical coefficients as follows:

Specific cutting pressure on the rake face (K_c , [N/mm²]), a common choice of empirical coefficient in cutting force modeling both for drilling and other machining operations for metals and composite materials alike. The value of this coefficient cannot be directly related to a single mechanical property of the work-piece, although using the shear angle theory of Merchant [1], models have been developed to related it to properties such as the shear and normal/compression strengths of the work-piece material. Although it is widely accepted that a similar relation should exist for composite materials, relating the specific cutting pressure to material properties (such as fracture toughness), none has been proposed so far. Using the shear angle theory, geometrical parameters (such as the rake angle) interfere in the definition of the specific cutting pressure, and it is generally accepted that, for example the rake angle has an influence on this coefficient. Therefore, even for composite materials, the specific cutting coefficient is often defined as a function including the rake angle as parameter or the cutting velocity (which is believed in fact to modify the material behavior in a similar way the temperature does). [2] even includes the depth of cut as a parameter in such a function, without any solid justification. The current thesis started with the simplest cases – constant specific cutting pressure on the rake face (K_c) and found that it provide reasonable results. Improved accuracy was also obtain by considering K_c as a function of the normal rake angle (more specifically $(1-\sin(\alpha_n))$ which is always positive). We have tested both a power law and a linear function of the above parameter and no significant difference was found between them, although in the case of metals it is often suggested that power law is better. The results using the following expressions for the specific cutting pressure on the rake face (K_c) are discussed further on:

Model	Function	Empirical coefficients
M0 – constant coefficients	$K_c = K_{c1}$	1
M1 – K_c linear function of the normal rake angle	$K_c = K_{c1} \cdot (1 - \sin(\alpha_n)) + K_{c2}$	2

Friction coefficient (K_f , [-]) is used to define the friction forces on both rake and relief faces as the proportion between the friction force on a surface and the normal force to it. As defined hereby, in metal cutting, high friction coefficients are observed (around or greater than unity, [1] and others) for models where the relief forces are ignored. When considering the forces on the relief face, the obtained value of the friction coefficient is usually smaller than the previous case, although still higher than the expected friction coefficient between work-piece and drill material. As many studies justify the difference (such as [36]) it is generally accepted that there is no equality relationship between the friction coefficient in metal cutting and as defined in classical friction laws. Therefore, some studies (i.e. [2]) prefer to define the friction force by an independent coefficient (a function of geometrical and kinematics parameters as employed for the specific cutting pressure on the rake face – K_c – in [2]). However, as there is no theoretical justification to consider different friction coefficients on rake and relief faces, we are assuming the two to be equal and constant for a work-piece/drill material combination. The only geometrical parameter which we believe it might have an influence on the friction coefficients is the curvature of the rake and relief surfaces, due to the helical nature of the rake surface for the twist drills (represented by tool T2 in our PhD thesis) and the conical nature of the relief face (although not encountered in the drills considered in the current PhD thesis). However, as this curvature exists only for a drill case among the drills considered in this study and only for the cutting lip region, we believe there is not enough variation of such a parameter to be able to capture its influence in the model at the current stage. Additionally we have conducted fitting tests assuming that the friction coefficient is a function of rake angle (a function similar to the one considered for the specific cutting pressure) without observing significant improvements. Therefore, for both models for the empirical coefficients considered hereby, the friction coefficient (K_f) was assumed constant.

The specific pressure on the relief face (K_p , [N/mm²]) is usually not employed in cutting force models in drilling as the forces acting on relief face are usually ignored. Forces on the relief face are believed to be independent on the depth of cut (or axial feed rate in drilling) and are caused by the rubbing action between the relief face and the work-piece. As the cutting edge has always a radius, a part of the uncut chip area (A_u) sweeps under the tool, rather than being cut and removed. This caused the work-piece material to be deformed elastically and plastically, causing a pressure on the contact length on the relief face. Based on an assumed cutting edge radius and a relief angle the contact length can be estimated as described in chapter 3.3. Rubenstein in [30], assumes a constant pressure and shows that for metals the value of the specific cutting pressure is less than or equal to three times the yield stress in uniaxial tension or frictionless compression. The specific pressure on the relief face (K_p) should be independent on the drill geometry, although edge radius, relief angle and the inclination angle will modify the contact area on the relief face and therefore the magnitude of the forces on the relief face. The edge radius has been assumed constant for all cutting edges, although it was suggested in some studies ([30]) that it varies with the rake angle. Although we have tried modeling the specific pressure on the relief face as a function of the normal rake angle without observing significant improvements on the accuracy of the predicted results a further study on the variation of the edge radius with the rake angle could be an improvement to the current model. Summarizing we have considered a constant specific pressure on the relief face (K_p) for all variations of the model presented here.

As discussed above, two structures of the empirical coefficients have been presented in the current thesis, the only difference between them consisting in different expression for the specific cutting pressure on the rake face (K_c – as in table 5.1). Therefore, the two variants will have 3 or 4 empirical coefficients respectively.

In addition to the empirical coefficients discussed above, the introduction of a fourth one was suggested to relate the chip flow angle (η_c) to the inclination angle. As there is uncertainty as to the chip flow direction in composite cutting it can be modeled as in the case of metals where chips are connected and continuous, such a solution seemed natural. However, upon implementation of such a coefficient we found that the model converges at rather arbitrary value of this coefficient and significantly different even for similar drilling cases. In addition the model results were only improved by small margins (as naturally happening when introducing a new degree of freedom). Therefore, although we note a need of clarification in this direction, we have opted to not include such coefficient in the current model.

The modeling of the cutting forces and the choice of empirical coefficients in our model follows a practical approach, considering rather the effects than the driving factors (i.e. a damage model, like the shear angle theory developed by Merchant in [1] for metals). Models like the current one are usually referred to as “mechanistic” ([3]). A theoretical model to account for the work-piece damage in the case of fiber-reinforced materials would obviously enrich our understanding of the cutting process and should prove more accurate. There might be however needed (and possible) to formulate or to directly develop such model in the current framework; for example determining the friction coefficient could allow the calculation of the heat generated through friction (which is believed to be the only source of heat in the machining process of fiber-reinforced composites, as fracture process does not normally generate such).

In the following table (5.2) the result of a literature survey it is introduced on other solutions employed by researchers to express the elementary cutting forces and the configuration and number of their empirical coefficients. The list is not exhaustive and is focused mostly for models applied to drilling and/or generic orthogonal/oblique cutting models developed for fiber reinforced composites using a “mechanistic” approach. Additionally, should be noted a model introduced by Watson in [31], [35], [49], [50] and [51] which covers a particular drill geometry (a type of 2-facet twist drill) in extensive detail but uses shear angle theory, therefore only applicable to metals.

It can be observed that most models for drilling consider a simplified geometry by employing orthogonal cutting ([3] and [4]). Seldom is the direction of the elementary forces defined directly along the tangential and axial directions ([3], [4] and [5]) as opposed to our model and [2] where the elementary cutting forces are defined normal and tangent to the rake face. Additionally, none of these models consider the forces

acting on the relief face. The model introduced by [2] seems by far the most realistic and complex. However, their empirical coefficients are defined as functions of 3 factors: normal rake angle (α_n), magnitude of the tangential velocity (V_t) and depth of cut (t_c). Although the first two can be justified by arguments introduced previously in the description of the coefficients, the later one is very questionable. Further on, this model uses different definition of the elemental forces for the chisel edge region of the drill, increasing the number of coefficients to 12. We also note that the cutting angle (μ) is ignored by all models along the cutting lips. As this angle is a function of feed rate (f , see equation 3.53), we believe that considering its influence in the cutting model, would make unnecessary the use of depth of cut (t_c) factor. Only [3] is a mechanistic model for drilling applied to composite materials and the results of our model will be compared with theirs in the next chapter.

Table 5.2 - State of art in the definition of elementary cutting forces

Ref.	Equations for elemental cutting forces	No. of empirical coeff.	Notes
[4]	$F_Z(\alpha_s, t_c) = B \cdot 10^{-a\alpha} t_c^{0.5} \quad ([4]\text{-eq.4a})$ $F_Y(\alpha_s, t_c) = A + B \cdot 10^{-b\alpha} t_c \quad ([4]\text{-eq.4b})$	4	Drilling model based on orthogonal cutting model; 4 empirical coefficients: A, B, a, b; a constrained to be equal to b; the power of t_c constrained to 0.5 and 1 respectively
[3]	$F_Z = A_u \cdot K_n(\rho) = A_u \cdot C_1 \rho^a \quad ([3]\text{-eq.3a})$ $F_Y = A_u \cdot K_t(\rho) = A_u \cdot C_2 \rho^b \quad ([3]\text{-eq.3b})$	4	Based on orthogonal cutting model; 4 empirical coefficients: C_1, C_2, a, b ; uses normalized radial coordinate (ρ)
[33]	$F_Z(\alpha, t_c) = C \cdot 10^{a\alpha} \gamma^b (t_c + D) + E \quad ([33]\text{-eq.10})$ $F_Y(\alpha, t_c) = A + B \cdot 10^{-c\alpha} t_c \quad ([33]\text{-eq.7})$	8	Orthogonal cutting model for unidirectional composites; 8 empirical coefficients: A, B, C, D, E, a, b, c
[5]	$F_Z(t_c, i, \alpha, V_t) = c_0 + c_1 t_c + c_2 t_c i + c_3 \alpha \cdot i + c_4 V_t + c_5 V_t^2 + c_6 t_c \alpha, \text{ for } \alpha < 5^\circ \quad ([5]\text{-eq.22})$ $F_Z(t_c, V_t) = d_0 + d_1 t_c + d_2 V_t, \text{ for } \alpha > 5^\circ \quad ([5]\text{-eq.23})$ $F_Y(t_c, \alpha, V_t, CL) = a_0 + a_1 t_c + a_2 \alpha + a_3 V_t CL + a_4 \alpha^2 + a_5 \alpha \cdot V_t \quad ([5]\text{-eq.20})$ $F_X(\alpha, i) = b_0 + b_1 \alpha \cdot i + b_2 i \quad ([5]\text{-eq.21})$	19	Drilling model based on oblique cutting model; 19 empirical coefficients: a_i, b_i, c_i, d_i (19); CL is a parameter for coolant (1 for flood coolant, 0 for no coolant); V_t is the tangential component of cutting speed
[2]	$F_c = K_n \cdot A_c \quad ([2]\text{-eq.3-17})$ $F_f = K_f \cdot A_c \quad ([2]\text{-eq.3-17})$ $\ln[K_n(t_c, V_t, \alpha_n)] = a_0 + a_1 \ln t_c + a_2 \ln V_t + a_3 \ln(1 - \sin \alpha_n) + a_4 \ln t_c \ln V_t \quad ([2]\text{-eq.3-15})$ $\ln[K_f(t_c, V_t, \alpha_n)] = b_0 + b_1 \ln t_c + b_2 \ln V_t + b_3 \ln(1 - \sin \alpha_n) + b_4 \ln t_c \ln V_t \quad ([2]\text{-eq.3-16})$	12	Similar model for drilling based on oblique cutting model (F_c – force normal to rake face; F_f – friction force along the direction of measurement of normal rake angle – α_n – see section 3.4.6); 10 empirical coefficients: a_{0-4}, b_{0-4} + 2 more empirical coefficients for the forces defined separately along the chisel edge area.

In the initial stage, our model is calibrated and compared with axial and tangential radial distribution curves obtained from experiments through a methodology introduced in chapter 4 and published in [15]. Most cutting force models are calibrated on the total thrust and torque forces with the exception of [2] and [3] which uses the partial distribution along the cutting lips only. However, they do not present and compare the results of their model in comparison with the experimental distribution used for calibration. Obtaining reasonable distribution functions is much more complex than obtaining reliable results for the total thrust and torque. By fitting our model on both distribution and total values of thrust and torque, we will show that very accurate results can be obtained for the total values of thrust and torque if the model is fitted on these totals. However, reasonable distribution of the elementary axial and tangential cutting forces can only be obtained if fitting is conducted on the experimentally obtained distribution rather than using the total thrust and torque values. The disadvantage of this fitting strategy would be that both the distribution and total values of thrust and torque only reasonably agree with the experimental data.

As detailed in chapter 4, the experiments were carried out using three different drills (although for modeling purposes only two are used and described geometrically in chapter 3.5) on two different work-pieces (carbon and glass-fiber reinforced composites). Axial feed rate (f – [mm/rev]) and spindle speed (n – [rpm]) were varied on four and five levels respectively within practical ranges. The experimental setup and planning are extensively discussed in chapters 4.2 and 4.3 respectively.

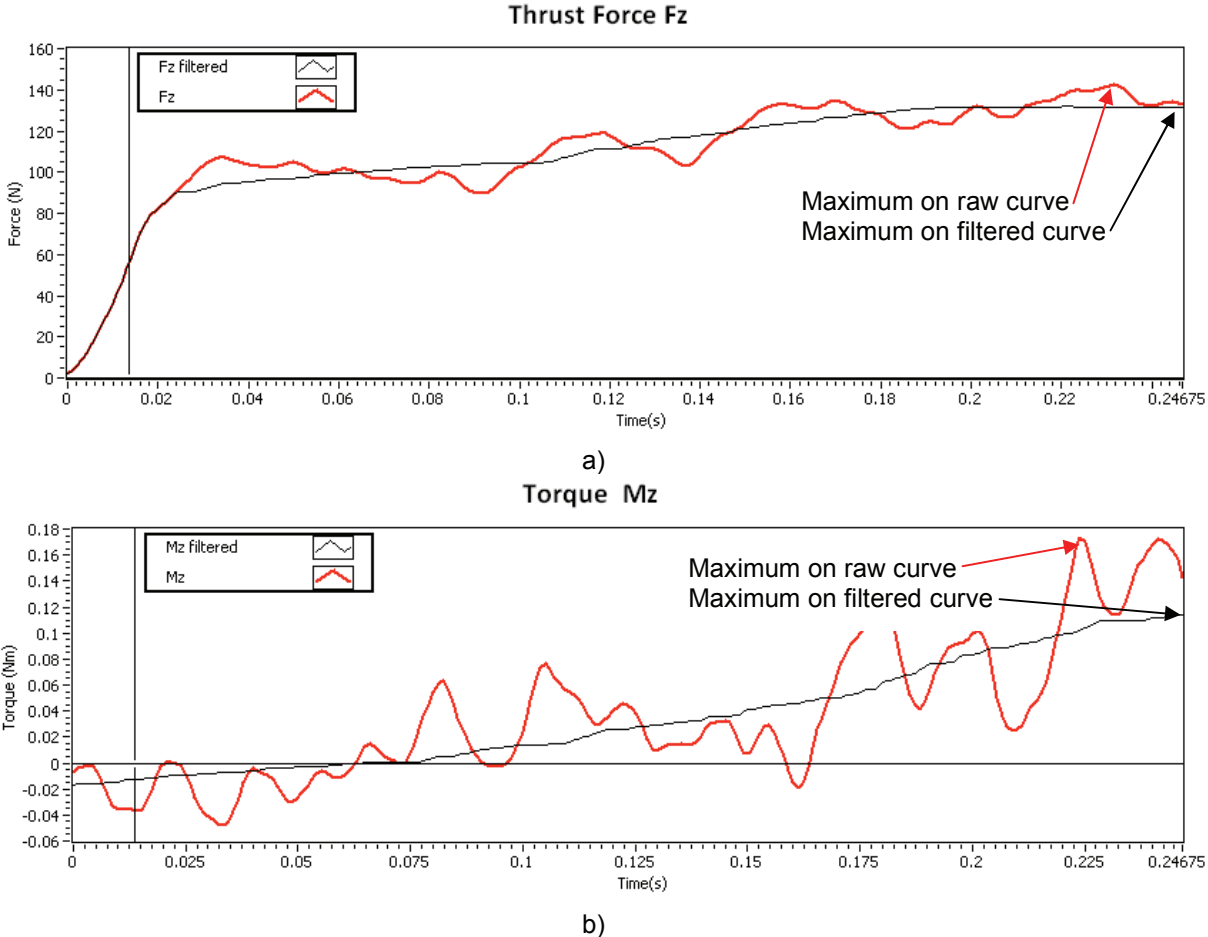


Fig. 5.1 – Sample cutting force measurement during drilling (CFRP, 2-facet twist drill (T2), $n=2750\text{rpm}$, $f=0.14\text{mm/rev}$) – a) thrust; b) torque

Figure 4.8 presents a typical thrust and torque curved in its raw and untrimmed form. Figure 5.1 above presents another example of thrust and torque curve obtained during drilling experiments in its raw form

and smoothed for obtaining the distribution which is trimmed from entry point to full engagement of the cutting edges. This later case-study is a more difficult scenario for post-processing of the experimental data, and we introduce it to illustrate a few encountered problems. The cursor indicates the point where the cutting lips start to become engaged in cutting. The filtered curve is used to calibrate the model as well as for comparison with the model results. The maxima on the filtered (nominal) curves are always smaller than on the raw curves and we find that the difference increases with the spindle speed. The difference is always larger for torque.

Furthermore, figure 5.2 shows the influence of the cutting parameters over the maximum thrust and torque recorded on the raw and filtered curves for drilling CFRP with T2 (2-facet twist drill). Similar results are observed for the rest of the work-piece/drill combinations.

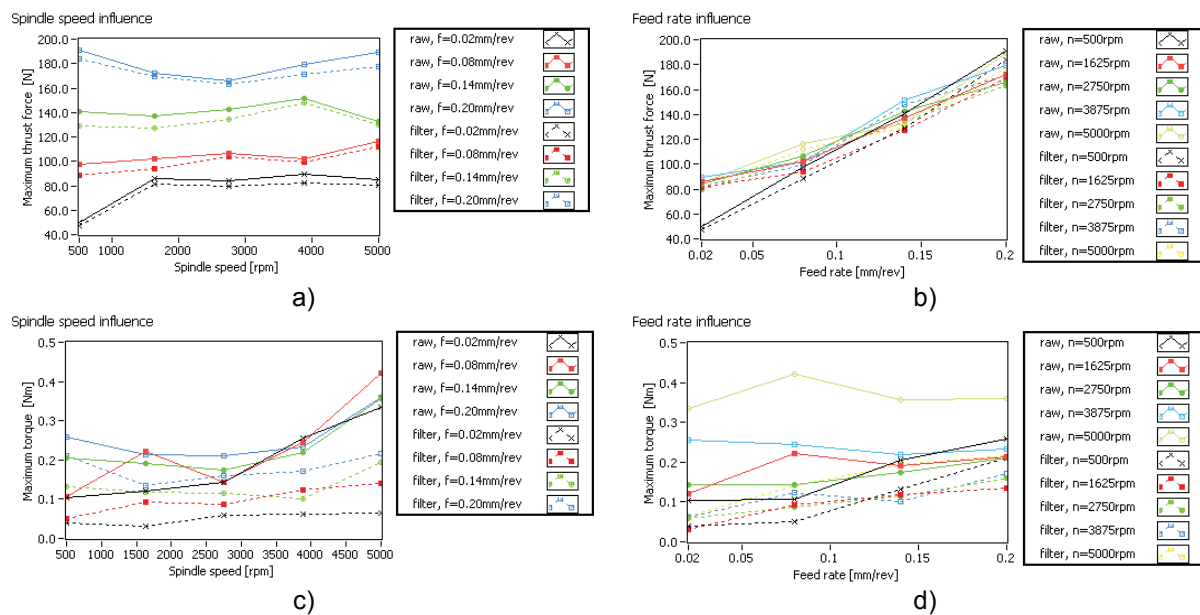


Fig. 5.2 – Influence of spindle speed and axial feed on maximum thrust (a,b) and torque (c,d) respectively for raw data and filtered curves (CFRP, 2-facet twist drill (T2))

It becomes clearer that the maximum forces recorded on filtered curves are always smaller than on the raw data, and this effect is more pronounced for torque. Furthermore, axial feed rate seems to have a clear linear influence on both thrust and torque (visible better on the filtered data), while spindle speed has a limited influence on thrust and torque (filtered data). When visible, the influence of the spindle speed is not consistent; different trends noted when changing the drill type or the work-piece material.

The cutting force model introduced in chapter 3 (summarized by equations 3.31 and 3.32) is almost a linear function of the feed rate with no parameter accounting for the spindle speed. In theory, the coefficients can be defined as functions of local velocity (in additions to others as discussed previously in this chapter) and therefore account for the influence of spindle speed. The local velocity (which can be expressed by eq. 3.52) varies linearly with the radius as well, from almost zero on the drill axis to its maximum on the outermost point on the cutting edge. However, as seen from figure 5.2 above and figures 4.9 to 4.11 in chapter 4 it was found that the local velocity influences only slightly the filtered forces used to calculate the distribution and the distribution themselves at least for the experimental domain considered hereby. If such an influence exists we believe that the experimental domain of cutting velocities needs to be further extended to capture it properly. Therefore, we have opted to not include the local velocity as a parameter in the functions of empirical coefficients. This decision has been supported by testing such models without obtaining significant improvement in the model's prediction capabilities.

As a suggestion, the influence of the spindle speed (especially on the maximum recorded values of torque in the raw measurement data) could be successfully modeled by a correction coefficient defined as a function of the spindle speed, which is however beyond the scope of the current study.

The forces on the relief face are independent of the axial feed rate (f) and represent the intercept (at $f=0$, corresponding to the theoretical case where the drill is only rotating rather than advancing axially as well) of the thrust and torque, as in figures 5.2b and 5.2d. For the thrust in the case-study considered above, the intercept is about 60 to 80N (ignoring the case of $n=500\text{rpm}$, where the intercept appears to be negative, which obviously indicate a measurement error), which is about 40% from the maximum thrust recorded at $f=0.2\text{mm/rev}$ (corresponding to an approximate depth of cut of 0.10mm). This value is rather high in comparison with metal drilling ([37] and others) where about 20% is expected for similar conditions. This fact leads us to believe that the forces on the relief face cannot be ignored and therefore they were not assumed to be zero, as in many of the cutting force models dedicated to metals and previous models for composites. As will be shown later, we believe that considering the forces acting on the relief face is the critical aspect that improved the results of the current model in comparison with previous mechanistic models applied to composite materials.

5.3 Model results and discussion

As outlined in the previous sub-chapter, we have tested a large number of expressions for the empirical coefficients (K_c , K_f and K_p) from constant coefficients to more complex functions of various parameters believed to have an influence on the cutting process. However, only the most representative cases have been selected to be introduced here and discussed.

In addition to various functions for the empirical coefficients we have also tested two different fitting strategies: (i) on the experimentally obtained distribution curves of axial and tangential elementary forces along the drill radius and (ii) on total values of thrust and torque for each experimental case.

The number and selection of experimental cases used to calibrate the model (calculate the coefficients) has also been varied. For the case of fitting on the distribution curves, in theory only one experiment is sufficient to determine a set of coefficients (statement valid for up to 12 unknowns in the functions of empirical coefficients). However, for usable data, at least two experimental cases with varying feed rate are required to capture the influence of the feed rate. As the distribution is calculated based on the derivative of the thrust and torque curves its variation interval is larger, therefore we recommend to use 4 experimental cases. From any other number of experimental cases used for calibration from 4 to 20, the variation of the solution is minor, although experimental cases where obvious errors in the distribution curves are observed should be avoided. For the case of fitting on the total values of thrust and torque a minimum of 2 experimental cases are required, but the results proved suitable for even this minimum requirement if the cases are considering with varying feed rate.

The empirical coefficients are determined individually for each of the 4 work-piece/drill combinations. They are calculated in Labview (using the Levenberg-Marquardt algorithm) to fit either the axial and tangential distribution curves or the total thrust and torque values for all 20 drilling cases (see table 4.4) for a work-piece/drill combination. We have opted for discussing the results obtained for all drilling cases in order to avoid the small variations obtained by using a smaller number and various selections of experimental cases.

Table 5.3 centralizes the solutions found for the empirical coefficients for the two variations of the empirical coefficients expressions as well as two different fitting strategies for each work-piece/drill combinations.

Table 5.3 – Obtained empirical coefficients

	Fitting on axial and tangential distribution		Fitting on total thrust and torque values	
	M0 – constant coefficients			
	CFRP	GFRP	CFRP	GFRP
T1	$K_c=330.06$ [N/mm ²] $K_f=0.560767$ [-] $K_p=2938.45$ [N/mm ²]	$K_c=325.75$ [N/mm ²] $K_f=0.503423$ [-] $K_p=3758.62$ [N/mm ²]	$K_c=778.65$ [N/mm ²] $K_f=0.586807$ [-] $K_p=1830.35$ [N/mm ²]	$K_c=851.57$ [N/mm ²] $K_f=1.00824$ [-] $K_p=581.57$ [N/mm ²]
T2	$K_c=279.72$ [N/mm ²] $K_f=0.278023$ [-] $K_p=4714.25$ [N/mm ²]	$K_c=327.33$ [N/mm ²] $K_f=0.167523$ [-] $K_p=4114.95$ [N/mm ²]	$K_c=163.71$ [N/mm ²] $K_f=0.62640$ [-] $K_p=3824.54$ [N/mm ²]	$K_c=143.07$ [N/mm ²] $K_f=2.15938$ [-] $K_p=443.24$ [N/mm ²]
	M1 – K_c linear function of the sinus of the normal rake angle ($K_c=K_{c1}*(1-\sin(\alpha_n))+K_{c2}$)			
	CFRP	GFRP	CFRP	GFRP
T1	$K_{c1}=406.43$ [N/mm ²] $K_{c2}=-146.34$ [N/mm ²] $K_f=0.586435$ [-] $K_p=2779.56$ [N/mm ²]	$K_{c1}=341.62$ [N/mm ²] $K_{c2}=-71.91$ [N/mm ²] $K_f=0.520918$ [-] $K_p=3562.94$ [N/mm ²]	$K_{c1}=-454.92$ [N/mm ²] $K_{c2}=1262.58$ [N/mm ²] $K_f=0.580706$ [-] $K_p=1909.99$ [N/mm ²]	$K_{c1}=-1211.98$ [N/mm ²] $K_{c2}=2121.28$ [N/mm ²] $K_f=1.11683$ [-] $K_p=520.48$ [N/mm ²]
T2	$K_{c1}=435.26$ [N/mm ²] $K_{c2}=-293.81$ [N/mm ²] $K_f=0.750408$ [-] $K_p=2810.35$ [N/mm ²]	$K_{c1}=499.97$ [N/mm ²] $K_{c2}=-298.63$ [N/mm ²] $K_f=0.600504$ [-] $K_p=1694.71$ [N/mm ²]	$K_{c1}=399.29$ [N/mm ²] $K_{c2}=-145.77$ [N/mm ²] $K_f=0.77615$ [-] $K_p=2269.78$ [N/mm ²]	$K_{c1}=84.26$ [N/mm ²] $K_{c2}=96.58$ [N/mm ²] $K_f=1.62644$ [-] $K_p=587.26$ [N/mm ²]

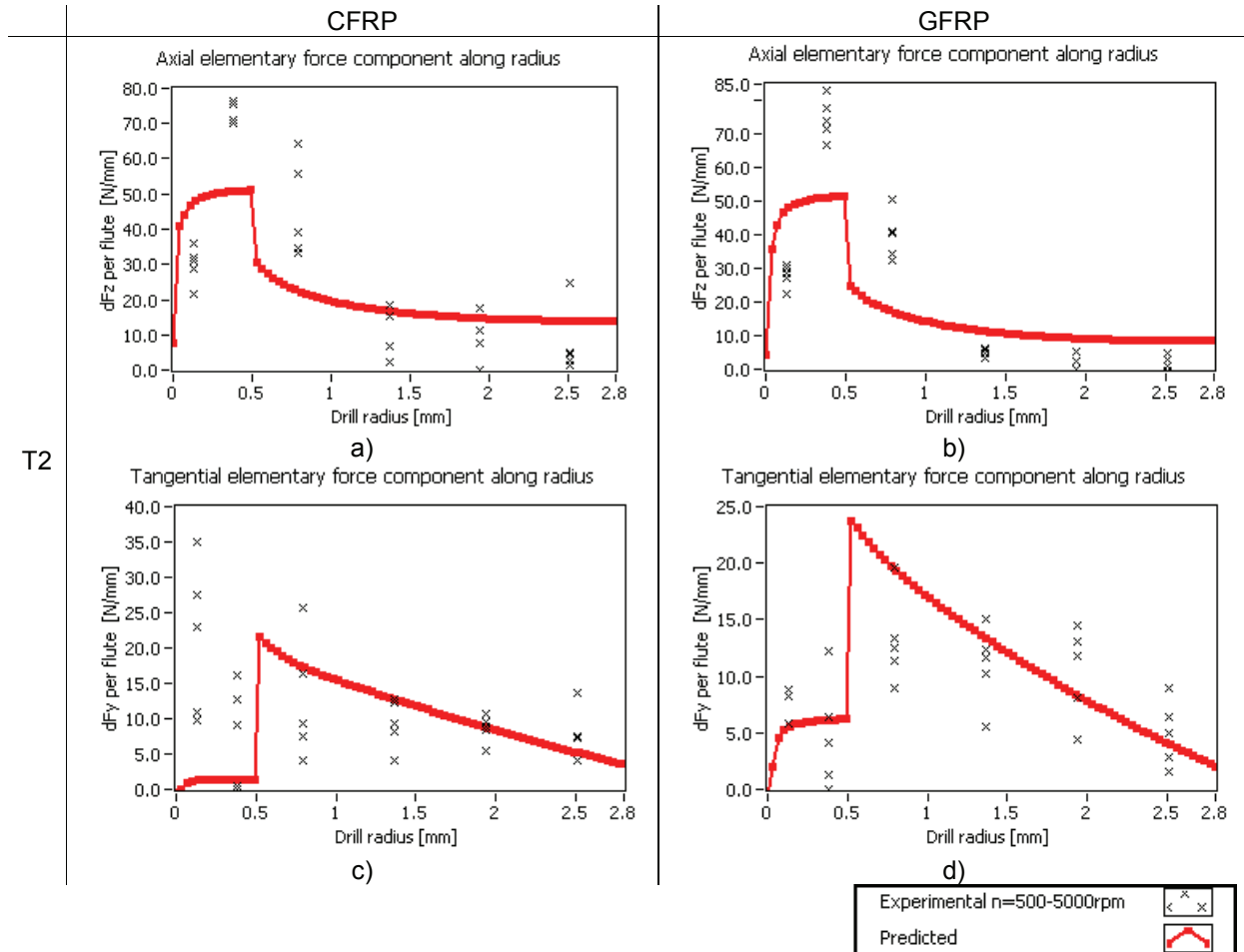
A preliminary observation best noticed on the constant coefficients model (M0) is that the values of the coefficients vary with both the drill type and the combination of work-piece/drill material. Considering that the material of the drills is of similar type (solid-carbide steels for both cases although from two different suppliers – see chapter 4.2), the desire was to obtain a set of coefficients valid for a certain work-piece/drill material combination for any drill geometry (i.e. this objective was not achieved since the values of the coefficients vary significantly with the drill type). An argument to justify the current results is that the machinability of the two work-piece materials proved to be comparable. The average maximum thrust for all tested conditions was only 3% higher for CFRP than GFRP, while the average maximum torque was 20% higher for GFRP, and probably due to increased vibrations noted during drilling of GFRP material (for further discussion see chapter 4.5). Therefore, we can conclude that there are still aspects of the influence of the geometrical and cutting parameters that are not fully understood and modeled before obtaining empirical coefficients depending only on the work-piece/drill material combination.

It can also be observed that there are significant differences in the solutions obtained for fitting on the distribution and total values of thrust and torque. Fitting on the total thrust and torque values attempts to calculate the best coefficients so that the integral of the distribution curves (eq. 3.39 and 3.40) matches the maxima of the thrust and torque (fig. 5.1), while fitting on the distribution attempts to match the discrete points on the radial coordinate of the axial and tangential elementary cutting forces calculated as described in chapter 4.4. A perfect fitting on the distribution curves would theoretically result in perfect results of the total thrust and torque values, while a perfect fitting on the total forces would not necessarily result in suitable distribution curves. When fitting on the distribution curves each point has the same importance although when integrating (according to eq. 3.39 and 3.40) different points (regions) will have different impact on the total thrust and torque, depending on the size of the region (dr), number of flutes (N) and most importantly for the tangential force the radial coordinate (r). Therefore, errors in predicting the distribution at various points will have different impact on the total forces, i.e. an error in predicting the tangential elementary cutting force component at small radius will have almost zero impact on the total force while an error at the outer radius will have a maximum impact. Summarizing, fitting on the distribution allows us to obtain relevant distribution curves of the elementary cutting forces while it is expected the total thrust and torque values to be less accurate. In the same time when fitting on the total thrust and torque values, the maximum forces can be estimated accurately while the distribution are not necessary relevant.

Additionally, we observe that for the M1 model and drill T1 when fitting on the total thrust and torque values we obtain negative K_{c1} values, which can be translated by the fact that the specific cutting pressure on rake face is inversely proportional to the sinus of the normal rake angle, contrary to the result for the rest of the cases. In the same time we note the large values for K_{c2} (the constant), which means that the influence of the rake angle is significantly less than for T2 drill (same model and fitting strategy). When analyzing fig. 3.26 (normal rake angle variation of both drills with the radius) we note that for the most part of the radial domain the normal rake angle for drill T1 remains mostly constant, with significant changes only for the small region of the chisel edge and in its close vicinity. As will be discussed later, the variation of the normal rake angle for this drill cannot explain the raise in cutting forces noted in stages 3 and 4. As the total thrust is affected more by the elementary forces in this larger region (in comparison with the small chisel edge) and even more the torque (as the points are closer to the outer radius), the fitting algorithm probably finds that the current values offer a better solution overall. When fitting on the distribution curves, we observe that K_{c1} and K_{c2} align with our expectation, although, as it will be later shown, the total values of thrust and torque are not predicted accurately. As it will be discussed later, we believe that there are some geometrical effects for this type of drill (T1) that our model currently is unable to capture.

We start by analyzing the results obtained for the 2-facet twist drill, which is extensively studied in the literature and although full distribution curves either experimental or predicted were not published there is a general knowledge about the proportion of the forces caused by the chisel edge and the cutting lips respectively from experimental drilling using pilot holes. When comparing the distributions, as expected, only the solutions found for fitting on the experimental distribution have significance, and although reasonable for the model with constant coefficients (M0), the best results were obtained using the specific

cutting pressure coefficient (K_c) as a linear function of sinus of the normal rake angle (M1). Figure 5.3 shows a representative case scenario of the cutting parameters ($f=0.14\text{mm/rev}$, $n=500$ to 5000rpm) for the 2-facet twist drill (T2) for both carbon- and glass-fiber reinforced composites.



T2

Fig. 5.3 – Comparison between predicted (M1 model, fitted on the distribution curves) and experimental elementary cutting force components distribution along the radius for $f=0.14\text{mm/rev}$, 2-facet twist drill and both work-piece materials

Although not perfect, the predicted curves manage to capture fairly well the variation of the cutting forces along the radius for this type of drill. The predicted axial elementary force component around the chisel edge ($r=0.5\text{mm}$) of the drill seems to be always lower than the experimental results would indicate. In theory, it could result that using a power law of the normal rake angle (its variation presented in fig. 3.24) could capture this effect better. However, from our trials, such a function will cause the model to converge at rather extreme values of the coefficients, resulting in a peak axial force around $r=0.5\text{mm}$ (much higher than predicted by experiments) and negative towards the outer radius ($r=2.8\text{mm}$). Additionally, we observe that the tangential force component is in general closer to the upper bounds of the experimental values in the same region ($r=0.5\text{mm}$) and using a power law will cause the overestimation of this force component in this region as well. Additionally, it should be noted that for all distribution curves, the interval of variation of a point is rather large (as they are calculated as the derivative of the thrust and torque entry curves) even for identical drilling cases. In the above figure and later on, we have used 5 drilling cases with varying spindle speed to illustrate the variation interval. Furthermore, in general the variation interval is greater for the experimentally obtained tangential force especially in the close vicinity of the drill axis (chisel edge region) due to reasons discussed in chapter 4.5.

Previous experimental studies [3] with pilot holes estimate that a percentage usually between 40 to 60% of the total thrust force is generated by the chisel edge region for uni-directional carbon fiber reinforced composite and various twist drills. Although it is difficult to make an exact comparison as the drill geometry and work-piece materials vary, our predicted results for T2 drill are that roughly 45% of the total force is generated by the chisel edge for the glass-fiber reinforced material while 35% for the carbon-fiber reinforced composite respectively which correspond well with our experimental data. When compared with standard twist drills (as the ones employed in [3]), our 2-facet twist drill (T2) has the chisel edge inclined with the drill axis which should decrease slightly the loads in this region. It is also noted that the previous mechanistic models for both metals and composites, in order to predict such variations, usually employ 2 different sets of coefficients for chisel edge area and cutting lip region respectively and even 2 different force models ([2], [3] etc.). Through the current results we have shown that, at least for composite materials it is not necessary to use two different sets of coefficients for the two cutting regions.

It is also interesting to present how our model captures the changes in the distribution with increasing the feed rate, one of the most useful features of mechanistic cutting force models. Therefore, figure 5.4 presents the predicted and experimental results for the axial elementary force component distribution (T2 drill, glass-fiber reinforced composites and with coefficients determined by fitting the experimental distribution – see table 5.3) for drilling cases with varying feed rate ($f=0.14\text{mm/rev}$ and $f=0.20\text{mm/rev}$).

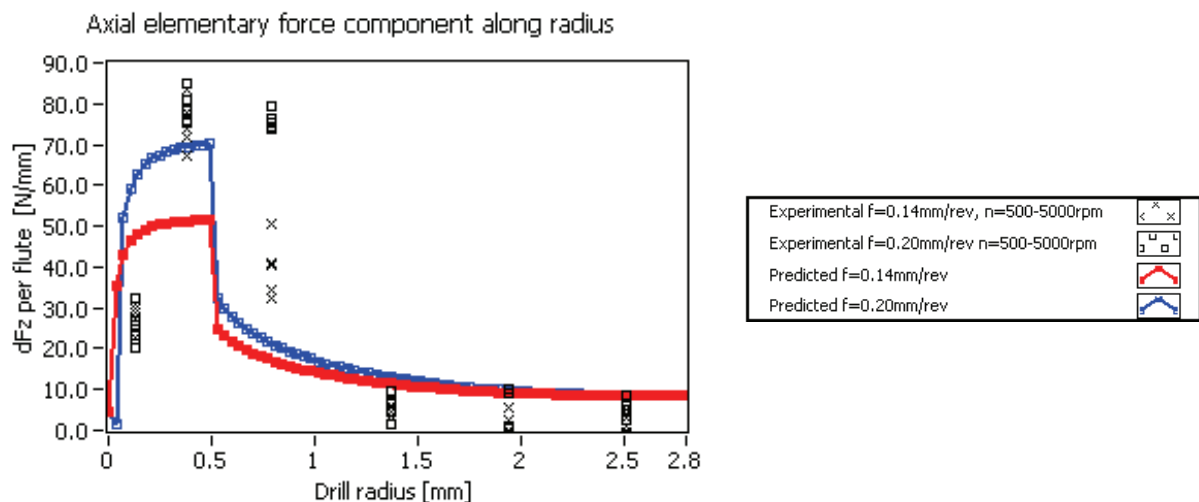


Fig. 5.4 – Comparison between experimental and predicted results for axial elementary cutting force component distribution along the radius for $f=0.14$ and 0.20mm/rev (T2/CFRP)

It can be observed that with increasing feed rate the distribution of the axial elementary cutting force (valid for the other components as well) does not increase uniformly along the radius. The experimental results indicate an increase of the forces in the chisel edge area, but more pronounced in the vicinity of the chisel edge on the cutting lips. Our model captures better the increase on the chisel edge area than in its vicinity, an effect which can be improved by considering a power law for the specific cutting pressure on the rake face (K_c), aspect discussed previously. From the results published in [3] for uni-directional composite materials we can observe that the proportion of the forces caused by the chisel edge changes with the feed rate, although from the small number of experiments reported it is difficult to establish a clear trend. Our overall experimental results detailed in chapter 4.5 show that there is more rapid increase of the forces on the chisel edge with increasing feed rate than overall. However, the area in the close vicinity of the chisel edge experiences a more dramatic increase, while for the remaining cutting lip, the increase is minimal or none-existing.

From figure 5.4 we can also observe the important role of not neglecting the cutting angle along the cutting lips region. If the cutting angle was to be assumed zero along the cutting lips (as in all the previous cutting force models), a constant offset would have been observed between the two distribution curves (corresponding to the two cases with varying axial feed) along the cutting lips. If the cutting angle, the

only difference between the two cases would be the uncut chip area, while all the angles affecting the cutting forces and their decomposition would have been identical. As the experimental data shows clearly that increasing the axial feed will cause an increase of the elementary forces more pronounced at the side of the cutting lips bordering the chisel edge, while almost no increase for the rest of the cutting lip; we can therefore state that such a variation could only be accounted for by considering the cutting angle (μ) in this region, and its effect on all angles involved in forces definitions and decomposition.

Next, in figure 5.5 we present the results obtained for the total thrust and torque for the 2-facet twist drill (T2) with the coefficients (structured according to M1) obtained by fitting the distribution curves (see table 5.3). To calculate these values the predicted distribution curves (as in fig. 5.3) have been integrated according to equations 3.39 and 3.40.

The thrust (fig. 5.5a and 5.5b) seems to be predicted accurately although the largest error is noted always at the maximum feed rate ($f=0.20\text{mm/rev}$), which can be explained by the arguments discussed previously. The predicted results for torque (fig. 5.5c and 5.5d) tend to underestimate the experimental values especially at higher axial feeds.

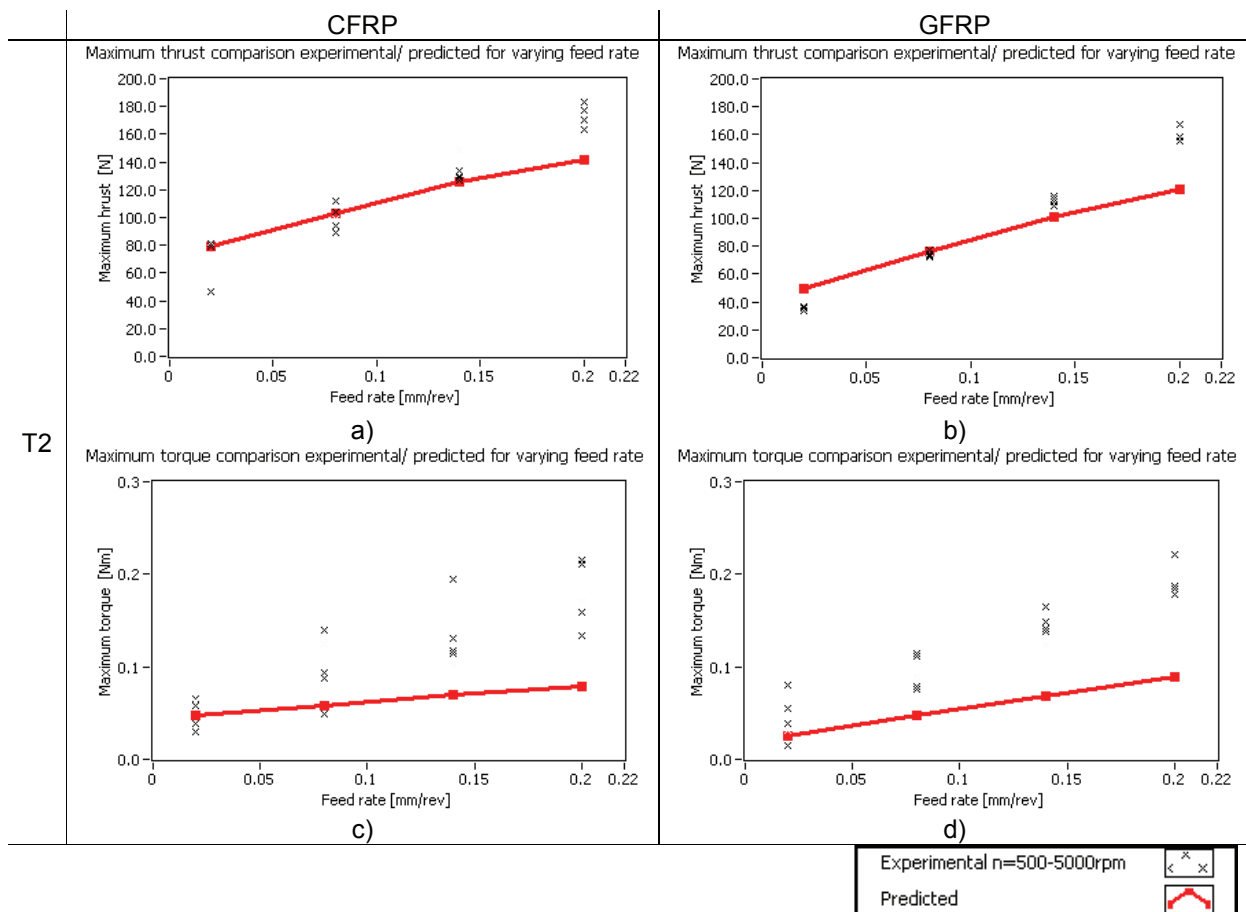


Fig. 5.5 – Comparison between predicted and experimental (filtered) results for maximum thrust and torque for varying axial feed, T2 and both work-piece materials, M1 fitted on the experimental distributions

The prediction capabilities of our model for the total thrust and torque values can be greatly improved by using the coefficients obtained by fitting on the total values of the forces rather than their distributions. For the same combination of work-piece/drill as before and using the alternative set of coefficients as in table 5.3, these results are presented in figure 5.6.

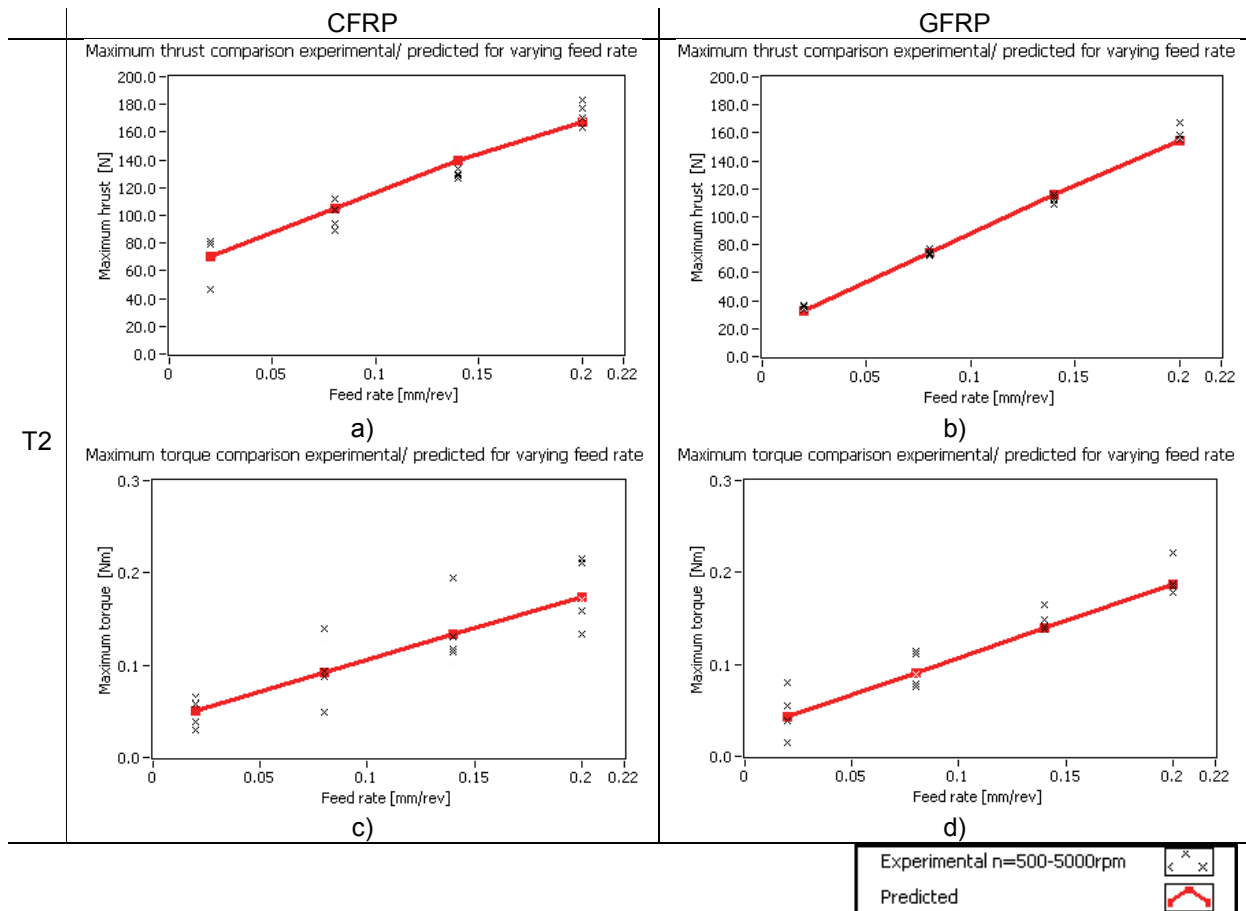


Fig. 5.6 – Comparison between predicted and experimental (filtered) results for maximum thrust and torque for varying axial feed, T2 and both work-piece materials, M1 fitted on the total forces values

We can compare the prediction capabilities of our model with the model introduced in [3], developed for standard twist drills drilling uni-directional carbon-fiber reinforced composites as in figure 5.7. The magnitude of the forces reported in [3] is significantly greater than our values mainly due to the difference in drill diameters (5.6mm in our case while 15.9 and 12.7mm respectively for [3]). It can be observed that the [3] model greatly underestimate their experimental results for composite materials. In [3] and [2] the same model is applied to metals with better performance. We believe that the main reason for their poor performance for composite materials while the model performs well for metals is due to the assumption that the forces on the relief face are ignored in both cases. If the forces on the relief face would have been ignored, the line uniting our predicted results (in fig. 5.7) would have been forced to pass through the origins (thrust equal zero when axial feed is zero). If the slope of the line would have been maintained, we would have been obtaining values about 50% of the experiments, similar to their model results. In chapter 5.2 the difference between the two models is discussed more widely and arguments are presented to justify why the forces on the relief face cannot be ignored in the case of composite materials.

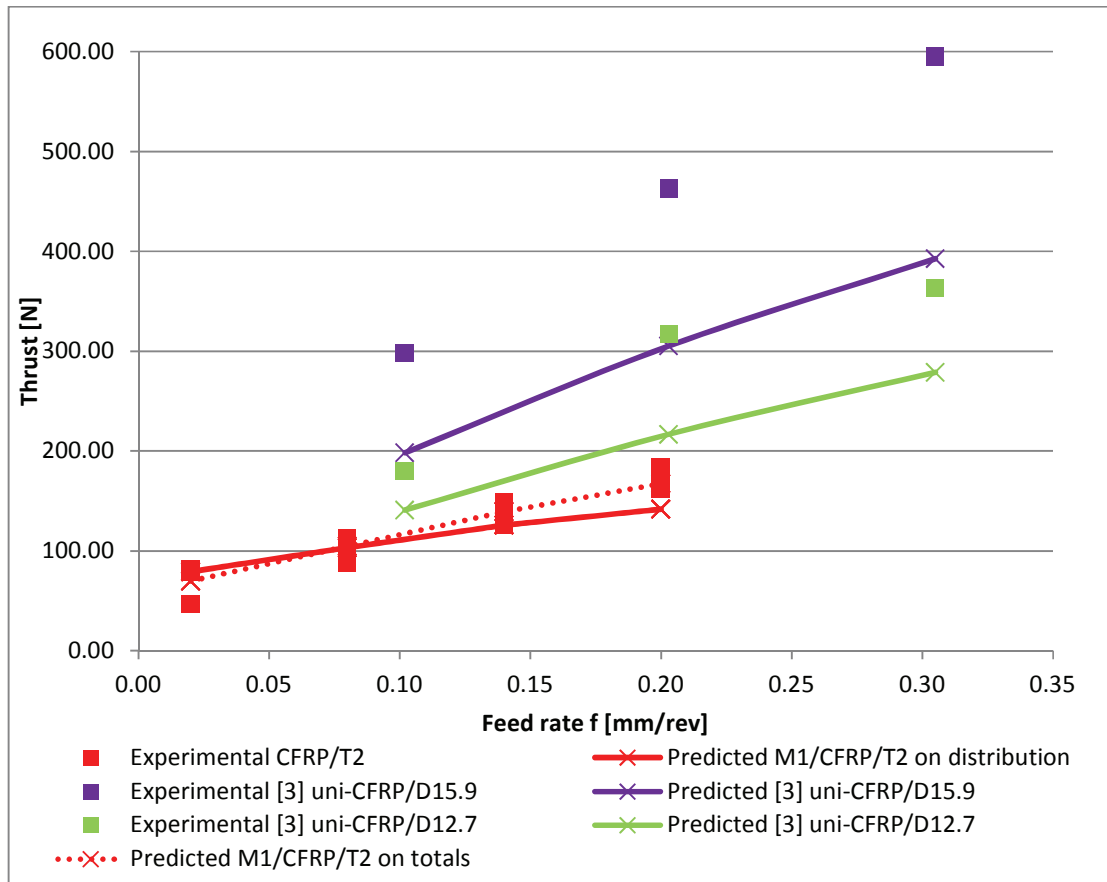


Fig. 5.7 – Comparison between experimental and predicted results of the current model and [3]

As mentioned in chapter 4.2, the tapered-drill reamer (T2) is a type of drill developed recently specifically for drilling composite materials. There is very little literature on its performance that we can relate to, except the experimental study in [16] and [22]. Although force values are reported, the study uses thin composite plates where full-engagement is not reached with this drill, therefore not easily comparable with our results. The geometry of tapered-drill reamer is rather different from any other type of drills employed in metal cutting and no analogy could be made with other drills.

The experiments reported in chapter 4.5 show that the distribution of the elementary cutting forces has a totally different pattern than for the previously analyzed drill. Using the M1 model fitted on the experimental distribution of the elementary cutting forces, the following curves (fig. 5.8) were predicted for the tapered-drill reamer case.

It is observed that the distribution of the elementary cutting forces along the radius is not captured completely for this drill; especially during stages 3 and 4 of the engagement (from $r=1.485\text{mm}$ to the outer radius – see chapter 4.4 and fig. 4.8). None of the variations of the expressions for the empirical coefficients tried (and discussed in chapter 5.2) managed to improve the results. Furthermore, the variations of the geometrical parameters as introduced along chapter 3.5, do not justify a drastic increase in the axial force component during these stages, such as recorded in the experiments.

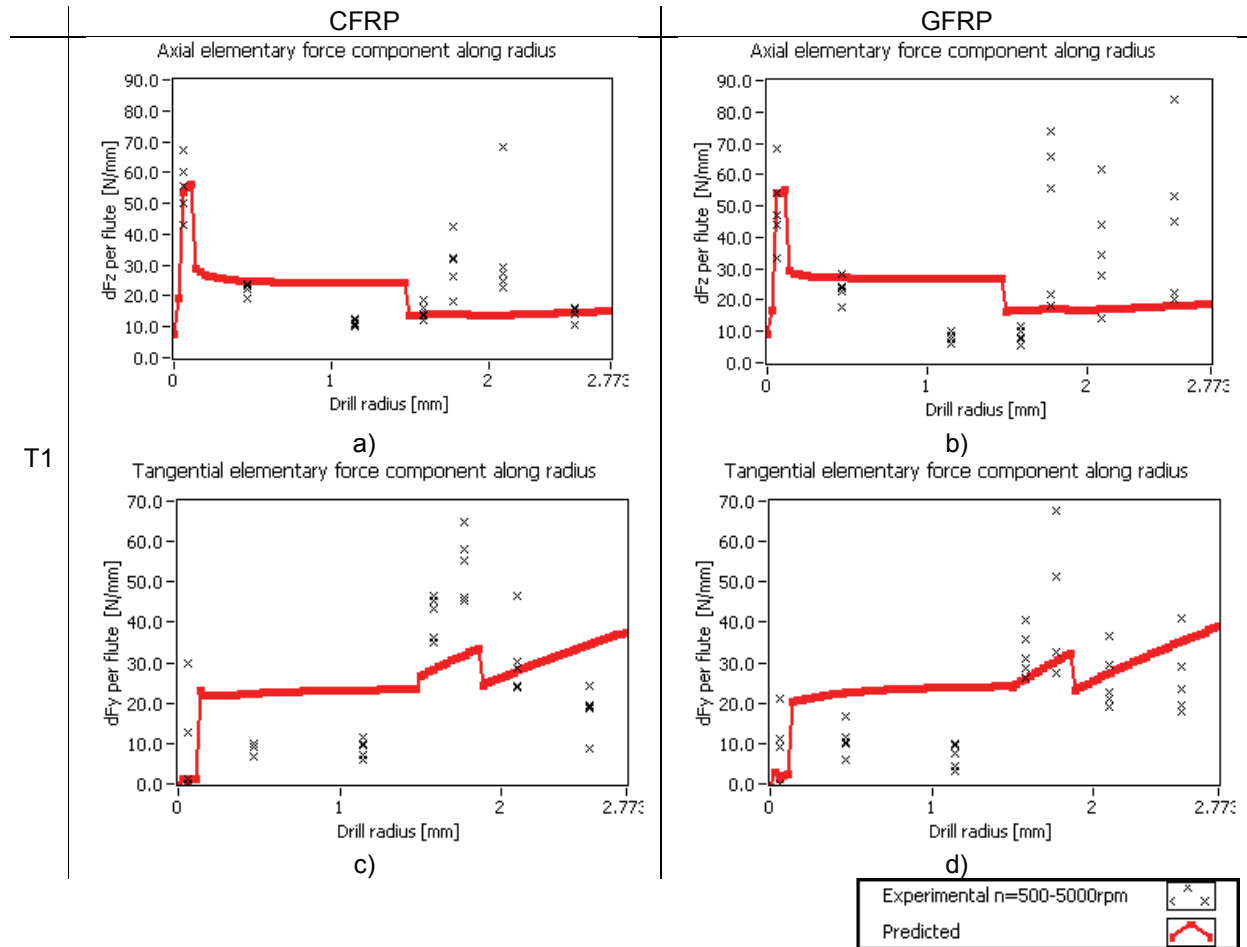


Fig. 5.8 – Comparison between predicted (M1 model, fitted on the distribution curves) and experimental elementary cutting force components distribution along the radius for $f=0.14\text{mm/rev}$, tapered-drill reamer and both work-piece materials

The following 2 hypotheses are proposed to justify this behavior, although at the current stage they cannot be accounted for in the model:

- (i) The transition from stage 3 to 4 is the theoretical point of engagement of the secondary pair of flutes (see fig. 4.6a). It is however probable that the secondary flutes will not engage suddenly (as assumed) but rather in a certain time interval, which might vary with the feed rate (depth of cut). This engagement interval would be probably captured in stage 3, where currently we consider only 2 flutes to be engaged. Additionally, the secondary flute seems to be (visually) poorly prepared for cutting (small relief angle) prior to the theoretical point of engagement, which could result in higher forces than usual. This hypothesis could help explain the rather large values recorded consistently for the second point of the stage 3, but fails to explain the rather large values recorded for stage 4 as well.
- (ii) From stage 2 to 3 (see fig. 4.6) there is a drastic change in the point angle (see fig. 3.21). Although this change is reflected in the variation of the 2nd Euler angle of rotation (τ , see fig. 3.23) which modifies the proportion between the axial and tangential elementary forces, the normal rake angle (α_n) and the inclination angle (i) which influence the efficiency of the cutting do not vary much. However, the orientation of the cutting lip changes also with respect to the fibers orientations of the composite materials. As composite materials are highly anisotropic, it might be expected that the material will behave differently and the specific cutting pressure (K_c) might experience a sudden change. However, the current model does not take into account the relative orientation between the cutting lip and cutting direction and the fibers orientation. Although it is often postulated that the

fiber direction might influence the cutting forces, no conclusive study (for bi-directional fiber composites) was previously published, based on which we could adapt our model to. We believe that such a dependency is best studied in orthogonal or oblique cutting experiments, rather than directly in drilling where the changes in the relative orientation vary discretely.

The experiments also show that there is a large variation interval of the elementary forces for the stages 3 and 4 of T1 drill. Further studies should also attempt to improve the reliability of the experimentally obtained distribution curves, following the suggestions made in chapter 4.5.

Although the fitting method on the distribution curves does not yield satisfying results, when fitted on the total thrust and torque values, the model becomes very accurate as outlined in figure 5.9 (the coefficients are reported in table 5.3).

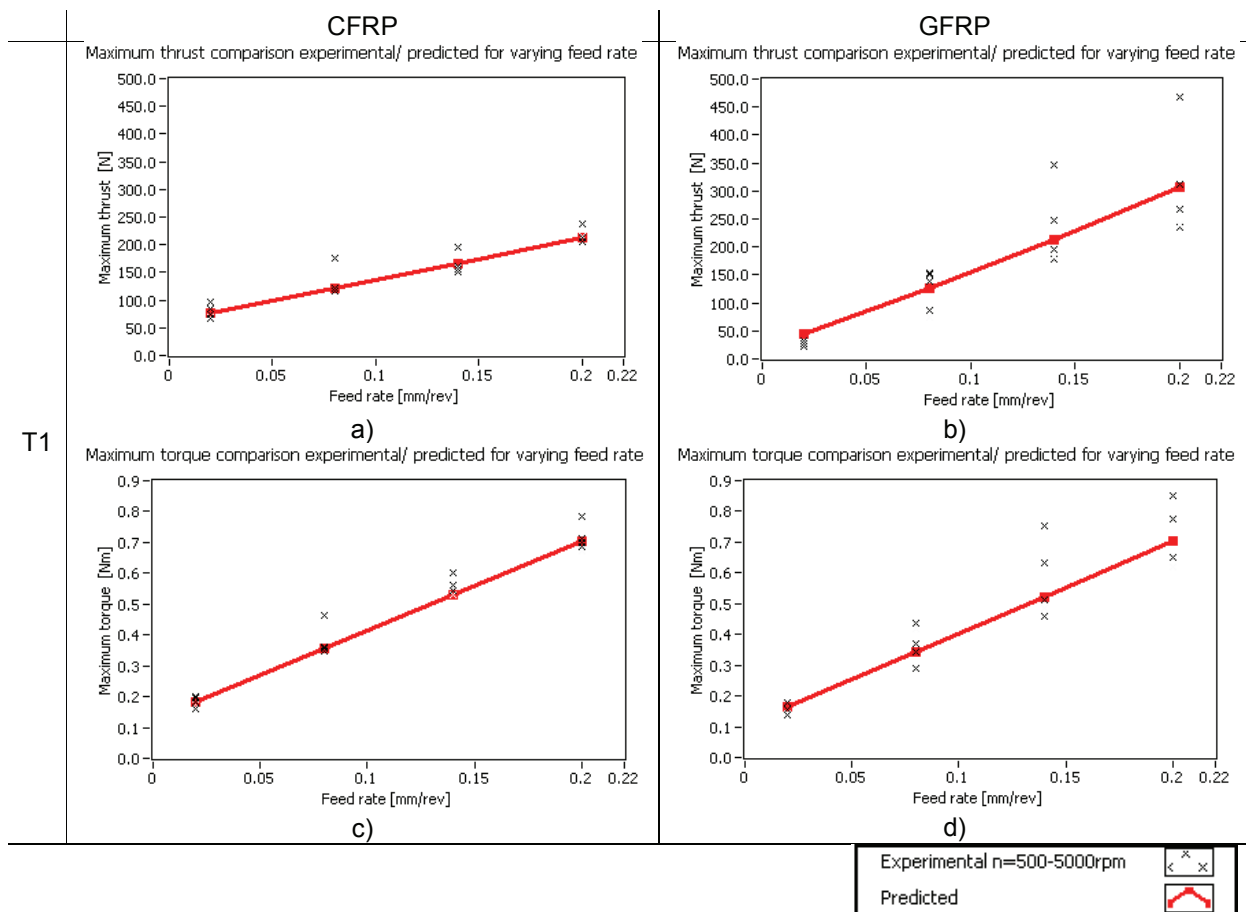


Fig. 5.9 – Comparison between predicted and experimental (filtered) results for maximum thrust and torque for varying feed rate, T1 and both work-piece materials, M1 fitted on the total forces values

Summarizing, in the current chapter we have shown the excellent capabilities of our mechanistic model to predict the total thrust and torque forces in drilling fiber reinforced composites. Additionally, the model can reasonably predict the distribution of the axial and tangential elementary forces along the drill radius for two different drill types. We are confident that the model can be applied to different types of drills as long as they can be described mathematically and also to different work-piece materials including metals. By improving the accuracy of the experimental distribution curves the influence of various geometric and cutting parameters over the empirical coefficients can be studied and implemented in the model, thus improving the prediction capabilities of the elementary cutting forces distribution.

Chapter 6

Conclusions

6.1 On experimental analysis of the drilling process

Through the experimental analysis presented in detail in chapter 4, it was shown that a greater amount of information can be extracted from simple cutting force measurements during drilling experiments. The distribution of the drilling loads (axial and tangential elementary force component) along the drill radius (or on each ply) is particularly useful for drilling analysis of layered structures such as long-fiber reinforced composite laminate materials, where inter-laminar damage (delamination) is likely to occur. Furthermore, this technique can also be used in solving problems related to drilling metals, such as the optimization of the drill geometry or the minimization of the exit burrs when drilling soft metallic alloys.

It was shown that the maximum loads occur on the plies in contact with the tool tip (see figures 4.12 and 4.13). It is the moment when the drill tip exits the work-piece that is very likely to initiate exit delamination. The consideration of the possibility that the initial inter-laminar crack extends beyond the boundaries of the future hole (generating measurable delamination), or additional propagation occurs as the drill continues its path towards exiting the work-piece is beyond the scope of the current study. However, it is believed that the results presented hereby can be used for more accurate simulations of the delamination defects during drilling by numerical models (such as [12, 14]). The experimentally obtained distribution (or by the model introduced in this thesis) can be used as inputs in a numerical simulation of the drilling process to study the behavior of the work-piece under the drilling loads (i.e. study the onset and propagation of the delamination defect). A recent numerical simulation of drilling published in [52] imposes a drill movement onto a work-piece (composite) and uses failure criterions to remove material, while recording resulting forces and delamination amounts. The authors state that it takes 4 months of simulation for a drilling case, which is to be expected from such a brute approach in modeling the drilling process. Implementing the drilling loads (obtained either experimentally or by the model presented in the current thesis) will most likely significantly decrease the computation time and probably provide better accuracy in the force modeling.

Although somewhat less accurate, it was shown that the distribution of the tangential forces as well can be determined. No delamination model currently considers the effect of the tangential forces (if any), but they are believed to play a key role in causing the entry delamination, which cannot be explained by only considering the axial loads.

For lowering the critical loads, it was shown (fig. 4.12 and 4.13) that the geometry of the drill (especially the geometrical configuration of the chisel edge area) and the axial feed rate (f) are the most important parameters. Lowering the size of the chisel edge (as for the tapered drill reamer - T1) or performing an additional web-thinning grinding (as for the 8-facet twist drill T3) will make the cutting in close vicinity of the tool axis more efficient and therefore lower the chances of delamination onset. The maximum loads, but also the overall cutting forces distribution, seem to be directly proportional with axial feed rate. Within the experimental domain, the spindle speed has only a limited influence on the cutting loads distribution; therefore this could be used as a means to increase productivity when needed without increasing the chances of delamination. When analyzing only the maximum values of thrust and torque (as in table 4.5), spindle speed seems to have an increased importance, especially on the value of the torque. It is believed that this effect is due to the increased amplitude around the nominal values at higher rotational speeds, an effect which is diminished by the smoothing of the data performed in order to obtain the distribution. These results of the cutting parameters' influences over the extent of delamination defect correspond to the conclusions of Davim in [46] and other researchers.

The mechanical properties of carbon-fiber reinforced plastics are better than those reinforced by glass-fiber (see table 4.1). However, the machinability (the ease with which a material can be machined) appears to be comparable. Overall, the average maximum thrust over all tested conditions is 3% higher for CFRP than GFRP, while the average maximum torque is 20% higher for GFRP (which is visible also for the small selection of experimental results reported in table 4.5). Small, powder-like chips were noted when drilling CFRP composites, while coarser and, under certain conditions, long chips were observed during GFRP drilling.

The current technique for obtaining the cutting forces distribution is the most reliable in analyzing the axial loads. Problems were encountered in its application to high spindle speeds (over 5000rpm) and low feed rates (0.02-0.08mm/rev). To extend the investigation to the high-speed domain more reliable torque measuring equipment must be employed. As alternatives, for experimental investigations, it is recommended to use an increased feed rate or a higher diameter tool.

The experimental results of maximum thrust and torque experience similar trends with the variation of the cutting parameters as reported by others reported in literature (see table 4.5 and chapter 4.5 for discussions). The method of obtaining the cutting forces distribution from simple drilling experiments is pushing the boundaries of the state-of-art in the field of experimental investigation of the drilling process for both fiber-reinforced composites and other materials to provide new insights into the process. The elementary cutting forces distribution during drilling is for the first time presented and analyzed. We note that the spindle speed plays a diminished role (fig. 4.9, 4.10 and 4.11), due to the fact that apparently it only affects the amplitude of the nominal force readings, and the nominal values (rather than the raw data, see fig. 5.1) are differentiated to obtain the distribution.

6.2 On modeling the cutting forces in drilling

The main objective of the current PhD thesis was to build a model for predicting the cutting forces in drilling of fiber reinforced composites with an emphasis on their distribution which was shown to be of interest for this particular type of material in chapter 1. Unlike metals, where the structure is isotropic, composite materials have a strong anisotropy, leading to different responses under drilling loads at various points within their structure, often resulting in internal defects (i.e. delamination).

A “mechanistic” model for predicting the cutting forces occurring during drilling of fiber reinforced composites, focused at obtaining reliable information on their distribution along the cutting edges of the drill was introduced in chapter 3. The “mechanistic” term refers to the definition of the elementary cutting forces along the normal and friction directions on both rake and relief faces, considering the oblique cutting model and using experimentally obtained coefficients.

The mathematical representation of drill geometry in the scope of cutting force modeling has been revised and improved. Most notable is the consideration given to the cutting angle (μ , an effect of the movement of the drill along its axis) and its influence across all the geometrical parameters describing the oblique cutting force elements and the elementary cutting forces decomposition to obtain the thrust and torque especially in the cutting lip region. The importance of this improvement is presented in fig. 5.4 and discussed in chapter 5.3 and allows us to capture the increase of the elementary cutting forces in particular regions of the drill when axial feed is increasing. Further clarifications on the underlying assumption used to derive the geometrical parameters of the element along the chisel edge are also given, and a new derivation is presented for a particular case (of the inclined chisel edge with respect to the drill axis).

Through experimental work introduced in chapter 4 and published in [15] as well as through model results (chapter 5.3), it was shown that the drill geometry plays a very important role in the distribution of the drilling loads along the cutting edges of the drill and that chances of internal defects could be minimized by optimizing the drill geometry. The current model manages to capture most of the influence of the geometry over the resulting drilling loads, proven by the fact that good results are obtained with only three constant coefficients (as detailed in chapter 5.2). However, as the coefficients are proved to be drill type dependent we believe that we were not able to capture all the geometrical influence on the development of the cutting forces (see discussion in chapter 5.3). The number of coefficients has been kept to a minimum and they have been selected to be as intuitive as possible for practical reasons of simplicity. The accuracy of the model can be further improved by considering the coefficients as functions of other parameters currently ignored (cutting velocity, rake angle etc.). It is also noted that only one model and set of coefficients are used for both the chisel edge and cutting lip regions of the drill, unlike many of the previously introduced drilling force models in both metal and composite cutting (which will need to employ drilling with pilot holes for model calibration).

The introduction of the coordinate system transformation matrix to easily relate oblique cutting to drilling (chapter 3.2) and allowing for a higher degree of generalization of the geometrical parameters of the drills (see chapter 3.4 and 3.5) was also found to be of practical importance. The same transformation matrix and mathematical model for drill geometry has been successfully used to apply the cutting force model to the drilling cases with two very different drill types (see chapter 3.5), showing the flexibility of the method.

The model has been calibrated for the cutting force distribution rather than the total thrust and torque forces in order to obtain reliable distribution functions (chapter 5.2 and 5.3). This method also has the potential to decrease the number of experiments needed to calculate a set of empirical coefficients, although the challenge lies in obtaining reliable distribution curves. For improving the accuracy of the model in predicting the total values of thrust and torque, the model can also be calibrated on these total values. Both calibration methods are proven to be having prediction capabilities much better than the previous cutting force models [3] developed for composite materials as shown in fig. 5.7. We believe that the foremost reason for this improvement is the consideration of the forces acting on the relief face. This

improvement has been obtained in the same time as the number of empirical coefficients has been decreased.

Several assumptions have been made (the “mechanistic” structure of the elemental cutting forces due to the lack of a more suitable theoretical model like the shear-angle model in metal cutting; the chip flow angle etc.) which deserve to be addressed and improved in further research efforts.

6.3 Outlook

The work presented in the current thesis was initially planned to be only a first part of a more extensive study focused on delamination-free drilling of fiber reinforced composites. The elementary cutting forces distribution was to be used in a numerical simulation model of the drilling process able to capture the onset and propagation of the delamination defect and an optimization tool for selecting the cutting parameters and the drill type for delamination-free drilling was initially proposed. These objectives however can be still achieved by further studies. The conclusions of the current thesis supports the fact that significant improvements towards delamination-free drilling of fiber reinforced composites can be achieved by selecting an appropriate drill or developing novel drill designs for composite materials, while the choice of drill should be correlated with the cutting parameters selection for improving production time.

The cutting forces prediction model can be further developed to take into consideration the thermal aspects of the drilling process and probably drill temperature prediction models can be obtained. Such insights could prove valuable in studying the tool wear, another major problem that machining fiber reinforced composites is facing. As the heat is believed to be mostly generated by friction between work-piece and tool, we believe that such a model could be fairly easily developed starting from the current model for predicting the cutting forces (including the friction forces), although a more important challenge would be to validate experimentally the predicted temperature field. Probably, the powder-like chips obtained when machining fiber reinforced composites are not suitable for evacuating the heat generated during cutting and temperature build-up occurs on the tool edges.

The modeling of the cutting forces could be also improved. There is currently a need for a fracture-based cutting force model which promises to better capture the particularities of machining fiber reinforced composites and brittle materials. Such a model will most likely be developed for orthogonal and oblique cutting, but could be later implemented in a drilling model using developments presented in the current thesis. A method to correlate the cutting direction with the fiber orientation is also desired for drilling and for other machining processes; although this relationship should also be captured in expressions of the elementary cutting forces (either if the current mechanistic approach is employed or a new theory based on fracture mechanics is proposed).

A lot of work is needed to model more drill geometries (or features) mathematically to extend the usability of the current model or others alike. Such work should be conducted in close collaboration with drill manufacturers, as information about the operations needed to obtain certain drill geometries is not available to the public. Such partnerships could also undertake optimization studies of the drill geometry; as such studies need also consider other functional properties of the drills (i.e. stiffness, centering capabilities, buckling resistance etc.) besides the cutting efficiency. The tools and methods for experimental analysis of the drilling process can also be improved. Several suggestions in this respect have been made in chapter 4.5.

Summarizing, there are important steps that could and probably will be undertaken in the next years to optimize the drilling process in general and to better adapt it to fiber reinforced composites or other novel materials. As the machining processes have the disadvantage of generating important mechanical and thermal loads upon the work-piece, and drilling in particular along the weakest direction of the composite plates, special attention should be given to new and non-conventional processes to obtain hole-like features in fiber reinforced composite plates. Among such processes, the author believes that sand-blasting (or known as powder-blasting) could satisfy many of the particular demands required for making such features in composite plates.

References

- [1] Merchant, M.E. – *Mechanics of the metal cutting process – I. Orthogonal cutting and type 2 chip*, Journal of Applied Physics, Vol. 16, no. 5, p. 267-275, 1945
- [2] Chandrasekharan, V. – *A model to predict the three-dimensional cutting force system for drilling with arbitrary point geometry*, PhD Thesis, University of Illinois at Urbana-Champaign, 1996
- [3] Chandrasekharan, V.; Kapoor, S.G.; DeVor, R.E. – *A mechanistic approach to predicting the cutting forces in drilling: with application to fiber-reinforced composite materials*, Transaction of the ASME, Journal of Engineering for Industry, vol. 117, p. 559-570, 1995;
- [4] Langella, A.; Nele, L.; Maio, A. – *A torque and thrust prediction model for drilling of composite materials*, Composites: Part A, vol. 36; p. 83-93, 2005;
- [5] Stephenson, D.A.; Agapiou, J.S. – *Calculation of main cutting edge forces and torque for drills with arbitrary point geometries*, International Journal of Machining Tools and Manufacturing, vol. 32, no. 4, p. 521-538, 1992
- [6] Hocheng, H.; Tsao, C.C. – *The path towards delamination-free drilling of composite materials*, Journal of Materials Processing Technology, vol. 167, p. 251-264, 2005
- [7] Hocheng, H.; Tsao, C.C. – *Comprehensive analysis of delamination in drilling of composite materials with various drill bits*; Journal of Materials Processing Technology, vol. 140; p.335-339; 2003;
- [8] Tsao, C.C.; Hocheng, H. – *Effect of eccentricity of twist drill and candle stick drill on delamination in drilling composite materials*, International Journal of Machine Tools & Manufacture, vol. 45, p. 125-130, 2005
- [9] Anderson, T.L. – *Fracture mechanics: Fundamentals and Applications*, 3rd edition, Taylor & Francis, 2005;
- [10] Redouane, Z. – *Analyse des conditions d'usinage lors du perçage de structures composites fibres longues en carbone epoxy*, Thèse de Doctorat, Université Paul Sabatier Toulouse, 2004
- [11] Durao, L.M.P; de Moura, M.F.S.F.; Marques, A.T. – *Numerical simulation of the drilling process on carbon/epoxy composite laminates*, Journal of Composites: Part A, vol. 37, p. 1325-1333, 2006
- [12] Zitoune, R.; Collombet, F. – *Numerical prediction of the thrust force responsible of delamination during the drilling of the long-fiber composite structures*, Journal of Composites: Part A, vol. 38, p. 858-866, 2007
- [13] Zitoune, R.; Collombet, F.; Lachaud, F.; Piquet, R. ; Pasquet, P. – *Experiment-calculation comparison of the cutting conditions representative of the long fiber composite drilling phase*, Journal of Composites Science and Technology, vol. 65, p. 455-466, 2005
- [14] Lachaud, F.; Piquet, R.; Collombet, F.; Surcin, L. – *Drilling of composite structures*, Journal of Composite Structures, vol. 52, p.511-516, 2001;
- [15] Lazar, M.B.; Xirouchakis, P. – *Experimental analysis of drilling fiber reinforced composites*, Int. J. Mach. Tool and Manufacture, vol. 51, p. 937-946, 2011
- [16] Fernandes, M.; Cook, C. – *Drilling of carbon composites using a one shot drill bit. Part I – Five stages representation of drilling and factors affecting maximum force and torque*, International Journal of Machine Tools & Manufacture, vol. 46, p. 70-75, 2006
- [17] Lin, S.C.; Chen, I.K. – *Drilling carbon fiber-reinforced composite material at high speed*, Wear, vol. 194, p. 156-162, 1996
- [18] Chen, W.C. – *Some experimental investigations in the drilling of carbon fiber-reinforced plastic (CFRP) composite*, International Journal of Machining Tools Manufacturing, vol. 37, no. 8, p. 1097-1108, 1997
- [19] Ucar, M.; Wang, Y. – *End-milling machinability of a carbon fiber reinforced laminated composite*, Journal of Advanced Materials, vol. 37, No. 4, p.46-52; 2005;
- [20] Stephenson, D.A.; Agapiou, J.S. – *Metal Cutting Theory and Practice*, 2nd edition, Taylor & Francis, 2006
- [21] Ramulu, M.; Young, P.; Kao, H. – *Drilling of Graphite/Bismaleimide Composite Material*, Journal of Materials Engineering and Performance, vol. 8, p.330-338, 1999
- [22] Fernandes, M.; Cook, C. – *Drilling of carbon composites using a one shot drill bit. Part II – Empirical modeling of maximum thrust force*, International Journal of Machine Tools & Manufacture, vol. 46, p. 76-79, 2006

- [23] Shaw, M.C.; Oxford, C.J. – *On drilling of metals 2 – The torque and thrust in drilling*, Transactions of ASME, vol. 79, p. 139-148, 1957
- [24] Rubenstein, C. – *The torque and thrust force in twist drilling – I. Theory*, Int. J. Mach. Tools Manufact., vol. 31, no. 4, p. 481-489, 1991
- [25] Tsao, C.C.; Hocheng, H. – *Computerized tomography and C-Scan for measuring delamination in the drilling of composite materials using various drills*, International Journal of Machine Tools & Manufacture, Vol. 45, p. 1282-1287, 2005
- [26] Seif, M.A.; Khashaba, U.A.; Rojas-Oviedo, R. – *Measuring delamination in carbon/epoxy composites using a shadow moiré laser based imaging technique*, Composite Structures, Vol. 79, p. 113-118, 2007
- [27] Drahan, C.K.H.; Ho-Cheng, H. – *Delamination during drilling in composite laminates*, Transactions of the ASME, Journal of Engineering for Industry, vol. 112, p. 236-239, 1990
- [28] Sakuma, K.; Seto, M. – *Tool wear in cutting glass-fiber-reinforced plastics (The relation between fiber orientation and tool wear)*, Bulletin of the JSME, vol. 26, no. 218, p. 1420-1427, 1983
- [29] Merchant, M.E. – *Mechanics of the metal cutting process – II. Plasticity conditions in orthogonal cutting*, Journal of Applied Physics, Vol. 16, p. 318-324, 1945
- [30] Connolly, R.; Rubenstein, C. – *The mechanics of continuous chip formation in orthogonal cutting*, Int. J. Mach. Tool Des. Res., vol. 8, p. 159-187, 1968
- [31] Watson, A.R. – *Drilling model for cutting lip and chisel edge and comparison of experimental and predicted results – I. Initial cutting lip model*, Int. J. Mach. Tool Des. Res., vol. 25, no. 4, p. 347-365, 1985
- [32] Altintas, Y. – *Manufacturing Automation – Metal Cutting Mechanics, Machine Tool Vibrations and CNC Design*, Cambridge University Press, 2000
- [33] Caprino, G.; Nele, L. – *Cutting forces in orthogonal cutting of unidirectional GRFP composites*, Journal of Engineering Materials and Technology, ASME, vol. 118, p. 419-425, 1996
- [34] Stabler, G.V. – *The chip flow law and its consequences*, Advances in Machine Tool Design and Research, vol. 5, p.243-251, 1964
- [35] Watson, A.R. – *Drilling model for cutting lip and chisel edge and comparison of experimental and predicted results – I. Revised cutting lip model*, Int. J. Mach. Tool Des. Res., vol. 25, no. 4, p. 367-376, 1985
- [36] Oxley, P.L.B. – *An analysis for orthogonal cutting with restricted tool-chip contact*, Int. J. Mech. Sci., vol. 4, p. 129-135, 1962
- [37] Rubenstein, C. – *The edge force components in oblique cutting*, Int. J. Mach. Tools Manufact., vol. 30, no. 1, p. 141-149, 1990
- [38] Basuray, P.K.; Misra, B.K.; Lal, G.K. – *Transition from ploughing to cutting during machining with blunt tools*, Wear, vol. 43, p. 341-349, 1977
- [39] Oxford, C.J.; Rochester, M. – *On drilling of metals 1 – Basic mechanics of the process*, Transactions of ASME, vol. 77, p. 103-114, 1955
- [40] Armarego, E.J.A.; Rotenberg, A. – *An investigation of drill point sharpening by the straight lip conical grinding method – I. Basic analysis*, Int. J. Mach. Tool Des. Res., Vol. 13, p. 155-164, 1973
- [41] Armarego, E.J.A.; Rotenberg, A. – *An investigation of drill point sharpening by the straight lip conical grinding method – II. A criterion for selecting a solution*, Int. J. Mach. Tool Des. Res., Vol. 13, p. 165-182, 1973
- [42] Galloway, D.F. – *Some experiments on the influence of various factors on drill performance*, Transactions of the ASME, p.191-231,1957
- [43] Armarego, E.J.A.; Pramanik, D.; Smith, A.J.R.; Whitfield, R.C. – *Forces and Power in Drilling – Computer Aided Predictions*, Journal of Engineering and Production, vol. 6, p. 149-174, 1983
- [44] Mallick, P.K. and others – *Composites engineering handbook*, Marcel Dekker Inc., 1997
- [45] Enemuoh, E.U.; El-Gizawy, A.S.; Okafor, A.C. – *An approach for development of damage-free drilling of carbon fiber reinforced thermosets*, International Journal of Machine Tools & Manufacture, vol. 41, p. 1795-1814, 2001
- [46] Davim, J.P.; Reis, P. – *Drilling carbon fiber reinforced plastics manufactured by autoclave – experimental and statistical study*, Journal of Materials and Design, vol. 24, p. 315-324, 2003
- [47] Mohan, N.S.; Ramachandra, A. ; Kulkarni, S.M. – *Influence of process parameters on cutting force and torque during drilling of glass-fiber polyester reinforced composites*, Composite Structures, vol. 71, p. 407-413, 2005

- [48] Malhotra, S.K. – *Some studies on drilling of fibrous composites*, Journal of Materials Processing Technology, vol. 24, p. 291-300, 1990
- [49] Watson, A.R. – *Geometry of drill elements*, Int. J. Mach. Tool Des. Res., vol. 25, no. 3, p. 209-227, 1985
- [50] Watson, A.R. – *Drilling model for cutting lip and chisel edge and comparison of experimental and predicted results – III. Drilling model for chisel edge*, Int. J. Mach. Tool Des. Res., vol. 25, no. 4, p. 377-392, 1985
- [51] Watson, A.R. – *Drilling model for cutting lip and chisel edge and comparison of experimental and predicted results – IV. Drilling tests to determine chisel edge contribution to torque and thrust*, Int. J. Mach. Tool Des. Res., vol. 25, no. 4, p. 377-392, 1985
- [52] Isbilir, O.; Ghassemieh, E. – *Finite element analysis of drilling of carbon fibre reinforced composites*, Appl. Compos. Mater., DOI 10.1007/s10443-011-9224-9, 2011

CURRICULUM VITAE

PERSONAL INFORMATION

Name **Mihai-Bogdan LAZAR**
Address Chemin du Mont-Blanc 9, 1023, Crissier, Vaud, Switzerland
Telephone Mobile: +41 (0) 78 626 02 83; Home: +41 (0) 21 545 67 32; Office: +41 (0) 21 693 38 68
E-mail bogdan.lazar@epfl.ch / webmaster@bogdanlazar.ro
Nationality Romanian (residence permit type "B" in Switzerland)
Marriage status Married, 1 child
Date of birth 10.06.1980

WORK EXPERIENCE

Dates : November 2004 – February 2007
Employer: Huro Super Mold SRL Timisoara, Romania (subsidiary of [Hummel Formen GmbH](#), Germany)
Type of business or sector: Design and manufacture of plastic molding tools for automotive industry
Occupation or position held: Computer Aided Design Engineer
Main activities and responsibilities: Design of plastic molding tools using CATIA V5 from concept, detailed 3D design, technical 2D drawings and user documentation.

EDUCATION AND TRAINING

Dates : March 2007 – present
Organization: Laboratory for Computer-Aided-Design and Production ([LICP](#)), Swiss Federal Institute of Technology in Lausanne (EPFL), Switzerland
Principal subjects: Cutting force modeling for drilling fiber-reinforced composites (PhD thesis); CAD/CAM methods, process planning, product life-cycle (teaching assistant)
Title of qualification awarded: (PhD title estimated to be awarded by February 2011)

Dates : October 2003 – September 2004
Organization: [Thermal Fluids Engineering Laboratory](#), Tokyo University of Agriculture and Technology, Japan
Principal subjects: Numerical simulation of heat and mass transfer by oscillating flow inside a "dream-pipe" (research project, FEM software "FLUENT");
Title of qualification awarded: Diploma for completing the Short-Term Exchange Program (STEP) as graduate student

Dates : October 2003 – October 2004
Organization: Mechanical Faculty, University "Politehnica" Timisoara, Romania
Principal subjects: Computer Aided Design systems
Title of qualification awarded: Master Engineer

Dates : October 1998 – July 2003
Organization: Material Science and Engineering Department, University "Politehnica" Timisoara, Romania
Principal subjects: Numerical Simulation of copper pipe extrusion by large deformations (Diploma project)
Title of qualification awarded: Engineer diploma (Material Science and Engineering)

Dates: September 1994 – July 1998
Organization: Theoretical High School no. 2 Resita
Principal subjects: Informatics
Title of qualification awarded: Diploma / Computer Operator and Programmer

PERSONAL SKILLS AND COMPETENCES

LANGUAGES	ROMANIAN: Mother tongue ENGLISH: Excellent (TOEFL: Paper-based Test Oct.2005 –Score 623/677; TWE:3.0) FRENCH: Intermediate (Level B2 – EPFL Language Center) JAPANESE: Basic (TUAT Language Center)
SOCIAL SKILLS AND COMPETENCES	Living in international environments (Japan 2003-2004 and Switzerland 2007-present) has greatly improved my understanding of foreign cultures and my communication skills.
ORGANIZATIONAL SKILLS AND COMPETENCES	Student association activities: - 1999 – 2001 – member and vice-president of Student Association in Mechanical Engineering Faculty, UP Timisoara, Romania; - 2008 – present – member of the organizational committee of Romanian Student Association – ARO at EPFL Lausanne, Switzerland
TECHNICAL SKILLS AND COMPETENCES	CAD/CAM: CATIA V5 (part and assembly design, surfaces and machining modules – 8 years) FEA: FLUENT (1 year), DEFORM (0.5 years), ANSYS SCIENTIFIC: MathCAD (4 years); LabView (1 years) OFFICE: Microsoft Word, Excel, PowerPoint, Outlook, Access IMAGE PROCESSING: Adobe Photoshop, Photomatix
ARTISTIC SKILLS AND COMPETENCES	Travel photography (www.bogdanlazar.ro)
OTHER SKILLS AND COMPETENCES	Autumn 2009 – attended and graduated “Venture Challenge” a VentureLab@EPFL practical course on start-ups
DRIVING LICENCE(S)	B category (since 2005)
PUBLICATIONS	Lazar, M.B.; Xirouchakis, P. – <i>Experimental analysis of drilling fiber reinforced composites</i> , Int. J. Mach. Tool and Manufacture, vol. 51, p. 937-946, 2011
REFERENCES	Available on request possibly from: <ul style="list-style-type: none">- Prof. Paul Xirouchakis (EPFL, Switzerland)- Prof. Sadanari Mochizuki (TUAT, Japan)- Prof. Roland Cucuruz (UPT, Romania)- Mr. Michael Rücker (Huro Supermold, Romania)